NIELS BOHR INSTITUTE
FACULTY OF SCIENCE
UNIVERSITY OF COPENHAGEN

Exploring the Dark and Dusty Universe with Gravitational Lensing

Árdís Elíasdóttir

Dark Cosmology Centre

Supervisor: Jens Hjorth
Co-supervisor: Anja C. Andersen

A thesis submitted for the degree of
Doctor of Philosophy
on December 12, 2007.

This thesis is dedicated to Sigrún Guðbrandsdóttir (1912-2002).

Nú afhjúpast ljósin um alstirndan himinvöllinn
unz endalaus geimurinn skín,
og vegmóðir geislar hans, sumir jafn-fornir og fjöllin
fljúga til mín og þín.

Jón Helgason

Acknowledgements

Let us be grateful to people
who make us happy;
they are the charming gardeners
who make our souls blossom.
Marcel Proust (1871-1922)

This thesis marks the end of a long journey which I could not have completed on my own and I wish to acknowledge some of the people who have helped me reach this goal.

First of all, I would like to thank my fantastic advisor Jens Hjorth for not resembling Prof. Smith[1]. More specifically I thank him for excellent advice, many motivating discussions and having the patience to explain to me what a 2D spectrum is. I thank my co-advisor Anja C. Andersen for being an endless source of encouragement and an inspiring role model. Many thanks go to Gunnlaugur Björnsson (Gulli) for his guidance and advice and especially for introducing me to Jens and his group. I thank all my collaborators who have, in addition to contributing to the work presented in this thesis, taught me various things about astrophysics - even observations. I would like to thank all my great co-workers at DARK for creating a motivating and fun environment to do science in. I also thank them for helpful discussions regarding astrophysical phenomena and for never (seemingly) getting tired of my questions or odd remarks. I thank the members of 'ANGLES' for all the fun that was had in workshops and schools. I thank the KITP at UCSB for hosting me during the 'Applications

---

[1] http://www.phdcomics.com/comics/archive.php?comicid=848

Abstract

In this thesis, gravitational lensing is used as a tool to study the dusty and dark distant universe. The first part of the thesis presents the first systematic study of dust extinction in lensing galaxies using gravitationally lensed background quasars. It is shown the these galaxies vary greatly both in the amount and type of dust and can vary significantly from the dust seen in the Milky Way. This is a significant result since, due to lack of knowledge on extragalactic dust, Milky Way type of extinction is frequently assumed when calibrating high precision cosmological data (e.g. supernova Ia dark energy surveys). Studying the dust extinction in the very large lensing data sets which will arise serendipitously in future planned space based missions (such as the SNAP dark energy survey), it will be possible to constrain the evolution of dust with redshift and morphology, providing these surveys with an independent estimate of one of their major sources of systematic error.

The second topic of this thesis is dark matter in galaxies and clusters. It starts with a theoretical study of the strong lensing properties of the Sérsic profile and compares it to those of the NFW profile. The NFW profile is the standard description of dark matter, but recently it has been suggested that the Sérsic profile, more commonly used to describe baryonic matter in galaxies, may be a more accurate description. The results show that it is often possible to find an NFW profile which accurately reproduces the strong lensing signal of a Sérsic profile. However, in other cases, the difference between these profiles could contribute to explaining the discrepancy in the mass and concentration estimates from strong lensing on the one hand, and from weak lensing and X-ray measurements on the other.

Next, a mass reconstruction of the galaxy cluster Abell 2218 is deduced using strong lensing constraints. The mass distribution is found to be bimodal in agreement with previous models of Abell 2218. However, the second large scale dark matter clump is found to be larger and with a flatter core than previous models have found. This flatness is further supported by 'blind tests' which do not place galaxy sized components near its centre. An analysis of the cluster galaxies in velocity space finds evidence for two substructures corresponding to the two large scale dark matter halos. The X-ray data and the distribution in velocity space are found to support the interpretation that the bimodal mass distribution arises from a cluster merger. It is also shown that strong lensing constraints can reliably detect substructure, dark or luminous, if the substructure is massive or locally perturbs a system.

Finally, the thesis closes with a short discussion on two smaller projects related to lens modelling. The first is the concentration of the mass distribution in the galaxy cluster Abell 1689, which is found to be marginally higher than values expected from numerical simulations. The second is the possible lensing of the gamma ray burst GRB 050509B. This gamma ray burst is associated both with an elliptical galaxy and with a galaxy cluster, which could be foreground objects lensing the burst. It is shown, assuming that the gamma ray burst is a background source, that it is most likely only weakly affected by lensing.

Contents

List of Figures

List of Tables

Chapter 1

Introduction

I want to know all Gods thoughts;
all the rest are just details.
Albert Einstein (1879-1955)

This thesis deals with subjects related to the dusty and dark universe as seen by gravitational lensing. Gravitational lensing is the deflection of a light ray due to the distortion of spacetime caused by a gravitational potential along its path. This can cause background images, perturbed by the gravitational potential of an intervening mass distribution, to be magnified, distorted or even multiply imaged as will be discussed in more detail in Chapter 2. This thesis does not deal with the gravitational lensing effect in itself, but rather utilises it to study various phenomena which are hard or impossible to study using other means.

The first topic of this thesis, presented in Chapter 3, is dust in extragalactic environments and the extinction it causes for light passing through. This work is important for any cosmological and astrophysical probe where the data need to be carefully calibrated, as incorrect assumptions on the dust properties can cause a non-negligible bias in derived quantities. As an example, a full understanding of the evolution of dust with redshift will be needed for the future planned supernovae IA (SNe Ia) surveys, which aim to study the evolution of the dark energy content as a function of redshift (see e.g., Wood-Vasey et al., 2007). Additionally, this work is important for galaxy formation studies, as the composition and amount of dust is related to the formation history of the galaxy.

1. INTRODUCTION

Probing dust extinction at high redshift is a challenging task, and the traditional method of comparing the line of sight to two standard stars is not applicable as individual stars cannot be resolved in distant galaxies. Therefore, although the dust extinction in the Milky Way has been extensively mapped, very little is known about dust extinction in more distant galaxies. The work presented in Chapter 3 looks at the extinction in 10 lensing systems at redshifts up to $z \sim 1$. The results show that the type and amount of extinction can vary greatly but no reliable trend is found with redshift, although the data can not exclude redshift evolution either. To reach more statistically robust results on the possible evolution of dust with redshift, larger samples are needed. The prospects of acquiring such samples in future dark energy mission (e.g. the SuperNova Acceleration Probe) are discussed.

The second part of this work is on inferring the dark matter distribution in galaxies and clusters using lensing. It opens with a theoretical study, presented in Chapter 4, on the differences in the strong lensing signals of two dark matter profiles, the Navarro-Frenk-White (NFW) and the Sérsic profiles. The NFW profile is the standard description of dark matter, but recently it has been suggested that the Sérsic profile, more commonly used to describe baryonic matter in galaxies, may be a more accurate description. The results show that the difference between these profiles could contribute to explaining the discrepancy in the mass and concentration estimates from strong lensing on the one hand, and from weak lensing and X-ray measurements on the other. The high mass estimates and the high concentration of the mass distribution in clusters seen in strong lensing is one of the major issues which need to be understood before applying cluster lensing to deduce cosmological parameters.

Moving on to real systems, Chapter 5, discusses the mass modelling of real lensing systems. Analysing the galaxy cluster Abell 2218, it is demonstrated that the majority of the mass must reside in a smoothly distributed dark matter halo, and not in the cluster galaxies, consistent with the Chandra X-ray measurements. However, the X-ray map becomes more circular at lower radii than the derived mass map, showing that the two maps do not trace one another completely. The mass map has two large scale clumps, consistent with Abell 2218 consisting of two sub-clusters which have undergone a merger. Analysis of the cluster galaxies

in velocity space is consistent with such a merger scenario, as is the offset of the X-ray peak emission from the centre of the mass map.

The last main chapter of the thesis, Chapter 6, presents lens modelling projects involving the galaxy cluster Abell 1689 and GRB 050509B. The first part discusses the NFW concentration parameter estimate for Abell 1689 and relates it to the results of Chapter 4. The second part presents the study of the environment of the short gamma-ray burst GRB 050509B. This burst is localised in the vicinity of an elliptical galaxy, which is a member of a larger cluster. As there is no redshift measured for the burst, it is not possible to determine whether the burst is associated with the galaxy or a background object. In Chapter 6 the system is analysed assuming that the burst is in the background, calculating its lensing probability and magnitude by constructing a mass map of the galaxy and cluster.

Most of the work presented in this thesis has been published before. A list of the publications is given in Appendix D along with co-author statements, stating which part of the work was conducted by the candidate.

The Figure on the front page shows jellyfish in the Monterey Bay Aquarium which have been 'lensed' by a foreground blackhole using a web-based lensing program[1]. Credit: Árdís Elíasdóttir.

---

[1]http://theory2.phys.cwru.edu/~pete/GravitationalLens/mypic.cgi

1. INTRODUCTION

Chapter 2

Gravitational Lensing

The scientist does not study nature because it is useful;
he studies it because he delights in it,
and he delights in it because it is beautiful.
Henri Poincaré (1854-1912)

This chapter provides a short introduction to gravitational lensing (the deflection of light due to a gravitational potential), setting the stage for the work presented in this thesis. Schneider et al. (1992) provide an excellent and thorough review of gravitational lensing, and a more recent review can be found in Meylan et al. (2006). Shorter reviews can be found in Narayan & Bartelmann (1996) and Wambsganss (1998). An introduction on cosmological distance measures can be found in Hogg (2000). The material presented in this chapter is in part based on these sources.

2.1 Historical Background

The first paper on what may be called gravitational lensing was published in 1805 by a German scientist by the name of Johann Georg von Soldner, where he derived the deflection angle of a light ray passing near the sun (Soldner, 1805). In 1911, Albert Einstein using Newtonian gravity, calculated the influence of gravity on the propagation of light, coming to a similar numerical value as Soldner (Einstein, 1911). However, it was not until the formulation of Einstein's theory of

2. GRAVITATIONAL LENSING

General Relativity, that Einstein derived the correct value for the deflection angle, differing by a factor of two from the classical Newtonian result (Einstein, 1916, 1922; Lebach et al., 1995). Other pioneering papers include Chwolson (1924) who discussed doubly imaged background stars and the appearance of a ring for a perfectly aligned lens (now called the 'Einstein ring'), and a similar discussion by Einstein (1936) who concluded that the image separation would be so small as to be undetectable, and therefore lensing would remain a theoretical curiosity. This pessimistic view was shot down by Fritz Zwicky who considered galaxies, and not stars, as the lensing objects. He found that such massive lensing systems would create detectable separations and their frequency would be so high as to make their detection "practically a certainty" (Zwicky, 1937a,b). However, such detection eluded astronomers, leaving gravitational lensing as a mostly dormant and purely theoretical field for several decades.

In the 1960s a series of theoretical papers by independent authors re-opened the field of gravitational lensing (Klimov, 1963; Liebes, 1964; Refsdal, 1964a,b). Two of the more noteworthy results were the calculations of Sidney Liebes Jr. on how the stars in the Milky Way could act as lenses for stars in the Andromeda galaxy (Liebes, 1964) and those of Sjur Refsdal who showed how the time delay between multiply images could be used to determine the Hubble constant (Refsdal, 1964b). Refsdal went on to discuss other applications of lensing, including the determination of the distance and masses of stars and testing cosmological theories (Refsdal, 1966a,b). More theoretical papers were to follow at a slow but steady rate (see e.g., Barnothy & Barnothy, 1968, 1972; Bliokh & Minakov, 1975; Bourassa & Kantowski, 1975), until the detection of the first gravitationally lensed quasar in 1979.

The first gravitational lens (see Figure 2.1) was discovered by Dennis Walsh, Robert Carswell and Ray J. Weymann in 1979 when they proposed, using radio data, that QSO 0957+561 was not a double quasar, but two images of the same background quasar lensed by a foreground source (Walsh et al., 1979). This hypothesis has later been confirmed and the system and its lensing galaxy have been studied further by various authors (see e.g., Greenfield et al., 1985; Keeton et al., 2000; Kundic et al., 1997c). Not long after, the first giant arcs, caused by massive galaxy clusters lensing background galaxies, were discovered by Roger
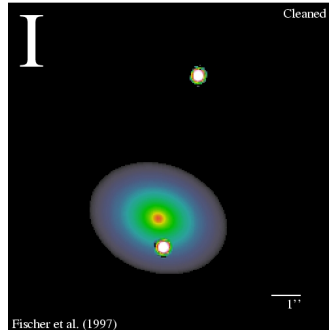
Figure 2.1 The first discovered lens system QSO 0957+561 as imaged in the I-band with the Hubble Space Telescope. *Credit: Fischer et al. (1997) and CASTLES[1].*

Lynds and Vahe Petrosian and independently by Genevieve Soucail, Bernard Fort, Yannick Mellier and Jean-Pierre Picat (see Figure 2.2 Lynds & Petrosian, 1986; Soucail et al., 1987). These discoveries were a turning point for

Figure 2.2 Giant arcs in lensing clusters. *Left panel:* The galaxy cluster Abell 2267. The most prominent lensing feature is a giant arc on the right hand side in the image. *Credit: NASA/ESA/Jean-Paul Kneib. Right panel:* The central region of the galaxy cluster Abell 2218. Prominent lensing features include the orange arc in the lower part of the image and various blue arcs. This cluster will be discussed further in Chapter 5.

gravitational lensing, as it moved from being a theoretical curiosity to being an

---

[1]http://cfa-www.harvard.edu/glensdata/

observationally detectable phenomenon, creating a very active field of research. The foundations laid out by the theorists in the preceding decades were tested and applied, and dedicated searchers for more lenses have been carried out.

Since then, gravitational lensing has been a growing field, and is actively studied both theoretically, numerically and observationally. New subfields such as microlensing, where lensing caused by individual stars is detected as a peak in the background object's light profile, has been used to discover new planets in distant solar systems, and weak lensing, when the lensing signal is not strong enough to split the image, but only distorts its shape, has been used to study cosmological parameters (see e.g., Bacon et al., 2000; Beaulieu et al., 2006; Wambsganss et al., 2004).

2.2 Theory

Gravitational lensing is the deflection of a light ray due to the distortion of space caused by mass along the line of sight. In theory, any mass along the path will contribute to the deflection. In practise however, the 'thin lens approximation' is valid for most situations. In this approximation, the deflection is dominated by a single massive structure along the line of sight. The depth of this structure is negligible compared to the distance to the lensed source and the observer. In this setup (see Figure 2.3), three natural planes arise, one at the redshift of the lensing object (the lens plane), one at the redshift of the background source (the source plane) and the last is the plane of the observer.

To calculate the lensing signal, the universe is assumed to be well described by the Friedmann-Lemaître-Robertson-Walker (FLRW) metric

$$\mathrm{d}\tau^2 = \mathrm{d}t^2 - a^2(t)\left(\frac{\mathrm{d}r^2}{1-kr^2} + r^2\left(\mathrm{d}\theta^2 + \sin^2\theta\mathrm{d}\phi^2\right)\right) \qquad (2.1)$$

where k describes the curvature and $a(t)$ is the time varying scale factor and (t, r, θ, ϕ) are the space time coordinates. Near the lens plane, where the light ray is deflected, the space-time is assumed to be described by a locally flat, Minkowskian metric which is weakly perturbed by the Newtonian gravitational potential of the mass distribution causing the lensing. This approximation is
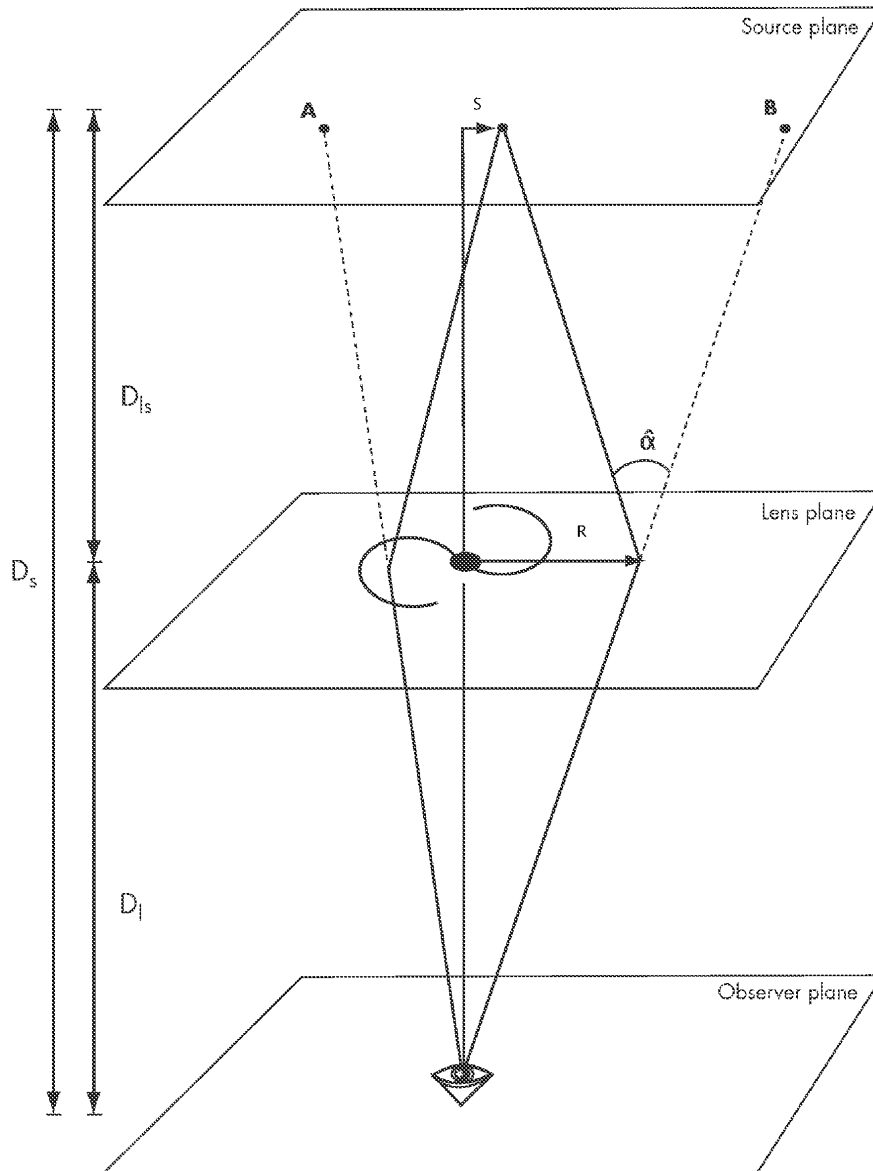
Figure 2.3 The lensing setup. D_l is the distance to the lens, D_s the distance to the source, D_{ls} the distance from the lens to the source, $\hat{\alpha}$ is the deflection angle (see eq. 3.1), **s** is the position vector of the source in the source plane, and **r** is the position vector in the lens plane. The figure shows a doubly imaged source, where one line of sight goes through the lensing galaxy and the other passes outside it.

9

valid if the Newtonian potential Ψ is small, $|\Psi| \ll c^2$ and if the peculiar velocity of the lens, v, is small, $v \ll c$, which is an approximation valid in nearly all cases of astrophysical interest.

Under these approximations, the deflection angle $\hat{\boldsymbol{\alpha}}(\mathbf{R})$ for a ray that intersects the lens plane at $\mathbf{R}$ is given by

$$\hat{\boldsymbol{\alpha}}(\mathbf{R}) = \frac{4G}{c^2} \int \frac{(\mathbf{R} - \mathbf{R}') \, \Sigma(\mathbf{R}')}{|\mathbf{R} - \mathbf{R}'|^2} \mathrm{d}^2 \mathbf{R}' \tag{2.2}$$

where $\Sigma(\mathbf{R})$ is the projected surface mass density, calculated from the 3D mass density $\rho(\mathbf{r}) = \rho(\mathbf{R}, z)$ by

$$\Sigma(\mathbf{R}) = \int \rho(\mathbf{R}, \mathrm{z}) \mathrm{dz}. \tag{2.3}$$

For a circularly symmetric mass distribution, the deflection angle reduces to

$$\hat{\boldsymbol{\alpha}}(\mathbf{R}) = \frac{4GM(R)}{c^2 R} \tag{2.4}$$

where $M(R)$ is the mass enclosed by radius R.

2.2.1 The lens equation

The geometrical configuration of the lensing setup is most simply expressed in terms of angular diametric distances (see § 2.2.6), which are defined so that 'normal' Euclidean distance-angle relationships hold. From Figure 2.4 one sees that for small angles

$$\hat{\boldsymbol{\alpha}}(\boldsymbol{\theta}) D_{ls} + \boldsymbol{\beta} D_s = \boldsymbol{\theta} D_s \tag{2.5}$$

i.e.

$$\boldsymbol{\beta} = \boldsymbol{\theta} - \boldsymbol{\alpha}(\boldsymbol{\theta}) \tag{2.6}$$

where $\boldsymbol{\alpha}(\boldsymbol{\theta}) \equiv \frac{D_{ls}}{D_s} \hat{\boldsymbol{\alpha}}(\boldsymbol{\theta})$ is the reduced deflection angle. Equation 2.6 is referred to as the lens equation and its solutions $\boldsymbol{\theta}$ give the angular position of the source as seen by the observer. It is in general a non-linear equation and can have multiple possible solutions of $\boldsymbol{\theta}$ for a given source position $\boldsymbol{\beta}$.
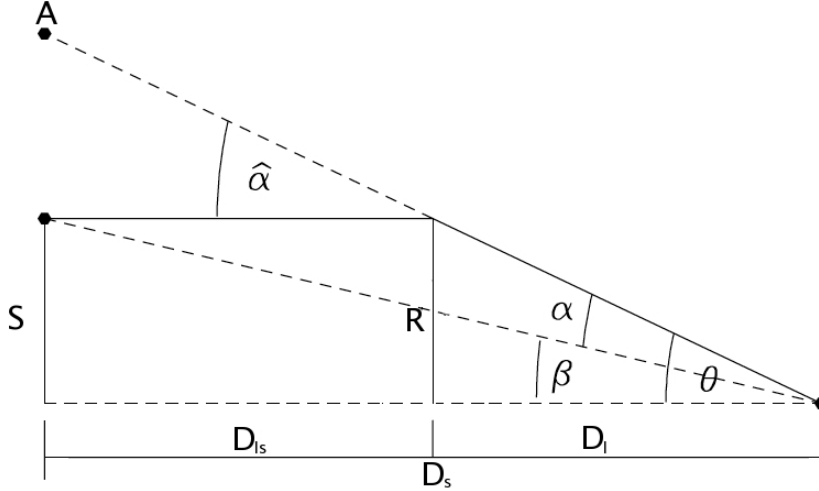
Figure 2.4 The geometrical lensing setup of the lens equation (eq. 2.6).

2.2.2 Einstein radius and critical surface mass density

For a point mass M and perfect alignment between the observer, lens and source (i.e. $\boldsymbol{\beta} = \mathbf{0}$), the lens equation becomes

$$0 = \theta - \frac{D_{ls}}{D_l D_s} \frac{4GM}{c^2 \theta}. \tag{2.7}$$

In this special case, the solution to the equation is given by

$$\theta_E = \sqrt{\frac{D_{ls}}{D_l D_s} \frac{4GM}{c^2}} \tag{2.8}$$

which defines a ring centred on the lens with angular radius θ_E, called the Einstein radius (see Figure 2.5). The Einstein radius defines the angular scale for a lensing setup, i.e. the typical separation of multiple images for a multiply imaged background source. For a galaxy, typical Einstein radii are of the order of $1''$ while for galaxy clusters they are of the order of $10''$.

Another quantity which is relevant for gravitational lensing is the critical surface mass density, Σ_{crit}, which is defined as

$$\Sigma_{\mathrm{crit}} = \frac{c^2}{4\pi G} \frac{D_s}{D_l D_{ls}}. \tag{2.9}$$

11
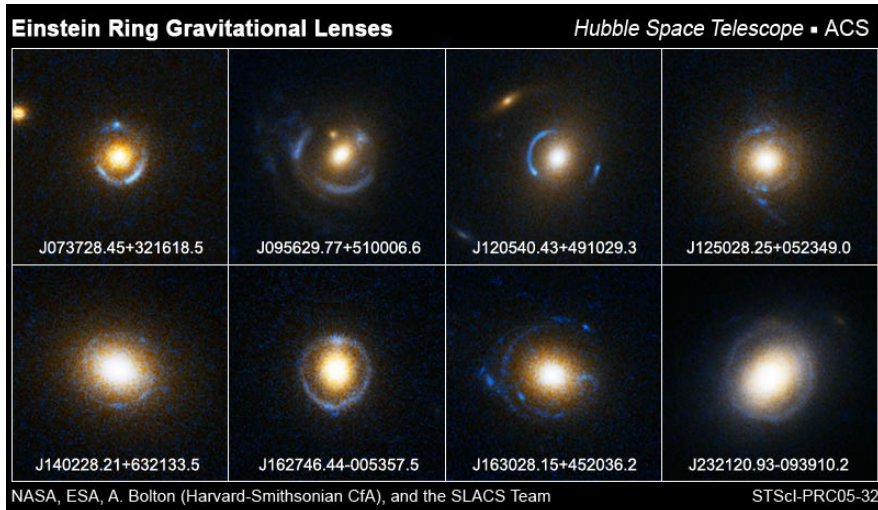
Figure 2.5 Einstein ring gravitational lenses. The background sources are nearly perfectly aligned with the lens galaxy and the observer, creating an image of a 'ring' (in blue) surrounding the lensing galaxy. *Credit: NASA, ESA, A. Bolton and the SLACS team.*

It corresponds to the mass density of total mass M spread out over a circle with radius $R_{\text{Ein}} = \theta_{\text{Ein}} D_l$, i.e.

$$\Sigma_{\text{crit}} = \frac{M}{\pi R_{\text{Ein}}^2}. \tag{2.10}$$

For any surface mass density Σ, the condition $\exists R$ such that $\Sigma(R) \geq \Sigma_{\text{crit}}$ is a sufficient (although not necessary) condition for an appropriately aligned background source to be multiply imaged. The dimensionless surface mass density,

$$\kappa \equiv \Sigma/\Sigma_{\text{crit}} \tag{2.11}$$

is referred to as the convergence.

2.2.3 Potentials

Various relations and quantities in lensing can be simplified by expressing them in terms of potentials. Defining a lensing potential, $\psi(\boldsymbol{\theta})$, as

$$\psi(\boldsymbol{\theta}) = \frac{1}{\pi} \int \kappa(\boldsymbol{\theta}') \ln \left| \boldsymbol{\theta} - \boldsymbol{\theta}' \right| \mathrm{d}^2\theta' \tag{2.12}$$

and using the identity $\nabla \ln |\boldsymbol{\theta}| = \boldsymbol{\theta} / |\boldsymbol{\theta}|^2$ the deflection angle can be expressed as

$$\boldsymbol{\alpha} = \nabla \psi. \tag{2.13}$$

From Eq. 2.12 one can further obtain that

$$\nabla^2 \psi = 2\kappa \tag{2.14}$$

which is the Poisson equation in two dimensions. Another useful potential is the Fermat potential, $\tau(\boldsymbol{\theta}; \boldsymbol{\beta})$, defined as

$$\tau(\boldsymbol{\theta}; \boldsymbol{\beta}) = \frac{1}{2}(\boldsymbol{\theta} - \boldsymbol{\beta})^2 - \psi(\boldsymbol{\theta}) \tag{2.15}$$

which is a function of $\boldsymbol{\theta}$ with $\boldsymbol{\beta}$ acting as a parameter. The lens equation, Eq. 2.6, can then also be expressed as

$$\nabla \tau(\boldsymbol{\theta}; \boldsymbol{\beta}) = \mathbf{0}. \tag{2.16}$$

2.2.4 Magnification and shear

Lensing will affect the observed position, the observed brightness and, for a finite size background source, the observed shape of the source. For a source of surface brightness $I_s(\boldsymbol{\beta})$ in the sourceplane, the observed surface brightness in the lensing plane will be

$$I(\boldsymbol{\theta}) = I_s(\boldsymbol{\beta}(\boldsymbol{\theta})). \tag{2.17}$$

This is in general a non-linear equation, but in the case where the lensing signal varies on angular scales much larger than the source size, it can be linearised locally. The distortion is then described by a Jacobian matrix

$$A(\boldsymbol{\theta}) = \frac{\partial \boldsymbol{\beta}}{\partial \boldsymbol{\theta}} = \left(\delta_{ij} - \frac{\partial^2 \psi(\boldsymbol{\theta})}{\partial \theta_i \partial \theta_j} \right). \tag{2.18}$$

The magnification tensor $M(\boldsymbol{\theta})$, giving the mapping from the source plane to the image plane, is the inverse of the Jacobian

$$M(\boldsymbol{\theta}) = A^{-1}. \tag{2.19}$$

Introducing the shear as

$$\gamma \equiv \gamma_1 + \mathbf{i}\gamma_2 = \frac{1}{2}(\psi_{,11} - \psi_{,22}) + \mathbf{i}\psi_{,12}, \tag{2.20}$$

where the subscripts denote differentiation with respect to θ_i, $A(\boldsymbol{\theta})$ can be rewritten as

$$A(\boldsymbol{\theta}) = \begin{pmatrix} 1 - \kappa - \gamma_1 & -\gamma_2 \\ -\gamma_2 & 1 - \kappa + \gamma_1 \end{pmatrix}. \tag{2.21}$$

The observed flux is then

$$I(\boldsymbol{\theta}) = I_s\left(\boldsymbol{\beta}_0 + A(\boldsymbol{\theta}_0) \cdot (\boldsymbol{\theta} - \boldsymbol{\theta}_0)\right) \tag{2.22}$$

for a given point $\boldsymbol{\theta}_0$. The magnification $|\mu(\boldsymbol{\theta}_0)|$ is found by taking the ratio of the integrals over the brightness distributions $I(\boldsymbol{\theta})$ and $I_s(\boldsymbol{\beta})$. For a pointlike source it is given by

$$\mu = \det M = \frac{1}{\det A} = \frac{1}{(1 - \kappa^2) - |\gamma|^2}. \tag{2.23}$$

It can be seen that lensing causes distortion in both the shape and the size of the background source. Both the convergence, κ, and the shear, γ, contribute to the magnification, while only the shear causes the shape distortion.

As mentioned in § 2.2.2 a sufficient condition for multiple images is that a point exists where the convergence is greater than unity. A stronger statement can be made in terms of A, as a sufficient and necessary condition for multiple images is that there exist a point where the determinant of A is negative. For proof of these theorems see e.g., Schneider et al. (1992).

Critical curves are closed smooth curves in the image plane where $\det A(\boldsymbol{\theta}) = 0$ and the magnification μ formally goes to infinity. In practise, images lying near critical curves have very high, although finite, magnification. The corresponding curves in the source plane, found by mapping the critical curves back to the source plane using the lensing equation, are referred to as caustics. They are not necessarily smooth and frequently display cusps. The location of a background source with respect to the caustics is important, as a source falling near a caustic will be highly magnified. In addition, it controls the number of multiple images formed, with each crossing of a caustic moving in towards the lens creating two additional images.

2.2.5 Time delays

The travel-time of the light ray is also affected by gravitational lensing. This is in part because the travel-path is longer in geometrical terms ('geometric time delay') and in part due to the effect of the gravitational potential itself ('Shapiro time delay'). The delay compared to a light ray travelling on a direct path in empty space is given in terms of the Fermat potential (see Eq. 2.15) and equals

$$\Delta t = \frac{D_l D_s}{c D_{ls}} \left(1 + z_l\right) \tau(\boldsymbol{\theta}; \boldsymbol{\beta}) + constant \tag{2.24}$$

where D_l, D_s, D_{ls} are angular diameter distances (see § 2.2.6), z_l is the redshift of the lens plane and the constant arises from the integration of the potential along the travel-path. As the constant term is indeterminate, the time delay for a given image can not be calculated. However, the difference in the travel time between two images A and B for a multiple imaged source can be measured and is given by

$$\Delta t_{A,B} = \frac{D_l D_s}{c D_{ls}} \left(1 + z_l\right) \left(\tau(\boldsymbol{\theta}_A; \boldsymbol{\beta}) - \tau(\boldsymbol{\theta}_B; \boldsymbol{\beta})\right), \tag{2.25}$$

i.e. $\Delta t_{A,B} = H_0^{-1} \times f(c, z_l, z_s, \Omega_k) \left(\tau(\boldsymbol{\theta}_A; \boldsymbol{\beta}) - \tau(\boldsymbol{\theta}_B; \boldsymbol{\beta})\right)$ where f is a function of c, z_l, z_s, Ω_k only, where c is the speed of light, z_s is the redshift of the source plane and Ω_k is quantifies the curvature of space (see § 2.2.6). Therefore, a measurement of the time delay can give an estimate of the Hubble constant H_0 (see also § 2.3.2).

2.2.6 Angular diameter distances

The lens equation is only valid for angular diameter distances, as the Euclidean relationship between distance, angle and separation does not hold in general for a curved space-time. The angular diameter distances are defined so that this relationship holds and depend on the space-time metric. They have some non-intuitive properties, e.g. $D_s \neq D_l + D_{ls}$.

   Here the angular diameter distances in the FLRW metric are expressed for a cosmology with matter density Ω_m, dark energy density Ω_Λ and Ω_k (which is a density measuring the curvature of space, related to the other density parameters

by $\Omega_m + \Omega_\Lambda + \Omega_k = 1$). To simplify the expressions one begins by defining the integral

$$I(z) = \int_0^z \frac{dz'}{E(z')} \qquad (2.26)$$

where

$$E(z) \equiv \sqrt{\Omega_m (1+z)^3 + \Omega_k (1+z)^2 + \Omega_\Lambda}. \qquad (2.27)$$

The angular diameter distance to an object at redshift z is then given by

$$D(z) = \frac{D_{\mathrm{M}}(z)}{1+z} \qquad (2.28)$$

where D_{M} is the transverse comoving distance given by
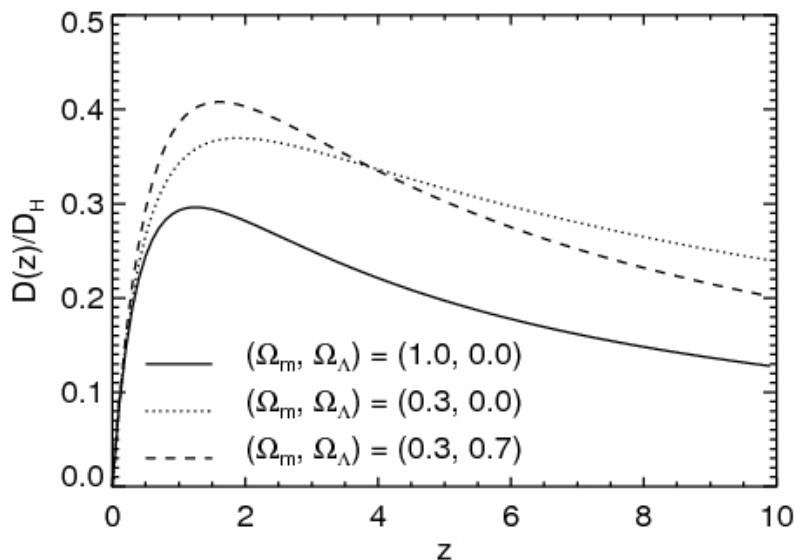
Figure 2.6 The angular diameter distance, as given by Eq. 2.28, scaled with D_H for different values of Ω_Λ and Ω_m.

$$D_{\mathrm{M}}(z) = \begin{cases} D_{\mathrm{H}} \frac{1}{\sqrt{\Omega_k}} \sinh\left[\sqrt{\Omega_k}\, I(z)\right] & \text{for } \Omega_k > 0 \\ D_{\mathrm{H}} I(z) & \text{for } \Omega_k = 0 \\ D_{\mathrm{H}} \frac{1}{\sqrt{|\Omega_k|}} \sin\left[\sqrt{|\Omega_k|}\, I(z)\right] & \text{for } \Omega_k < 0 \end{cases} \qquad (2.29)$$

and where D_{H} is the Hubble distance defined by

$$D_{\mathrm{H}} \equiv \frac{c}{H_0}. \tag{2.30}$$

Here H_0 is the Hubble constant, defined in terms of the scale factor of the FLRW metric as $H_0 = \dot{a}/a$ at $t = 0$ where the dot stand for a derivative with respect to t. Similarly, the redshift of an object, z is defined in terms of the scale factor of the FLRW metric, $1 + z = \frac{a(t_o)}{a(t_e)}$, where t_e is the time the light from the object was emitted, and t_o is the time it was observed.

For $\Omega_k \geq 0$, the more general case for the angular diameter distance between z_2 and $z_1 < z_2$ is given by

$$D(z_1, z_2) = \frac{1}{1 + z_2} \left[D_{\mathrm{M}}(z_2) \sqrt{1 + \Omega_k \frac{D_{\mathrm{M}}^2(z_1)}{D_{\mathrm{H}}^2}} - D_{\mathrm{M}}(z_1) \sqrt{1 + \Omega_k \frac{D_{\mathrm{M}}^2(z_2)}{D_{\mathrm{H}}^2}} \right] \tag{2.31}$$

and *not* by the difference of $D(z_2)$ and $D(z_1)$.

2.3   Applications of Gravitational Lensing

Initially, before the detection of the first multiply imaged gravitationally lensed quasars, the field of gravitational lensing focused on the theoretical aspects of the lensing effect itself. However, with the large number of known lenses today, the focus has shifted towards the application of gravitational lensing to answer various astrophysical and cosmological questions, both by studying single systems and with 'lensing statistics' where large ensembles of lenses are used to derive, for example, cosmological parameters.

2.3.1   Mass - from planets to clusters

Gravitational lensing can be efficiently used to study the mass distribution of the lensing object, a method referred to as 'lens modelling' (see e.g., Elíasdóttir et al., 2007; Falco et al., 1997; Limousin et al., 2007b; Rusin et al., 2002). For galaxy lenses, i.e. when the lensing object is a galaxy, there is usually only one set of a multiply imaged background source, which gives a tight constraint on the enclosed mass within the Einstein radius. Using additional information,

e.g. the magnification ratio, the time delays or using a pixelated approach if the background source is not a point source, further constraints can be placed on the mass distribution of the lens. For cluster lenses, it is possible to find numerous sets of multiply imaged background sources at various redshifts, which constrain the mass distribution of the cluster. However, although clusters lenses have more numerous constraints, they can be harder to model as they are intrinsically much more complicated structures than galaxies.

The lensing mass maps can be combined with mass estimates from alternative approaches. For example, lensing and stellar dynamics (the study of the dynamics of the stars in the galaxy) have been successfully combined to estimate the slope of the mass distribution of elliptical galaxies in the field, showing that they are on average consistent with being isothermal (Koopmans et al., 2006). For cluster lenses, a combined analysis of lensing and X-rays can show whether the mass and the gas in the cluster are displaced from one another. When that is the case, it is believed to be evidence for the cluster having undergone a merger, which is for instance seen in the recent study of the spectacular 'Bullet Cluster' (see Figure 2.7, Clowe et al., 2006).

Lensing can also be used to probe substructure in the lensing object. In clusters, the multiply imaged background sources can be used to constrain not only the overall shape of the mass distribution, but also the smaller variations due to galaxy scale perturbers. In galaxies, the effect of individual stars on the lensing signal can be detected via microlensing. As the stars move relative to the lensed background source, their lensing effect will vary with time, giving rise to a time variation in the lensing amplitude. This method has also been used to detect planets moving around stars in our own galaxy, and the first 'earth-like' planet was found using this technique (see Figure 2.8, Beaulieu et al., 2006).

Strong lensing only occurs in environments with high mass density. However, any mass density along the line of sight to a source will cause a lensing signal, in the form of a weak distortion or magnification. Although such weak lensing signals can not be analysed for single background sources, a statistical analysis of a large catalogue of distorted background objects can be used to map e.g. the outskirts of galaxy clusters or even the large scale structure of the universe (Bacon et al., 2000; Limousin et al., 2007b).
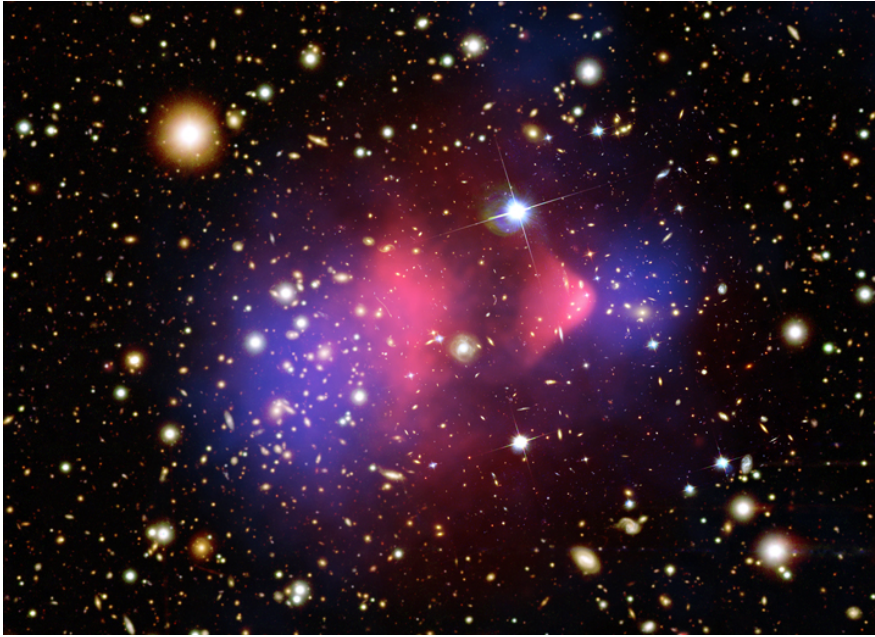
Figure 2.7 A composite picture of the galaxy cluster 1E 0657-56, also known as the 'Bullet Cluster'. The X-ray emission, tracing the gas, is shown in pink, while the total matter density, as derived from lensing, is shown in blue. The complex structure is believed to be due to the cluster having formed via a merging of two clusters. The gas, experiencing a drag force, was slowed down, while the dark matter only interacts via gravity and was therefore not slowed down in the collision. This creates the separation of the gas and dark matter seen in the image. *Credit: X-ray: NASA/CXC/CfA/Markevitch et al. (2004); Optical: NASA/STScI; Magellan/U.Arizona/Clowe et al. (2006); Lensing Map: NASA/STScI; ESO WFI; Magellan/U.Arizona/Clowe et al. (2006)*
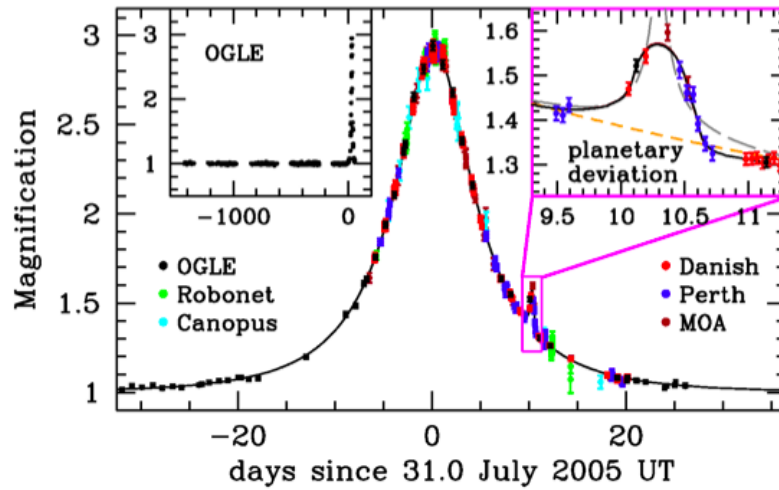
Figure 2.8 The light-curve of the OGLE-2005-BLG-390 microlensing event. The main bell shaped curve is due to microlensing from a star in our galaxy but the smaller deviation on the right-hand side of the curve is a signature of a planet orbiting the star. More details on this particular system can be found in Beaulieu et al. (2006). *Credit: Beaulieu et al. (2006).*

2.3.2 Constraining cosmology

Gravitational lensing is not only dependent on the mass distribution, but also on the path the light rays travel, which depends on the geometry of the universe. Therefore, in principle, gravitational lensing can be used to constrain cosmological parameters. Various studies of gravitationally lensed multiply imaged quasars have used the measured time delay between the arrival time of the different images to estimate the Hubble constant H_0 (Kundic et al., 1997c; Schechter et al., 1997). These have usually lead to a lower estimate of H_0 than the 'concordance' value of around 70 km s^{-1}Mpc^{-1}, although a recent study of an ensemble of such systems analysed using simplified modelling finds a value consistent with the 'concordance' value (Oguri, 2007).

The total matter density, Ω_M, and dark energy content, Ω_Λ, may also be determined using gravitational lensing (see Figure 2.9). Two approaches may be used, the first depends on the number statistics of lenses, as the redshift distribution of lensed sources will depend on the cosmology (Wambsganss et al., 2004). The second involves simultaneously fitting for both the cosmology and the mass distribution in the lens equation (Golse et al., 2002; Soucail et al., 2004). This is possible if the same lens system has multiple sets of lensed background sources at different redshifts, as is frequently the case for clusters. However, the complex mass distribution of the clusters themselves has prevented lensing from putting competitive constraints on these parameters to date. Finally, weak lensing can be used to constrain the matter density and the normalisation of the density fluctuations (σ_8) (see, e.g., Bacon et al., 2000).

2.3.3 Detecting the faintest sources

Massive galaxy clusters act as magnifying glasses for distant background sources. This magnification can lead to the detection of faint sources which normally would be undetectable with current telescopes. Therefore, galaxy clusters act as natural gravitational telescopes making them ideal places to search for the faint sources of the early universe. For example, in Abell 2218, a multiply imaged galaxy at
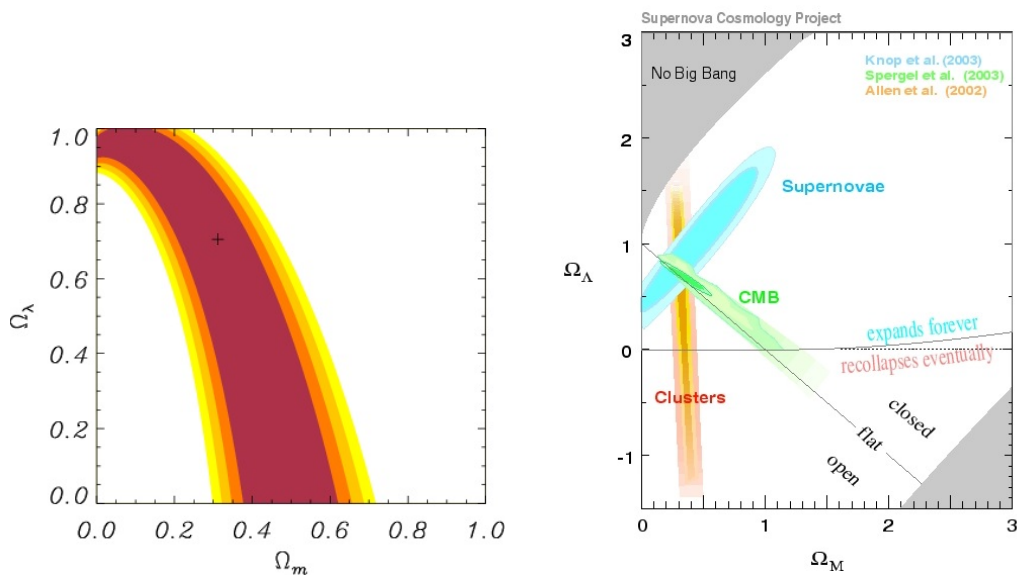
Figure 2.9 *Left panel:* The degeneracy between the matter content, Ω_m, and the dark energy content, Ω_Λ, derived from cluster lensing with multiple sources at different redshifts. *Credit: Golse et al. (2002). Right panel:* For comparison, this figure shows the degeneracy between Ω_m and Ω_Λ from other major cosmological surveys: the cosmic microwave background (WMAP), supernova Ia and cluster surveys. *Credit: the Supernova Cosmology Project[2]).*

a redshift of $z \sim 7$ was detected, making it one of the highest redshift galaxies known (see Figure 2.10, Egami et al., 2005).
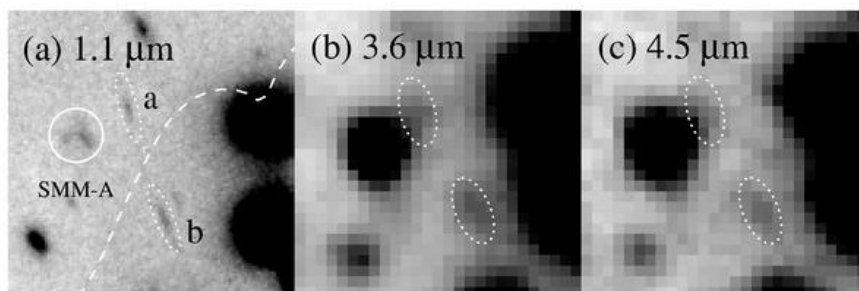
Figure 2.10 Gravitational lenses, such as massive galaxy clusters, can act as natural telescopes, magnifying faint distant sources to a level where they are detectable with current instruments. The panels above show HST/NICMOS (panel a) and Spitzer/IRAC (panels b and c) images of a highly magnified (~ 25) lensed source at redshift $z \sim 7$ in Abell 2218 (Kneib et al., 2004a). *Credit: Egami et al. (2005).*

2.3.4 Dust extinction

Gravitational lensing may also be used to probe extinction due to dust in distant galaxies when a background source is multiply imaged (Elíasdóttir et al., 2006; Falco et al., 1999; Nadeau et al., 1991). This can in theory be used to probe dust extinction as a function of both redshift and morphology. Such information can be crucial for various astrophysical and cosmological surveys where accurate calibration of data is required. To date, due to the lack of knowledge about extragalactic dust, typical Milky Way extinction is frequently assumed when calibrating data, which can lead to biased results if the type of dust differs significantly from Milky Way dust. This will be further discussed in Chapter 3.

---

[2]http://supernova.lbl.gov/

Chapter 3

Extinction Curves of Lensing Galaxies

The true harvest of my life is intangible
- a little star dust caught,
a portion of the rainbow I have clutched.
Henry David Thoreau (1817-1862)

Probing extragalactic dust extinction is a challenging but important task. Dust extinction can affect cosmological surveys where accurate calibration of data is required. However, very little is known about dust outside the Milky Way, leading researchers to frequently assume Milky Way type of dust in the data calibration. One of the most successful methods for probing extragalactic dust is based on comparing the multiple images of the same background quasar. This chapter presents a survey of extragalactic dust properties in lensing galaxies using multiply imaged background quasars. Most of this chapter has been published before in Elíasdóttir et al. (2006).

3.1 Introduction

The study of extinction curves of galaxies at high redshift has generated a lot of interest in recent years (see e.g., Falco et al., 1999; Goicoechea et al., 2005; Goudfrooij, 2000; Kann et al., 2006; Murphy & Liske, 2004; Riess et al., 1996a;

3. EXTINCTION CURVES OF LENSING GALAXIES

York et al., 2006). Light reaching us from distant sources is extinguished by dust along its path making it important to correct measurements for the amount and properties of the extinction. Extragalactic dust extinction can for example affect measurements of Type Ia supernovae (SNe Ia) used to determine various cosmological parameters (e.g., Perlmutter et al., 1999; Riess et al., 1998) and the star-formation rates for high redshift starburst galaxies which are used as probes of galaxy evolution (see e.g., Madau et al., 1998). Yet, even if dust properties and thus extinction may vary with redshift and environment, an average Galactic extinction law is often applied when calibrating extragalactic data due to the lack of knowledge of the extinction properties of higher redshift galaxies.

Traditionally, extinction curves are measured by comparing the spectra of two stars of the same spectral type, which have been reddened by different amounts (see e.g., Massa et al., 1983). As it becomes significantly harder to measure spectra of individual stars with distance this method is limited in its application to the Milky Way and the nearest galaxies. The extinction curves of the Milky Way along different lines of sight have been mapped extensively using this method and have been shown to follow an empirical parametric function which depends only on one parameter, $R_V = A(V)/E(B-V)$, where $A(\lambda)$ is the total extinction at wavelength λ and $E(B-V) = A(B) - A(V)$ (Cardelli et al., 1989). The mean value of R_V in the Milky Way is 3.1 (Cardelli et al., 1989) but for different lines of sight the value ranges from as low as $R_V \approx 1.8$ toward the Galactic bulge (Udalski, 2003) and as high as $R_V \approx 5.6$–5.8 (Cardelli et al., 1989; Fitzpatrick, 1999). A lower R_V corresponds to a steeper rise of the extinction curve into the UV, whereas it has little effect on the extinction in the infrared.

Extinction curves have also been obtained for the Small and Large Magellanic Clouds (hereafter, SMC and LMC, respectively) and M31 using this method. The mean extinction curve of the LMC differs from the Galactic extinction law in that the bump at 2175 is smaller by a factor of two (as measured by the residual depth of the bump when the continuum has been extracted) and the curve has a steeper rise into the UV for wavelengths shorter than 2200 (Nandy et al., 1981). The extinction curve of the SMC is well fitted by an $A(\lambda) \propto \lambda^{-1}$ curve which deviates significantly from the Galactic extinction law and the LMC extinction for $\lambda^{-1} \geq 4 \ \mu m^{-1}$ and in particular shows no bump at 2175 and a steeper rise

into the UV (Prevot et al., 1984). Bianchi et al. (1996) found that the extinction of M31 follows that of the average Galactic extinction law. The various extinction properties shown by these galaxies, especially in the UV and shorter wavelengths, further strengthens the need to find a method to study the extinction curves of more distant galaxies.

A few methods have been proposed for measuring extinction curves for more distant galaxies. One method is basically an extension of the traditional method of comparing stars of the same spectral type to comparing the SNe Ia (Perlmutter et al., 1997; Riess et al., 1996a). The extinction is estimated from comparison with unreddened, photometrically similar SNe Ia. A subset of SNe Ia, with accurately determined extinction and relative distances, is then used to further determine the relationship between light and colour curve shape and luminosity in the full sample. SN Ia extinction studies usually give lower R_V values than the mean Galactic value of $R_V = 3.1$ (Krisciunas et al., 2000; Riess et al., 1996b; Wang et al., 2006).

Quasars with damped Lyα systems (DLAs) in the foreground have also been studied by Pei et al. (1991) and were found to be on average redder than those without. By comparing the optical depths derived from the spectral indices and the ones derived from excess extinction at the location of the Galactic extinction law bump they found that their sample of five quasars with DLAs is not consistent with the Galactic extinction law, marginally compatible with the LMC extinction and fully compatible with SMC extinction. Murphy & Liske (2004) studied a larger sample of the Sloan Digital Sky Survey quasars with damped Lyα systems in the foreground and found no sign of extinction. They suggest that the difference between their results and that of Pei et al. (1991) may be due to the small number statistics in the study by Pei et al. (1991). Ellison et al. (2005) also found that intervening galaxies cause a minimal reddening of background quasars in agreement with the results of Murphy & Liske (2004) while York et al. (2006) found $E(B - V)$ of up to 0.085 for quasars from the Sloan Digital Sky Survey with Mg II absorption. In their study York et al. (2006) found no evidence of the 2175 bump (at variance with Malhotra (1997)) and found that the extinction curves are similar to SMC extinction. Östman et al. (2006) studied the feasibility of measuring extinction curves by using quasars shining through galaxies. For

the two such systems which survived their cuts, they argued that the extinction curves in the foreground spiral galaxies were consistent with Galactic extinction. They further suggested a possible evolution in the dust properties with redshift, with higher z giving lower R_V by studying values obtained from the literature in addition to their own.

Extinction curves of high redshift galaxies have also been studied by looking at the spectral energy distribution of gamma-ray bursts (GRBs). For example, Jakobsson et al. (2004) fitted a Galactic extinction law, an SMC and an LMC extinction law to the afterglow of GRB 030429. The afterglow, at $z = 2.66$, was best fit by an SMC like extinction curve with $A(V) = 0.34 \pm 0.04$. Kann et al. (2006) studied the extinction of a sample of 19 GRB afterglows and fitted them to various dust extinction models. They found that the SMC extinction law was preferred by a great majority of their Golden Sample (seven out of eight) while one afterglow was best fit by a Galactic extinction law (the other eleven were equally well fit by SMC, LMC and Galactic extinction). The mean extinction in the V-band was $A(V) = 0.21 \pm 0.04$.

Goudfrooij (2000) reviewed the dust properties of giant elliptical galaxies and found that they are typically characterised by small R_V if they are in the field or in loose groups, but that if they are in dense groups or clusters their R_V values are close to the mean Galactic $R_V = 3.1$. Early type elliptical galaxies typically have low $A(V)$ (see e.g., Goudfrooij et al., 1994, who found $A(V) \lesssim 0.35$ for dust lanes in ellipticals).

Nadeau et al. (1991) pointed out that gravitationally lensed quasars could be used to measure the extinction curves of higher redshift galaxies. Falco et al. (1999) explored a large sample of 23 lensing galaxies using this method and found that only seven were consistent with no extinction. This method has also been applied to single systems by e.g. Goicoechea et al. (2005); Jaunsen & Hjorth (1997); Motta et al. (2002); Muñoz et al. (2004); Toft et al. (2000); Wisotzki et al. (2004); Wucknitz et al. (2003) and shows varying extinction properties between different lensing systems.

Here a systematic study of the extinction curves of gravitational lenses is presented based on an ESO VLT survey of 10 lens systems (see Figure 3.1). A dedicated effort has been made to minimise the number of unknowns and effects

that can mimic extinction. The data have broad wavelength coverage in nine different optical and NIR broad bands. An effort was made to minimise the time between the observations for each system in the different bands to minimise the effect of intrinsic quasar variability and microlensing. All the systems have spectroscopically determined redshifts for both the quasar and the lensing galaxy. Finally, the systems span the range of $z = 0.04$–1.01 giving us the possibility to explore possible evolution with redshift.
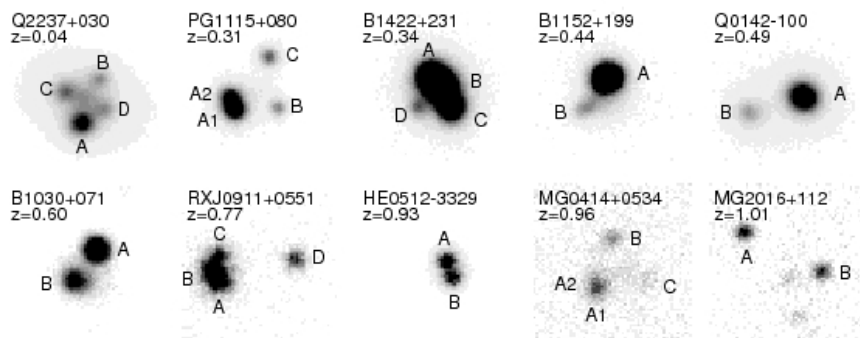
Figure 3.1 Gallery of the 10 gravitational lensed quasars in the sample as they appear in the R-band VLT images. The size of the stamps is $6'' \times 6''$.

The outline of this chapter is as follows: In § 3.2 the details of the employed method are described and different sources of systematics and of random errors which may affect the results are discussed. The results of simulations which explore the effects of these errors on data sets similar to those obtained in the survey are presented. The results of the analysis of each individual system in § 3.3.1 and the analysis of the full sample are presented in § 3.3.2. Finally the results are summarised in § 3.4 and the impact they can have on future dark energy surveys is discussed in § 3.5.

3.2   Method and Simulations

This section introduces the method and explores the different sources of systematic and random errors through simulations. In particular, the effects of achromatic microlensing and of extinction along both lines of sight are studied, and

simulations are used to explore the conditions, under which it will be possible to recover and distinguish between different extinction laws.

3.2.1 Lensing

Gravitational lensing is the deflection of light rays due to the gravitational field of the matter distribution through which the light passes (see Chapter 2 for a more detailed introduction to gravitational lensing). For a geometrically thin lens, i.e., where the depth of the lens is small compared to the distance between the lens and observer, D_l, and the lens and the light source, D_{ls}, the deflection angle is given by

$$\hat{\alpha}(\mathbf{R}) = \frac{4G}{c^2} \int d^2 R' \Sigma(\mathbf{R}') \frac{\mathbf{R} - \mathbf{R}'}{|\mathbf{R} - \mathbf{R}'|^2} \tag{3.1}$$

where G is the gravitational constant, c is the speed of light, $\Sigma(\mathbf{R})$ is the surface mass density of the lensing mass and $\mathbf{R}$ is the impact vector of the light ray (see Figure 2.3 for a sketch of the lensing setup). For a position vector $\mathbf{s}$ in the source plane one will see images at locations $\mathbf{r}$ in the lens plane which satisfy the lens equation

$$\mathbf{S} = \frac{D_s}{D_l} \mathbf{r} - D_{ls} \hat{\alpha}(\mathbf{R}) \tag{3.2}$$

where D_{ls} is the angular diameter distance between the lens and the source and where it has been assumed that the size of the lens is small compared to D_l, D_s and D_{ls}. When eq. (3.2) has more than one solution multiple images of the source are seen in the lens plane which are in general located at different distances from the centre of the mass distribution. In the case of distant quasars being lensed by foreground galaxies, the condition that the lens size be small compared to D_l, D_s and D_{ls} is fulfilled.

The multiple images of lensed quasars act as 'standard candles' shining through different parts of the lensing galaxy and can therefore be used to study its extinction curve (as first pointed out by Nadeau et al., 1991). As lensing is achromatic in nature, the flux ratio of any two lensed images should be independent of wavelength. If, however, one of the images shines through a dusty part of the galaxy and the other image does not, the first image will appear red compared to the other. By mapping the flux ratio as a function of wavelength one can in principle

directly trace the differential extinction curve between the two images, without making any assumptions about the intrinsic spectrum of the quasar (as it cancels in the calculation of the flux ratios). Depending on the number of images, it will be possible to obtain differential extinction curves for several paths through the lensing galaxy.

As the light rays travel along different paths for multiple images, their travel times do in general differ, introducing a time delay between different images. If the quasar is variable, the variability will show up at different times in the different images which can lead to inaccurate estimates of the dust extinction. Ideally one would like to measure each image with a time separation according to the time delay to correct for this effect. Time delays are, however, difficult to measure and measurements exist for only a few lenses. Alternatively one can observe simultaneously in all the observing bands. This would mean that any achromatic variability would cancel out when comparing the images (but would lead to biased estimates of the intrinsic brightness ratio of the images). Simultaneous observations also have the additional benefit that the effects of achromatic microlensing will, to first order, only affect the intrinsic ratio estimate and not the shape of the extinction curve, which would in general not be the case if the images were observed according to a time schedule given by the time delay. The effects of microlensing are the greatest potential source of systematic error in the extinction curve analysis and are addressed in greater detail in § 3.2.4.

3.2.2 Extinction

As lensing is an achromatic process one would expect the magnitude difference in all bands to be constant for each pair of lensed images in the absence of extinction. Extinction reduces the brightness of the measured images by a different amount for each band (and image) depending on the amount and properties of the dust along the line of sight to the images. It is this difference which gives rise to the extinction curve as a function of wavelength. As both the images might be affected by extinction what one is really measuring is the differential extinction between the pair of images. The extinction affects each measured data point as:

$$m(\lambda) = \hat{m}(\lambda) + A(\lambda), \qquad (3.3)$$

where $m(\lambda)$ is the measured magnitude of the image, $\hat{m}(\lambda)$ is the intrinsic magnitude of the image and $A(\lambda)$ is the extinction at wavelength λ. When comparing images A and B one therefore gets:

$$
\begin{aligned}
\Delta m(\lambda) &\equiv m^B(\lambda) - m^A(\lambda) \\
&= (\hat{m}^B - \hat{m}^A) + A^B(\lambda) - A^A(\lambda) \\
&\equiv \Delta\hat{m} + A^{diff}(\lambda),
\end{aligned} \tag{3.4}
$$

where $\Delta\hat{m} \equiv \hat{m}^B - \hat{m}^A$ is the intrinsic magnitude difference which does not depend on wavelength and $A^{diff}(\lambda) \equiv A^B(\lambda) - A^A(\lambda)$ is the effective differential extinction law as a function of the wavelength.

Three different extinction laws are considered and it is assumed that the extinction of one of the images dominates the other (see further discussion on extinction in both images in § 3.2.3). The first extinction law to consider is the empirical Galactic extinction law as parametrised by Cardelli et al. (1989):

$$
\begin{aligned}
A(\lambda) &= E(B-V)\left[R_V a(x) + b(x)\right] \\
&= A(V)\left[a(x) + \frac{1}{R_V}b(x)\right],
\end{aligned} \tag{3.5}
$$

where $A(\lambda)$ is the total extinction at wavelength λ, $E(B-V) = A(B) - A(V)$ is the colour excess, $R_V = A(V)/E(B-V)$ is the ratio of total to selective extinction, $a(x)$ and $b(x)$ are polynomials and $x = \lambda^{-1}$. Next an extinction law is considered which is linear in inverse wavelength which is characteristic for the extinction in the SMC:

$$
A(\lambda) = A(V)\left(\frac{\lambda}{5500}\right)^{-1}. \tag{3.6}
$$

Finally the linear law is extended to a power law:

$$
A(\lambda) = A(V)\left(\frac{\lambda}{5500}\right)^{-\alpha}. \tag{3.7}
$$

To fit data points to the extinction laws one first shifts the wavelength of the measured bands to the rest frame of the lensing galaxy, i.e. $\lambda_j = \lambda_j^O/(1+z_l)$ where λ_j^O is the observed wavelength in band j and z_l is the redshift of the lensing

galaxy. For each image pair one can then calculate the magnitude difference of the images in each measured band:

$$m^B(\lambda_j) - m^A(\lambda_j) = -2.5 \log_{10} \left(\frac{f_j^B}{f_j^A} \right), \tag{3.8}$$

where f_j^B/f_j^A is the flux ratio between images labelled B and A at λ_j. One can then perform fits for eq. (3.5) where one replaces $A^{diff}(V)$ with $A(V)$:

$$m^B(\lambda) - m^A(\lambda) = A(\lambda) + \Delta \hat{m}, \tag{3.9}$$

where $A(\lambda)$ is one of the extinction laws described in eqs. (3.5), (3.6) and (3.7). If radio measurements exist for the flux density of the images, one can use them to constrain the intrinsic magnitude difference, $\Delta \hat{m}$, as radio measurements are not affected by extinction.

3.2.3 Extinction along both lines of sight

As the method used measures differential extinction curves, the systematics of extinction along both lines of sight in the results need to be investigated. A study of the effects of a Galactic extinction law along both lines of sight but with different values of R_V is conducted. When both images suffer extinction one expects to get an effective extinction law which may have different properties to those of either line of sight. In the general case, when $E^B(B-V) \neq E^A(B-V)$, the difference in extinction suffered by image A vs. image B will be given by an effective Galactic extinction law:

$$
\begin{aligned}
A^{diff}(\lambda) &\equiv A^B(\lambda) - A^A(\lambda) & (3.10) \\
&= E^B(R_V^B a(\lambda^{-1}) + b(\lambda^{-1})) - & (3.11) \\
&\quad E^A(R_V^A a(\lambda^{-1}) + b(\lambda^{-1})) \\
&= \left(E^B - E^A \right) \left(\frac{E^B R_V^B - E^A R_V^A}{E^B - E^A} a(\lambda^{-1}) + b(\lambda^{-1}) \right) & (3.12) \\
&\equiv \left(E^B - E^A \right) \left(R_V^{diff} a(\lambda^{-1}) + b(\lambda^{-1}) \right)
\end{aligned}
$$

where $E(B-V) = E$ has been written for simplicity, the assumption $E^B \neq E^A$ has been explicitly used in the step from equation (3.11) and (3.12) and $R_V^{diff} \equiv$

$(E^B R_V^B - E^A R_V^A)/(E^B - E^A)$ is the effective R_V one measures. For completeness it should be noted that in the special case of $E^A = E^B$ the resulting effective extinction curve is not given by the Galactic extinction law parametrisation. Taking $E^B > E^A$, one finds that the ratio of R_V^{diff} to the R_V^B (which is what is being measured) is given by:

$$
\begin{aligned}
\frac{R_V^{diff}}{R_V^B} &= \frac{E^B - E^A R_V^A / R_V^B}{E^B - E^A} \\
&= 1 + \frac{E^A}{E^B - E^A}\left(1 - \frac{R_V^A}{R_V^B}\right) \\
&\equiv 1 + \eta
\end{aligned}
\tag{3.13}
$$

so the error introduced in the estimate due to the non-zero extinction of image A is

$$
\eta = \frac{E^A/E^B}{1 - E^A/E^B}\left(1 - \frac{R_V^A}{R_V^B}\right).
\tag{3.14}
$$

It should be noted that if $R_V^A > R_V^B$, the inferred value of R_V for image B will be lowered, and vice versa, and that, in theory, any value of R_V can be obtained. A contour plot of η can be seen in Figure 3.2. Taking the most extreme values of the Milky Way ($2 \lesssim R_V \lesssim 6$) one sees that the bracket in equation (3.14) can realistically range from $(1 - 6/2) = -2$ to $(1 - 2/6) = 2/3$. In the worst case scenario, when $R_V^B \ll R_V^A$, the ratio of $E^A/(E^B - E^A)$ needs to be half that of the desired accuracy, i.e., for a desired accuracy of 10% in R_V, $E^A/(E^B - E^A) \leq 0.05$ is needed. For more realistic cases of $R_V = 3$ for image B and $R_V = 4$ for image A one only needs $E^A/(E^B - E^A) \leq 0.3$. In general, for an accuracy of $|\eta| \leq \eta_0$, one needs:

$$
\frac{E^A}{E^B} \leq \frac{\eta_0/|1 - R_V^A/R_V^B|}{1 + \eta_0/|1 - R_V^A/R_V^B|}.
\tag{3.15}
$$

Finally it is noted for completeness that a linear extinction in both images trivially produces a linear differential extinction whereas a power law extinction along both lines of sight does not in general produce a power law for the differential extinction.

McGough et al. (2005) did a similar study of the effect of non-zero extinction along both lines of sight, where they also found that, in theory, any value of R_V can be obtained. They suggest that cases where only one of the images is lightly
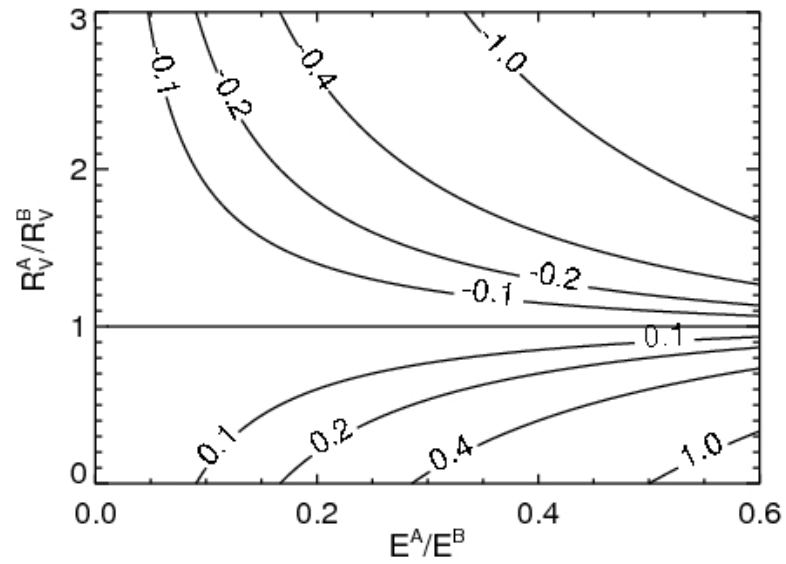
Figure 3.2 Contour plot of η as defined in eq. (3.14) which measures the relative error of the effective R_V^{diff} to R_V^B as a function of E^A/E^B and R_V^A/R_V^B for extinction along both lines of sight.

reddened or the dust properties are the same for both sight lines are likely rare and hard to confirm. However, the above shows that it is not crucial that one of the images have no or little extinction in absolute terms, but only relative to the image one is comparing it to, and that in practice, one of the images often shows less extinction than the others. When dealing with multiply imaged quasars, in particular for doubly imaged systems, one of the images is often situated at a greater distance from the lens galaxy than the others and therefore may be less affected by extinction. In some cases this lack of extinction in one of the components can be confirmed by studying the images in the X-rays (K. Pedersen et al., 2006, in preparation).

3.2.4 Microlensing

Microlensing, lensing by stars or other compact objects in the lens galaxy, can also affect the data and in particular it can affect the continuum part of the emission. This is because, according to standard quasar models (Krolik, 1999), the regions giving rise to the continuum and emission lines are of different size and therefore affected differently by microlensing which is more effective on small scales. As the emission lines arise from regions several orders of magnitude larger than the region emitting the continuum, the microlensing acts strongest on the continuum emission but should be nearly absent for emission lines.

To allow for possible corrections due to this effect one calculates for each quasar the ratio of the spectral line emission to the total emission in each band (this varies for the systems as the quasars are at different redshifts). A composite quasar spectrum is used for the calculations as derived by Vanden Berk et al. (2001) using 2200 spectra from the Sloan Digital Sky Survey. In accordance with their results the continuum is modelled as a broken power law ($f_\lambda \propto \lambda^{\alpha_\lambda}$) with $\alpha_\lambda = -1.56$ for $\lambda \leq 4850$ and $\alpha_\lambda = 0.45$ for $\lambda > 4850$. Taking into account spectral lines with equivalent width $W \geq 1$ and they are modelled as Gaussians which are added to the continuum to get the final template spectrum. Using this standard quasar template the ratio of the flux coming from the continuum compared to the total emission is calculated for each measurement band shifted to

the corresponding band at the redshift of the lensing galaxy using the transmission curves of the corresponding filter (see Figure 3.3).

An effect from an achromatic microlensing signal, which affects the different bands proportionally to the ratio of the continuum to the total emission (consisting of the continuum with the added spectral lines), is added to the fit. Achromatic microlensing affects the fluxes of the images as $f_j \to f_j(1 + sr_j)$ where r_j is the ratio of the continuum emission to the total emission in band j and s is a microlensing parameter giving the strength of the microlensing signal (which is a constant in the achromatic case). The measured magnitude is therefore:

$$
\begin{aligned}
m(\lambda_j) &= -2.5 \log_{10}\left(f_j(1 + sr_j) \right) + A(\lambda_j) \\
&= \hat{m}(\lambda_j) - 2.5 \log_{10}(1 + sr_j) + A(\lambda_j).
\end{aligned}
\tag{3.16}
$$

The additional term in eq. (3.16) modifies eq. (3.9) to:

$$
\begin{aligned}
(m^B - m^A)(\lambda_j) &= A(\lambda_j) + \Delta\hat{m} - 2.5 \log_{10}\left(\frac{1 + s^B r_j}{1 + s^A r_j} \right) \\
&\approx A(\lambda_j) + \Delta\hat{m} - 2.5 \frac{r_j(s^B - s^A)}{\ln(10)} \\
&\equiv A(\lambda_j) + \Delta\hat{m} + sr_j,
\end{aligned}
\tag{3.17}
$$

where $s \equiv 2.5(s^A - s^B)/\ln(10)$ and the approximation is made to reduce the number of parameters in the fit. For the approximation in eq. (3.17) to be valid one needs $r_j|s^B - s^A| \lesssim 1$. The value of r_j can in theory lie between 0 and 1 but in the case lies between 0.8 and 1, so therefore one needs $|s^B - s^A| \lesssim 1$ in practice. In physical terms this is roughly equivalent to the condition that the change in magnitude difference between the two images due to microlensing should be less than 1 mag. Most microlensing studies show magnitude changes of less than 0.5 mag so therefore this approximation should not affect the results.

Microlensing can also introduce a smooth chromatic signal similar to an extinction signal if the source has different colours in different locations. The method employed in this chapter does not take this into account as the broad band photometry does not contain enough information to disentangle such an effect from extinction. To separate the two it is necessary to study the spectra of the object itself (and not a mean quasar spectrum) along the lines of Wucknitz et al. (2003).
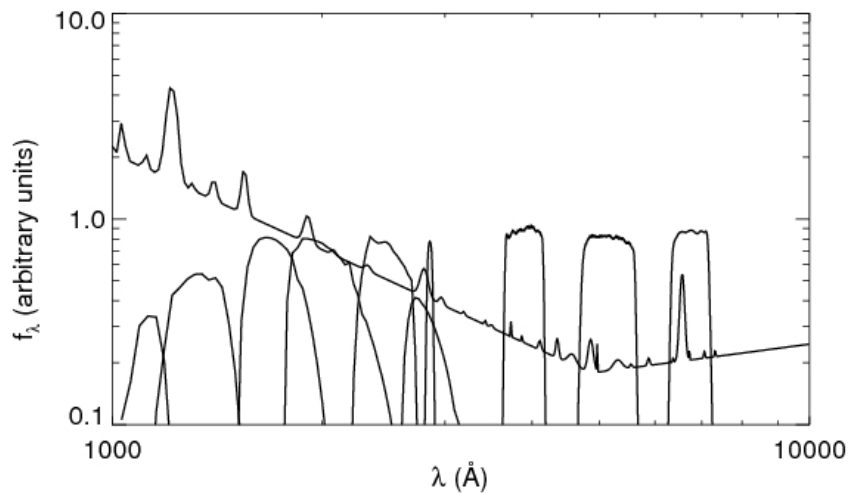
Figure 3.3 The composite quasar spectra modelled as a broken power law with spectral lines with equivalent width $W \geq 1$ added on as Gaussians. The superimposed transmission curves correspond to the FORS1 and ISAAC U, B, V, R, I, z (Gunn) , z (special), J_s, H and K_s bands. The transmission curves have been shifted to show which part of the spectrum they correspond to for a quasar of $z = 2.2$.

3.2.5   Monte Carlo analysis

The errors of the parameters of the fitted extinction curves are estimated using Monte Carlo simulations. A thousand realisations of the data set are generated by allowing each data point to vary with a Gaussian distribution centred on the measured point and with a variance corresponding to the error estimate of the data point. The extinction law fits are then applied separately to each data set. If the fits are good, i.e., there is no degeneracy or systematic errors, the resulting fitted parameters should also follow a Gaussian distribution. The median of the parameter distribution is quoted as the 'best fit parameter' and the quoted error is the standard deviation of the parameter distribution. For the Galactic extinction law the constraint $0 \leq R_V \leq 7$ has been used unless otherwise noted. This method is applied to both the simulations in § 3.2.6 and the real data sets in § 3.3.

3.2.6   Simulated data

To test the ability of the analysis to recover and distinguish between different extinction curves, and the effects of microlensing and noise, the method is applied to simulated data. The simulated data consist of data in nine bands, $UBVRIzJsHK$, with an applied signal corresponding to extinction, noise and microlensing. Runs are performed for different kinds of the three extinction laws, with or without noise, and with or without microlensing effects.

3.2.6.1   Pure extinction in one image

The first set of runs consists of pure extinction in one image with a 0.05 mag 1σ uncertainty in each data point. The purpose of those runs is twofold, first to test the routines and secondly to see whether there is a significant difference between the goodness of fit for the different extinction laws. In all cases it is found that the routines converge to the given initial parameters. In addition it is found that the ability to recognise one extinction law from the other depends on the strength of the extinction and the redshift of the simulated data. This is not surprising as the three fitted extinction laws behave very similarly for $\lambda \geq 2500$

and for $z = 0$ all the bands lie above that limit. The importance of the strength of the extinction is also easy to understand, as the ability to detect any difference between extinction laws will be overwhelmed by the photometric errors for very weak extinction.

At $z = 0$ for a Galactic extinction law input the reduced chi-squared, χ_ν^2, for a Galactic extinction law is somewhat lower than for the other extinction laws (≈ 1.0 for the Galactic extinction law, ≈ 1.0–1.6 for the power law, ≈ 1.0–6 for the linear law). The difference depends both on the strength of the extinction, $A(V)$ (with $A(V) \lesssim 0.1$ resulting in equal goodness of fits), and on the value of R_V with more extreme values ($R_V = 1$, $R_V = 6$) giving a greater difference than $R_V = 3.0$ (see Table 3.1 for representative values and Figures 3.4 and 3.5 for representative plots). When the input extinction law is a linear law, λ^{-1}, the power law yields the same goodness of fit ($\chi_\nu^2 \approx 1.0$) but the Galactic extinction law gives a slightly higher value (≈ 1.0–1.9). Finally, when the input extinction law is a power law with power index $\alpha = 2$, there is a significant difference in the goodness of fit with the power law fit giving $\chi_\nu^2 \approx 1.0$ but the Galactic extinction law giving $\chi_\nu^2 \approx 1.0$–1.7 and λ^{-1} giving $\chi_\nu^2 \approx 1.0$–6.5. Here the difference in the goodness of fit for the Galactic extinction law and λ^{-1} depends on the value of $A(V)$, with lower $A(V)$ (i.e., less extinction) giving lower χ_ν^2 for the two extinction laws.

Simulations for two non-zero values of the redshift, at $z = 0.30$ and $z = 0.80$ are also performed. At these higher redshifts the difference in the extinction laws becomes more prominent which is reflected in the goodness of the fits (see Table 3.1 and Figs. 3.4 and 3.5) making them in general easier to distinguish from one another. This is because the extinction laws are all very similar for $\lambda^{-1} \lesssim 3~\mu m^{-1}$, and for redshift of $z = 0$ the lowest wavelength band, the U-band, lies below this limit. At the higher redshifts, the lowest wavelengths move into the UV, which is more sensitive for differences in the extinction laws. For very weak extinction ($A(V) \lesssim 0.1$) it is still the case that the different types of extinction laws become hard to separate, as the error bars can dominate the extinction signal.

From the simulations one can deduce that given a strong enough extinction the different kinds of extinction laws should be recognisable from each other. As can be seen from Table 3.1, the needed strength is dependent on the redshift of

Table 3.1.   Goodness of fits from simulations

Input parameters				Output χ_ν^2 from the different fits					
z	Type	$A(V)$	Parameter	(1)	(2)	(3)	(4)	(5)	(6)
0.0	Galactic	0.5	$R_V = 1.0$	0.94	0.93	1.6	1.6	5.9	3.5
0.3	Galactic	0.5	$R_V = 1.0$	0.97	0.96	1.9	1.6	8.5	4.2
0.8	Galactic	0.5	$R_V = 1.0$	0.95	0.94	3.4	2.9	15	6.8
0.0	Galactic	1.0	$R_V = 3.0$	0.95	0.94	1.4	1.1	2.5	1.1
0.3	Galactic	1.0	$R_V = 3.0$	0.96	0.96	1.9	1.2	2.3	1.5
0.8	Galactic	1.0	$R_V = 3.0$	0.96	0.94	1.8	1.7	2.9	1.6
0.0	Galactic	0.5	$R_V = 3.0$	0.95	0.94	1.1	1.0	1.5	1.0
0.3	Galactic	0.5	$R_V = 3.0$	0.95	0.95	1.2	1.0	1.4	1.1
0.8	Galactic	0.5	$R_V = 3.0$	0.96	0.94	1.2	1.2	1.6	1.2
0.0	Galactic	0.1	$R_V = 3.0$	0.97	0.97	0.95	0.94	0.98	0.92
0.3	Galactic	0.1	$R_V = 3.0$	0.95	0.94	0.97	0.98	0.97	0.96
0.8	Galactic	0.1	$R_V = 3.0$	0.95	0.95	0.97	0.98	0.99	0.96
0.0	Galactic	0.5	$R_V = 6.0$	0.96	0.96	1.3	1.0	1.2	1.3
0.3	Galactic	0.5	$R_V = 6.0$	0.96	0.96	1.7	1.3	1.9	1.8
0.8	Galactic	0.5	$R_V = 6.0$	0.95	0.94	1.6	1.3	2.7	1.9
0.0	Power law	1.0	$\alpha = 2$	1.6	1.7	0.96	0.95	6.5	3.5
0.3	Power law	1.0	$\alpha = 2$	2.3	2.1	0.95	0.95	11	5.7
0.8	Power law	1.0	$\alpha = 2$	4.7	4.5	0.95	0.93	21	11
0.0	Power law	0.5	$\alpha = 2$	1.1	1.2	0.97	0.96	3.4	1.9
0.3	Power law	0.5	$\alpha = 2$	1.4	1.3	0.96	0.95	5.5	3.0
0.8	Power law	0.5	$\alpha = 2$	2.4	2.3	0.94	0.94	11	5.5
0.0	Power law	0.3	$\alpha = 2$	1.0	1.0	0.97	0.97	2.2	1.4
0.3	Power law	0.3	$\alpha = 2$	1.1	1.1	0.96	0.95	3.4	1.9
0.8	Power law	0.3	$\alpha = 2$	1.6	1.6	0.95	0.94	6.4	3.4
0.0	Power law	0.1	$\alpha = 2$	0.95	0.95	0.94	0.94	1.2	1.0
0.3	Power law	0.1	$\alpha = 2$	0.97	0.96	0.95	0.96	1.4	1.1
0.8	Power law	0.1	$\alpha = 2$	1.0	1.0	0.94	1.0	2.3	1.4
0.0	Linear	1.0	$\alpha = 1$	1.9	1.1	0.96	0.94	0.96	0.96
0.3	Linear	1.0	$\alpha = 1$	2.2	1.2	0.95	0.95	0.96	0.95
0.8	Linear	1.0	$\alpha = 1$	1.9	1.5	0.95	0.95	0.96	0.95
0.0	Linear	0.5	$\alpha = 1$	1.3	1.0	0.96	0.96	0.96	0.96
0.3	Linear	0.5	$\alpha = 1$	1.4	1.0	0.96	0.94	0.96	0.95
0.8	Linear	0.5	$\alpha = 1$	1.3	1.1	0.94	0.93	0.96	0.94
0.0	Linear	0.3	$\alpha = 1$	1.1	0.96	0.96	0.95	0.96	0.96
0.3	Linear	0.3	$\alpha = 1$	1.1	0.97	0.96	0.95	0.95	0.95
0.8	Linear	0.3	$\alpha = 1$	1.1	1.0	0.94	0.92	0.95	0.94
0.0	Linear	0.1	$\alpha = 1$	0.98	0.95	0.95	0.95	0.95	0.95
0.3	Linear	0.1	$\alpha = 1$	0.98	0.97	0.96	0.99	0.97	0.96
0.8	Linear	0.1	$\alpha = 1$	0.97	0.95	0.95	0.99	0.96	0.95

Note. — Table of χ_ν^2 for representative values of the simulated data. The output columns correspond to Galactic extinction law with $\Delta\hat{m}$ fixed (1) and free (2), power law with $\Delta\hat{m}$ fixed (3) and free (4), and linear law with $\Delta\hat{m}$ fixed (5) and free (6).
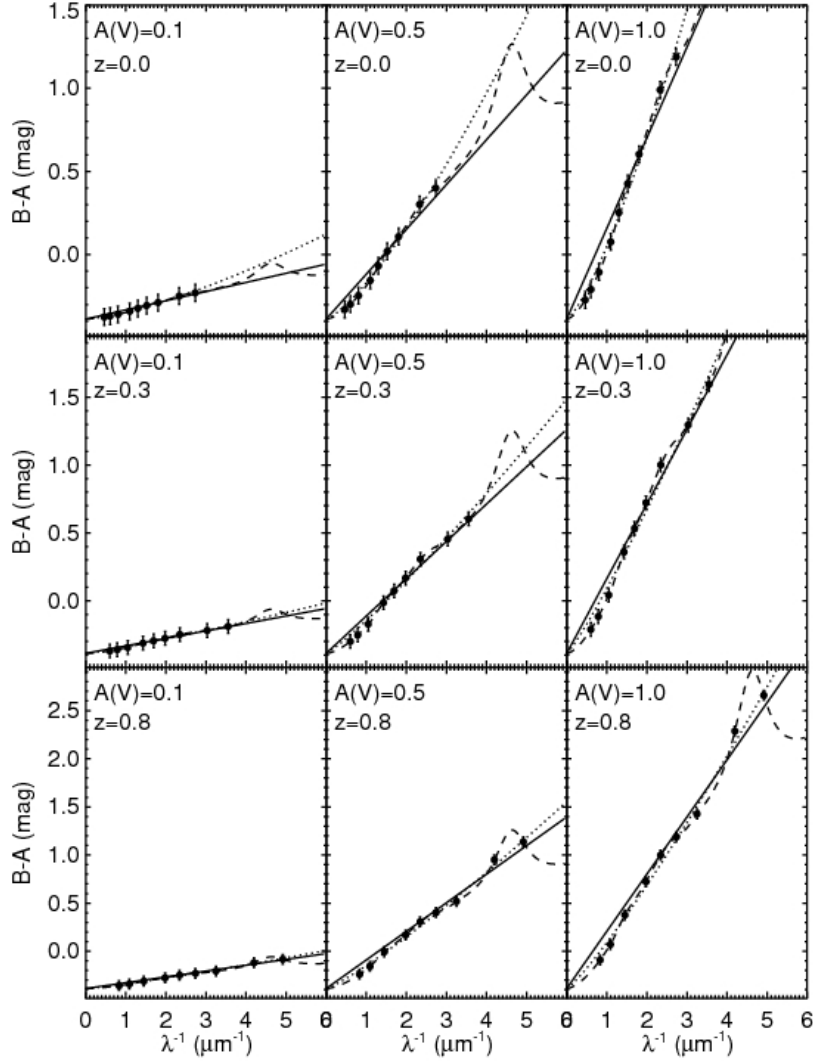
Figure 3.4 A sample plot for simulations showing three data sets at redshift of $z = 0.0, 0.3$ and 0.8. The extinction law applied is the Galactic extinction law with $R_V = 3$ and $A(V) = 0.1, 0.5, 1.0$ and the three fits shown are the Galactic extinction law (dashed line, eq. (3.5)), power law (dotted line, eq. (3.7)) and linear law (solid line, (3.6)).
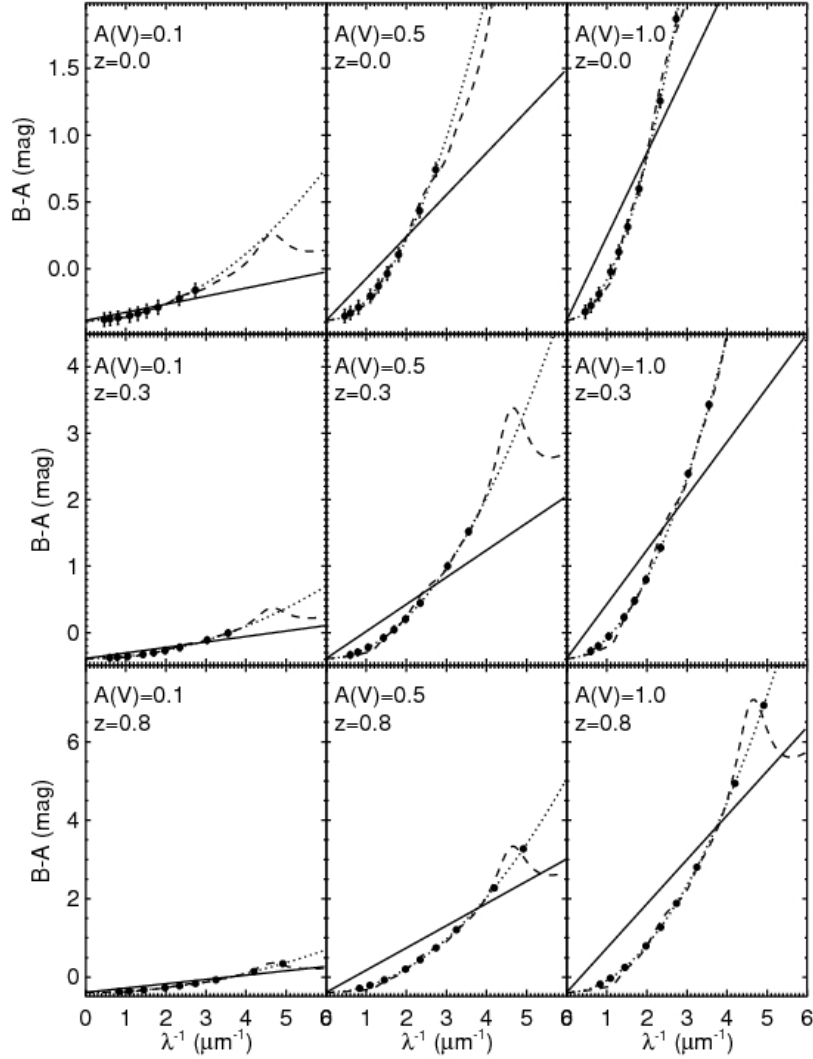
Figure 3.5 A sample plot for simulations showing three data sets at redshift of $z = 0.0, 0.3$ and 0.8. The extinction law applied is the power law with $\alpha = 2$ and $A(V) = 0.1, 0.5, 1.0$ and the three fits shown are the Galactic extinction law (dashed line, eq. (3.5)), power law (dotted line, eq. (3.7)) and linear law (solid line, (3.6)).

the lens, with more nearby lenses requiring stronger extinction to distinguish the different extinction laws. In general, it is found that for $A(V) \gtrsim 0.3$ one can distinguish the different extinction laws, in particular if one has constraints on $\Delta\hat{m}$. The parameters of the power law fit tend to be more poorly constrained than those of the other fits. This is due to the added degree of freedom which can result in several sets of parameters giving similar χ^2_ν. It is also seen that if one can constrain the intrinsic magnitude ratio, the different extinction laws become easier to distinguish.

3.2.6.2 Extinction in both images

First data are simulated where the same extinction law is applied to both images (i.e., R_V and α are constant respectively) but at different strengths. Here it is found that unless $A^A(V) \approx A^B(V)$ (i.e., in effect a very weak differential extinction), the fits converge to the starting parameters and give the shape of the 'real' extinction curves.

To see what effect extinction in both images would have on a data set, simulate data having different kinds of Galactic extinction laws are created, to find within which accuracy the input parameters of the more strongly extinguished line of sight are found (see Fig. 3.6). Again it is found, that if the differential extinction between the images, $E^B(B-V) - E^A(B-V)$, is low, then the fits are not well constrained and the resulting parameters represent the extinction of neither line of sight. However, if one image is significantly more extinguished than the other then the parameters of the fit converge to the parameters of that line of sight as expected (see discussion in § 3.2.3). It is not crucial that one image be non-extinguished, but it does need to have significantly lower extinction than the other line of sight. It is found that for the fits to be within one sigma of the real parameters for the line of sight for the stronger extinction one needs roughly $E(B-V)_{weaker}/E(B-V)_{stronger} \lesssim 0.2$ when the R_V values lie in the range of $2-4$. This is consistent with the results from §3.2.3 (in particular, see eq. (3.14) and (3.15)).
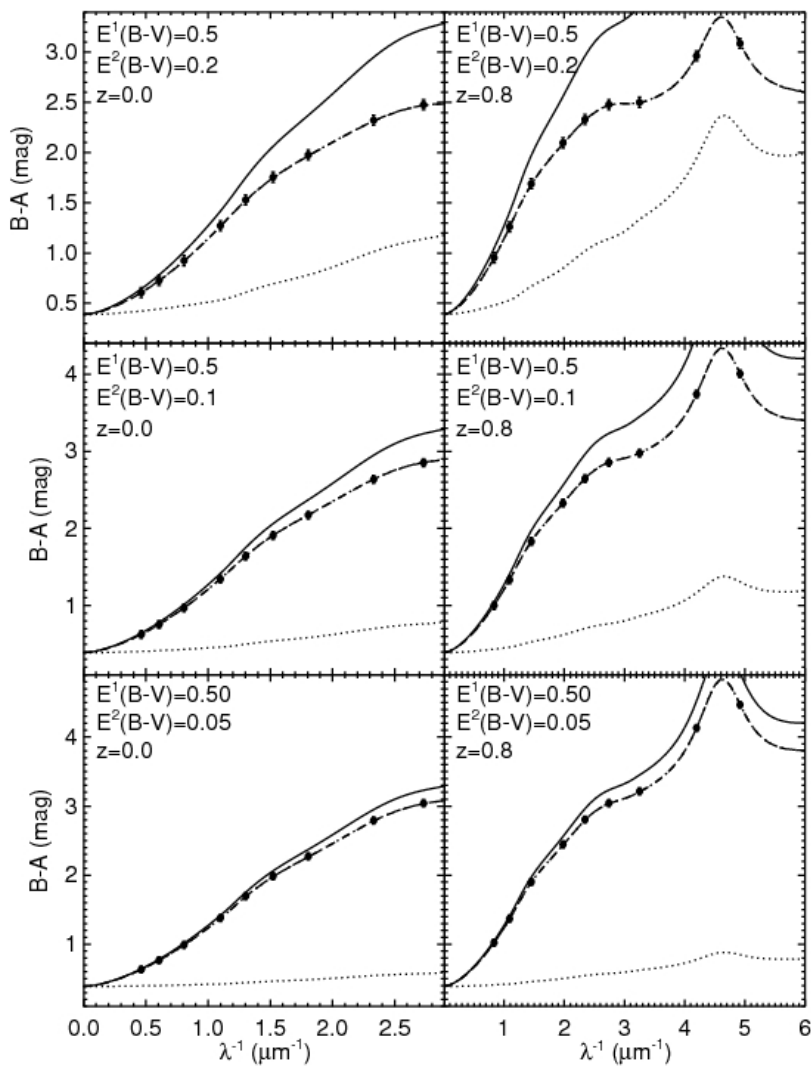
Figure 3.6 A sample plot for simulations with Galactic type extinction in both images at two different redshifts ($z = 0.0$ and 0.8). The solid and the dotted lines are the input extinction laws and the dashed line is the effective differential extinction between the two images. It is shown that when the extinction along one line of sight is much stronger than the other, then the effective extinction law approaches the extinction of the more strongly extinguished image.

3.2.6.3 The effects of noise

When dealing with real data one can expect the data sets to be contaminated by various sources of noise. To see how this may affect the analysis data sets with artificial random noise are generated (see Fig. 3.7 for representative plots). The noise is generated as normally distributed random numbers with a mean of 0 and standard deviation of 0.05 magnitudes (which is an estimate of the lowest noise expected from deconvolved ground based data as the data set used in this chapter). One still gets qualitatively the same results, i.e., the lowest χ^2_ν is obtained for the Galactic type extinction fit to the Galactic extinction law data (provided the extinction is strong enough), and the fitted parameters agree with the input parameters, within the uncertainty. The χ^2_ν values for the fits are increased and the uncertainty on the parameters for the noisy data is generally larger. If the noise becomes too large, i.e. of the order of the extinction effects, the fits become badly constrained. This emphasises the need for a strong extinction signal to outweigh random noise effects when analysing the real data sets.

3.2.6.4 Achromatic microlensing

Several sets of data consistent with the Galactic extinction law with an effective microlensing parameter $0.01 < s < 0.3$ are created to test the effects of achromatic microlensing on the methods (see Fig. 3.8). IT is found that for very weak microlensing ($s = 0.01$) there is no noticeable effect on the results (given $E(B - V) \geq 0.1$), in particular not when noise (of 0.05 mag) is included in the data points as the noise dominates the effects of the microlensing. For a stronger microlensing signal ($0.05 \lesssim s$) one finds that the effects are indeed noticeable but to be able to quantify them it is crucial to be able to constrain the intrinsic magnitude ratio difference. It is found that a fit with a free intrinsic ratio can often give as good a fit (as measured by the χ^2_ν) as the fit which allows for correction due to the microlensing signal. This is because the effects of the microlensing can in part be mimicked by shifting the whole data set up and down along the magnitude difference axis by changing the intrinsic magnitude difference if the ratio of the continuum emission to the total emission is similar for the different bands (see eq. (3.17)).
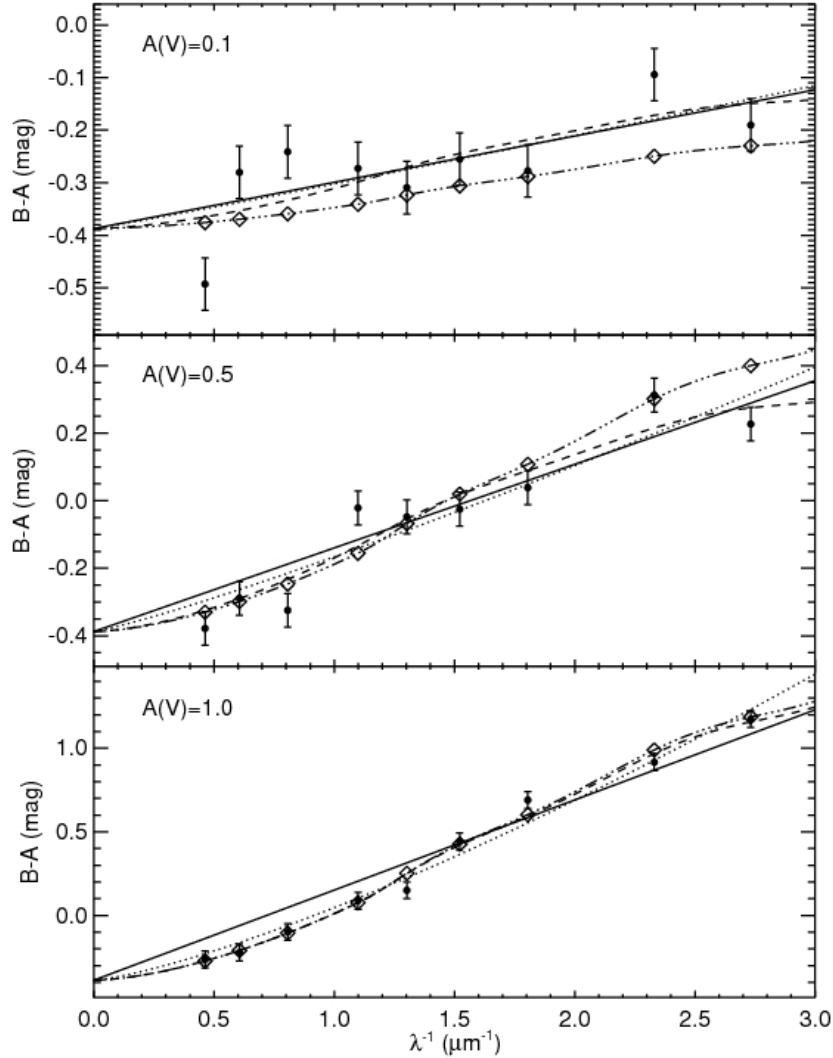
Figure 3.7 A sample plot for simulations with noise showing three data sets with $A(V) = 0.1, 0.5$ and 1.0. The diamonds and the dash-dotted line show the noise-less input extinction law (Galactic extinction law with $R_V = 3.0$), and the solid dots show the data points with random noise applied. The three fits shown are the Galactic extinction law (dashed line, eq. (3.5)), power law (dotted line, eq. (3.7)) and linear law (solid line, (3.6)). One sees that for low extinction $(A(V) \lesssim 0.1)$ the noise is of the order of the amount of the extinction signal, and therefore significantly affects the quality of the fits.
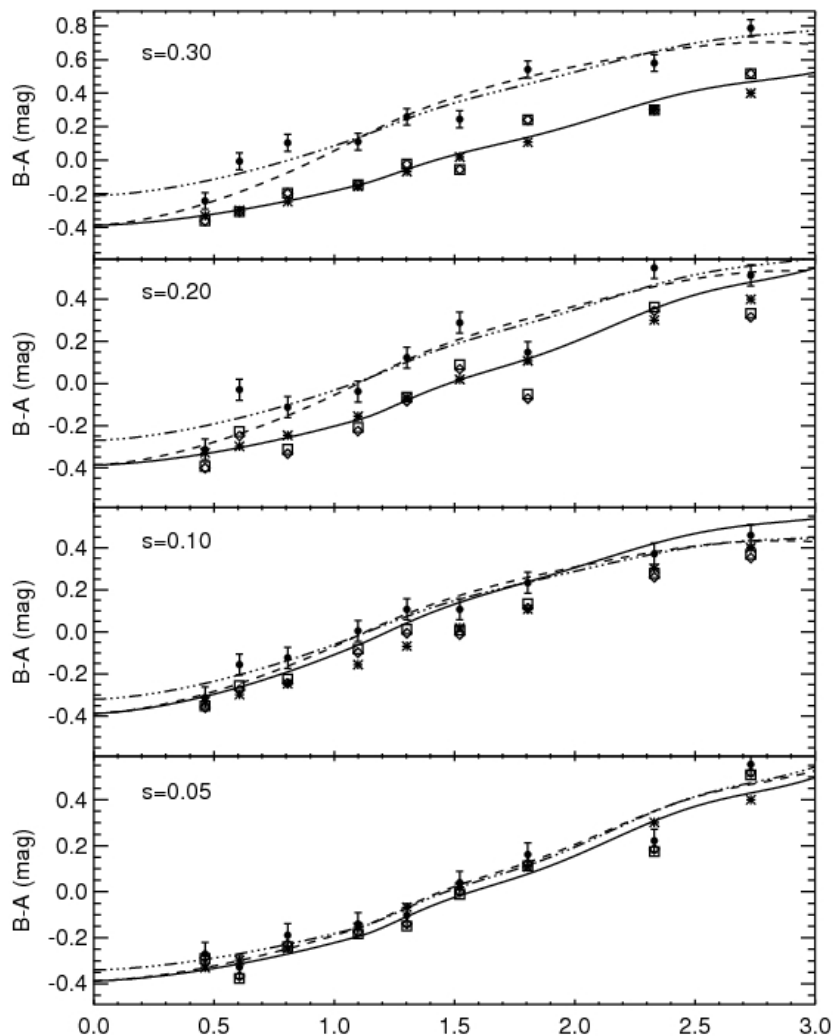
Figure 3.8 A sample plot for simulations with an achromatic microlensing signal $s = 0.05, 0.10, 0.20, 0.30$ and noise. The asterisks are the noise free input data points, the boxes are the input data points with noise, the solid circles are the microlensed data points which are fitted and the diamonds are the microlensing corrected points from the fit. The dashed and dash-dotted lines are the best fitting Galactic extinction law with $\Delta \hat{m}$ free and fixed through the microlensed data points and he solid line shows the best fitting Galactic extinction law with $\Delta \hat{m}$ free with a microlensing correction. The microlensing signal starts dominating the noise when the average distance from the asterisks to the boxes becomes smaller than the average distance from the boxes to the filled circles which happens around $s = 0.05$.

Table 3.2.   Table of Lenses

Lens	z_l	z_Q	Type	d_s $(\log d_s/'')$	Images	d_g $('')$	Ref.
Q2237+030	0.04	1.70	Late[a]	-0.59 ± 0.08	(A,B,C,D)	(0.92, 0.97, 0.76, 0.88)	1, 2
PG1115+080	0.31	1.72	Early	-0.33 ± 0.02	(A1,A2,B,C)	(1.18, 1.12, 0.95, 1.37)	1, 3
B1422+231	0.34	3.62	Early	-0.50 ± 0.13	(A,B,C,D)	(0.95,0.89,1.04,0.36)	1, 4
B1152+199	0.44	1.02	Late[b]	-0.8 ± 0.2[c]	(A,B)	(1.14, 0.47)	5, 6
Q0142−100	0.49	2.72	Early	-0.29 ± 0.02	(A,B)	(1.86, 0.38)	1, 7
B1030+071	0.60	1.54	Early	-0.35 ± 0.06	(A,B)	(1.28, 0.58)	1, 7
RXJ0911+0551	0.77	2.80	Early	-0.17 ± 0.04	(A,B,C,D)	(0.87, 0.97, 0.82, 2.24)	8, 9
HE0512−3329	0.93	1.57	Late	-1.0 ± 0.3[c]	(A,B)	(0.035, 0.66)	10, 11
MG0414+0534	0.96	2.64	Early	-0.11 ± 0.08	(A1,A2,B,C)	(1.19, 1.17, 1.38, 0.96)	1, 12
MG2016+112	1.01	3.27	Early	-0.66 ± 0.05	(A,B)	(2.48, 1.25)	1, 11

Note. — The table lists various properties of the lensing systems known from the literature. The properties listed are the lens and quasar redshifts (z_l and z_Q), the type and the scale length (d_s) of the lensing galaxy, and the image names and their distance from the centre of the lens galaxy (d_g). The scale length, d_s, is the effective radius of a de Vaucouleurs profile fit from Rusin et al. (2003). The final column lists the references from which the values were obtained if they have not been previously quoted in the text.

[a]The bulge is responsible for the lensing.

[b]The spectra taken by Myers et al. (1999) shows O II emission line associated with the lens. Therefore B1152+199 is typed as a late type galaxy.

[c]For the purposes of the plotting of Figure 3.21 these scale lengths are adopted although they are not reported in the literature.

References. — (1) Rusin et al. (2003), (2) Rix et al. (1992), (3) Kristian et al. (1993), (4) Yee & Ellingson (1994), (5) Myers et al. (1999), (6) Rusin et al. (2002), (7) Lehár et al. (2000), (8) Rusin et al. (2003), (9) Burud et al. (1998a), (10) Gregg et al. (2000), (11) CASTLES (http://www.cfa.harvard.edu/castles/), (12) Falco et al. (1997).

3.3 Results and Discussion

This chapter opens by presenting in § 3.3.1 the results of the extinction curve analysis for each of the 10 lensing systems. The detailed analysis of systems where at least one image pair has a two sigma detection of extinction for one of the three applied extinction laws are presented. The systems are presented in order of increasing redshift. In § 3.3.2 the overall results of the analysis are discussed, as well as statistical properties of the full sample. The data and their reduction used for the analysis are presented in Appendix A.

3.3.1 The individual systems

3.3.1.1 Q2237+030

Q2237+030 was discovered by Huchra et al. (1985) and consists of a quasar at redshift $z = 1.70$ and a spiral lensing galaxy at $z = 0.04$ making it the nearest known lensing galaxy to date. The system was later resolved into four images forming an Einstein cross with the lensing galaxy in the middle (Schneider et al., 1988; Yee, 1988). Schneider et al. (1988) modelled the system in detail and found a predicted time delay of order of one day between the images and amplifications of $4.6, 4.5, 3.8$ and 3.6 for images A, B, C and D, respectively. Falco et al. (1996) studied the system with the VLA at radio wavelengths and obtained flux density ratios of $1.00, 1.08, 0.55$ and 0.77 for images A, B, C, D, respectively. Q2237+030 has previously been noted in the literature as having high variability which is uncorrelated between the four images (see e.g., Corrigan et al., 1991; Irwin et al., 1989).

This system is difficult to interpret as it shows a lot of scatter in the points which cannot be explained by extinction alone nor microlensing (see Figures 3.9 and 3.10). None of the extinction laws applied give a good fit to the data for any pair of images (as the redshift of this system is very low, $z = 0.04$, one does not expect to see much difference between the quality of the fits for the different extinction laws, see § 3.2.6.1). All the image pairs, except C−A and D−A, yield $A(V)$ consistent with zero. The data points and fits for C−A and D−A can be seen in Figures 3.9 and 3.10 and the parameters of the fits in Tables 3.3 and 3.4.

Table 3.3.   Extinction curve fit results for Q2237+030: C−A

Extinction	$A(V)$	R_V	α	$\Delta\hat{m}$	s	χ^2_ν
Galactic	0.53 ± 0.03	> 7	$\cdots$	*0.65*	$\cdots$	3.6 ± 0.4
Galactic	0.29 ± 0.06	2.9 ± 1.4	$\cdots$	0.85 ± 0.04	$\cdots$	3.4 ± 0.4
Galactic	0.27 ± 0.07	2.6 ± 1.5	$\cdots$	*0.65*	-0.23 ± 0.05	3.4 ± 0.4
Power law	0.49 ± 0.02	$\cdots$	0.6 ± 0.1	*0.65*	$\cdots$	3.2 ± 0.4
Power law	0.3 ± 0.5	$\cdots$	1 ± 4	0.8 ± 0.5	$\cdots$	3.4 ± 0.4
Power law	0.3 ± 0.2	$\cdots$	1 ± 3	*0.65*	-0.2 ± 0.1	3.4 ± 0.4
Linear law	0.49 ± 0.02	$\cdots$	*1.0*	*0.65*	$\cdots$	3.2 ± 0.4
Linear law	0.35 ± 0.05	$\cdots$	*1.0*	0.78 ± 0.04	$\cdots$	3.1 ± 0.4
Linear law	0.34 ± 0.05	$\cdots$	*1.0*	*0.65*	-0.15 ± 0.05	3.1 ± 0.4

Note. — The extinction of image C compared to image A. Numbers quoted in italics were fixed in the fitting procedure.

Table 3.4.   Extinction curve fit results for Q2237+030: D−A

Extinction	$A(V)$	R_V	α	$\Delta\hat{m}$	s	χ^2_ν
Galactic	1.23 ± 0.03	> 7	$\cdots$	*0.28*	$\cdots$	7.1 ± 0.4
Galactic	0.35 ± 0.06	3.1 ± 1.5	$\cdots$	1.05 ± 0.05	$\cdots$	1.9 ± 0.4
Galactic	0.28 ± 0.07	2.1 ± 1.2	$\cdots$	*0.28*	-0.85 ± 0.05	1.9 ± 0.4
Power law	1.11 ± 0.03	$\cdots$	0.27 ± 0.04	*0.28*	$\cdots$	1.9 ± 0.4
Power law	0.4 ± 1.1	$\cdots$	0.9 ± 0.4	0.9 ± 1.1	$\cdots$	2.0 ± 0.4
Power law	0.3 ± 0.4	$\cdots$	1.3 ± 0.6	*0.28*	-0.8 ± 0.4	2.0 ± 0.4
Linear law	1.18 ± 0.03	$\cdots$	*1.0*	*0.28*	$\cdots$	5.9 ± 0.4
Linear law	0.41 ± 0.06	$\cdots$	*1.0*	0.97 ± 0.05	$\cdots$	1.9 ± 0.4
Linear law	0.39 ± 0.06	$\cdots$	*1.0*	*0.28*	-0.75 ± 0.05	1.9 ± 0.4

Note. — The extinction of image D compared to image A. Numbers quoted in italics were fixed in the fitting procedure.

Figure 3.9 Q2237+030, C−A: The upper panel shows the data points and the best fit extinction curves. The lower panel shows the original data points and their shift due to a microlensing signal, along with the best fit through the shifted points. The parameters of the fits are given in Table 3.3. *Annotation:* Filled circles are the original data points with error bars. The curves correspond to the Galactic extinction law (eq. 3.5) with $\Delta\hat{m}$ free (dash-dot) and fixed (solid), the power law (eq. 3.7) with $\Delta\hat{m}$ free (dash-dot-dot-dot) and fixed (dotted) and the linear law (eq. 3.6) with $\Delta\hat{m}$ free (long dash) and fixed (short dash). Shifted data points due to a microlensing signal are plotted in open boxes (Galactic extinction law), triangles (power law) and diamonds (linear law).

Figure 3.10 Q2237+030, D−A: The upper panel shows the data points and the best fit extinction curves. The lower panel shows the original data points and their shift due to a microlensing signal, along with the best fit through the shifted points. The parameters of the fits are given in Table 3.4. See the caption of Figure 3.9 for annotation overview.

3. EXTINCTION CURVES OF LENSING GALAXIES

Radio measurements of Falco et al. (1996) are used to fix $\Delta\hat{m}$ and in particular for the D−A image pair this changes the results significantly. As the flux density ratios in the radio agree with the model predictions for the D−A image pair it is interesting to note that none of the extinction laws applied give good fits to the data unless one allows for corrections due to achromatic microlensing (see Figures 3.9 and 3.10 and Tables 3.3 and 3.4). This might suggest that either D is demagnified by a strong microlensing signal, or that image A is magnified (or both) and the residual 'extinction curve' which is being fitted may be effects of chromatic microlensing. The same effect, but not as strong, is seen in the C−A image, again suggesting a slight demagnification of C, a magnification of A or a combination of the two. In previous microlensing studies, component D has not been seen to have as strong a microlensing signal as A and C have (Alcalde et al., 2002; Gil-Merino et al., 2005; Irwin et al., 1989) so therefore it is perhaps more likely that one is seeing the magnification of image A.

Another explanation for the shift in $\Delta\hat{m}$ might be intrinsic variations of the quasar components as discussed in §3.2.1. Such variability could introduce an overall shift of the data, resulting in inaccurate estimates of $\Delta\hat{m}$.

By inspecting the V-band lightcurves from Kochanek (2004) one sees that component A is indeed in a bright phase at the time of the observations (Julian date of around 2451670). Component D is fairly stable but component C is getting dimmer climbing down from a peak in its brightness and is still fairly bright, perhaps making the C−A shift in $\Delta\hat{m}$ less prominent than the D−A shift.

3.3.1.2   PG1115+080

PG1115+080 is a multiply imaged system discovered by Weymann et al. (1980) as a triply imaged system with the quasar at redshift $z = 1.72$. The A component was later resolved into two separate images, A1 and A2, by Hege et al. (1981) making the system a quad. The lensing galaxy was located by Christian et al. (1987) and is an early type galaxy (Rusin et al., 2002). Its redshift and that of three neighbouring galaxies were determined to be at $z = 0.31$ by Kundic et al.

Table 3.5.   Extinction curve fit results for PG1115+080

Extinction	$A(V)$	R_V	α	$\Delta\hat{m}$	χ^2_ν
Galactic	0.12 ± 0.06	3.3 ± 1.9	$\cdots$	0.29 ± 0.05	1.2 ± 0.3
Power law	0.3 ± 2.0	$\cdots$	0.5 ± 1.5	0.1 ± 2.0	1.2 ± 0.3
Linear law	0.13 ± 0.03	$\cdots$	*1.0*	0.28 ± 0.04	1.2 ± 0.3

Note. — The extinction of image A2 compared to reference image A1. Numbers quoted in italics were fixed in the fitting procedure.

(1997a). The time delays between the components were determined by Schechter et al. (1997).

The system shows very weak differential extinction for all the images (all but A2−A1 have $A(V)$ equal to 0 within two sigma, see Table 3.15). The data points and fits for A2−A1 are shown on Figure 3.11 and the parameters of the fits in Table 3.5. The low extinction signal is in agreement with the results of Falco et al. (1999).

3.3.1.3   B1422+231

B1422+231 is a quadruply imaged system first discovered by Patnaik et al. (1992) in the JVAS survey and confirmed to be a lensing system by Lawrence et al. (1992). The lensing system consists of an early type main galaxy (Yee & Ellingson, 1994) at $z = 0.34$ (Kundic et al., 1997b; Tonry, 1998) and five nearby galaxies (Bechtold & Yee, 1995; Remy et al., 1993). The quasar is at a redshift of $z = 3.62$ and the maximum image separation is $1.3''$ (Patnaik et al., 1992). The images show intrinsic variability which has been used to determine the time delay by studying radio light curves (Patnaik & Narasimha, 2001).

Only three of the four images are used in the analysis as D was too faint to give usable results (all the visible bands gave zero detection). As for the other components they show very weak differential extinction and give very weak constraints on the differential extinction curves. All the fits have $A(V)$ consistent with zero (see Table 3.15). It is also found that $A(V)$ is consistent with zero when $\Delta\hat{m}$ is fixed (where the values for the $\Delta\hat{m}$ are taken to be the average between
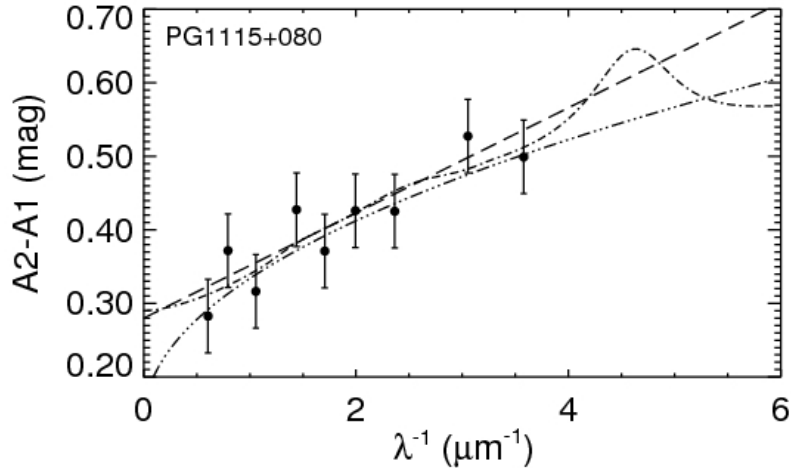
Figure 3.11 PG1115+080, A2−A1: Best fit extinction curves for A2−A1. The parameters of the fits can be seen in Table 3.5. See the caption of Figure 3.9 for annotation overview.

those deduced by Patnaik et al. (1992) in the 5 GHz and 8 GHz bands). The low differential extinction between the images is in agreement with the results of Falco et al. (1999).

3.3.1.4 B1152+199

B1152+199 is a doubly imaged system first discovered by Myers et al. (1999) in the CLASS survey with a background quasar at $z = 1.02$, a lensing galaxy at $z = 0.44$ and image separation of $1''56$. It was observed in radio wavelengths (at frequencies $1.4, 5, 8.4$ and $15\ GHz$) by Rusin et al. (2002). The extinction curve has previously been studied and fitted by a Galactic extinction law with $1.3 \leq R_V \leq 2.0$ and $E(B - V) \sim 1$ (Toft et al., 2000) suggesting that it is a heavily extinguished system.

   B1152+199 shows a very strong extinction signal as can be seen in Figure 3.12 and Table 3.6. It has the strongest extinction signal of all ten systems with $A(V) = 2.43 \pm 0.09, 2.7 \pm 0.1, 3.57 \pm 0.07$ at $\chi_\nu^2 = 2.0, 2.8, 3.4$ for the Galactic extinction law, power law and linear law respectively. Using the ra-

Table 3.6. Extinction curve fit results for B1152+199

Extinction	$A(V)$	R_V	α	$\Delta\hat{m}$	s	χ^2_ν
Galactic	2.03 ± 0.03	1.61 ± 0.05	$\cdots$	*1.18*	$\cdots$	2.7 ± 0.4
Galactic	2.43 ± 0.09	2.1 ± 0.1	$\cdots$	0.85 ± 0.07	$\cdots$	2.0 ± 0.4
Galactic	2.41 ± 0.09	2.0 ± 0.1	$\cdots$	*1.18*	0.32 ± 0.07	2.1 ± 0.4
Power law	2.01 ± 0.03	$\cdots$	1.98 ± 0.04	*1.18*	$\cdots$	4.0 ± 0.4
Power law	2.7 ± 0.1	$\cdots$	1.45 ± 0.08	0.6 ± 0.1	$\cdots$	2.8 ± 0.4
Power law	2.6 ± 0.1	$\cdots$	1.52 ± 0.07	*1.18*	0.6 ± 0.1	3.2 ± 0.4
Linear law	1.94 ± 0.03	$\cdots$	*1.0*	*1.18*	$\cdots$	10.0 ± 0.4
Linear law	3.57 ± 0.07	$\cdots$	*1.0*	-0.23 ± 0.06	$\cdots$	3.4 ± 0.4

Note. — The extinction of image B compared to reference image A. Numbers quoted in italics were fixed in the fitting procedure.

dio measurements of Rusin et al. (2002) to fix $\Delta\hat{m}$ one similarly gets $A(V) = 2.03 \pm 0.03, 2.01 \pm 0.03, 1.94 \pm 0.03$ at $\chi^2_\nu = 2.7, 4.0, 10.0$. The data are also analysed with respect to a possible achromatic microlensing signal, keeping $\Delta\hat{m}$ fixed. This yields a non-zero microlensing correction for the Galactic extinction law and power law of $s = 0.32 \pm 0.07, 0.6 \pm 0.1$ and $A(V) = 2.41 \pm 0.09, 2.6 \pm 0.1$ at $\chi^2_\nu = 2.1, 3.2$ respectively. The best fit for the linear law lies outside the validity of the method with $s > 1$ (see § 3.2.4) which would correspond to a microlensing signal of > 1 mag.

It is clear that in all cases the Galactic extinction law provides the best fit to the data suggesting Galactic type dust although the best fit R_V values are lower than those commonly seen in the Milky Way. It is possible that the measured R_V value is being lowered by a non-zero extinction in the A image provided it has a higher value of R_V (see discussion in § 3.2.3). However, given the very strong extinction signal this would require very strong extinction along both lines of sight in addition to a strong differential signal. This is unlikely given the fact that component A is at more than twice the distance from the centre of the lensing galaxy than component B with A at $1''\!.14$ and B at $0''\!.47$ from the centre (Rusin et al., 2002). Measurements in the X-ray further suggest that the A component is non-extinguished (K. Pedersen et al., 2006, in preparation).
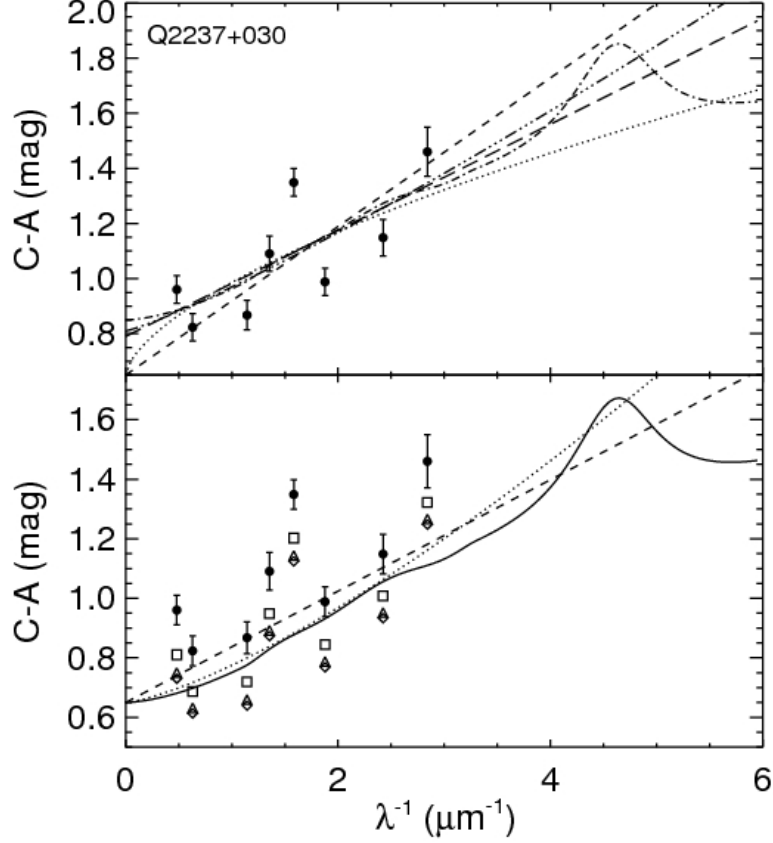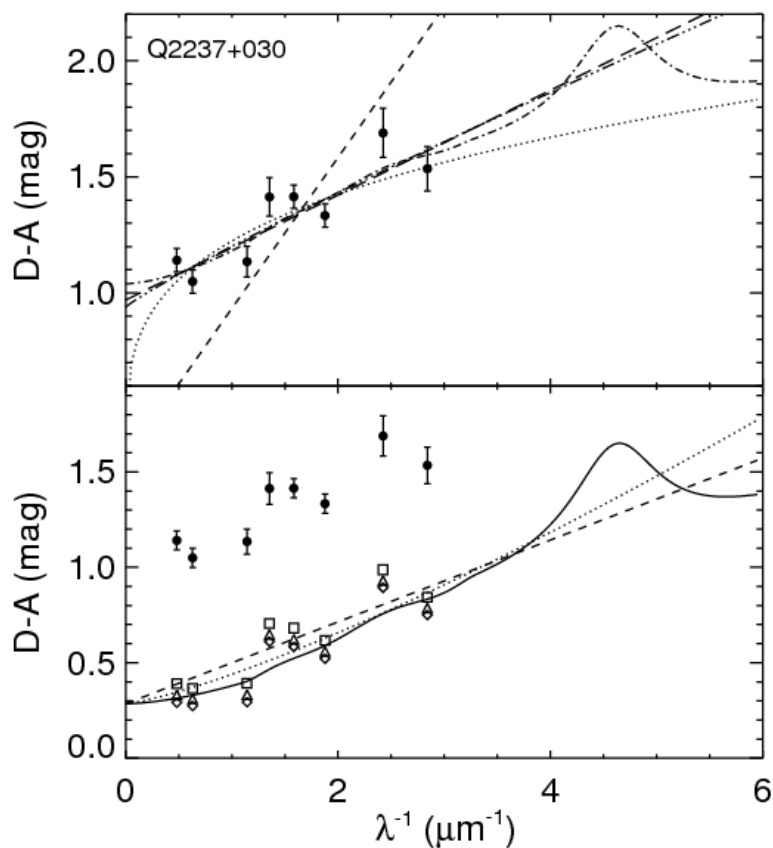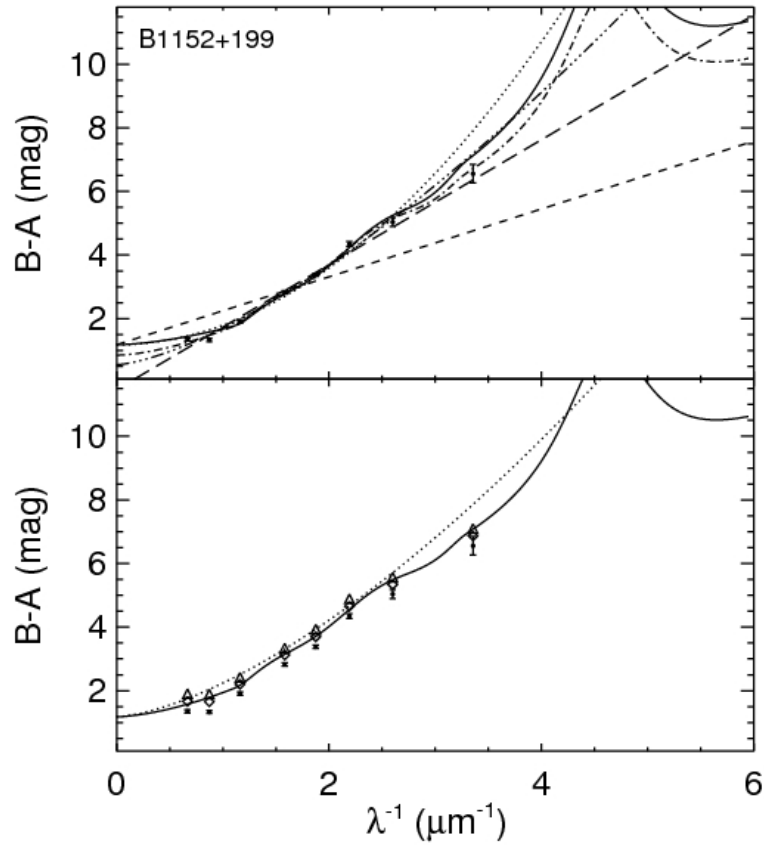
Figure 3.12 B1152+199: The upper panel shows the data points and the best fit extinction curves to them. The lower panel shows the original data points and their shift due to a microlensing signal. The parameters of the fits are given in Table 3.6. See the caption of Figure 3.9 for annotation overview.

Table 3.7.   Extinction curve fit results for Q0142−100

Extinction	$A(V)$	R_V	α	$\Delta\hat{m}$	χ^2_ν
Galactic	0.40 ± 0.03	4.8 ± 0.7	$\cdots$	1.64 ± 0.04	1.2 ± 0.5
Power law	4.1 ± 3.8	$\cdots$	0.1 ± 0.8	-2.1 ± 3.8	1.1 ± 0.5
Linear law	0.27 ± 0.08	$\cdots$	*1.0*	1.8 ± 0.1	1.1 ± 0.4

Note. — The extinction of image B compared to reference image A. Numbers quoted in italics were fixed in the fitting procedure.

3.3.1.5   Q0142−100

Q0142−100 is a doubly imaged system first discovered by Surdej et al. (1987) and also known in the literature as UM 673. The quasar is at a redshift of $z = 2.72$ (MacAlpine & Feldman, 1982) and the lensing galaxy, which is of early type (Rusin et al., 2002), is at a redshift of $z = 0.49$ (Surdej et al., 1987). Wisotzki et al. (2004) studied this system using spectrophotometric observations and found signs of differential extinction but no microlensing.

The data points and the fits for Q0142−100 can be seen in Figure 3.13 and the parameters of the fits in Table 3.7. All the fits give similar χ^2_ν but the parameters, in particular for the power law, are poorly constrained due to the lack of data points (measurements in the infrared for this system were not obtained). The extinction is high for an early type galaxy and is not consistent with that found by Falco et al. (1999) who found negligible extinction. The data are suspect, as they may be contaminated by the lens galaxy as the B component is located near the galaxy centre (at $0\rlap{.}''38$) and the seeing was not optimal for this system (the mean seeing was $0\rlap{.}''87$ compared to $0\rlap{.}''57$ for the full data set). As there are no published radio measurements available one does not have constraints on $\Delta\hat{m}$ to analyse the system with respect to a possible microlensing signal.

3.3.1.6   B1030+071

B1030+071 is a doubly imaged system first discovered by Xanthopoulos et al. (1998) in the JVAS survey. They monitored the system in radio wavelengths,

Figure 3.13 Q0142−100: The plot shows the data points and the best fit to them. The parameters of the fits can be seen in Table 3.7. See the caption of Figure 3.9 for annotation overview.

finding that the flux density ratios between image A and B range from 12.0 to 18.8 and seem to vary with both time and frequency. The redshift of the background source was determined to be at $z = 1.54$ and the redshift of the lensing object to be at $z = 0.60$ (Fassnacht & Cohen, 1998). Falco et al. (1999) determined a differential extinction of $E(B - V) = 0.02 \pm 0.04$ assuming a fixed $R_V = 3.1$ Galactic extinction law.

It was not possible to perform an extinction analysis on this system as the deconvolution did not succeed in separating the B component from the main lens galaxy (separated by $0\rlap{.}''11 \pm 0\rlap{.}''01$ (Xanthopoulos et al., 1998)) making the photometric values unreliable. For a further study of the extinction of this system higher resolution images would be required.

3.3.1.7   RXJ0911+0551

RXJ0911+0551 is a multiply imaged system first discovered by Bade et al. (1997) in the ROSAT All-Sky Survey with the quasar at $z = 2.80$. It was later studied by Burud et al. (1998a) who resolved the system into four images and found that

Table 3.8.   Extinction curve fit results for RXJ0911+0551: B

Image pair	Extinction	$A(V)$	R_V	α	$\Delta \hat{m}$	χ^2_ν
B−A	Galactic	0.33 ± 0.06	4.9 ± 0.6	$\cdots$	-0.10 ± 0.05	1.3 ± 0.4
B−D	Galactic	0.20 ± 0.08	4.1 ± 1.1	$\cdots$	-1.00 ± 0.06	1.6 ± 0.5
B−A	Power law	0.9 ± 3.7	$\cdots$	0.3 ± 0.3	-0.7 ± 3.7	1.3 ± 0.4
B−D	Power law	0.2 ± 1.4	$\cdots$	0.8 ± 0.6	-1.1 ± 1.4	1.6 ± 0.5
B−A	Linear law	0.23 ± 0.03	$\cdots$	*1.0*	-0.04 ± 0.04	1.5 ± 0.4
B−D	Linear law	0.17 ± 0.03	$\cdots$	*1.0*	-1.00 ± 0.04	1.5 ± 0.4

Note. — The extinction of image B compared to reference images A and D. Numbers quoted in italics were fixed in the fitting procedure.

Table 3.9.   Extinction curve fit results for RXJ0911+0551: C

Image pair	Extinction	$A(V)$	R_V	α	$\Delta \hat{m}$	χ^2_ν
C−A	Galactic	0.20 ± 0.10	3.3 ± 1.5	$\cdots$	0.66 ± 0.07	1.2 ± 0.4
C−D	Galactic	0.09 ± 0.08	2.2 ± 1.5	$\cdots$	0.26 ± 0.06	1.3 ± 0.4
C−A	Power law	0.3 ± 2.1	$\cdots$	0.9 ± 0.5	0.6 ± 2.1	1.2 ± 0.4
C−D	Power law	0.1 ± 1.8	$\cdots$	1.3 ± 1.5	03 ± 1.8	1.2 ± 0.4
C−A	Linear law	0.23 ± 0.04	$\cdots$	*1.0*	0.62 ± 0.04	1.1 ± 0.4
C−D	Linear law	0.17 ± 0.04	$\cdots$	*1.0*	0.31 ± 0.05	1.2 ± 0.4

Note. — The extinction of image C compared to reference images A and D. Numbers quoted in italics were fixed in the fitting procedure.

large external shear, possibly due to a cluster, was required to explain the image configuration. Kneib et al. (2000) confirmed that the lensing galaxy belongs to a cluster at $z = 0.769$. Observed reddening in at least two (images B and C) of the four images suggest differential extinction by the early type lensing galaxy (Burud et al., 1998a). Hjorth et al. (2002) measured the time delay of the system between images A,B,C on the one hand and D on the other and found the time delay to be 146 ± 8 days (2σ).

A relatively strong extinction is found in images B and C compared to images A and D. Image D also shows some extinction when compared to A but the effect is consistent with zero within two sigmas. The extinction curves of B and C compared to A and D are analysed. The data points and the fits can be seen in Figures 3.14 and 3.15 and the parameters of the fits can be seen in Tables 3.8 and 3.9.

Assuming image A is completely unextinguished one can estimate the lower limit of the relative extinction of D compared to B and C, $E_D(B-V)/E_{B,C}(B-V)$. For both B and C, one finds that this ratio is around 1/3 so one expects the extinction curve properties to be affected by both lines of sight (see discussion in § 3.2.3). That is, one does not expect the extinction curve obtained from comparing B and C to D to represent the extinction curve along either line of sight unless their extinction properties are identical. It is seen that the R_V value of both B and C are lower when compared to image D than those one gets from comparing them to image A suggesting that the extinction properties are indeed different (with image D having a higher R_V value). It should be noted that the values of R_V do agree within one sigma for both the differential extinction curves for both B and C.

3.3.1.8 HE0512−3329

HE0512−3329 is a doubly imaged system first discovered by Gregg et al. (2000) with an image separation of $0\overset{''}{.}644$ and quasar redshift of $z = 1.565$. They estimated a redshift of $z = 0.9319$ for the lensing object and found that the lens is most likely a spiral galaxy. In addition, they estimate the differential reddening assuming negligible microlensing and a standard Galactic extinction law with

Figure 3.14 RXJ0911+0551, B: The upper panel shows the data points and the fits for the extinction of image B compared to image A. The lower panel shows the corresponding plot for image B compared to image D. The parameters of the fits can be seen in Table 3.8. See the caption of Figure 3.9 for annotation overview.

Figure 3.15 RXJ0911+0551, C: The upper panel shows the data points and the fits for the extinction of image C compared to image A. The lower panel shows the corresponding plot for image C compared to image D. The parameters of the fits can be seen in Table 3.9. See the caption of Figure 3.9 for annotation overview.

Table 3.10.   Extinction curve fit results for HE0512−3329

Extinction	$A(V)$	R_V	α	$\Delta\hat{m}$	χ^2_ν
Galactic	0.14 ± 0.04	1.7 ± 0.4	$\cdots$	-0.67 ± 0.03	2.1 ± 0.4
Power law	0.23 ± 0.09	$\cdots$	1.3 ± 0.3	-0.76 ± 0.09	1.4 ± 0.4
Linear law	0.35 ± 0.02	$\cdots$	*1.0*	-0.86 ± 0.04	1.4 ± 0.4

Note. — The extinction of image A compared to image B. Numbers quoted in italics were fixed in the fitting procedure.

$R_V = 3.1$. This yields $A(V) = 0.34$ with the A image being redder than the B image. Wucknitz et al. (2003) worked further on disentangling microlensing and differential extinction, and estimated $A(V) = 0.07$ with A being the extinguished image. This fit results in an effective $R_V = -2.0$ which can be achieved if the two lines of sight have different R_V.

In the case of HE0512−3329, it is the brighter image, A, which shows extinction with respect to the B image. The system is interesting as one of the redshifted data points falls in the range where the 2175 bump in the Galactic extinction law should lie (see Figure 3.16). There is however no sign of a bump at $\lambda = 2175$ and both the power law and the linear extinction law give a much better fit (see Table 3.10 for the parameters of the fits). The fits are redone with no constraints on the R_V values to see if the data could be fit by a negative R_V value but this does not change the result of $R_V = 1.7 \pm 0.4$. As there is no radio data available the intrinsic ratio is not constrained in the fits and the microlensing signal can not be constrained.

The results are not in agreement with those of Wucknitz et al. (2003) who found that fits with the 2175 bump better reproduced their data than those without, although the result was not highly significant. In addition, they found that it is crucial to take microlensing into account when analysing the extinction curve, which might explain the discrepancy. However, the detected microlensing signal is only important at wavelengths lower than those probed here, with a small possible effect in the B- and V-bands. Therefore, a microlensing signal consistent with the results of Wucknitz et al. (2003) should not affect the results
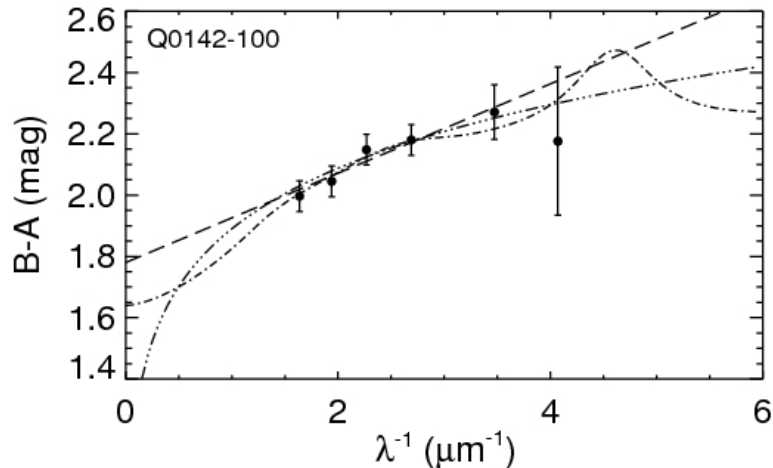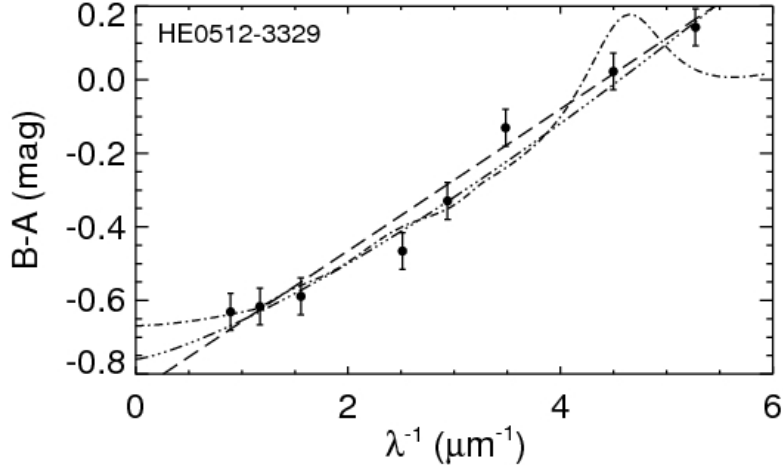
Figure 3.16 HE0512−3329: The plot shows the data points and the best fit to them. The parameters of the fits can be seen in Table 3.10. See the caption of Figure 3.9 for annotation overview.

significantly. In addition, it is noted that for their best fitting R_V their fit curves downwards for $\lambda^{-1} < 1 \ \mu m^{-1}$ which is not consistent with the measurement in the K-band (see Figure 3.16).

3.3.1.9 MG0414+0534

MG0414+0534 is a quadruply imaged system first discovered by Hewitt et al. (1992) with image separation of up to $2''$. The quasar, at redshift of $z = 2.64$, shows evidence of being heavily reddened by dust in the lensing galaxy (Lawrence et al., 1995). The lens, which has early type spectrum, is at redshift $z = 0.9584$ (Tonry & Kochanek, 1999) and was modelled by Falco et al. (1997) who found the brightness profile to be well represented by a de Vaucouleurs profile which is characteristic of an elliptical galaxy. Falco et al. (1999) studied the extinction curve of this system and fitted it to a Galactic extinction law giving a best fit of $R_V = 1.5$, assuming that all lines of sight have the same R_V. Angonin-Willaime et al. (1999) studied the origin of the extinction and found, that while the differential extinction is likely due to the lensing galaxy, then there is also

evidence for significant reddening which is intrinsic to the source. Katz & Hewitt (1993) did an extensive radio survey of the system and found that there was no sign of variability in the radio flux ratios between their measurements and those of Hewitt et al. (1992) except for the C/B image ratio.

For MG0414+0534, components A1 and A2 show extinction when compared to images B or C with A2 being the more strongly extinguished image (see Table 3.15). For the A1 image different effective extinction laws are found depending on whether the comparison is with image B or C (see Table 3.11 and Figure 3.17). In all cases the power law gives the best fit and the linear law the worst (using the radio measurements of Katz & Hewitt (1993) to fix $\Delta\hat{m}$). For the Galactic extinction law the R_V values do not agree suggesting that perhaps the extinction of images B and C is affecting the differential extinction curve. It should also be noted though, that one would expect $A(V)$ for A1−B to be around 0.3, to be consistent with the other values in Table 3.15, but the best fitting values give a lower value. Therefore another fit is performed where $A(V) = 0.3$ is fixed in the fits for the A1−B pair and this gives $R_V = 2.1 \pm 0.2; 1.8 \pm 0.1$ for $\Delta\hat{m}$ fixed and free respectively, which are marginally consistent with the results compared to the C image. However, the $\chi^2_\nu = 2.6; 2.0$ of these fits are significantly worse than those of the original fits. No evidence for microlensing is seen except in the case of SMC-like linear extinction which still results in a worse fit than the other two extinction laws.

For image A2 the Galactic extinction law gives the best fit when $\Delta\hat{m}$ is kept fixed but otherwise the different extinction laws give similar results (see Table 3.12 and Figure 3.18). The parameters of the Galactic extinction law are consistent when compared with images B and C suggesting that either A2 dominates the extinction signal or that B and C have similar extinction properties. There is no evidence for microlensing except in the case of the linear extinction law. It is noted that the absolute extinction of image A2, which must be greater or equal to the differential extinction in Table 3.12, is very high given that the lens is an early type galaxy (Goudfrooij et al. (1994) find $A(V) \lesssim 0.35$ for their sample of early type galaxies).

As the extinction of A1 is significant compared to A2 one expects the extinction properties of both lines of sight to affect the A2−A1 extinction curve
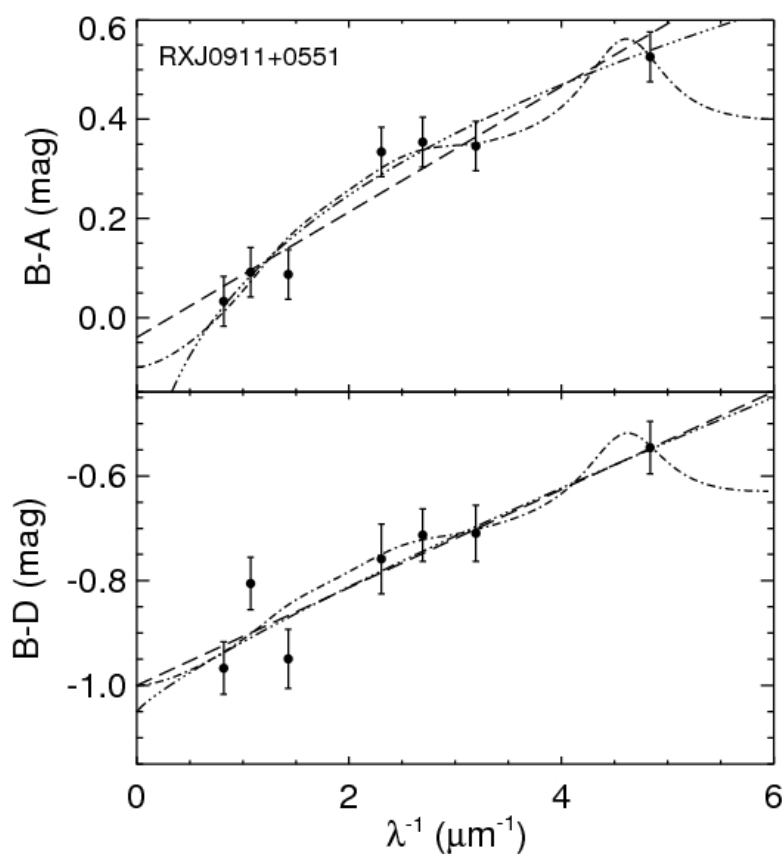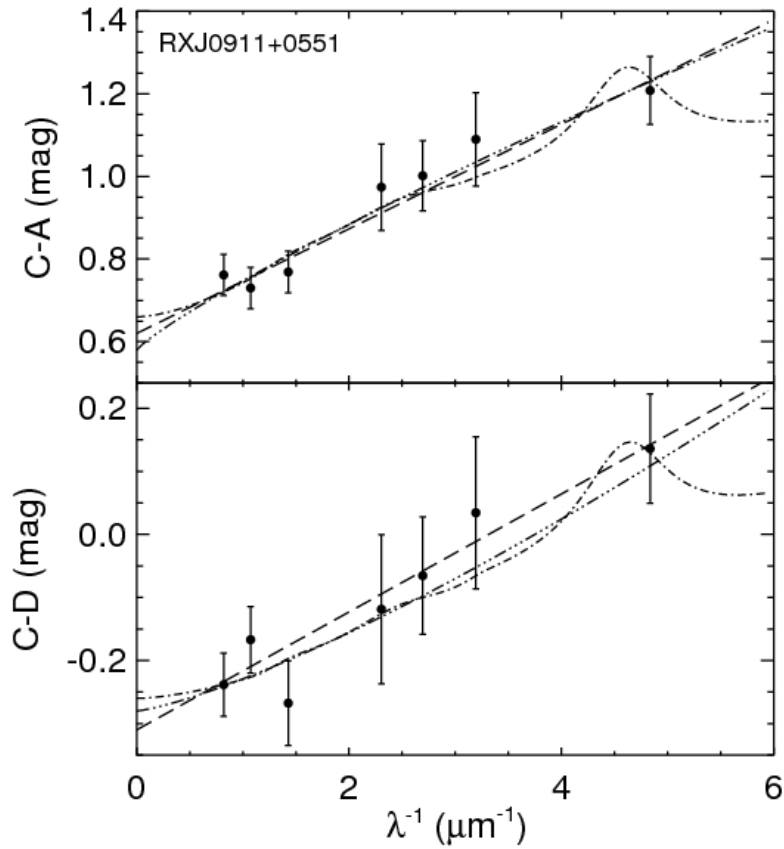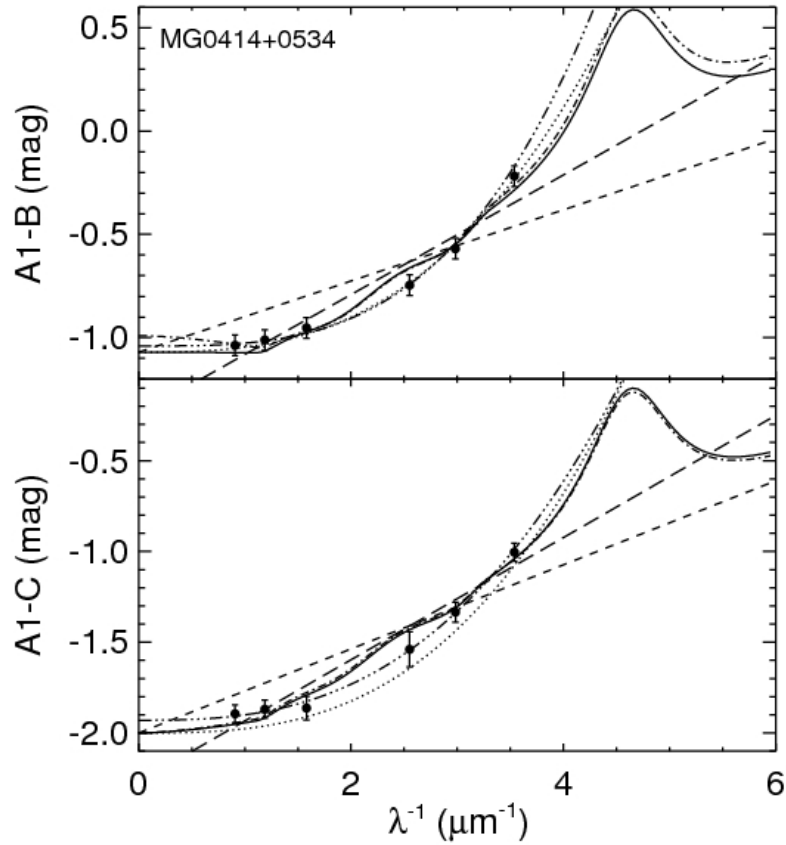
Figure 3.17 MG0414+0534, A1: The upper panel shows the data points and the fits for the extinction of image A1 compared to image B. The lower panel shows the corresponding plot for image A1 compared to image C. The parameters of the fits can be seen in Table 3.11. See the caption of Figure 3.9 for annotation overview.
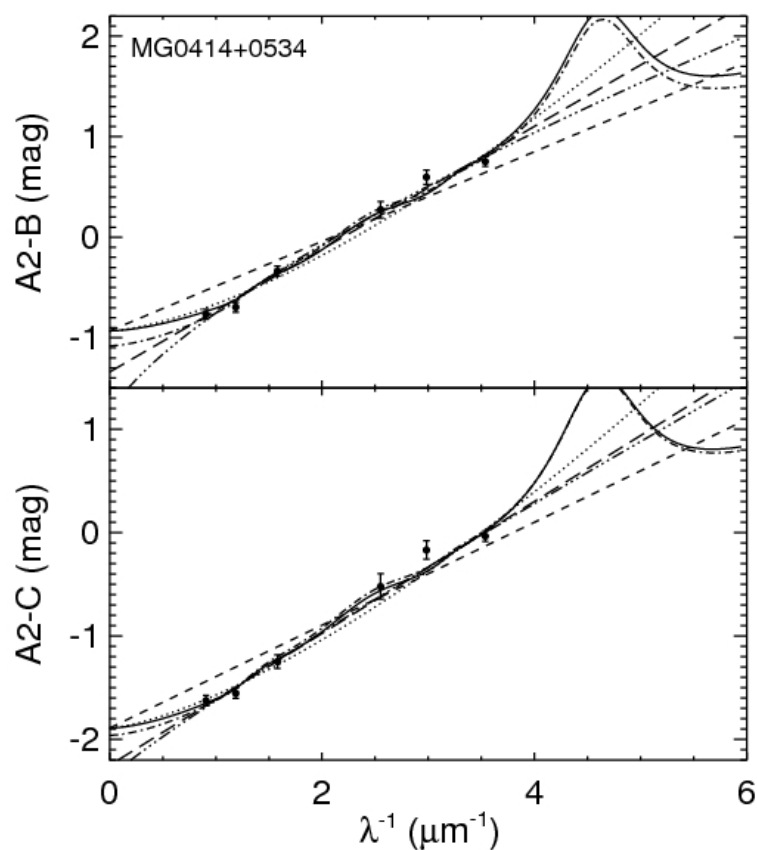
Figure 3.18 MG0414+0534, A2: The upper panel shows the data points and the fits for the extinction of image A2 compared to image B. The lower panel shows the corresponding plot for image A2 compared to image C. The parameters of the fits can be seen in Table 3.12. See the caption of Figure 3.9 for annotation overview.

3. EXTINCTION CURVES OF LENSING GALAXIES

Table 3.11.   Extinction curve fit results for MG0414+0534: A1

Images	Extinction	$A(V)$	R_V	α	$\Delta\hat{m}$	s	χ^2_ν
A1−B	Galactic	0.07 ± 0.02	0.4 ± 0.1	$\cdots$	-0.99 ± 0.03	$\cdots$	1.5 ± 0.5
A1−B	Galactic	0.15 ± 0.03	0.9 ± 0.2	$\cdots$	*-1.07*	$\cdots$	1.6 ± 0.5
A1−C	Galactic	0.29 ± 0.04	1.5 ± 0.2	$\cdots$	-2.00 ± 0.04	$\cdots$	1.7 ± 0.5
A1−C	Galactic	0.27 ± 0.04	1.4 ± 0.2	$\cdots$	*-2.0*	$\cdots$	1.5 ± 0.4
A1−B	Power law	0.10 ± 0.05	$\cdots$	3.1 ± 0.6	-1.04 ± 0.05	$\cdots$	0.9 ± 0.4
A1−B	Power law	0.13 ± 0.03	$\cdots$	2.8 ± 0.4	*-1.07*	$\cdots$	1.0 ± 0.4
A1−C	Power law	0.15 ± 0.07	$\cdots$	2.7 ± 0.6	-1.93 ± 0.05	$\cdots$	1.0 ± 0.4
A1−C	Power law	0.24 ± 0.04	$\cdots$	2.1 ± 0.3	*-2.0*	$\cdots$	1.1 ± 0.4
A1−B	Linear law	0.53 ± 0.04	$\cdots$	*1.0*	-1.37 ± 0.05	$\cdots$	2.2 ± 0.5
A1−B	Linear law	0.31 ± 0.02	$\cdots$	*1.0*	*-1.07*	$\cdots$	3.4 ± 0.4
A1−B	Linear law	0.49 ± 0.03	$\cdots$	*1.0*	*-1.07*	0.28 ± 0.05	2.3 ± 0.4
A1−C	Linear law	0.61 ± 0.04	$\cdots$	*1.0*	-2.27 ± 0.05	$\cdots$	1.9 ± 0.5
A1−C	Linear law	0.42 ± 0.02	$\cdots$	*1.0*	*-2.0*	$\cdots$	2.9 ± 0.4
A1−C	Linear law	0.58 ± 0.03	$\cdots$	*1.0*	*-2.0*	0.26 ± 0.05	1.9 ± 0.5

Note. — The extinction of image A1 compared to reference images B and C. Numbers quoted in italics were fixed in the fitting procedure.

Table 3.12.   Extinction curve fit results for MG0414+0534: A2

Images	Extinction	$A(V)$	R_V	α	$\Delta\hat{m}$	s	χ^2_ν
A2−B	Galactic	0.87 ± 0.05	2.7 ± 0.2	$\cdots$	-1.08 ± 0.04	$\cdots$	1.8 ± 0.5
A2−B	Galactic	0.69 ± 0.03	2.2 ± 0.2	$\cdots$	*-0.93*	$\cdots$	1.8 ± 0.5
A2−C	Galactic	0.91 ± 0.04	2.6 ± 0.1	$\cdots$	-1.96 ± 0.04	$\cdots$	1.8 ± 0.5
A2−C	Galactic	0.81 ± 0.04	2.3 ± 0.2	$\cdots$	*-1.89*	$\cdots$	1.6 ± 0.5
A2−B	Power law	1.6 ± 1.2	$\cdots$	0.7 ± 0.2	-1.8 ± 1.2	$\cdots$	1.7 ± 0.5
A2−B	Power law	0.65 ± 0.03	$\cdots$	1.49 ± 0.07	*-0.93*	$\cdots$	2.3 ± 0.5
A2−C	Power law	1.3 ± 0.5	$\cdots$	0.9 ± 0.2	-2.4 ± 0.5	$\cdots$	1.8 ± 0.5
A2−C	Power law	0.75 ± 0.03	$\cdots$	1.42 ± 0.07	*-1.89*	$\cdots$	1.9 ± 0.5
A2−B	Linear law	1.11 ± 0.04	$\cdots$	*1.0*	-1.34 ± 0.05	$\cdots$	1.7 ± 0.5
A2−B	Linear law	0.81 ± 0.02	$\cdots$	*1.0*	*-0.93*	$\cdots$	4.0 ± 0.4
A2−B	Linear law	1.07 ± 0.04	$\cdots$	*1.0*	*-0.93*	0.39 ± 0.05	1.6 ± 0.5
A2−C	Linear law	1.16 ± 0.04	$\cdots$	*1.0*	-2.25 ± 0.05	$\cdots$	1.6 ± 0.4
A2−C	Linear law	0.91 ± 0.02	$\cdots$	*1.0*	*-1.89*	$\cdots$	3.5 ± 0.4
A2−C	Linear law	1.13 ± 0.04	$\cdots$	*1.0*	*-1.89*	0.35 ± 0.05	1.5 ± 0.4

Note. — The extinction of image A2 compared to reference images B and C. Numbers quoted in italics were fixed in the fitting procedure.

Table 3.13.   MG0414+0534: The extinction properties of A2−A1

		$\Delta\hat{m}$	$A(V)$	R_V
Fit	Free	0.61 ± 0.11	3.8 ± 0.7
Fit	Fixed	0.53 ± 0.03	3.5 ± 0.4
C	Free	0.62 ± 0.06	4.0 ± 0.9
C	Fixed	0.54 ± 0.06	3.4 ± 1.0
B	Free	0.80 ± 0.05	5.4 ± 2.5
B	Free	0.54 ± 0.04	3.7 ± 1.3

Note. — The first two lines give the results from the Galactic extinction law fit to the data. The last four lines give the extinction properties calculated from eq. (3.14) using the properties of A2 and A1 compared to images B and C from Tables 3.11 and 3.12.

(see § 3.2.3). The fit of A2−A1 for the Galactic extinction curve gives us $R_V = 3.5 \pm 0.4, 3.8 \pm 0.7$ at $A(V) = 0.53 \pm 0.03, 0.61 \pm 0.11$ when $\Delta\hat{m}$ is kept fixed or free respectively. If one assumes that images B and C have zero extinction one can calculate the effective R_V one expects to get from eq. (3.14). The results can be seen in Table 3.13 and are in good agreement with the results of the fits.

The extinction of MG0414+0534 is high for an early type galaxy. The possibility that the extinction may be due to an unknown foreground object and not the lensing galaxy itself can not be excluded. Finally it is noted that the estimates of the differential extinction agree with those of Falco et al. (1999) which were obtained by assuming standard Galactic extinction with $R_V = 3.1$.

MG2016+112 was discovered by Lawrence et al. (1984) and has a giant elliptical lensing galaxy at redshift $z = 1.01$ (Schneider et al., 1986, 1985). The system consists of two images, A and B, of the quasar at redshift $z = 3.273$ and an additional image C which may be a third image of the quasar with an additional signal from another galaxy and has been challenging to model (Lawrence et al., 1993, 1984; Nair & Garrett, 1997). The flux of images A and B in the radio at 5 GHz was determined by Garrett et al. (1994) to be 15.8 mJy and 17.2 mJy respectively.

Table 3.14.   Extinction curve fit results for MG2016+112

Extinction	$A(V)$	R_V	α	$\Delta\hat{m}$	s	χ^2_ν
Galactic	0.20 ± 0.03	3.0 ± 0.5	$\cdots$	*-0.092*	$\cdots$	1.7 ± 0.4
Galactic	0.1 ± 0.1	1.8 ± 1.0	$\cdots$	-0.01 ± 0.10	$\cdots$	1.9 ± 0.5
Galactic	0.11 ± 0.09	1.8 ± 1.3	$\cdots$	*-0.092*	-0.1 ± 0.1	1.8 ± 0.5
Power law	0.18 ± 0.03	$\cdots$	1.4 ± 0.2	*-0.092*	$\cdots$	1.4 ± 0.4
Power law	0.11 ± 0.09	$\cdots$	1.8 ± 0.6	-0.02 ± 0.10	$\cdots$	1.5 ± 0.5
Power law	0.12 ± 0.09	$\cdots$	1.7 ± 0.5	*-0.092*	-0.06 ± 0.11	1.5 ± 0.5
Linear law	0.23 ± 0.01	$\cdots$	*1.0*	*-0.092*	$\cdots$	1.6 ± 0.4
Linear law	0.28 ± 0.03	$\cdots$	*1.0*	-0.18 ± 0.06	$\cdots$	1.6 ± 0.5
Linear law	0.27 ± 0.03	$\cdots$	*1.0*	*-0.092*	0.08 ± 0.06	1.6 ± 0.5

Note. — The extinction of image B compared to reference image A. Numbers quoted in italics were fixed in the fitting procedure.

This is the highest redshift system in the sample, and is also interesting since one of the data points lands in the range where the 2175 bump in the Galactic extinction law should be (see Figure 3.19). However, the extinction signal is very weak with $A(V) = 0.1 \pm 0.1, 0.11 \pm 0.09, 0.28 \pm 0.03$ at $\chi^2_\nu = 1.9, 1.5, 1.6$ for the Galactic extinction law, power law and linear law respectively (see Table 3.14 for the parameters of the fits). When $\Delta\hat{m}$ is fixed a somewhat higher extinction of $A(V) = 0.20 \pm 0.03, 0.18 \pm 0.03, 0.23 \pm 0.01$ at $\chi^2_\nu = 1.7, 1.4, 1.6$ is found. In both cases a power law or a linear law is marginally preferred to a Galactic extinction law. The data are also analysed with respect to a possible microlensing signal but only find a weak microlensing signal (see Table 3.14 and Figure 3.19). Finally it is noted that the results for the Galactic extinction law are consistent with the results of Falco et al. (1999).

3.3.2   The full sample

In this section the properties of the sample as a whole are studied. Correlations between various parameters and, in particular, any dependence on the redshift or the morphology of the galaxies are searched for. Furthermore, the low R_V values found in SN Ia studies are discussed and the possible complementarity of lensing extinction curve studies. On the one hand, a 'golden sample' is studied and, on
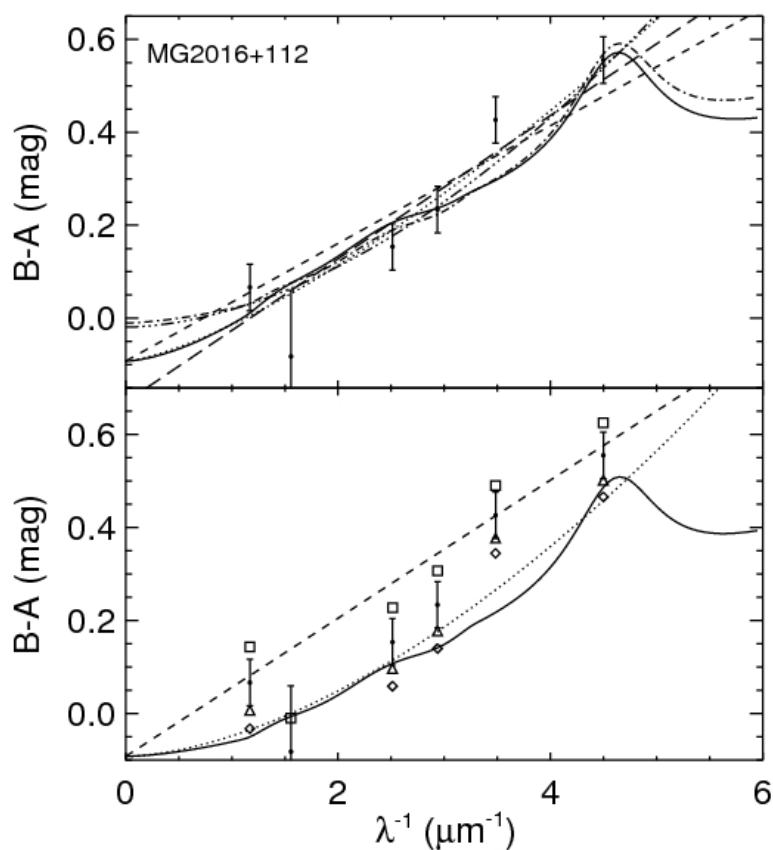
Figure 3.19 MG2016+112: The upper panel shows the data points and the best fit extinction curves as given in Table 3.14. The lower panel shows the original data points and their shift due to a microlensing signal. The parameters of the fits can be seen in Table 3.14. See the caption of Figure 3.9 for annotation overview.

Table 3.15. Overview of extinction properties for the
Galactic extinction law fit.

Lens	Lens redshift	Image pair	$A(V)$	R_V
Q2237+030	0.04	B−A	0.04 ± 0.04	
		C−A	0.29 ± 0.06	2.9 ± 1.4
		D−A	0.35 ± 0.06	3.1 ± 1.5
		C−B	0.2 ± 0.1	
		D−B	0.27 ± 0.15	
		D−C	0.08 ± 0.05	
PG1115+080	0.31	A2−A1	0.12 ± 0.06	3.3 ± 1.9
		B−A1	0.05 ± 0.04	
		C−A1	0.03 ± 0.05	
		A2−B	0.05 ± 0.03	
		A2−C	0.07 ± 0.05	
		B−C	0.03 ± 0.05	
B1422+231	0.34	B−A	0.08 ± 0.20	
		A−C	0.1 ± 0.3	
		D−A	$\cdots$	
		B−C	0.1 ± 0.3	
		D−B	$\cdots$	
		D−C	$\cdots$	
B1152+199	0.44	B−A	2.43 ± 0.09	2.1 ± 0.1
Q0142−100	0.49	B−A	0.40 ± 0.03	4.7 ± 0.7
B1030+071	0.60	B−A	$\cdots$	
RXJ0911+0551	0.77	B−A	0.33 ± 0.06	4.9 ± 0.6
		C−A	0.20 ± 0.10	3.3 ± 1.5
		D−A	0.12 ± 0.06	
		B−C	0.02 ± 0.06	
		B−D	0.20 ± 0.08	4.1 ± 1.1
		C−D	0.09 ± 0.08	2.2 ± 1.5
HE0512−3329	0.93	A−B	0.14 ± 0.04	1.7 ± 0.4
MG0414+0534	0.96	A2−A1	0.6 ± 0.1	3.8 ± 0.7
		A1−B	0.07 ± 0.02	0.4 ± 0.1
		A1−C	0.29 ± 0.04	1.5 ± 0.2
		A2−B	0.87 ± 0.05	2.7 ± 0.2
		A2−C	0.91 ± 0.04	2.6 ± 0.1
		B−C	0.01 ± 0.06	
MG2016+112	1.01	B−A	0.1 ± 0.1	1.8 ± 1.0

Note. — Table of extinction properties for the 10 lensing systems. The systems are ordered according to increasing redshift. The fit results are from the Galactic extinction law with $\Delta \hat{m}$ free.

the other hand, the full sample is analysed. The 'golden sample' is defined to include the image pair with the strongest differential extinction for each lens. In addition Q0142−100 is excluded from the 'golden sample' (see §3.3.1.5). The 'golden sample' therefore consists of eight pairs of images, of which seven have strong enough extinction to analyse the extinction curve. If not otherwise stated, the results apply to the full sample.

3.3.2.1 $A(V)$ as a function of distance from centre of the lensing galaxy

To study the distribution of $A(V)$ as a function of distance from the lens galaxy, the sample is analysed using two methods. First, in Figure 3.20, the differential $A(V)$ of the image pairs (from Table 3.15) is plotted as a function of the ratio of the distances from the centre of the galaxy (from Table 3.2). A negative value is assigned to the $A(V)$, in those cases where the more distant image is the more strongly extinguished one. One can see, that when the ratio is small, the image which is nearer the centre of the galaxy is the more extinguished one. However, when the ratio approaches one, the $A(V)$ becomes more evenly scattered around zero.

For the second method, it is assumed that the image with the weakest extinction signal is indeed non-extinguished. An absolute $A(V)$ is defined for the other images, by taking the differential extinction compared to this reference image, which is plotted as a function of distance from the centre of the galaxy, scaled by the lens galaxy scale length[1] (see Figure 3.21 and Table 3.2). From the plot one can see that most $A(V)$ values lie in the range of 0–0.5 for distances smaller than around four scale lengths, but drop for more distant images.

Both of these results are consistent with the expectation that the more distant image is on average more likely to pass outside the galaxy and thus not be affected by extinction. When the distances become similar, secondary effects due to the non-symmetric shape of the lens start becoming important, creating a scatter in the $A(V)$ vs. distance plots. This is in particular the case for the quads where the distances tend to be similar.

---

[1]The scale length is taken to be the effective radius of a de Vaucouleurs profile fit from Rusin et al. (2003).
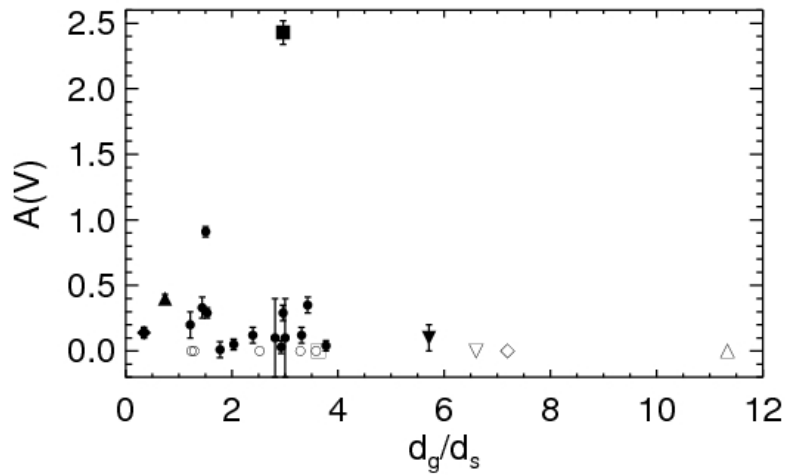
Figure 3.20 The differential $A(V)$ for a pair of images vs. the ratio of the distances from the centre of the lensing galaxy. The differential $A(V)$ is defined as negative if the image closer to the galaxy is less extinguished. The figure shows that images closer to the galaxy tend to be the more extinguished but that when the ratio approaches 1 the scatter increases.
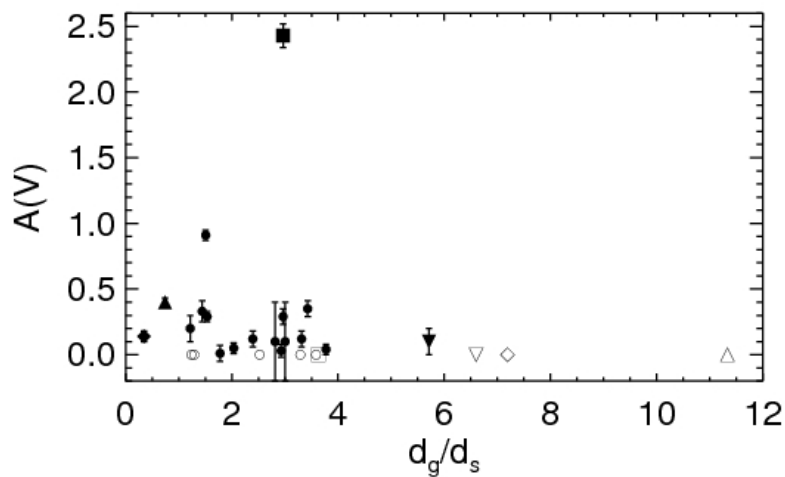
Figure 3.21 $A(V)$ as a function of the distance of the image relative to the scale radius of the lensing galaxy. An absolute $A(V)$ is assigned to the images by assuming that the least extinguished image for each system is non-extinguished. The quads are symbolised as circles and the four doubles are symbolised as triangles (up and down facing), a diamond and a box. The non-extinguished reference images are marked on the plot by open symbols. The error bars for d_g/d_s are smaller than the plotted symbols. One sees that the $A(V)$ values mostly lie in the range of $0 - 0.5$ for $d_g/d_s \lesssim 4$ and drop for higher values.

3.3.2.2 The different extinction laws

In this section, it is investigated whether the sample shows a preference for one type of extinction law to another and whether the type of extinction depends on the galaxy type. The correlation between the parameters of the different fits are also studied.

It is found that when $\Delta\hat{m}$ is allowed to vary, the sample does not show a preference for one extinction law over the other (the mean of the χ^2_ν is $\bar{\chi}^2_\nu = 1.7, 1.6, 1.8$ for the Galactic extinction law, power law and linear law) although individual systems can show a strong preference. If alternatively the fits where $\Delta\hat{m}$ was fixed are studied, one sees that the power law and Galactic extinction law are preferred over the linear law in the sample as a whole (with $\bar{\chi}^2_\nu = 2.7, 2.1, 4.3$) but again individual systems can show different behaviours.

There are three late type galaxies in the sample. One (HE0512$-$3329) shows a clear preference for an SMC linear law extinction, one (B1152+199) shows a preference for a Galactic extinction law and the third (Q2237+030) gives equally good fits to all the extinction laws (which is expected due to its low redshift, see § 3.2.6.1). For the early type galaxies there is also no clear preference for one type of extinction law. Three systems (PG1115+080, Q0142$-$100, RXJ0911+0551) show no preference for one extinction law over the other, one (MG0414+0534) favours a power law with power index $\alpha = 2-3$ for one of the images (which may be affected by extinction along both lines of sight) and one (MG0216+112) shows a weak preference for a power or a linear law over the Galactic extinction law. The conclusion is therefore that there is no evidence for a correlation between galaxy type and type of extinction in the sample.

When confining the analysis to a Galactic extinction, the mean R_V (for the 'golden sample') of the late type galaxies ($\bar{R}^{late}_V = 2.3 \pm 0.5$) is found to be marginally lower than that of the early type galaxies ($\bar{R}^{early}_V = 3.2 \pm 0.6$), however they are consistent within the error bars and the difference may be due to low number statistics. This is further discussed in §3.3.2.4.

The correlation of the parameters R_V and α are also studied for each system to demonstrate the consistency of the two approaches. As expected, a strong correlation is found with larger R_V giving smaller α, as seen in Figure 3.22,
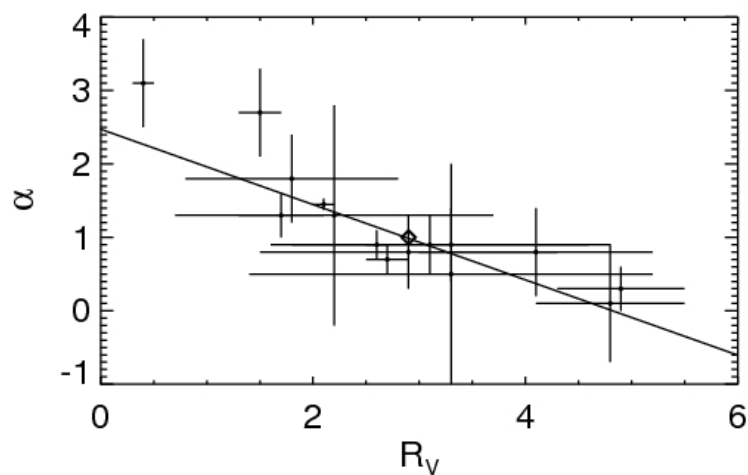
Figure 3.22 The power index α vs. R_V. The data points consist of all image pairs where the extinction curves were analysed (from fits with $\Delta\hat{m}$ free). The plot shows a clear correlation between α and R_V, with lower α giving higher R_V, which is consistent with lower R_V giving a steeper rise into the UV. The point corresponding to $\alpha = 1.0$ (SMC type extinction) and $R_V = 2.9$ (the mean R_V for the SMC, as determined by Pei, 1992), is marked by a diamond.

consistent with smaller R_V giving steeper rise into the UV. The exact relationship between R_V and α can be derived by solving equations (3.5) and (3.7) and is wavelength dependent. A first order linear fit to the data gives $\alpha = (2.5 \pm 0.2) - (0.51 \pm 0.09)R_V$ which is an applicable approximation within the wavelength range of the data. In addition it is checked whether the strength of the extinction is correlated to R_V, but no evidence for such a correlation is found (see Figure 3.23).
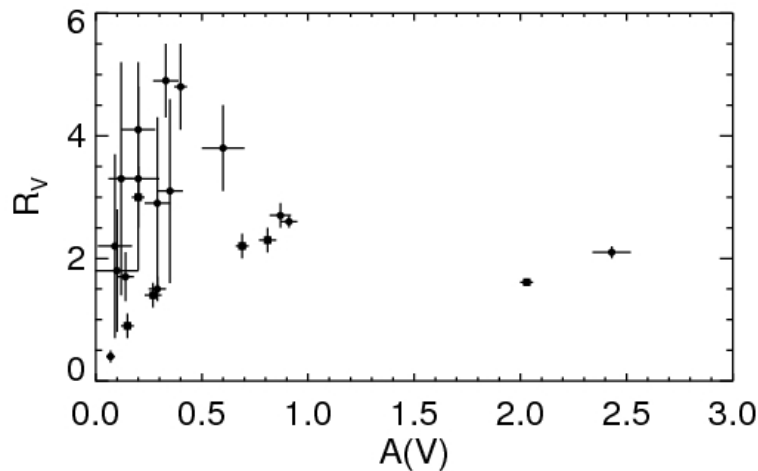
Figure 3.23 The figure shows R_V vs. $A(V)$. The data points consist of all image pairs where the extinction curves were analysed (filled circles from fits with $\Delta\hat{m}$ free and filled boxes from fits with $\Delta\hat{m}$ fixed). The figure shows, as expected, no correlation between R_V and the amount of extinction.

Finally the correlation between the values of $A(V)$ which were found corresponding to the different extinction laws are studied. The results can be seen in Figure 3.24. One sees that when $\Delta\hat{m}$ is free, the power law favours higher $A(V)$ than the other two extinction laws (see left bottom and top panels in Fig. 3.24). When $\Delta\hat{m}$ is fixed, the correspondence becomes much better with the power law giving marginally lower values. The agreement between the $A(V)$ values derived for the Galactic extinction law and the linear law are in general good, regardless of whether $\Delta\hat{m}$ is kept fixed or free (with the exception that for $A(V) \gtrsim 1$ the linear law gives higher results when $\Delta\hat{m}$ is free).
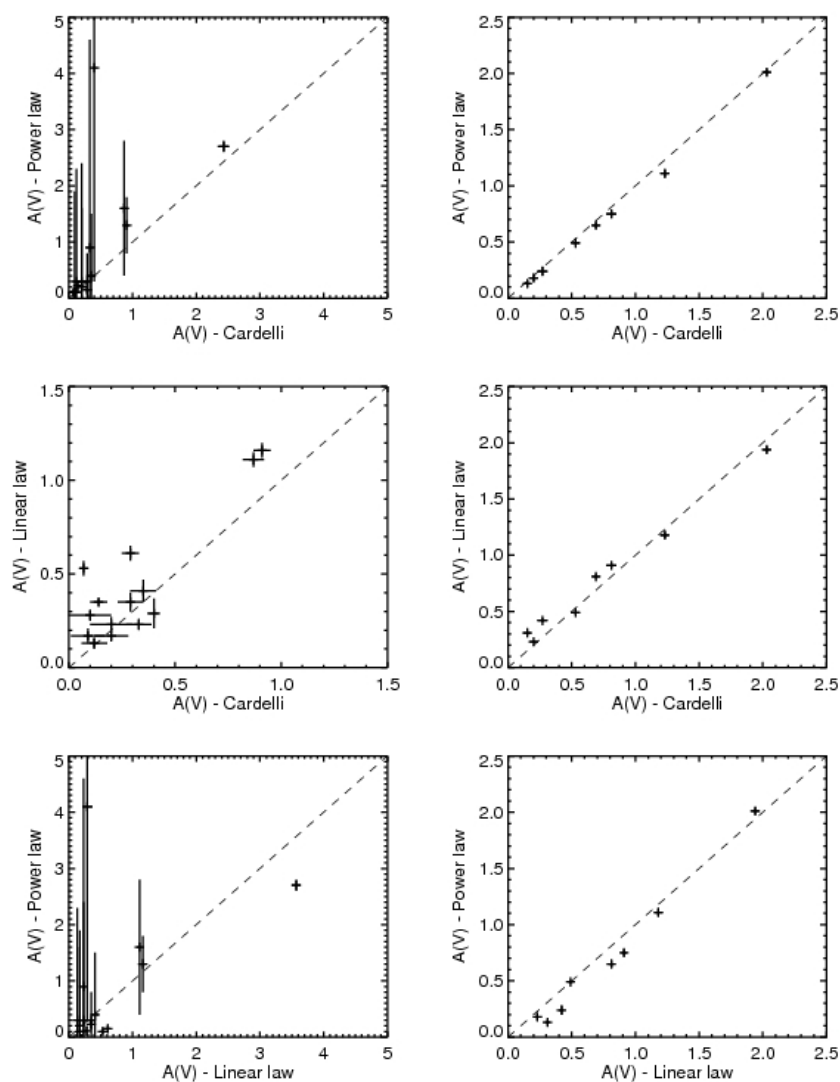
Figure 3.24 The graphs show the correlation between the values of $A(V)$ derived for the different fits. The left column shows the distribution for the fits where $\Delta\hat{m}$ is a fitted parameter and the right column gives the corresponding distribution when $\Delta\hat{m}$ is fixed. The dashed line corresponds to $x = y$, which would correspond to perfect agreement in $A(V)$ between the fits, and is plotted for reference.

Figure 3.24 also clearly demonstrates that the $A(V)$ values become much better constrained when $\Delta\hat{m}$ is fixed in the fitting. This suggests that it would be valuable for a future extinction survey, to do a simultaneous radio survey for the systems, in order to constrain the intrinsic magnitude ratio of the images.

3.3.2.3 Evolution with redshift

Next, the behaviour of the sample as a function of redshift is investigated. The plots of R_V and α as a function of redshift can be seen in the upper two panels of Figure 3.25. No strong correlation is seen, in either the full nor the 'golden sample', although the lower values of R_V and the higher values of α seem to appear at higher z. The results do not confirm evolution of R_V with redshift, with lower R_V at higher z, as suggested by Östman et al. (2006), but do not exclude such evolution either. It is stressed that a larger sample would be needed to make any conclusive claims.

The possibility of an evolution in the amount of dust extinction with redshift is also investigated. Again, the two samples are used, the 'golden sample' as defined above, and a sample consisting of the highest differential extinction deduced for each image. The resulting plot can be seen in the bottom panel of Figure 3.25 and does not show any correlation between $A(V)$ and z.

3.3.2.4 Low R_V values and Type Ia SNe

Recent studies of SNe Ia have suggested that R_V values for SN hosts (which are mostly late type, see Sullivan et al., 2003) could be lower than those for the Milky Way (see e.g., Krisciunas et al., 2000; Riess et al., 1996b; Wang et al., 2006) suggesting that SN hosts are systematically different from the Milky Way. Wang (2005) however suggest that the reason for the low values of R_V might be due to circumstellar dust around the SNe themselves. The presence of such dust would cause inaccurate estimates of the dust extinction of the host galaxies of the SNe Ia.

Lensing studies have also seen more extreme R_V values than those in the Milky Way (see e.g., Motta et al., 2002; Wucknitz et al., 2003) but this has been criticised as possibly being due to extinction along both lines of sight. However,
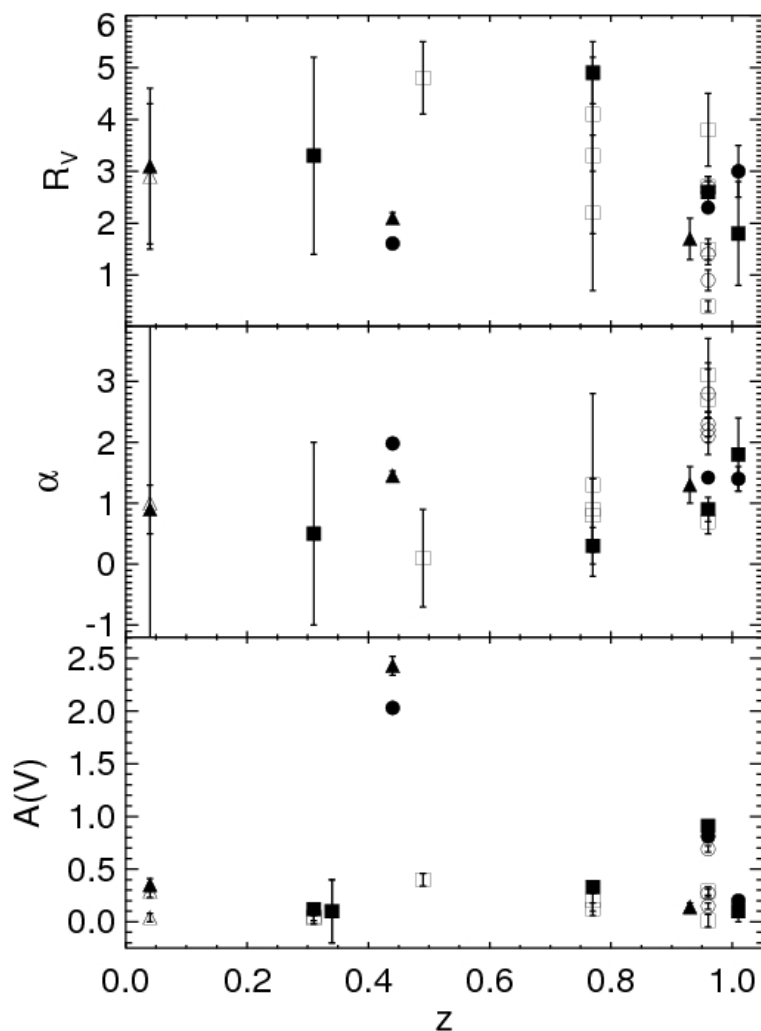
Figure 3.25 The top panel shows R_V as a function of z. The middle panels shows α vs. z. The bottom panels shows $A(V)$ (as given by a Galactic extinction law fit) vs. z. On all panels, triangles denote late type galaxies and boxes denote early type galaxies where the values are taken from the fits with $\Delta\hat{m}$ kept free. Circles denote the corresponding fits where $\Delta\hat{m}$ was fixed. Filled symbols correspond to a 'golden' sample as defined in §3.3.2. No strong evolution with z is seen but lower values of R_V seem to appear at higher z.

by choosing systems where the extinction of the measured image dominates the extinction of the reference image, this effect can be avoided (see discussion in § 3.2.3). In the sample presented here the mean R_V value is $\bar{R}_V = 2.8 \pm 0.3$ (with RMS scatter of 1.2) for the full sample, and $\bar{R}_V = 2.8 \pm 0.3$ (with RMS scatter of 1.1) for the 'golden sample'. These values are marginally lower than, but consistent with, the Milky Way mean value of $R_V = 3.1$. If one looks at R_V for the late and early type galaxies separately, one finds $\bar{R}_V^{early} = 3.2 \pm 0.6$ and $\bar{R}_V^{late} = 2.3 \pm 0.5$ for the 'golden' sample. These values are consistent with each other within the quoted error bars, but it is interesting that the late type galaxies have a lower mean R_V, in agreement with SN Ia studies. A larger sample would be needed to determine whether this is a real trend, or due to low number statistics.

The mean extinction in the 'golden sample' is $\bar{A}(V) = 0.56 \pm 0.04$ (with RMS scatter of 0.80). This gives a lower limit to the mean absolute extinction, as the mean $A(V)$ value is lowered if the reference image is also extinguished. If one removes the highly extinguished system B1152+199 from the sample, the mean of the 'golden sample' reduces to $\bar{A}(V) = 0.29 \pm 0.05$ (with RMS scatter of 0.29). If instead one takes the highest differential extinction for each image for the full sample into account one gets $\bar{A}(V) = 0.33 \pm 0.03$ (with RMS scatter of 0.56 (or $\bar{A}(V) = 0.21 \pm 0.03$ without B1152+199). All these values are high enough to cause systematic effects in the calibration of SNe Ia.

A lower mean R_V from a lensing study would strengthen the results of low R_V values from SN studies applying to the interstellar medium. A lower real R_V value than the assumed one would lead to an overestimation of $A(V)$ given a measurement of $E(B - V)$ (as $A(V) = R_V E(B - V)$). It is therefore important that the extinction properties of higher redshift galaxies, and SN hosts in particular, be further investigated as assuming a mean Galactic extinction with $R_V = 3.1$ in the analysis of SNe Ia could affect the cosmological results.

Lensing galaxies and SN Ia hosts are distributed over a similar redshift range (from $z = 0$ to $z \sim 1$) and consist of both early type and late type galaxies. The majority of lensing galaxies are massive early type galaxies (Kochanek et al., 2000) whereas the SN Ia hosts are mostly late type (Sullivan et al., 2003). It would however be possible to select sub-samples of either group which would

have the same morphology distribution as the other. Therefore, studies of the extinction properties of lensing galaxies can complement future dark energy SN Ia surveys, providing an independent measurement of the extinction properties of the SN Ia type hosts (see § 3.5).

3.4 Summary

This chapter has presented an imaging survey of the extinction properties of 10 lensing galaxies using multiply imaged quasars observed with the ESO VLT in the optical and the NIR. A dedicated effort has been made to reduce the number of unknowns and effects which can mimic extinction. The effects of extinction along both sight lines have been explored, analytically and in simulations. It is found that it is not crucial for the reference image to have zero extinction, as long as its extinction is small compared to the other image. The effects of achromatic microlensing have also been studied and it is found that to account for such an effect in photometric data, it is crucial to have constraints on the intrinsic magnitude difference of the images.

It was possible to study the extinction of 9 out of 10 of the systems in the survey, the last one had to be discarded due to contamination by the lensing galaxy. Out of the 9 systems, 8 have a two sigma extinction signal for at least one image pair, which was the limit for doing further extinction curve analysis. However, it is suspected that one of those is also contaminated by the lensing galaxy (Q0142$-$100) and it is excluded from the 'golden sample'. The mean extinction for the 'golden sample' is $\bar{A}(V) = 0.56 \pm 0.09$, using Galactic extinction law parametrisation, and the mean R_V is $\bar{R}_V = 2.8 \pm 0.4$ (compared to $\bar{R}_V = 2.8 \pm 0.3$ for the full sample), which is consistent with the mean $R_V = 3.1$ found for the Galaxy. The systems show various extinction properties. There is no strong evidence for a correlation between morphology and extinction properties. As the sample covers a broad range in redshifts ($z = 0.04$–1.01) an evolution with redshift has been looked for. However, the results neither confirm nor refute evolution of extinction parameters with redshift and it is stressed that a larger sample would be needed to make any conclusive claims.

Finally it is pointed out that large studies of gravitationally lensed quasars are ideal to study the possible evolution of extinction properties as they are spread over a redshift range from $z = 0$ to $z \approx 1$. Furthermore, the quasars do not affect the environment of the galaxy to be studied as is the case in SN Ia studies. For further improvements, however, higher resolution and deeper imaging for a larger sample would be required making a dedicated study with space based telescopes of considerable interest. A simultaneous radio survey, in order to constrain the intrinsic ratio of the images, would also further improve the results. Such a study could complement future dark energy SN Ia surveys, providing an independent measurement for the extinction properties of SN Ia type host galaxies (see § 3.5).

3.5   SNAPping at Dust

Future dark energy surveys aim at measuring not only the dark energy content of the universe but its evolution with redshift. To do so, very accurate calibration of the data is required. One of the major uncertainties facing these future surveys is the correction of data for dust extinction (Wood-Vasey et al., 2007). In particular, any evolution of dust with respect to redshift which is not taken into account in the calibration could lead to a biased estimate of the evolution of the dark energy content. Lensing galaxies have a similar redshift range to the supernova and can therefore be used to independently probe the dust evolution. Lensing galaxies are predominantly early type (elliptical), while supernova galaxies are predominantly late type (spiral), but around 10-20% of the lens population is expected to be late type (Keeton & Kochanek, 1998) making it possible to define a relevant subsample if the initial sample is sufficiently large. Therefore it is of great interest to expand the study of extinction curves of lensing galaxies to a statistically significant sample size.

Fortunately, the dark energy surveys themselves will provide such samples. For example, the SuperNova Acceleration Project (SNAP)[1] is expected to find serendipitously around 100-1000 quasar-galaxy lenses (i.e. systems where the background source is a quasar and the lensing mass is a galaxy) and around

---

[1]http://snap.lbl.gov/

50000 galaxy-galaxy lenses (Marshall et al., 2005) which will be imaged in nine filters at high resolution. Therefore, even in the worst case scenario, the sample size compared to the VLT survey will increase by a factor of ten, and in the best case scenario by a factor of 5000.

To take advantage of the full sample, it is necessary to develop the method of using gravitationally lensed quasars (which are essentially point sources) to be applicable to gravitationally lensed galaxies (which have finite size). There are several complications involved in having finite source sizes, e.g. the regions might have varying magnification and it may prove hard to define a well determined equivalent regions of the source to use as the 'standard candles'. However, using finite sources is not without its advantages either, as the effect of microlensing will become negligible as it will only affect a very small region of the total source size.

While it is beyond the scope of this thesis to conduct such a survey - indeed SNAP, if funded, is not expected to launch for another decade - it is of great interest to prepare for such an opportunity by developing the formalism and technique needed to deal with such large data sets. This can be done using simulated data sets, similar to those discussed in § 3.2.6. One thing which should be studied, is the needed sample size to reach accuracy in the dust evolution estimates to impact the dark energy surveys and other cosmological surveys sensitive to dust extinction.

Chapter 4

Dark Matter Profiles - Sérsic vs. NFW

All cases are unique
and very similar to others.
T.S. Eliot (1888-1965)

Lensing studies are ideal for measuring the matter distribution in distant objects as lensing is sensitive to all mass along the line of sight, regardless of its nature (dark or luminous) or state. The details of the lensing signal are dependent on the precise distribution of the matter. Gravitational lensing can therefore be used to test the predictions of the shape of the expected density profiles for dark matter found from numerical simulations. This chapter discusses the difference in the lensing signal from two such profiles and addresses whether current lensing data could be used to separate the two in real astrophysical systems. The majority of the work presented in this chapter has been published previously in Elíasdóttir & Möller (2007) and Jullo et al. (2007) (§ 4.5).

4.1   Introduction

According to ΛCDM simulations, dark matter is expected to dominate baryonic matter on both galactic and cluster scales. Observations, including X-ray studies, gravitational lensing and rotational velocity curve measurements, also suggest

that the luminous matter is only a fraction of the total matter in the Universe, although it dominates the dark matter in the innermost regions of galaxies and clusters. Understanding the nature of dark matter is one of the key challenges in modern astrophysics. In particular, a knowledge of the spatial distribution of the dark matter is crucial for understanding its interplay with the baryonic matter and gaining insight into its nature.

The dark matter distributions for halos from ΛCDM simulations are usually described by the Navarro, Frenk, & White (NFW) profile (Navarro et al., 1995), but recently Navarro et al. (2004) found a better fit using a Sérsic profile for the 3D density distribution. That work was expanded in Merritt et al. (2005) which found that the Sérsic distribution also provides a good fit to the 2D distribution of dark matter halos and found the deprojected Sérsic profile to give the best fit to the 3D distribution. It is intriguing that the Sérsic law, which is often fit to the 2D luminosity profiles of elliptical galaxies (Caon et al., 1993; Ciotti, 1991; Graham & Guzmán, 2003; Sersic, 1968), should also describe the surface density profiles of dark matter halos from simulations. In fact, work by e.g. Hayashi et al. (2004) suggests that the Sérsic profile provides a better fit in particular to the inner regions of dark matter halos, where the DM density profile affects the kinematics of the central galaxies in these halos more strongly. As lensing can probe the surface density profiles of galaxies (see e.g., Ferreras et al., 2005; Rusin et al., 2002) and clusters (see e.g., Broadhurst et al., 2005; Kneib et al., 2003), especially in their central regions, it is of interest to compare the lensing properties of the Sérsic and the NFW profiles; does the use of an NFW profile for lensing mass reconstructions introduce a significant bias given an actual Sérsic lens profile, or are the two essentially indistinguishable for lensing mass reconstructions?

The question of the slope for the inner profile in lens systems like galaxies and clusters has been addressed by several authors before (Oguri & Keeton, 2004; Sand et al., 2004). Others have predicted and/or attempted to reconstruct the slope of lensing systems from the observed positions and magnifications of multiply-imaged sources (Broadhurst et al., 2005; Koopmans et al., 2006). In this work, a very theoretically motivated approach is taken: given either an NFW or Sérsic profile for dark mass distributions, how would their lensing properties differ? The fact that in actual lens systems, the lensing mass also includes a

baryonic component that is parameterised in a different way is thereby neglected. Even if the stellar mass component of early-type galaxies can also be described by a Sérsic profile, the scale length and central densities are very different than those found in simulations for the Sérsic profiles for the dark matter component. The work presented here therefore only describes the *difference* in lensing properties between NFW and Sérsic profiles if the total mass distribution can be described by a single Sérsic profile. For cluster systems, the dark matter component is a more significant contributor to the lensing properties and the baryonic component plays a smaller role than for galaxy lens systems. In this sense the results in this chapter are more readily compared with current lensing constraints on the dark matter profiles of clusters. The analytical lensing relations derived in § 4.2 are, however applicable to all lens systems that can be described by a Sérsic profile, irrespective of the scale and whether the matter is baryonic or dark.

Throughout this chapter standard ΛCDM cosmology is assumed with $\Omega_\Lambda = 0.70$, $\Omega_m = 0.30$ and $H_0 = 70$ km s^{-1} Mpc^{-1} ($h = 0.7$). For numerical lensing calculations the lens is placed at a redshift of $z = 0.3$ (a realistic redshift for both galaxy and cluster lenses) and the source at $z = 10$ (chosen to approximate a source at $z = \infty$, although for any $z \gtrsim 1$ the results are similar). For the given cosmology, $1''$ corresponds to 4.45 kpc at $z = 0.3$. The chapter is organised as follows: It starts with an introduction of the NFW and the Sérsic profiles in the remainder of § 4.1. In § 4.2 the magnification properties of the Sérsic profile are derived and discussed. In § 4.3 the differences in the lensing properties of a Sérsic surface matter density and a corresponding best fitting NFW is studied and discussed. It is studied whether applying an NFW fit to an underlying Sérsic profile leads to a bias in the mass and concentration parameter and there's a discussion on the implications the results could have on modelling of observed lenses. A summary of the conclusions is given in § 4.4.

4.1.1 The NFW profile

The NFW profile (Navarro et al., 1995, 1996) has been extensively used to fit ΛCDM halos from simulations and in 3D is given by:

$$\rho_{\mathrm{nfw}} = \frac{\delta_c \rho_c}{(r/r_s)(1 + r/r_s)^2} \tag{4.1}$$

where $r_s = r_{200}/c_{200}$ is the (3D) scale radius, c_{200} is a dimensionless number called the concentration parameter, ρ_c is the critical (3D) density at the redshift of the halo, r_{200} is the radius inside which the mass density of the halo equals $200\rho_c$ and δ_c is the characteristic over-density for the halo given by

$$\delta_c = \frac{200}{3} \frac{c_{200}^3}{\ln(1 + c_{200}) - c_{200}/(1 + c_{200})}. \tag{4.2}$$

The 2D projection of the NFW profile is frequently used in the modelling of gravitational lenses (Broadhurst et al., 2005; Golse & Kneib, 2002; Wayth et al., 2005; Williams & Saha, 2004). It is found by integrating equation (4.1) along the line of sight, giving

$$\Sigma_{\text{nfw}}(X) = \frac{2r_s\delta_c\rho_c}{X^2 - 1} \begin{cases} \left(1 - \frac{2}{\sqrt{1-X^2}}\text{arctanh}\sqrt{\frac{1-X}{1+X}}\right) & (X < 1) \\ \\ \left(1 - \frac{2}{\sqrt{X^2-1}}\arctan\sqrt{\frac{X-1}{1+X}}\right) & (X > 1) \end{cases} \tag{4.3}$$

and the shear is given by

$$\gamma_{\text{nfw}}(X) = \frac{2r_s\delta_c\rho_c}{\Sigma_{\text{crit}}} \left[\frac{2}{X^2}\ln\left(\frac{X}{2}\right) - \frac{1}{X^2 - 1} + 2\left(\frac{2}{X^2} + \frac{1}{X^2 - 1}\right)f(X)\right] \tag{4.4}$$

with

$$f(X) = \begin{cases} \frac{\text{arctanh}\sqrt{(1-X)/(1+X)}}{\sqrt{(1-X^2)}} & (X < 1) \\ \\ \frac{\arctan\sqrt{(X-1)/(1+X)}}{\sqrt{X^2-1}} & (X > 1) \end{cases}$$

where $X = R/r_s$ (Wright & Brainerd, 2000). These lensing relations of the NFW have previously been studied and can also be found in e.g. Bartelmann (1996); Golse & Kneib (2002); Wright & Brainerd (2000).

4.1.2 Sérsic profile

The Sérsic law for surface density profiles is given by

$$\ln\left(\frac{\Sigma_{\text{ser}}}{\Sigma_e}\right) = -b_n\left[\left(\frac{R}{R_e}\right)^{1/n} - 1\right], \tag{4.5}$$

where Σ_{ser} is the 2D density, R is the 2D radius, n is the Sérsic index, b_n is a constant chosen such that R_e is the radius containing one-half of the projected mass and Σ_e is the density at R_e. The constant b_n is found by solving the equation $\Gamma(2n, b_n) = \Gamma(2n)/2$ and can be approximated as $b_n \approx 2n - 1/3 + 4/(405n) + 46/(25515n^2)$ (Ciotti & Bertin, 1999). With $n = 4$ the Sérsic profile reduces to the de Vaucouleurs profile, whereas $n = 1$ gives the exponential law. A previous study of the lensing properties of the Sérsic profile focussed on $n = 3, 4, 5$ (Cardone, 2004). In Merritt et al. (2005) the mass distribution of dwarf- and galaxy-sized halos has a mean of $n \sim 3.0$ but $n \sim 2.4$ for cluster-sized halos with values as low as $n = 2$.

4.2 Lensing and the Sérsic Profile

This section begins by calculating the total magnification, μ, for the Sérsic profile. From standard equations for gravitational lensing (Schneider et al., 1992) one has:

$$\mu = \frac{1}{(1 - \kappa)^2 - \gamma^2} \tag{4.6}$$

where $\kappa = \Sigma/\Sigma_{\mathrm{crit}}$ is the convergence and

$$\Sigma_{\mathrm{crit}} = \frac{c^2}{4\pi G} \frac{D_s}{D_l D_{ls}} \tag{4.7}$$

is the critical mass density, which depends on the angular diameter distances to the source (D_s), the lens (D_l) and between the source and the lens (D_{ls}), c is the speed of light in vacuum and G is the gravitational constant. For a spherically symmetric mass profile, the shear γ can be calculated as

$$\gamma = \frac{\bar{\Sigma} - \Sigma}{\Sigma_{\mathrm{crit}}} \equiv \bar{\kappa} - \kappa, \tag{4.8}$$

where

$$\bar{\Sigma}(Y) = \frac{2}{Y^2} \int_0^Y Y' \Sigma(Y') dY' \tag{4.9}$$

is the mean surface mass density as a function of radius (Schneider et al., 1992, see also Chapter 2).

Applying this to the Sérsic profile, one finds

$$\mu_{\text{ser}} = \left[(1 - \bar{\kappa}_{\text{ser}})(1 + \bar{\kappa}_{\text{ser}} - 2\kappa_{\text{ser}}) \right]^{-1}, \tag{4.10}$$

where

$$\kappa_{\text{ser}} = \frac{\Sigma_e}{\Sigma_{\text{crit}}} \exp\left[-b_n \left(-1 + Y^{1/n} \right) \right], \tag{4.11}$$

$$\bar{\kappa}_{\text{ser}} = \frac{\Sigma_e}{\Sigma_{\text{crit}}} 2b_n^{-2n} n \exp[b_n] \frac{\Gamma[2n] - \Gamma[2n, b_n Y^{1/n}]}{Y^2} \tag{4.12}$$

and $Y = R/R_e$. From equation (4.10) it can be seen that the Sérsic profile has two sets of critical curves (i.e. curves in the lens plane where the magnification formally goes to infinity), which are defined by $1 - \bar{\kappa}_{\text{ser}} = 0$ (tangential critical curve) and $1 + \bar{\kappa}_{\text{ser}} - 2\kappa_{\text{ser}} = 0$ (radial critical curve).

These equations define two rings and the radii can be found by solving the equations numerically. The larger of the rings, given by $1 - \bar{\kappa}_{\text{ser}} = 0$, is the so called Einstein ring. Its radius is called the Einstein radius, R_{ein}, which, for the spherical profiles considered here, corresponds to the radius at which the mean surface density equals the critical surface density. Figure 4.1 (solid lines) shows a plot of the magnification as a function of radius for different values of n and constant $\Sigma_e/\Sigma_{\text{crit}}$ and R_e. One can see that the two critical curves move further apart for steeper profiles, and correspondingly, that the lowest magnification between them decreases. This result is not in agreement with those of Cardone (2004), who only found tangential critical curves when studying lensing properties of the Sérsic profile for $n = 3, 4, 5$. It is found that this discrepancy is due to a sign error in the calculations of Cardone (2004) and it is noted that, provided there is a tangential critical curve at $R = R_{\text{ein}} > 0$, there will always be a radial critical curve for the Sérsic profile. This is because $(1 + \bar{\kappa}_{\text{ser}} - 2\kappa_{\text{ser}})|_{R=\infty} = 1 > 0$ and $(1 + \bar{\kappa}_{\text{ser}} - 2\kappa_{\text{ser}})|_{R=0} = 1 - \kappa_{\text{ser}}|_{R=0} < 0$ and as both κ_{ser} and $\bar{\kappa}_{\text{ser}}$ are continuous functions, there must exist an $R > 0$ where a radial critical curve will occur.

4.3   Comparing the Sérsic and the NFW Profiles

In this section a comparison of the lensing properties of the Sérsic and the NFW profiles is made. The Sérsic 2D mass profile is used as an input, and a corresponding NFW is found which gives the best reproduction of the lensing constraints,
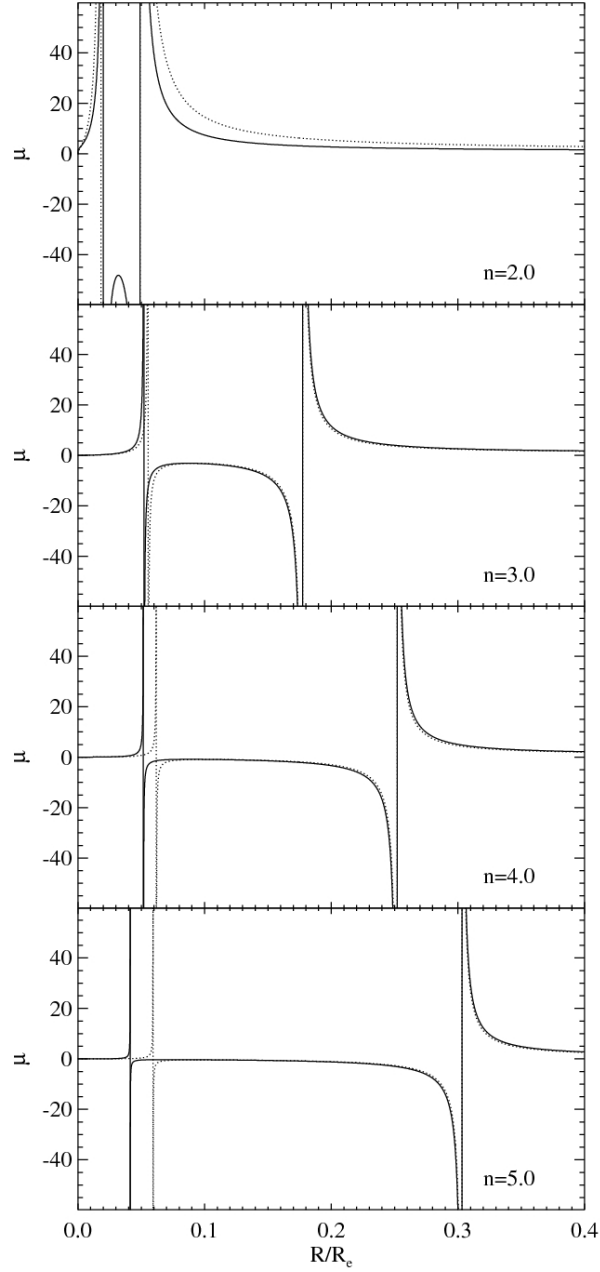
Figure 4.1 Plot of the magnification properties of the Sérsic profile (solid line) and the best fitting NFW profile (dotted line) for different values of the Sérsic index n, and constant $\Sigma_e = 10^8 \mathrm{M}_\odot \mathrm{kpc}^{-2}$ and $R_e = 100$ kpc. One sees that for the Sérsic profile, the two critical curves move further apart for higher values of n, corresponding to a steeper profile.

as described below. Following Merritt et al. (2006), values of $R_e \sim 100$ kpc with $3 \lesssim n \lesssim 5$ are representative parameter values for galaxy sized halos, while $R_e \sim 1000$ kpc with $2 \lesssim n \lesssim 3.5$ are a realistic parameter range for the Sérsic profile for cluster-sized halos, with lower n being found for more massive clusters (which are more likely to act as lenses). In particular, $500 \leq R_e \leq 2500$ kpc for cluster sized halos is taken as input parameters for the simulations. The third input parameter, Σ_e, has a minimum value for strong lensing to occur, i.e. $\Sigma_{\mathrm{ser}}|_{R=0} = \Sigma_e e^{b_n} > \Sigma_{\mathrm{crit}}$. Typical Einstein radii for galaxies are of the order of $1''$ (Lehár et al., 2000), while for clusters they are of the order of $10''$ with the largest known Einstein radius to date being $45''$ (Broadhurst et al., 2005; Kneib et al., 2003). Therefore the input Sérsic profiles are constrained to have Einstein radii in this range, and for each given Einstein radii n and R_e are varied, while Σ_e is calculated from the three input parameters R_{ein}, n and R_e.

The goal is to study whether strong lensing data of an accuracy currently available can be well fitted by an NFW profile even if the lensing mass distribution actually follows a Sérsic profile. In particular, the aim is to explore whether the corresponding NFW can reproduce the strong lensing data, and if so, what the parameters of the NFW profile are and how these relate to typical NFW parameter values obtained for simulated cluster halos. Therefore the Sérsic profile is taken as the assumed input and a fit is made for the corresponding NFW profile given certain constraints.

The constraints from strong lensing are in general the Einstein radius, relative locations of the images and their magnification ratio, which are all sensitive to the mass distribution within the disc defined by the outermost image. Of these the Einstein radius (deduced from the total separation of the multiple images) is the best constrained value, while the precise location of images can be affected by nearby substructure and the magnification ratio can be biased by both microlensing and dust extinction in the lensing galaxy (Elíasdóttir et al., 2006; Lewis & Gil-Merino, 2006; Schechter & Wambsganss, 2002). The inner critical curve may also give additional constraints on the mass profile if central images or merging radial arcs are observed. Under the assumption of spherical symmetry, time delay measurements between images provide a further constraint on the mass in an annulus, bounded by the radii of each of the images, but are hard to measure, in
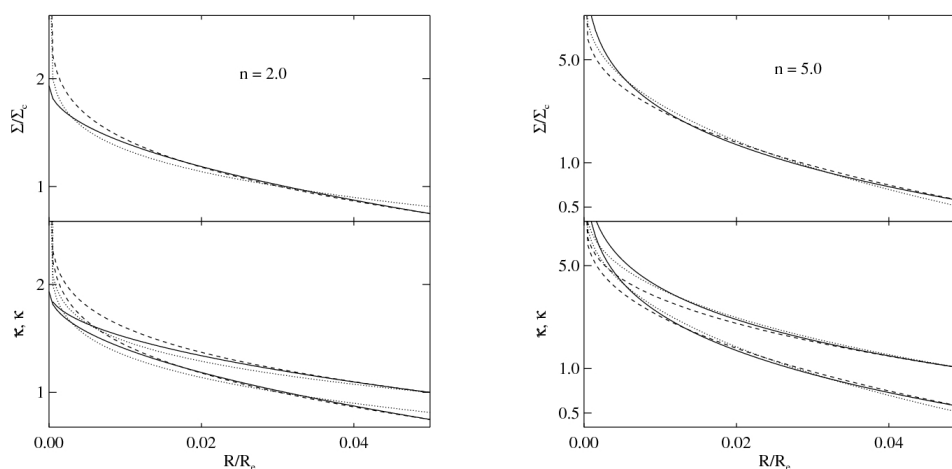
Figure 4.2 The top panels show $\kappa = \Sigma/\Sigma_{\rm crit}$ for the Sérsic profile (solid line) for n=2,5 and $0 \leq R \leq R_{\rm ein}$. Also shown are the best fitting NFW profile (dotted line) as defined in § 4.3.1 and an alternative fit (dashed line) which is optimised in a tight area around $R_{\rm ein}$. The lower panels show the corresponding $\bar{\kappa}$ (upper set of curves) and κ for comparison (lower set of curves). Although the detailed shape of the NFW varies with the choice of fitting, the resulting analysis presented in this chapter is not sensitive to it. The value of the other input parameters for the Sérsic profile were $R_e = 1000$ kpc and $R_{\rm ein} = 50$ kpc.

particular in strong cluster lensing where most of the known lensed images are background galaxies and not quasars.

Two main approaches to the fitting are chosen. The first approach assumes that one has multiple systems at different redshifts allowing for constraints on the total mass within a number of radii. This approach reflects the common situation that several arc systems are used to constrain the lensing mass distribution of clusters (Limousin et al., 2007b). The second approach assumes that only a single Einstein ring is detected and used for the lensing analysis (Comerford & Natarajan, 2007). In this case the Einstein radii of the two profiles is fixed to be the same, and the inner mass density profile is fitted as described below in § 4.3.1. This choice is motivated mainly by the fact that the Einstein radius is easy to constrain accurately observationally and that the magnification of multiply imaged arcs and arclets in strong lensing clusters constrain the surface mass density on a scale given by the Einstein radius.

4.3.1   Fitting method

For the case when only one Einstein ring is used to constrain the system, the fit is underconstrained, so an additional constraint must be chosen on the NFW profile that relates it to the input Sérsic profile. Since the magnification and shear for a series of observed extended and highly magnified arcs of the same source is sensitive to the surface mass density in the inner regions of the cluster, it is required that the NFW profile fits the input Sérsic projected mass distribution in an inner region bounded by R_{ein} with the Einstein radius itself as a constraint. The fitting itself is done numerically, using Levenberg-Marquardt least-squares minimisation. As the primary mode of fitting, the Sérsic surface mass density profile is taken at $N = 10000$ points, linearly distributed from $R = 0$ to $R = R_{\mathrm{ein}}$, and a constant relative error is applied in each of the points. To check the dependence of the results on the precise choice of fitting, several other fitting methods are applied consistent with the previously described framework. In particular, the analysis is redone using fits where the points are distributed differently, where $\log \Sigma$ is fitted instead of Σ, and where the weight of the points is altered, giving more emphasis to different regions. For example, instead of distributing the points over

$0 < R < R_{\text{ein}}$, the fit is constrained to a tight area around the Einstein radius ($0.95R_{\text{ein}} < R < 1.05R_{\text{ein}}$) or to an area around the Einstein radius and the inner critical curve of the Sérsic profile. In addition the absolute weights of the points are changed to be equal, putting an emphasis on the inner points (where there are less constraints from lensing). Although the detailed shape of the best fitting NFW profile varies depending on the choice of fitting (see Figure 4.2 for a plot of the $\Sigma, \bar{\kappa}, \kappa$ from two fits for $n = 2$ and 5), and it is noted that the method is not sensitive to whether the profile is very cuspy or not in the very centre as could be achieved using central images as constraint, the analysis presented in the rest of the chapter remains qualitatively the same. This leads to the conclusion that the precise method of fitting used does not affect the conclusions.

When multiple Einstein radii are used, there are enough constraints to find the best fitting NFW without additional constraints. As each Einstein radii gives an estimate of the mass of the system within that radius, the mass profile is fitted (rather than the mass density profile) of the NFW to the mass profile of the input Sérsic profile. It is assumed that there are 9 independent systems at distances of 10-170 kpc for a cluster sized lens (Limousin et al., 2007b). The uncertainty of the mass estimated at each of the points is set to be 10%, corresponding roughly to the level of current observational accuracy. It is found that the results from the lensing analysis remain qualitatively the same as for the fitting of a single Einstein radius.

The figures in the chapter are based on the single Einstein radius constraint, fitting Σ in the range of $0 < R < R_{\text{ein}}$ using the $1/N$ weighting, unless otherwise noted.

4.3.2 General properties

Figure 4.3 shows R_{ein} as function of n for different values of R_e. The figure shows that R_{ein} is a strong function of R_e and n for low values of n, while for the higher range of n the values level off. A similar plot may be obtained keeping R_e constant and varying Σ_e, which shows R_{ein} increasing with Σ_e. As explained above, the focus on the strong lensing properties of the Sérsic profile as compared to the NFW profile motivates fixing the Einstein radius or fitting for the total
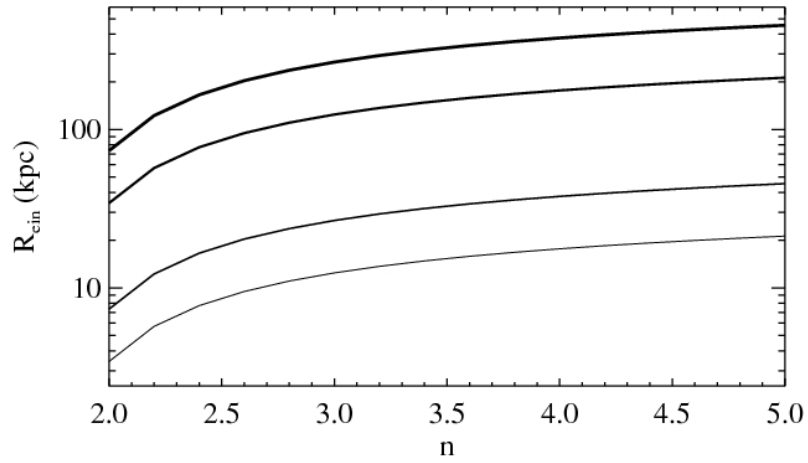
Figure 4.3   The Einstein radius, R_{ein}, as a function of n, for $R_e = 70, 150, 700, 1500$ kpc (denoted by increasing line thickness) and constant $\Sigma_e = 10^8$ M$_\odot$ kpc^{-2}. The Einstein radius is strongly dependent on R_e, with larger values of R_e resulting in a larger Einstein radius, and is also dependent on n, with larger n giving larger R_{ein}. The n dependence is strongest for low $n \sim 2$–3 but levels off for higher n. A similar plot can be obtained by holding R_e constant and varying Σ_e, showing R_{ein} increasing with Σ_e.

mass at multiple Einstein radii when making further comparisons. In the following figures the Einstein radius is set to $R_{\text{ein}} = 50\,\text{kpc}$, corresponding to a cluster sized halo, but all the results presented also apply to systems with different Einstein radii (e.g. galaxies) and to systems with measurements of several Einstein radii corresponding to multiple sources.

Fitting an NFW profile to a Sérsic lens will not always give a good fit to the data. In fact, given that the number of parameters of the NFW is less than that of the Sérsic one does not expect a good fit in general. Different indices n of the Sérsic profile correspond to different slopes in the inner mass profile, whereas the slope of the NFW profile is not a free parameter. Fig. 4.4 shows the 'goodness of
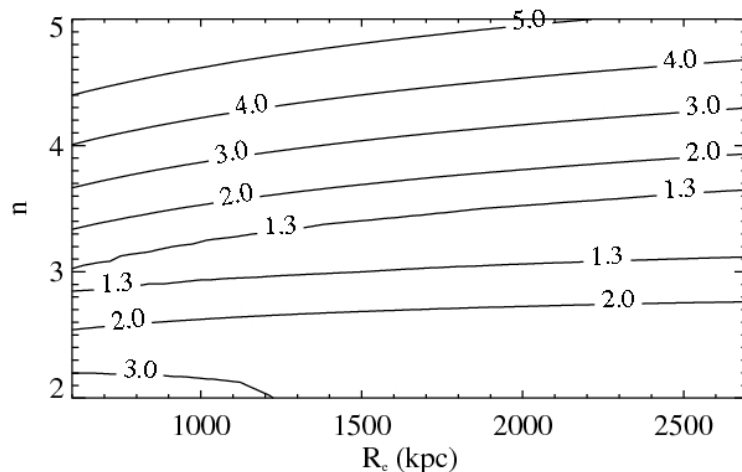
Figure 4.4 The reduced χ^2 of the best-fit NFW as a function of the Sérsic parameters n and R_e, normalised with the lowest χ^2 in the ensemble. Some set of parameters give significantly worse fits than others, consistent with the fact that the number of free parameters for the NFW is less than for the Sérsic profile. The Einstein radius is kept fixed at $R_{\text{ein}} = 50\,\text{kpc}$, as described in the text.

fit', the χ^2 normalised with the lowest χ^2 in the ensemble. As expected, good fits (low values of χ^2) are obtained only for a small region around a specific value of n. It should be noted, however, that in most lensing analysis an NFW profile is assumed and the best-fit parameters are obtained, even if the actual χ^2 is high.

In such cases, the results suggest that a fit using a Sérsic profile should be used instead and will give a much better fit if the underlying profile is in fact a Sérsic. Figure 4.5 shows how the best-fit NFW scale length varies with the input Sérsic
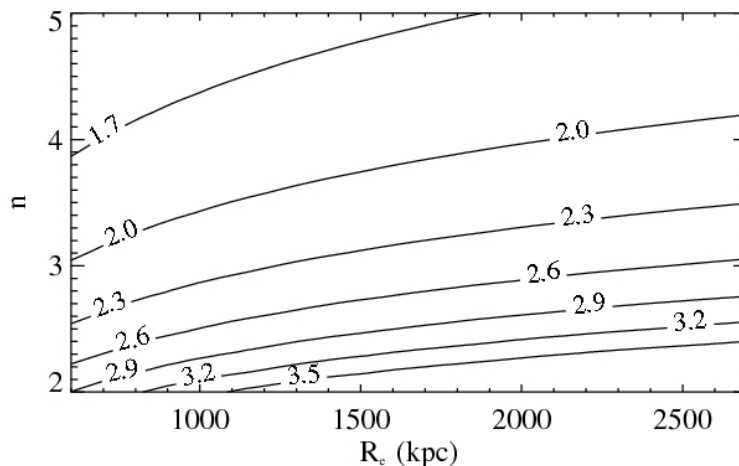
Figure 4.5 Scale lengths, $\log\left(r_\mathrm{s}/\mathrm{kpc}\right)$, for the best-fit NFW profile as a function of Sérsic parameters, R_e and n. The scale length is strongly dependent on n, with low n giving rise to high scale lengths. The Einstein radius is fixed as in the previous figures.

parameters. Higher values of n give rise to steeper profiles and hence a lower value for the scale length r_s of the best-fit NFW profile.

4.3.3 Magnification and image configuration

In Figure 4.1 shows the magnification for the best fit NFW profile for $n = 2, 3, 4, 5$ and constant R_e and Σ_e (note that for this plot R_ein is not kept constant). The figure shows that the difference in the magnification properties is not very large, except for $n = 2$. For $n = 3$, the fits are very similar, whereas for $n = 4, 5$ the main difference lies in the location of the inner critical lines. The exact location of the inner critical lines depends to some extent also on the choice of fitting, and is therefore not a very robust measurement of differences in the two profiles. In addition, the inner critical line is usually observationally less well determined

than the Einstein radius. Measurements of different Einstein radii, due to sources at different redshifts, are a more common and practical additional constraint on the inner mass profile. It is found that constraining the mass profiles in this way at several different Einstein radii results in very similar magnification profiles.

For a more quantitative analysis of the magnification differences, $r(\mu)$ is defined as the ratio the area on the source plane where magnified images (i.e. images with $\mu \geq 1$) with magnification greater or equal to μ occur. Taking R_{ein} to be constant, Figure 4.6 shows $r(\mu)$ calculated over an area in the source plane, corresponding to $4R_{\text{ein}}$ times $4R_{\text{ein}}$ in the image plane (shown for the Sérsic profile in Figure 4.7). Figure 4.6 shows that the difference in the magnification is indeed small, although for $n = 2$ the NFW profile is more likely to produce highly magnified images, whereas for higher n the reverse is true to a smaller degree. As the difference in the magnification properties of the Sérsic and the best fitting NFW profiles is small, the results demonstrate that, given current observational accuracy, an NFW profile is adequate to describe the magnification for these strong lensing systems.

In many strong gravitational lens systems the observed images do not lie exactly on the Einstein radius, but are displaced in an asymmetric fashion; one image being within the Einstein radius and another outside. To illustrate the difference between Sérsic and NFW models the image displacements are shown in Fig. 4.7 for two different choices of the source position. For a fixed source position, the image positions for the best-fitting NFW profile is indistinguishable from that of the Sérsic profile for high n, while for low values of n, there is a slight offset between the image positions, in line with the findings from above: NFW profiles produce very similar lensing signatures to Sérsic profiles, and are distinguishable only for low values of the Sérsic index $n \lesssim 3$ unless the goodness of fit can be used to separate the profiles.

4.3.4 Mass and concentration

Lensing, both strong and weak, is frequently used to estimate the mass and the NFW concentration parameter of clusters, which are then compared to those from simulations or X-ray measurements, with lensing usually finding a higher mass
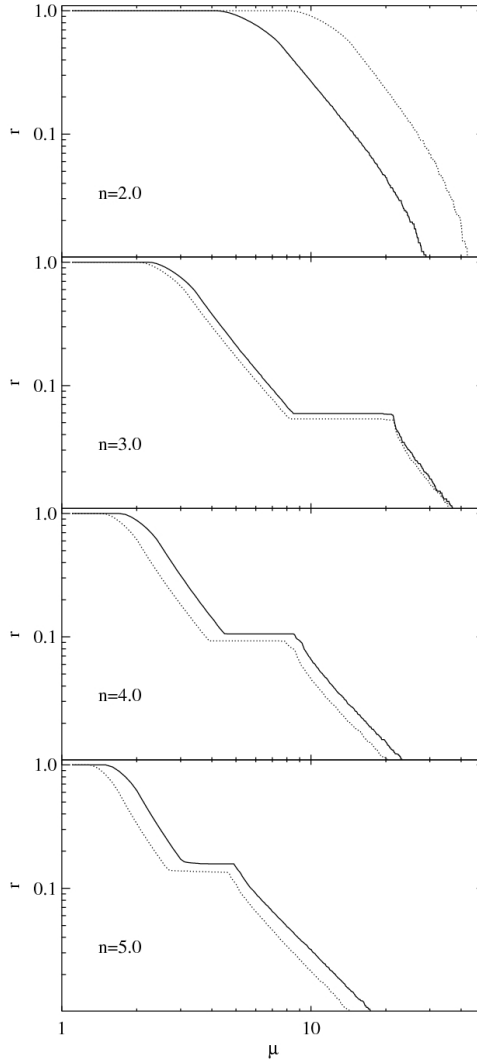
Figure 4.6 The ratio of the number of images with amplification equal or greater than μ to the total number of amplified images, $r(\mu)$, for the Sérsic (solid line) and the NFW (dotted line) profiles for different values of n. The calculation of $r(\mu)$ is done in the source plane, corresponding to magnification maps of size $4R_{\mathrm{ein}}$ times $4R_{\mathrm{ein}}$ in the image plane, shown in Figure 4.7, with $R_{\mathrm{ein}} = 50$ kpc and $R_e = 1000$ kpc (corresponding to a cluster sized lensing halo). The plots show that the magnification properties are similar for the two profiles, although the NFW over predicts highly magnified images for $n \sim 2$, while it to a smaller degree under-predicts them for $n \gtrsim 3$.
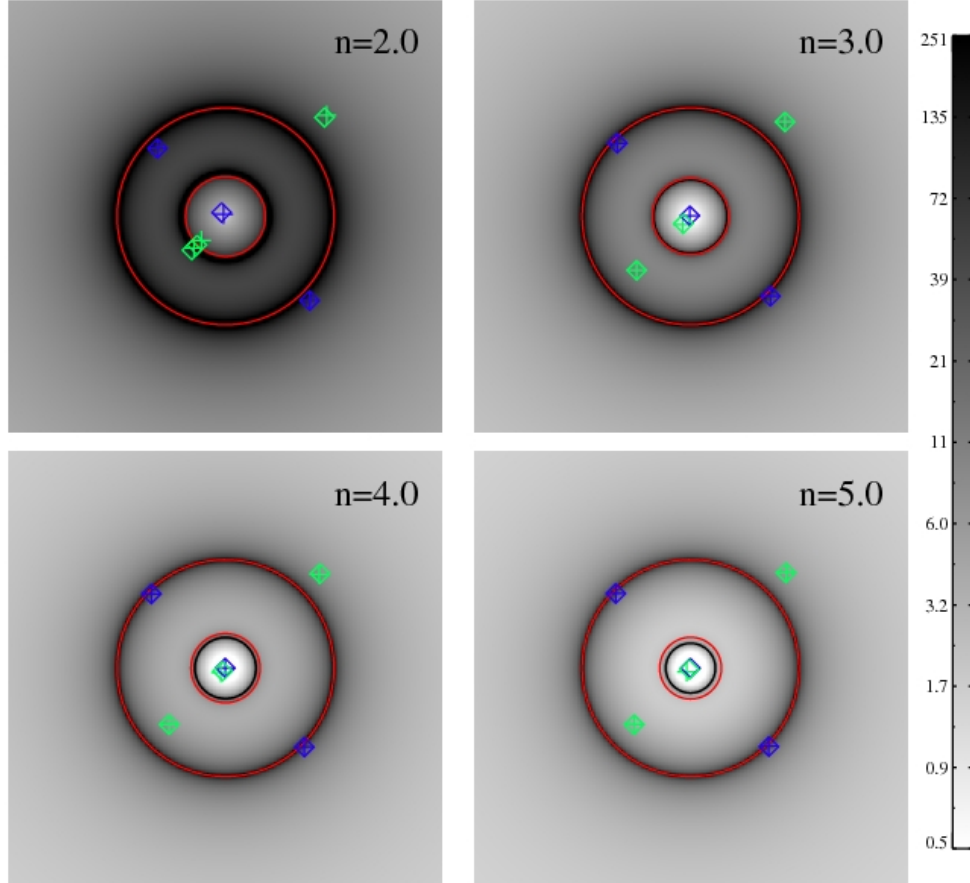
Figure 4.7 The image plane magnification map for the Sérsic profile for different values of n with $R_{\mathrm{ein}} = 50$ kpc and $R_e = 1000$ kpc (corresponding to a cluster sized lensing halo). The images are centred on the lens and are of size $4R_{\mathrm{ein}}$ times $4R_{\mathrm{ein}}$. The black circles correspond to the tangential and radial critical curves for the Sérsic profile, and the red circles are the critical curves of the best fit NFW profile, where the magnification formally goes to infinity. Also shown are the image geometries for double images of the Sérsic (diamonds) and the NFW (plus signs) profiles for two different source positions (blue and green). The symmetrical configuration of images are not distinguishable for any n, whereas for an asymmetric configuration the images are only marginally distinguishable for $n = 2$.

and concentration (Comerford & Natarajan, 2007; Halkola et al., 2006; Kling et al., 2005; Kneib et al., 2003; Limousin et al., 2007b). Therefore, it is of interest to study whether an underlying Sérsic profile could cause a bias in the mass and c estimate, if an NFW profile is assumed in the strong lensing modelling. As strong lensing is only sensitive at small radii, one should keep in mind when making these comparison, that a small deviation in the assumed profile can lead to large errors in both the mass and concentration parameter. However, although weak lensing should be more accurate for such comparisons as it probes a similar distance scale, it is very sensitive to contamination of the background galaxy catalogue by cluster members. In fact, Limousin et al. (2007b) find for Abell 1689, that the concentration parameter derived from strong lensing is consistent between different data sets and methods, while that derived from weak lensing still shows large scatter which are an artefact of the method applied. Fig. 4.8
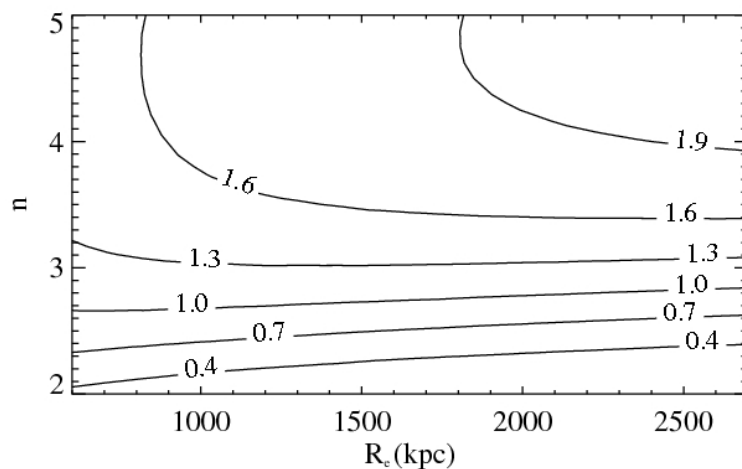
Figure 4.8 The ratio of projected Sérsic input masses over the best-fit NFW masses within r_{200} as a function of R_e and n of the input Sérsic profile. For low n the NFW profile overestimates the mass by a factor of around ~ 2, while the opposite holds for high n. The Einstein radius is kept fixed at $R_{\mathrm{ein}} = 50\,\mathrm{kpc}$, as in the previous figure.

shows the ratio of the projected masses for the input Sérsic and the best-fit NFW

within r_{200} (of the NFW profile). The mass ratio depends most strongly on the Sérsic index n. Roughly speaking, a higher value of n gives rise to lower projected masses for the corresponding NFW fits. Therefore, applying an NFW profile to a Sérsic lens can lead to a significant error in the mass estimation, with the mass at r_{200} being overestimated by a factor of ~ 2 for low n. Similarly, Figure 4.9
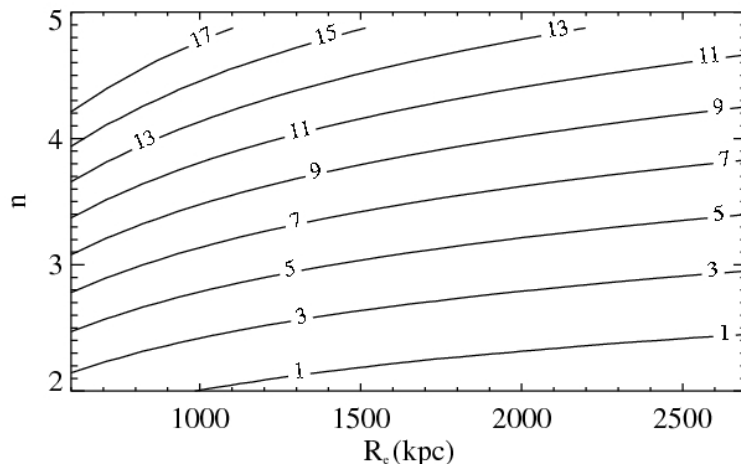
Figure 4.9 Concentration parameter for the best-fit NFW halo as a function of the input Sérsic profile parameters n and R_e. For low n, the concentration parameter takes on values of c which are lower than those expected from simulations, while for higher n the values of c become higher than expected. Therefore, although the lensing properties can be reproduced, the parameters of an NFW fit to a Sérsic lens can become unrealistic (see also Figs. 4.8 and 4.5). The Einstein radius is kept fixed as in the previous figure.

shows the concentration parameter of the best fit NFW profile as a function of the Sérsic index n and scale R_e. The figure shows how the concentration parameters increase mostly with increasing n from very low concentrations to $c \sim 17$ for high n. Extreme values of the concentration parameter (i.e. $c < 3$ or $c > 10$), can be found and correspond to the input Sérsic parameters where the NFW fit is worse and where the mass estimate is biased (see Figs. 4.4 and 4.8).

Therefore applying an NFW profile to an underlying Sérsic profile, can lead to

wrong mass estimates. For cluster sized halos with $n \sim 2$, fitting lensing data with an NFW profile would give values of c which would be lower than those expected when compared to CDM simulations. Such low values of c have been found in strong lensing analysis, although in general lensing overpredicts c compared to X-ray measurements (Comerford & Natarajan, 2007; Hennawi et al., 2007). For higher values of n, this trend gets reversed: for $n \gtrsim 3$ concentration parameters of NFW fits are higher than those seen in simulations. However, such high values of n are not expected to describe cluster size halos, but galaxy scaled halos (Merritt et al., 2005).

Observationally it is thus likely that NFW lens models of clusters that give rise to mass or concentrations which seem inconsistent or only marginally consistent with simulations or X-ray measurements would be better described by a Sérsic profile. It should be stressed that these results are consistent for all the fitting methods applied, and whether one or several sets of Einstein radii are used as constraints.

4.3.5 Extrapolating to the weak lensing regime

The previous sections have focused on comparing the difference in the strong lensing properties of the Sérsic and the NFW profiles, making R_{ein} the most relevant distance scale. A thorough analysis of the difference in the weak lensing properties of the two profiles would require optimising the fits in the weak lensing regime and is beyond the scope of this chapter. However, one can compare the predicted total mass and the weak lensing shear γ in the weak lensing regime by extrapolating the derived functions to higher radii. The projected mass within r_{200} for different values of n and R_e have already been compared(see Figure 4.8), but the NFW: Sérsic mass ratio is studied as a function of radius for a halo with $R_e = 1000$ kpc and $R_{\mathrm{ein}} = 50$ kpc, corresponding to a cluster sized halo. Figure 4.10, shows the difference in the projected mass over the projected mass of the Sérsic profile. It can be seen that for $n = 2$, the best fitting NFW profile overestimates the mass by a factor of > 2 for $R \gtrsim 10R_{\mathrm{ein}}$, while it underestimates it by ~ 2 for $n \geq 3$. This is due to the fact that in order to fit the low $n = 2$ Sérsic profiles, the estimated r_s of the NFW (the scale radius at which the density
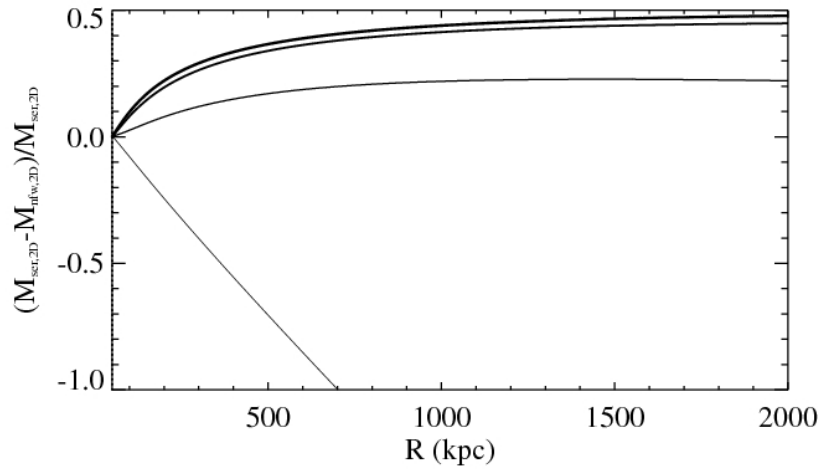
Figure 4.10 The difference in the projected mass vs. the mass of the Sérsic profile at radii $R > R_{\rm ein}$ for $n = 2, 3, 4, 5$ (denoted by increasing line thickness) with $R_{\rm ein} = 50$ kpc and $R_e = 1000$ kpc. The NFW fit to the Sérsic profile, extrapolated to higher radii, underestimates the mass for an underlying Sérsic profile for $n \gtrsim 3$, whereas it overestimates it for low n.

slope increases) is overestimated, making the NFW profile fall off less steeply than expected in the outer regions. Similarly, Figure 4.11 shows the difference in the
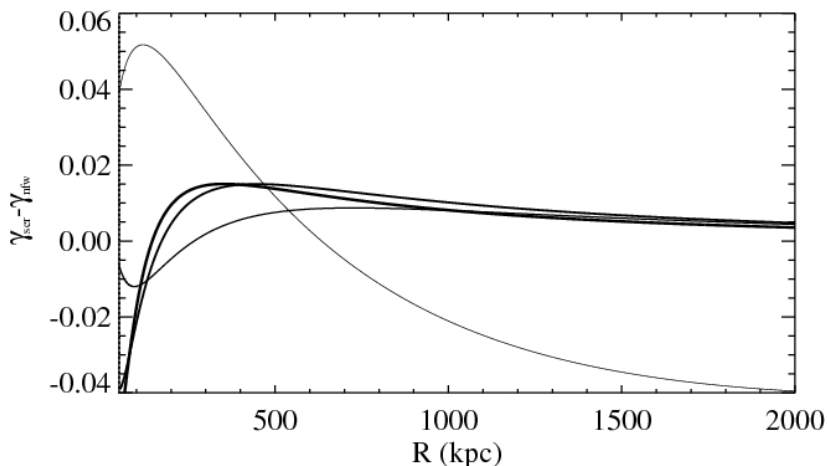
Figure 4.11 The difference in the shear of the Sérsic and NFW profiles at radii $R > R_{ein}$ for $n = 2, 3, 4, 5$ (denoted by increasing line thickness) with $R_{ein} = 50$ kpc and $R_e = 1000$ kpc. For $n \gtrsim 3$ the NFW fit to the Sérsic profile, extrapolated to higher radii, underestimates the shear by ~ 0.01. For low n, the shear can be more strongly affected: it is underestimated by up to ~ 0.05 for low radii and overestimated by a similar amount for $R \gtrsim 10R_{ein}$.

projected shear γ as a function of radius. It is found that for $n \gtrsim 3$, the difference is of the order of 0.01 while for $n = 2$ it is of the order of 0.05. As weak lensing measurements of clusters are usually looking at shear signals around $0.01 - 0.05$, this is a significant difference, in particular for the low n. Therefore, using an NFW to model an underlying Sérsic profile with low n would significantly over predict the weak lensing signal at large radii, and, depending on the measurement errors, result in a poor fit.

4.3.6 Observational implications

As a starting point, this work has taken a Sérsic profile as the underlying description of the matter profile and studied how lensing analysis applying an NFW fit

would differ and lead to biased results, depending on the input Sérsic index. It has been found that for $n \sim 2$ the mass can be overestimated by a factor of two and give low concentration. However, the issue of which profile is a better description of real dark matter halos has not been addressed. To do so, one should model a real system using the Sérsic profile and compare it to the results found when using an NFW profile. While such a study is beyond the scope of this thesis, the implications the results have on lens modelling of real systems is discussed here.

For galaxy scale lenses, various authors (Chae et al., 2002; Koopmans et al., 2006; Li & Ostriker, 2002) have established that lenses on average are well fitted by an isothermal profile, although there can be significant scatter for individual lenses (Koopmans et al., 2006). These all apply however to the *total* matter distribution, both luminous and dark, while this work has studied the differences for dark matter only profiles. More recent studies have attempted separating the dark and luminous matter profiles in lensing of galaxies (Baltz et al., 2007; Dye et al., 2007), but in general the constraints from lensing alone are not sufficient for separating the two.

Group or cluster scale lenses, with which this work is primarily concerned, are more dark matter dominated. This means they are also better suited for an observational test of whether real clusters are better described by an NFW or a Sérsic profile. Regarding observational strong lensing constraints the main observable is the total mass and the slope of the mass profile in the innermost (strong lensing) region of the cluster or group. The NFW and the Sérsic profile differ in that the Sérsic profile has an extra independent parameter, n that directly relates to the inner slope of the mass distribution. Even though the concentration parameter of the NFW profile is related to the slope of the profile, it is also related to the overall scale and mass of the cluster and is not an independent parameter. From an observational perspective the key quantities then are the slope and mass of the dark matter in the inner region of real clusters, and whether they are consistent with an NFW profile as expected from CDM simulations. As pointed out recently (Comerford & Natarajan, 2007) NFW fits to observed strong lensing clusters very often give masses or concentration parameters that seem inconsistent with CDM predictions. In general the trend is that observed clusters have higher concentration parameters than predicted in simulations –

but some lensing clusters have also yielded very low concentration parameters when fit with an NFW profile (e.g. MS1137.5+6625 (Maughan et al., 2007) and MS 2053.7-0449 (Verdugo et al., 2007)). Clusters with unusually high or low concentration values may very well be fit much better with a Sérsic profile – since the Einstein radius then becomes a function of n, even for a fixed scale, R_e, an index n (and hence slope) and a total mass M may be found that match the predicted shape of the mass profile from CDM more closely. It is important to note that the lensing fits of clusters are often quite poor, i.e. the χ^2 is high or the rms of the predicted image position is larger than the uncertainty in their measured positions (Limousin et al., 2007b; Verdugo et al., 2007).

4.4   Discussion and Conclusions

In this chapter, the Sérsic and NFW dark matter surface density profiles have been compared with respect to their strong lensing properties. Taking Sérsic profiles, with parameters that are in the range found for clusters and galaxies in large N-body simulations, the parameters of the NFW profile that fits the inner projected surface mass density of the Sérsic best have been explored. The NFW profiles were constrained to have the same Einstein radius as the input Sérsic profile, as this is the most accurately determined observable in lens systems. As an alternative approach, a data set consisting of several multiply imaged systems at different redshifts has been assumed, giving a constraint on the mass profile at different radii. It is found that an NFW profile can in general accurately produce the magnification and image positions of a Sérsic matter distribution only for $n \gtrsim 3$. For lower Sérsic index values, which are more likely to occur in cluster sized halos, the difference in the lensing properties increases, to the level where it could affect results of lens modelling, in particular for the magnification estimates. Although one can in general find an NFW profile which gives similar lensing properties, the parameters of the profile may become unrealistic. For $n \sim 2$, as simulations suggest can be the case for clusters, the mass is overestimated by a factor of ~ 2 while the concentration parameter is $\sim$ 1-3, which is lower than expected from simulations, although such low values have been seen in lensing studies (Comerford & Natarajan, 2007). Extrapolating into the weak lensing

regime it is found that the NFW overestimates both the total mass and the shear for $n = 2$, while it underestimates them for $n \gtrsim 3$.

Therefore, if an underlying Sérsic profile with $n \sim 2$, as is found for massive systems, is fit with an NFW using strong lensing constraints, it will overpredict both the mass (by a factor of a few) and the shear (up to $\sim 4\%$) of the halo at large radii, and could therefore contribute to explaining why lensing mass estimates are greater than those found by X-rays. Conversely, weak lensing data can in principle be used to demonstrate whether the Sérsic or the NFW profile is a more accurate description of the mass distribution. However, in practice a good S/N ratio is required – even for Sérsic profiles with low n an accuracy of better than $\sim 4\%$ is needed to distinguish the profiles and identify the shape of the mass profile accurately enough to obtain reliable parameters. Most weak lensing data is not yet of sufficient accuracy to rule out an NFW profile as a good representation of the mass distribution even if the mass distribution is in fact a Sérsic profile with low n.

In the analysis the contribution of baryons has been neglected – the results are therefore most applicable to massive systems, like clusters of galaxies where the dark matter dominates. Even though the results clearly show that for a range of Sérsic parameters, in particular for halos with low n (corresponding to the most massive halos), strong lensing data can not always be well reproduced by an NFW profile, the question which of the two mass distribution is in fact a better fit to the mass distribution in clusters is not addressed. However, the results from N-body simulations suggest (Merritt et al., 2005) that the Sérsic profile is a better fit, at least in the inner regions, which are also the regions probed by strong lensing. Even if the overall mass profile of clusters is often fit well by an NFW profile, the NFW profile may not reproduce the mass distribution in the inner part adequately. As demonstrated here, the sensitivity of the strong lensing properties on the form of the mass profile in that region then means that fitting an NFW profile to the lensing data will lead to rather meaningless parameters; the concentration parameters and masses of NFW profiles recovered in this way *can not* simply be compared to the values obtained in simulations. In this work the strong lensing properties of the Sérsic profile have been discussed, important lensing relations given, and a comparison made to the NFW profile for the first

time. The differences are important enough to warrant the inclusion of Sérsic profile for future analysis of strong lensing clusters.

4.5   Towards Analysing Real Systems

To facilitate the inclusion of the Sérsic profile in future analysis of real strong lensing systems, it has been incorporated into the publicly available lensing software Lenstool as an alternative description of the matter density (Jullo et al., 2007; Kneib, 1993). This is motivated by the results of this chapter and additionally by the fact, mentioned in § 4.1, that the Sérsic profile describes the 2D luminosity profile of elliptical galaxies and can therefore be used to separately model the baryonic matter component (assuming it traces the light) in elliptical lensing galaxies. Finally the Sérsic profile can be used to model spiral galaxies as the special case of $n = 1$ corresponds to an exponential disk.

The Sérsic 2D density profile has been included in the Lenstool software using the parameters (n, R_e, Σ_e) in addition to its redshift, position in the sky, position angle and ellipticity. The elliptical version of the profile is introduced using a pseudo-elliptical approximation developed by Golse & Kneib (2002). It is introduced in the expression of the circular potential by substituting R with $R_{\hat{\epsilon}}$, using the following elliptical coordinate system:

$$
\begin{aligned}
X_{\hat{\epsilon}} &= \sqrt{1 - \hat{\epsilon}} X \\
Y_{\hat{\epsilon}} &= \sqrt{1 - \hat{\epsilon}} Y \\
R_{\hat{\epsilon}} &= \sqrt{X_{\hat{\epsilon}}^2 + Y_{\hat{\epsilon}}^2} \\
\phi &= \arctan\left(Y_{\hat{\epsilon}}/X_{\hat{\epsilon}}\right)
\end{aligned}
$$

where $\hat{\epsilon} = (A^2 - B^2)/(A^2 + B^2)$, and A and B are the semi-major and semi-minor axis of the elliptical potential (see also Appendix B for a similar discussion for the Dual Pseudo Isothermal Elliptical Mass Distribution (dPIE)). Golse & Kneib (2002) then propose a generic expression to compute the elliptical deviation angle, convergence, shear and projected mass density from the elliptical lens potential $\Phi_{\hat{\epsilon}}(R) \equiv \Phi(R_{\hat{\epsilon}})$ which can be incorporated in a straightforward way into the lensing code. The advantage of using a pseudo-elliptical description is that it is

relatively simple and speeds up the calculations. However, the drawback is that it is only an approximation to the fully elliptical description and therefore only applicable for small values for the ellipticity. Golse & Kneib (2002) discuss these limits for the pseudo-elliptical-NFW profile, whereas Jullo et al. (2007) discuss it more specifically for the Sérsic profile.

The Sérsic profile in Lenstool has been compared further to the NFW and the dPIE profiles in Jullo et al. (2007) on simulated data of lensing clusters. These have shown that the parameters of a Sérsic profile may be harder to recapture than those of the other two profiles. The Sérsic profile has however not yet been applied to real lensing cluster as the description of the dark matter halo. There are plans to do so for the lensing cluster Abell 2218 although they have not yet been realised. The general lensing analysis of this cluster is presented in the next chapter.

Chapter 5

Where is the Matter in the Merging Cluster Abell 2218?

Who has seen the wind?
Neither you nor I:
But when the trees bow down their heads
The wind is passing by.
Christina Rossetti (1830-1894)

As mentioned previously in this thesis, lensing is ideal to probe the matter distribution of distant objects. This is because the lensing signal is sensitive only to the total mass and not its form, state or interactions. This chapter presents a strong lensing analysis of the mass distribution in the galaxy cluster Abell 2218. In addition to the lensing constraints, X-ray data and the distribution of the cluster galaxies in velocity space are studied to gain a better understanding of the matter distribution in the cluster and its history. This chapter is based on work previously published in Elíasdóttir et al. (2007).

5.1 Introduction

Dark matter dominates over baryonic matter in the universe, but its nature is not known. The study of the inner parts of dark matter halos can give insight into the nature of the dark matter, as the steepness of the profile is correlated

5. WHERE IS THE MATTER IN THE MERGING CLUSTER ABELL 2218?

with the interaction between the dark matter itself and with the baryonic matter. According to ΛCDM simulations, the mass distribution of galaxy clusters should be dominated by their dark matter halos. Gravitational lensing, which is sensitive to the total matter distribution, visible or dark, is ideal for studying the mass distribution of clusters. Strong lensing features, consisting of multiply imaged and strongly distorted background sources, provide constraints on the inner parts of the cluster, while weak lensing features, consisting of weakly distorted singly imaged background sources, provide constraints on the outer slope of the surface mass profile (see e.g., Abdelsalam et al., 1998; Bradač et al., 2006; Gavazzi & Soucail, 2007; Kneib et al., 1996; Limousin et al., 2007b; Natarajan et al., 2002b; Smail & Dickinson, 1995; Smail et al., 1997, 1995).

Lensing can therefore provide unique information about the total mass distribution of clusters, from the inner to the outer parts. In addition, lensing can in principle be used to deduce various cosmological parameters (e.g. H_0, Ω_Λ, Ω_m). This has already been extensively applied to lensing on galaxy scales (see e.g., Koopmans et al., 2003; Schechter et al., 1997) and to a smaller degree for lensing on cluster scales (see e.g., Meneghetti et al., 2005; Soucail et al., 2004), where the accuracy of the mass map is a limiting factor. The accuracy of the mass map is strongly dependent on the number of multiply imaged systems used to constrain it. Therefore, to construct a robust model of the dark matter distribution, accurate enough for cosmography and for using the cluster as a gravitational telescope, it is important to include as many spectroscopically confirmed multiply imaged systems as possible (see e.g., Ellis et al., 2001).

Abell 2218 is one of the richest clusters in the Abell galaxy cluster catalogue (Abell, 1958; Abell et al., 1989) and has been successfully exploited as a gravitational lens. A parametric lens model has previously been constructed by Kneib et al. (1996, 1995) (using 1 and 2 spectroscopically confirmed systems respectively) and by Natarajan et al. (2007, 2002b) (using 4 and 5 spectroscopically confirmed systems) building on the model of Kneib et al. (1996) and including weak lensing constraints from HST WFPC2 data. A non-parametric model was constructed by Abdelsalam et al. (1998) using three spectroscopically confirmed multiply imaged systems. In all of these models, a bimodal mass distribution was required to explain the image configurations (i.e. the models include two large

scale dark matter clumps), but the number of constraints were not sufficient to accurately constrain the second large scale dark matter clump. Abell 2218 has also been used as a gravitational telescope, with Ellis et al. (2001) discovering a source at $z = 5.6$ and Kneib et al. (2004a) discovering an even more distant source at $z \sim 6.7$, later confirmed by Egami et al. (2005) using Spitzer data. Soucail et al. (2004) estimated cosmological parameters based on a lensing model of Abell 2218 using 4 multiply imaged systems. The latest published lens model of Abell 2218 is by Smith et al. (2005), who incorporated four multiply imaged systems and weak lensing constraints, using the WFPC2 data. Although the number of constraints has increased from the initial models, all previous models have assumed that the location of the second dark matter clump coincided with the brightest galaxy in the South East, due to a lack of constraints in its vicinity.

The motivation for revisiting the modelling of Abell 2218 comes from the new ACS data which have not been used before for modelling this cluster and are superior in both resolution, sensitivity and field of view to the previous WFPC2 data set. These new high quality data have enabled the identification of several sub-components in previously known multiple images, thus adding more constraints, and in one case, two more multiple images of a known system. In addition, a spectroscopic redshift for has been measured for an arc around the second dark matter clump, which the model in this chapter predicts to be singly imaged. Several new candidate multiply imaged systems are proposed, which are added as constraints and their redshifts estimated with the model. In total there are 7 multiply imaged systems with measured spectroscopic redshift and 6 multiply imaged systems without spectroscopic data (of which 5 are new candidate systems). Finally, the lensing code Lenstool, has undergone significant improvements from previous models, with the incorporation of a Monte Carlo Markov Chain (MCMC), which enables it to not only find the best model in the lowest χ^2 sense, but the most likely model as measured by its Evidence (Jullo et al., 2007). The MCMC also allows for a reliable estimate of the uncertainties in the derived model parameters.

The chapter is organised as follows: A list of all currently known and new multiply imaged systems in Abell 2218 is compiled and the reliability of the redshift estimate of each one is discussed in § 5.2. The methodology of the strong

lensing modelling is described in § 5.3. In § 5.4 the results of the lensing analysis are presented and compared to previous models. In § 5.5 degeneracies in the modelling are discussed. In § 5.6 the reliability of the model is addressed, and the smoothness of the dark matter distribution discussed. In § 5.7 the bimodality of the model, along with X-ray measurements and an analysis of the distribution of cluster members in velocity space is interpreted. The main conclusions are summarised n § 5.8. Throughout the chapter, a flat Λ-dominated Universe is adopted with $\Omega_\Lambda = 0.7$, $\Omega_m = 0.3$ and $H_0 = 70$ km s^{-1} Mpc^{-1}. Following Smith et al. (2005) the cluster is placed at $z = 0.171$. At this redshift $1''$ corresponds to 2.91 kpc in the given cosmology.

5.2 Data and Multiply Imaged Systems

Data from several different sources are used for the lens modelling and analysis. They are presented in Appendix C. Multiply imaged systems are the basis of the analysis, and are particularly useful as constraints if their redshifts are accurately determined. In this section the multiple images, with or without spectroscopically confirmed redshifts, used as constraints in the lens modelling are listed. Several new candidate systems found in the ACS data are proposed. All systems are listed in Table 5.1 and shown on Figure 5.1.
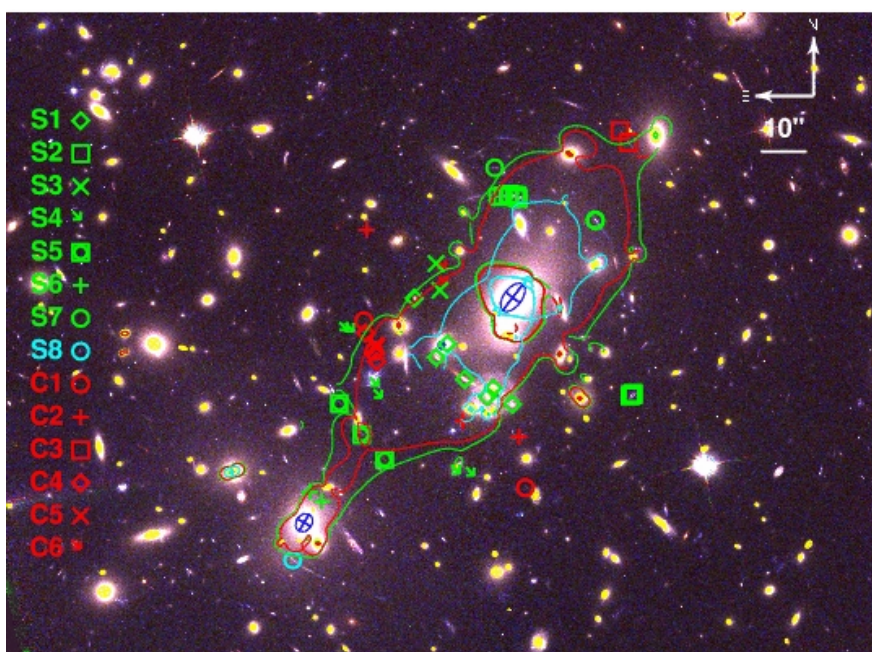
Figure 5.1 A colour image of Abell 2218 based on ACS data (F775W, F625W and F475W filters in the red, green and blue channel respectively). The cluster galaxies are marked in yellow (modelled using scaling relations) or blue (individually fitted). The multiple images are labelled in green for spectroscopically confirmed systems and red for candidate systems. The arc for which a spectroscopic redshift has been obtained, S8, is labelled in cyan. Also shown are the critical lines corresponding to $z = 0.702$ (cyan), $z = 2.515$ (red) and $z = 6.7$ (green).

5. WHERE IS THE MATTER IN THE MERGING CLUSTER ABELL 2218?

Table 5.1.   Lensed systems

System id	R.A (J2000)	Dec. (J2000)	$z^{\dagger}$	Comments
S1.a	248.96976	66.212219	0.702	(1)
S1.b	248.96646	66.208627	0.702	
S1.c	248.96478	66.209439	0.702	
S1.d	248.96218	66.207296	0.702	
S1.e	248.95876	66.206237	0.702	
S1.f	248.95790	66.206762	0.702	
S1.g	248.95500	66.205771	0.702	
S2.1.a	248.95540	66.218525	2.515	(2)
S2.1.b	248.95451	66.218469	2.515	
S2.1.c	248.93684	66.206345	2.515	
S2.2.a	248.95562	66.218536	2.515	
S2.2.b	248.95426	66.218458	2.515	
S2.2.c	248.93681	66.206424	2.515	
S2.3.a	248.95642	66.218428	2.515	
S2.3.b	248.95441	66.218347	2.515	
S2.3.c	248.93723	66.206355	2.515	
S2.4.a	248.95405	66.218258	2.515	
S2.4.b	248.95715	66.218375	2.515	
S2.4.c	248.93728	66.206269	2.515	
S3.a	248.96646	66.214324	5.576	
S3.b	248.96591	66.212701	5.576	
S4.1.a	248.97894	66.210224	2.515	
S4.1.b	248.97519	66.206897	2.515	
S4.1.c	248.96075	66.201462	2.515	
S4.2.a	248.97981	66.210279	2.515	
S4.2.b	248.97463	66.206179	2.515	
S4.2.c	248.96296	66.201575	2.515	
S5.a	248.981043	66.205816	2.515	(3)
S5.b	248.977680	66.203939	2.515	
S5.c	248.974235	66.202425	2.515	
S6.a	248.9855	66.200483	1.034	(4)
S6.b	248.98371	66.199906	1.034	
S7.a	248.94254	66.216974	1.03	(5)
S7.b	248.94244	66.216909	1.03	
S7.c	248.95763	66.220132	1.03	
S8.a	248.98805	66.19633	2.74	
C1.a	248.97735	66.210845	$\sim$6.7	(6)
C1.b	248.97585	66.208989	$\sim$6.7	
C1.c	248.95303	66.200703	$\sim$6.7	
C2.a	248.95398	66.203803	[2.6 $\pm$ 0.1]	
C2.b	248.96247	66.204748	[2.6 $\pm$ 0.1]	
C2.c	248.97692	66.216365	[2.6 $\pm$ 0.1]	
C3.a	248.93879	66.22238	[2.8 $\pm$ 0.6]	

Table 5.1 (cont'd)

System id	R.A (J2000)	Dec. (J2000)	$z^{\dagger}$	Comments
C3.b	248.93749	66.221662	$[2.8 \pm 0.6]$	
C4.a	248.97708	66.210108	$[2.2 \pm 0.2]$	
C4.b	248.97542	66.208369	$[2.2 \pm 0.2]$	
C5.a	248.97543	66.209244	$[2.3 \pm 0.8]$	
C5.b	248.97556	66.209383	$[2.3 \pm 0.8]$	
C6.a	248.96481	66.213039	$[2.6 \pm 0.3]$	
C6.b	248.96505	66.214017	$[2.6 \pm 0.3]$	

Note. — The multiply imaged systems used to constrain the model. The systems and their properties, along with references to the papers reporting their redshifts, are given in Section 5.2. Systems C2-C6 are new candidate systems reported in this chapter. Systems with a spectroscopic redshift measurement are denoted by an S in their id, while those without spectroscopic redshifts are denoted by a C. Roman letters (a,b,c,...) denote the different images of each set of multiple images. If several components are identified in system, each component is sub-labelled, e.g. 2.1 and 2.2 denote two different components of the same multiple imaged system. (1) Two pairs of images are caused by splitting by a local cluster galaxy. (2) Also known in the literature as #384 and #486. (3) The redshift is measured for an associated singly imaged galaxy (4) Also known in the literature as #289 (5) Also known as #444 and H6. The redshift estimate is based on one feature. (6) Redshift estimate based on photometric redshift, lensing and a tentative Lyα break.

†Lens model redshift predictions are reported in square brackets.

5.2.1 Previously known systems

The first system, system S1, is at a redshift of $z = 0.702$ as measured by Le Borgne et al. (1992) (system 359 in their catalogue). Thanks to the new ACS observations, it has seven identified images (previously it had five identified images (Kneib et al., 1996)), of which two pairs are located close to individual galaxies #1028 and #993 in the galaxy catalogue) which affect the lensing signal.

System S2 is a star-forming galaxy at a redshift of $z = 2.515$ (Ebbels et al., 1996). It consists of a fold and a counter image (listed as images #384 and #468 in Ebbels et al. (1996)). The fold image is separated into two images and four components identified, giving four sets of triple images from this system (referred to as S2.1, S2.2, S2.3 and S2.4).

5. WHERE IS THE MATTER IN THE MERGING CLUSTER ABELL 2218?

System S3 is a faint star-forming doubly imaged system at a high redshift $z = 5.576$ discovered by Ellis et al. (2001).

System S4 is a triply imaged submillimeter source at $z = 2.515$ reported by Kneib et al. (2004b). In each image they identify three components labelled α, γ, β. All three images are identified in the ACS data. However, only the α and β components are detected. Both are included as constraints on the model (referred to as S4.1 and S4.2 respectively). Image S4.1 seems to consist of further three subcomponents. As they are not clearly distinguish in all three images, they are not added as separate constraints.

The fifth system, S5, is a triply imaged system, believed to be the triply imaged outskirts of an associated singly imaged galaxy. It is believed that the galaxy partially crosses the caustic, with the central part being singly imaged and the outskirts being triply imaged. Kneib et al. (2004a) measured a redshift of $z = 2.515$ for the galaxy (labelled as #273 in their notation) but an independent spectroscopic redshift has not been determined for the faint triply imaged component. Although it is likely (and consistent with the models) that they belong to the same background source, it is not certain, making the redshift determination for S5 less certain.

The sixth system, S6, consists of an arc in two parts at $z = 1.034$ (Kneib et al., 1996; Swinbank et al., 2003, called 289 in their notation).

The seventh system, S7, first reported by Kneib et al. (1996), consists of a merging image and a counter image (also known as #444 and H6 respectively). Ebbels et al. (1998) measured a spectroscopic redshift at $z = 1.03$ for the merging image but this is listed as a tentative identification (as the only identified feature in the spectra was the Fe II doublet at $\lambda\lambda 2587, 2600$).

The final previously known multiply imaged system, C1, is a high redshift ($z \sim 7$) triply imaged system (Kneib et al., 2004a). Egami et al. (2005) further constrained the redshift of the system to lie in the range $6.6 - 6.8$. For the purposes of the modelling $z = 6.7$ is assigned to this system, noting that changing the redshift within the range $6.6 - 6.8$ does not affect the model.

5.2.2 New candidate systems and a spectroscopic redshift for an arc

A total of 5 new candidate systems are proposed which are identified in the new ACS data. There are no spectroscopic redshift determination for these systems, but their redshifts are estimated using the model prediction.
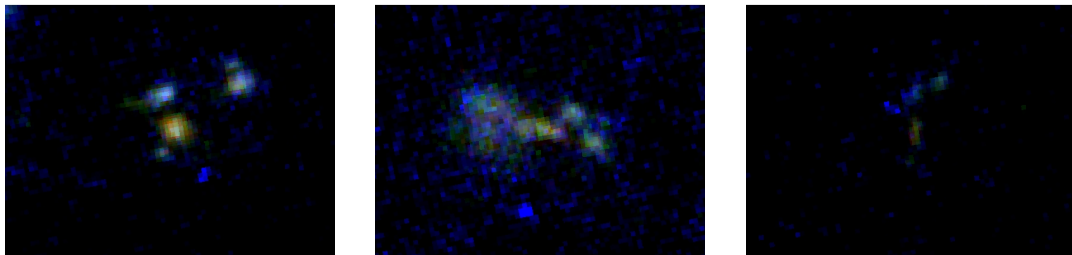
Figure 5.2 The new candidate system, C2, identified in the ACS images. The three panels show the three images of C2, marked in Figure 5.1. The colours are the same as in Figure 5.1. The system is characterised by a central 'yellow' spot, flanked by blue spots.

The first candidate is a triply imaged system, called C2. Figure 5.2 shows colour stamps of the three images, and the locations are given in Table 5.1. The morphology of the three images, suggests that it is of the same background source, with a 'yellow' spot in the middle, flanked by a fainter blue on the sides.

A new faint arc is identified in the north-west part of the cluster, called C3 (see Figure 5.3). In the vicinity of system 6, two arclike images are identified, which are labelled C4 and C5. The first, C4, is a very faint blue double arc, while in the second, C5, two bright spots of a merging arc can be seen. Finally, a pair of blue extended images, C6, is found in the vicinity of system 3. These candidate systems are shown in a colour image in Figure 5.3 and are listed in Table 5.1 along with their redshift estimates (see § 5.4.4 for details). The positions of these images are used to constrain the final model, but their redshift is kept free in the modelling.
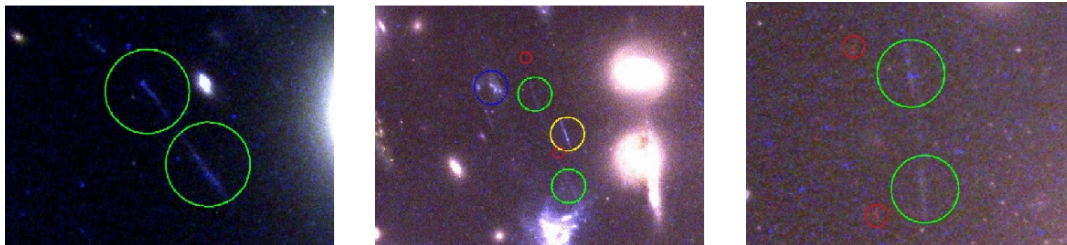
Figure 5.3 The new candidate arcs identified in the ACS images. *Left panel:* The candidate arc C3 (green circles). *Middle panel:* The candidate systems C4 (green circles) and C5 (yellow circle). The red circles are the locations of two of the images of system C1 (at $z = 6.7$), while the blue circle shows the location of images belonging to system S4 (components a and b). *Right panel:* The candidate system C6 (green circles). The high redshift system S3 ($z = 5.6$) is marked with red circles.

A spectroscopic redshift for an arc, S8 was also obtained (see Appendix C for details), showing it to be at $z = 2.74$.

5.3 Modelling

Following e.g., Kneib et al. (1996); Limousin et al. (2007b); Smith et al. (2005) a parametric mass reconstruction of Abell 2218 is performed. The multiply imaged systems form the basis of the analysis, with each n-tuply imaged system giving $2(n-1)$ constraints if the redshift is known. As the number of constraints needs to be greater than the number of free parameters in the fit, the number of known multiply imaged systems limit the complexity of the model. The MCMC sampling and optimisation is done using the Lenstool software (Jullo et al., 2007; Kneib, 1993). The optimisation is performed in the source plane, as it is faster and has been found to be equivalent to optimising in the image plane (Halkola et al., 2006; Jullo et al., 2007). The new version of Lenstool (Jullo et al., 2007), gives a distribution of values for each of the parameters, thus making it possible to estimate the uncertainty of the parameters. In addition, it returns the Evidence

of a model, which is a measure of how likely a model is, penalising unnecessarily complicated models. Thus, a model with a lower χ^2 but more free parameters, may have a lower Evidence, suggesting that one should choose the simpler model. For each image its rms (root-mean-square) value for its position in the source plane, rms_s, and image plane, rms_i, is found given by

$$\mathrm{rms}_s \;=\; \sqrt{\frac{1}{n}\sum_{j=1}^{n}\left(X_s^j - <X_s^j>\right)^2} \tag{5.1}$$

$$\mathrm{rms}_i \;=\; \sqrt{\frac{1}{n}\sum_{j=1}^{n}\left(X_{\mathrm{obs}}^j - X^j\right)^2} \tag{5.2}$$

where n is the number of images for the system, X_s is the position in the source plane, X the position in the image plane and X_{obs} the observed position in the image plane. The overall rms is defined by summing and averaging over all the images for all the systems. A detailed overview of the Lenstool software, including definitions of χ^2 and the Evidence, can be found in Jullo et al. (2007).

5.3.1   Model components

The individual components of the model are referred to as 'clumps', where each clump is denoted by its position, ellipticity, position angle and the parameters of the profile used to describe it. The parametric profile used is the dual Pseudo Isothermal Elliptical mass distribution (dPIE, derived from Kassiola & Kovner (1993b)) and its form and main properties are given in Appendix B. The dPIE profile is defined in Lenstool by three parameters, the core radius a, the scale radius s and a fiducial velocity dispersion σ_{dPIE}. For $a < r < s$, the profile behaves as $\rho \sim r^{-2}$, while it falls like r^{-4} in the outer regions. For a vanishing core radius the scale radius corresponds to the radius containing half the 3D mass.

The clumps are called 'large scale clumps' if their mass within the outermost multiply imaged constraint is greater than 20% of the total mass. Smaller clumps are referred to as 'galaxy scale clumps', and are in general associated with the cluster members. Large scale dark matter clumps are optimised independently. The redshift is fixed at the location of the cluster, but the central position (R.A., Dec.), the ellipticity and the position angle (P.A.) are allowed to vary.

A galaxy scaled clump is associated with each of the cluster galaxies, fixing the central location, ellipticity and position angle of the mass distribution to that of the light distribution. A few of the cluster galaxies are fitted individually (optimising their a, s and σ_{dPIE}, see Table 5.2 for an overview), but due to a lack of constraints, most of the galaxies are optimised in a combined way. The parameters $(a, s, \sigma_{\mathrm{dPIE}})$ are optimised together using the following scaling relations for the luminosity L:

$$a = a^{\star} \left(\frac{L}{L^{\star}} \right)^{1/2} \tag{5.3}$$

$$s = s^{\star} \left(\frac{L}{L^{\star}} \right)^{1/2} \tag{5.4}$$

$$\sigma_{\mathrm{dPIE}} = \sigma_{\mathrm{dPIE}}^{\star} \left(\frac{L}{L^{\star}} \right)^{1/4}. \tag{5.5}$$

A discussion of these scaling relations can be found in Limousin et al. (2007b) and Halkola et al. (2007). For a given $L^{\star}$ luminosity, $a^{\star} = 0.25$ kpc is fixed, while $\sigma_{\mathrm{dPIE}}^{\star}$ and $s^{\star}$ are allowed to vary. Fixing the core radius to be small, makes the profile approximately equivalent to the profile used by Brainerd et al. (1996) to describe galaxies (see also Appendix B). Following de Propris et al. (1999) the apparent magnitude of an $L^{\star}$ in the K-band is taken to be $K^{\star} = 15$ at $z = 0.171$ (redshift of Abell 2218).

5.4   The Strong Lensing Mass Distribution

In this section the strong lensing model (optimised in the source plane) is presented, its implications discussed and a comparison is made to previous results. All reported error bars correspond to 68% confidence levels. For the best model an rms$_s$ = 0.″12 is found, which gives rms$_i$ = 1.″49 (see Table reftab:chires).[1]

---

[1] A parameter file containing all the following information, and which can be used with the Lenstool software package, along with a FITS file of the mass map generated from the best-fit model are available at `http://archive.dark-cosmology.dk/`. These can be used to find relevant critical lines for using Abell 2218 as a gravitational telescope and to predict/confirm candidate lensed systems.

Table 5.2.   Model parameters

Clump	Δ R.A. $''$	Δ Dec. $''$	$\hat{\epsilon}$	$\theta_{\hat{\epsilon}}$	σ_{dPIE} (km/s)	a $('')$	s $('')$
DM1	$3.9^{+0.3}_{-0.4}$	$23.1^{+1.7}_{-0.7}$	$0.033^{+0.03}_{-0.001}$	56^{+6}_{-6}	806^{+10}_{-10}	26^{+1}_{-1}	274^{+110}_{-4}
DM2	$-20.4^{+0.1}_{-0.6}$	$-23.1^{+0.6}_{-0.6}$	$0.39^{+0.01}_{-0.01}$†	8^{+1}_{-2}	1029^{+13}_{-49}	44^{+2}_{-3}	462^{+85}_{-60}
1193 (BCG)	-0.5	0.07	0.46	52.4	514^{+7}_{-11}	$3.14^{+0.04}_{-0.45}$	56^{+12}_{-8}
617	-46.1	-49.1	0.20	59.4	288^{+7}_{-8}	$2.5^{+0.3}_{-0.5}$	87^{+10}_{-9}
1028	-16.0	-10.3	0.18	80.4	396^{+13}_{-128}	$0.3^{+0.2}_{-0.1}$	$0.6^{+0.5}_{-0.1}$
					$\sigma^{\star}_{\mathrm{dPIE}}$ (km/s)	$a^{\star}$ $('')$	$s^{\star}$ $('')$
L* galaxy	$\cdots$	$\cdots$	$\cdots$	$\cdots$	185^{+10}_{-11}	0.09	$2.9^{+0.5}_{-0.3}$

Note. — Values quoted without error bars were kept fixed in the optimisation. The error bars correspond to 68% confidence levels. The location and the ellipticity of the matter clumps associated with the cluster galaxies were kept fixed according to the light distribution. The centre is defined at (R.A., Dec.)=(248.9546, 66.2122) in J2000 coordinates.

†The posterior probability distribution pushes towards the highest values of our input prior. Therefore these error bars do not represent the full uncertainty in the value, but the uncertainty given a prior of $\hat{\epsilon} < 0.4$

5.4.1   A bimodal mass distribution

The mass density model is shown in Figure 5.4 and critical lines predicted by the model at $z = 0.702, 2.515, 6.7$ in Figure 5.1. The total projected mass as a function of radius, centred on the BCG, is shown in Figure 5.5. The mass distribution is strongly preferred to be bimodal, even for a simple model where all the galaxies are modelled based on the scaling relations, but the dark matter clumps are optimised independently using only systems 1 and 2 as constraints (28 constraints in all). The second dark matter clump is located to the south east of the central clump for this simple model, near galaxy #617, which is in agreement with previous models of Abell 2218. The bimodal mass distribution is also strongly preferred with more constraints. The two large scale dark matter clumps will be referred to as DM1 (for the one associated with the BCG) and DM2 (for the one associated with galaxy #617). A three clump model was also constructed, but its bayesian Evidence was worse, leading us to reject it as the best model.

Table 5.3.   Goodness of the fit

System	χ^2	rms$_s$ ($''$)	rms$_i$ ($''$)
S1	21.7	0.171	0.60
S2.1	10.0	0.090	0.60
S2.2	11.8	0.098	0.82
S2.3	37.9	0.167	1.49
S2.4	55.8	0.197	2.17
S3	4.9	0.043	0.57
S4.1	9.8	0.089	0.53
S4.2	2.1	0.042	0.43
S5	15.6	0.060	4.61
S6	0.3	0.016	0.03
S7	8.4	0.052	1.45
S8	0.0	0.000	0.00
C1	13.4	0.102	1.26
C2	20.5	0.178	0.63
C3	17.5	0.122	1.64
C4	4.7	0.052	0.70
C5	0.2	0.009	0.27
C6	0.5	0.011	0.14
	χ^2/d.o.f.	rms$_s$	rms$_i$
Full model	235.1/34	0.12	1.49

Note. — The χ^2 and rms in the source plane (where the model is optimised) and the image plane. The zero values found for S8 mean that the system is consistent with being singly imaged.
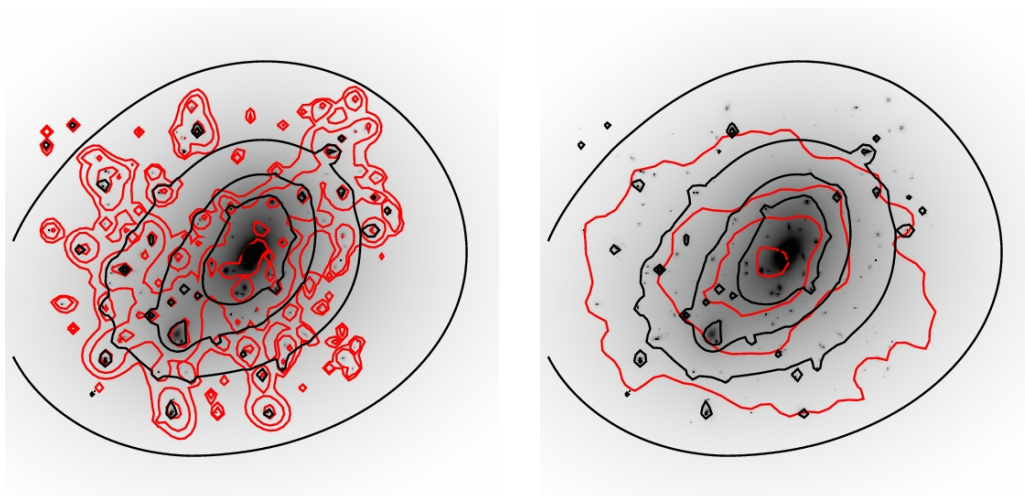
Figure 5.4 The mass density map and its contours (black). The maps are $300'' \times 300''$ and centred on the BCG with North being up and East being left. The red contours show the light distribution (left panel) and the X-ray distribution (right panel). The overall shape of the light-contours and the mass map contours are similar, with the light being slightly more 'pear'-shaped, as it broadens in the SE direction. The overall shape of the light-contours and the mass map contours also agree, although the X-rays become more spherical for in the outer regions. See § 5.7.
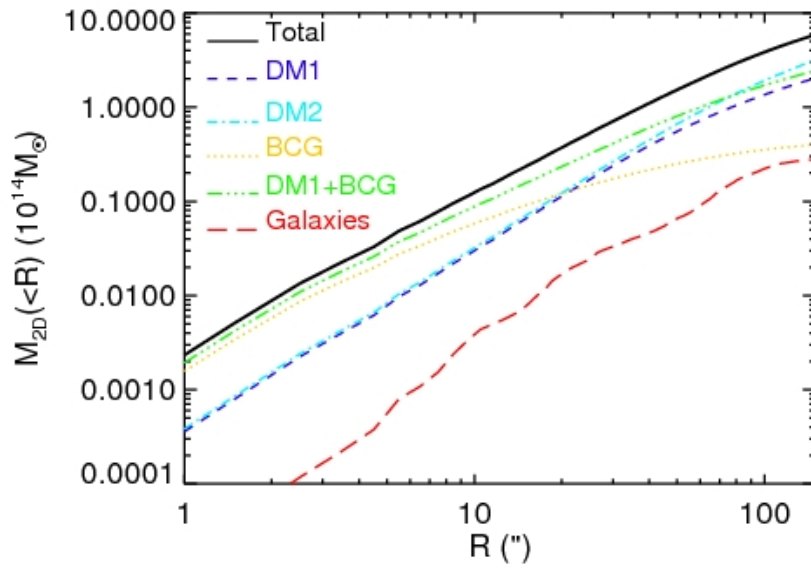
Figure 5.5 Total projected mass as a function of aperture radius (centred on the
BCG) for different model components. The two large scale clumps, DM1 and
DM2, contribute a similar amount to the mass, but the halo associated with the
BCG dominates in the inner regions, and the combined halo of DM1 and the
BCG dominates the mass in the region where most of the constraints lie (within
$80''$). The galaxies (excluding the BCG) only contribute a small amount to the
overall mass, of the order of $5 - 6\%$.

In previous models, the location of the second clump has been fixed at the centre of the brightest galaxy in the south east corner (#617), but it is found that when the location is allowed to vary it is offset from this galaxy by $\sim 35''$. It is also found that DM2 has high ellipticity and is comparable in mass to DM1, although significantly less massive than the DM1 and BCG halos combined (see Figure 5.5). The light distribution is similar to the derived matter distribution (see Figure 5.4), supporting the finding that there is a significant matter component in the vicinity of DM2 (see also § 5.7).

5.4.2   Dark matter halos of galaxies

The potential contribution of the individual dark matter halos associated with cluster galaxies was first proposed by Natarajan & Kneib (1997). Typically it is found that contribution of dark matter halos associated with the bright, early-type cluster galaxies in the inner regions are required to explain the positions and geometries of multiply lensed images in the strong lensing regime (Meneghetti et al., 2007).

Three galaxies are fit individually (for the parameters of these galaxies see Table 5.2), two are the brightest galaxies near the centres of the large scale dark matter clumps (#1193 - the BCG - and #617), while the third is an elliptical galaxy important to the lensing of system S1. The halo associated with the BCG is very massive, and in particular in the inner $10''$ it dominates the mass distribution (see Figure 5.5). Even at the outermost Einstein radii of a multiply imaged system ($80''$) it still contributes around 10% of the mass of the cluster.

System S1 has seven images, and two of the pairs are strongly affected by nearby galaxies (an elliptical #1028 and a spiral #993). Keeping the parameters of the spiral free did not significantly affect the model, while adding the elliptical did. Although both galaxies would at first glance appear equally important to be fitted individually due to their strong effects on system S1, Figure 5.6 provides an important insight to why only #1028 needs to be included individually. This is because the scaling relations (see § 5.3.1) assume that the galaxies follow a Faber-Jackson relation (Equation 5.5) without any scatter. As can be seen from Figure 5.6 and discussed in Ziegler et al. (2001) the galaxies in Abell 2218 show
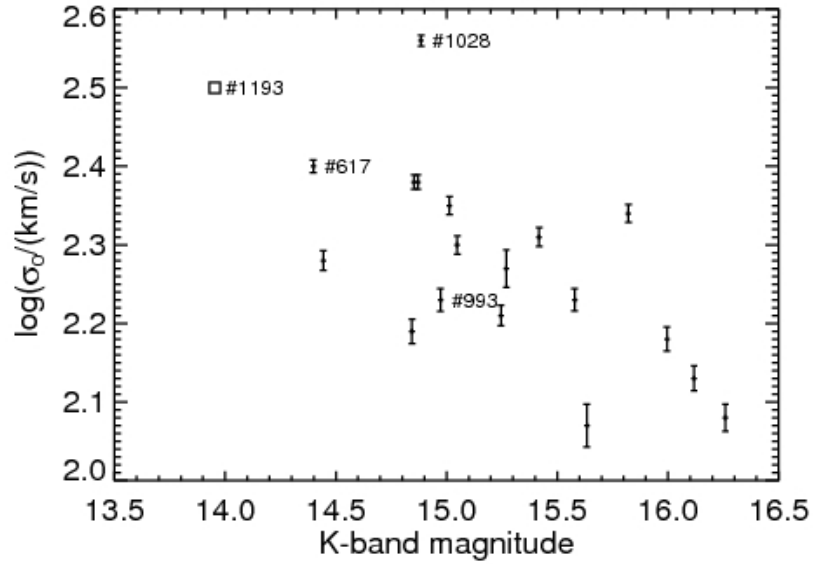
Figure 5.6 The Faber-Jackson relation for the K-band using σ_0 measurements from Ziegler et al. (2001). Also plotted is the central velocity dispersion of the BCG (#1193) as obtained by Jørgensen et al. (1999). The individually marked galaxies are discussed in § 5.3.1 and 5.4.2.

a significant scatter and therefore the above scaling relations can give very unrealistic values for individual galaxies which lie far from the mean behaviour. The elliptical #1028 is one such galaxy, with a measured central velocity dispersion which is greater than the central velocity dispersion of the BCG as measured by Jørgensen et al. (1999), while #993, although a spiral galaxy, is more consistent with the mean.

For the other cluster galaxies, they are included in the model via the scaling relations given in § 5.3.1. For $L^\star$ corresponding to $K = 15$ at $z = 0.171$, $\sigma_{\mathrm{dPIE}}^\star = 185^{+10}_{-11}$ km s^{-1} and $s^\star = 2\rlap{.}''9^{+0.5}_{-0.3}$, but there is some degeneracy between the two values (see discussion in § 5.5).

5.4.3 Comparison with measured velocity dispersions

Velocity dispersion measurements, σ_0, of Ziegler et al. (2001) and Jørgensen et al. (1999) for Abell 2218 are used to compare with the results from the lens model. Ziegler et al. (2001) have a total of 48 galaxies in their sample, of which nearly half fall within the ACS image and are included in the galaxy catalogue, while the Jørgensen et al. (1999) data contains the BCG and seven other cluster members in the galaxy catalogue. Using the velocity dispersion measurements for Abell 2218 cluster members from Ziegler et al. (2001) the Faber-Jackson relationship for the K-band data is plotted in Figure 5.6. The mean and the standard deviation of galaxies with K-band magnitudes in the range from 14.8 to 15.2 are calculated, excluding the individually fitted galaxy (galaxy #1028 in the catalogue, or #1662 in the notation used by Ziegler et al. (2001)). This gives $\sigma_{0,ziegler}^\star \approx 195\pm35$ km s^{-1} for a typical K=15 galaxy.

In Figure 5.7 σ_0 from Ziegler et al. (2001) and Jørgensen et al. (1999) vs. the fiducial velocity dispersion, σ_{dPIE} for the BCG, the two individually fitted galaxies and L^* is plotted. Although the values from direct velocity dispersion measurements can not be directly related to the values obtained from the dPIE profile (as the measured values are calculated based on an isothermal profile and are not aperture corrected) it is found that they are consistent with σ_{dPIE} being related to the measured velocity dispersion by $\sigma_0 \approx 0.85\sigma_{\mathrm{dPIE}}$ as found in § B.7.
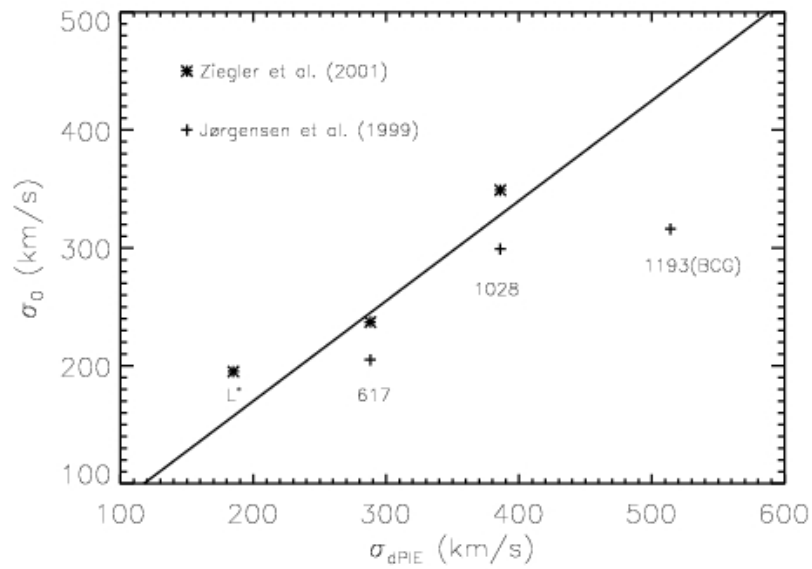
Figure 5.7 The velocity dispersion of the dPIE, σ_{dPIE} vs. σ_0 measurements from Ziegler et al. (2001) and Jørgensen et al. (1999). The line is not a fit, but shows the relationship $\sigma_0 = 0.85\sigma_{\mathrm{dPIE}}$ found in § B.7.

5.4.4 Redshift estimates of the new candidate systems

The redshifts of the new candidate systems are estimated using the model predictions. The three component candidate system C2 is found to have $z = 2.6 \pm 0.1$. For the merging arcs the model gives $z = 2.8 \pm 0.6$ for C3, $z = 2.2 \pm 0.2$ for C4, $z = 2.6 \pm 0.3$ for C6 while C5 is poorly constrained with $z = 2.3 \pm 0.8$. The estimated redshifts are reported in Table 5.1. These redshifts are consistent with a preliminary photometric redshift analysis done using the Hyperz photometric redshift code (Bolzonella et al., 2000).

5.4.5 A strongly lensed galaxy group at z=2.5

Three multiply imaged systems, S2, S4 and S5, all have the same redshift of $z = 2.515$. To check whether these three systems belong to a background galaxy group, they are lensed back to their source plane (see Figure 5.8).

It is found that S4 is in the middle with S5 and S2 at a separation of $5\overset{''}{.}4$ and $10\overset{''}{.}3$ respectively, with the maximum separation being $15\overset{''}{.}7$, corresponding to 127 kpc in the source plane ($1'' = 8.06$ kpc at $z = 2.515$), suggesting that the three systems belong to the same background group of galaxies. This is in agreement with the findings of Kneib et al. (2004b) who found the maximum separation of the systems in the source plane to be 130 kpc. It may be of interest to do a dedicated search for more systems at $z = 2.515$, either multiply imaged or singly imaged, to further study this high redshift group of galaxies, and it should be noted that all the candidate systems have a predicted z consistent with $z = 2.515$. If one assumes that these candidate systems have $z = 2.515$, their location in the source plane is consistent with them belonging to this same group (see Figure 5.8).

5.4.6 Comparison with previous results and weak lensing

Although the overall results of the model are in agreement with previous models of Abell 2218, previous models have found the second clump to be less massive (see e.g., Abdelsalam et al., 1998; Kneib et al., 1996; Natarajan et al., 2007; Smith et al., 2005). There are several possible reasons for the discrepancy, with the first
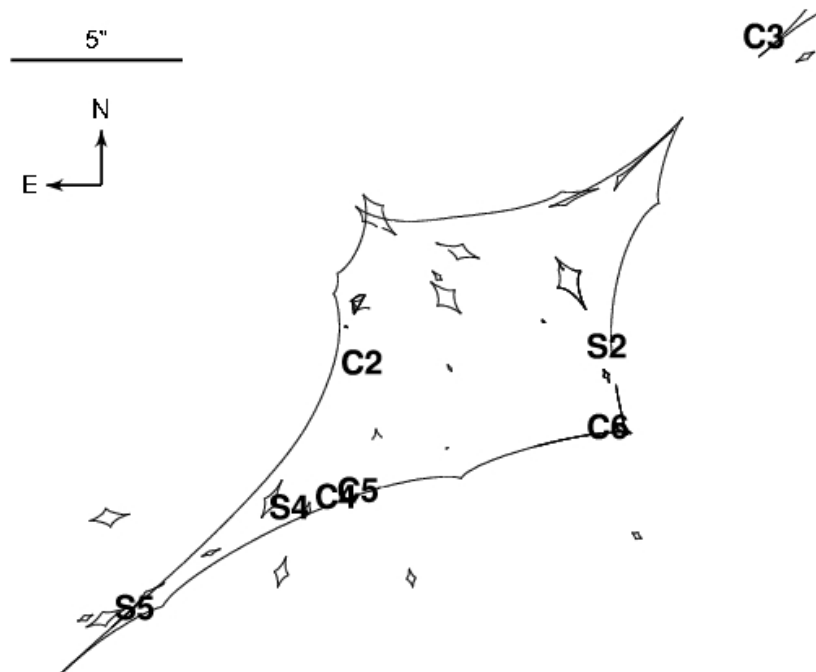
Figure 5.8 A plot of the source plane at $z = 2.515$ showing systems S2, S4 and S5 and the caustic lines. Their maximum separation is around 130 kpc, consistent with them belonging to the same group of galaxies. Also shown are the candidate systems C2, C3, C4, C5 and C6 when their redshift is assumed to be $z = 2.515$. Under that assumption, their locations are consistent with them also belonging to this group of galaxies.

one being the new constraints used in this model. The modelling has therefore been redone using only the previously known spectroscopically confirmed systems, but it is still found that DM2 is massive and with a large core. It is also possible, that the previous models constructed using the older version of the lenstool package which did not involve MCMC sampling, have been caught in local minima. Indeed, when forcing DM2 to be smaller, a comparable χ^2 is found but with the posterior probability distribution of the core radius a pushing toward the upper limit of the input range. However, this can not explain the discrepancy found for the non-parametric model of Abdelsalam et al. (1998).

A third possible explanation is that the models of Abdelsalam et al. (1998); Natarajan et al. (2007); Smith et al. (2005) all incorporated weak lensing to 'anchor' the outer part of the mass distribution. Using the model to predict the weak lensing shear profile at large radii, it is found that the profile overestimates the signal compared to the measured signal of Bardeau et al. (2007) from ground based observations with the Canada-France-Hawaii Telescope (see Figure 5.9). The central part of the Bardeau et al. (2007) profile is flat, characteristic of contamination of the background galaxy catalogue by foreground cluster members (see Limousin et al. (2007b) for discussion on contamination). Therefore, an agreement between the weak lensing result and the strong lensing result is not expected. At around $\sim 300 - 400''$ the contamination should be negligible, and there a better agreement is found although the model still overpredicts the signal (although they are consistent within 2σ). It should be stressed however that at this radius, the strong lensing model based on constraints within $100''$ is being extrapolated, and the prediction becomes more uncertain the further out one goes.

5.5   Degeneracies

In § 5.4 the strong lensing model of Abell 2218 was presented. In this section the degeneracies of the parametric strong lensing modelling are discussed, both those inherent to the parametric profile and the model components. Jullo et al. (2007) have also discussed the various degeneracies of the dPIE profile in lensing, addressing how different image configurations can break some degeneracies.
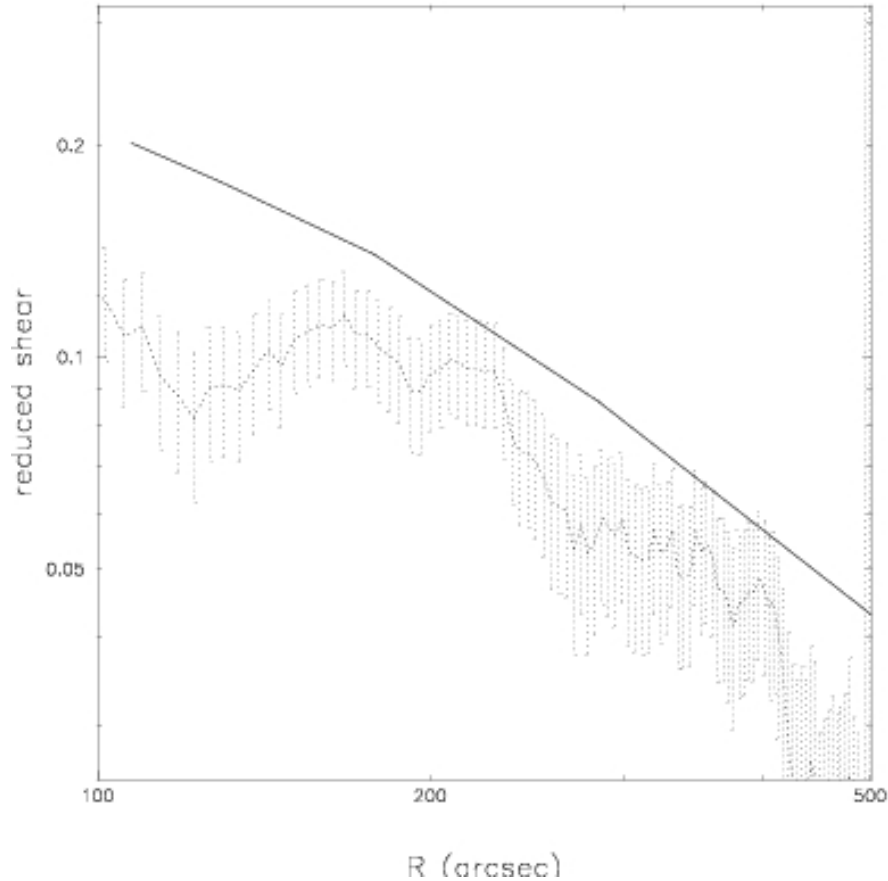
Figure 5.9 The weak lensing signal predicted by the model (solid line) compared to the weak lensing found by Bardeau et al. (2007) (dotted line - 1σ error bars). The Bardeau et al. (2007) shows a very flat inner profile, characteristic of contamination of the background galaxy catalogue by cluster members. Therefore, an agreement is not expected in the inner regions. In the outer regions, where the contamination should be negligible, the model overpredicts the weak lensing signal, but it should be noted that the prediction is an extrapolation of a strong lensing model with constraints within $100''$.

Lensing most strongly constrains the projected mass, and therefore one expects to see degeneracies arising from Equation B.10, although ellipticity may complicate that picture further. In agreement with Jullo et al. (2007) it is found for the large scale halos, that the scale radius, s, is poorly constrained (as it lies beyond the outermost multiply imaged system). This is also the case for the BCG and the #617 which have large scale radii. For the smaller halos, i.e., the scaled galaxies and #1029, the scale radius, s, is small enough to affect the projected mass, and one finds that lower s requires higher σ_{dPIE} to keep the mass constant (see Figure 5.10). However, the favoured region for s is always small, consistent
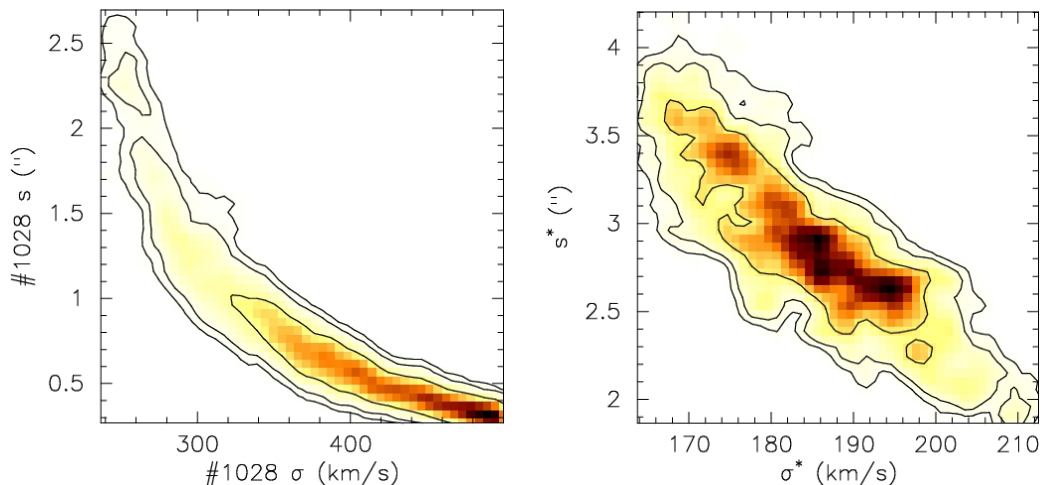
Figure 5.10 The degeneracy between the scale radius, s, and σ_{dPIE} for #1028 (left) and the scaled galaxies (right). These arise from equation B.10 which gives the aperture mass, showing that to keep the enclosed mass constant, an increase in the scale radius requires a lower value of σ_{dPIE}. The contours correspond to 1σ, 2σ and 3σ confidence levels.

with the tidal stripping of cluster galaxies proposed by Limousin et al. (2007a,c); Natarajan et al. (2002a, 1998, 2002b).

Also, in agreement with Jullo et al. (2007), and as discussed by e.g. Kochanek (1996) for more general cored profiles, a larger core radius, a, requires higher σ_{dPIE} to keep the mass constant (see Figure 5.11). As the model has both a large core radius a and σ_{dPIE} for DM2 compared to previous models of A2218, it has been
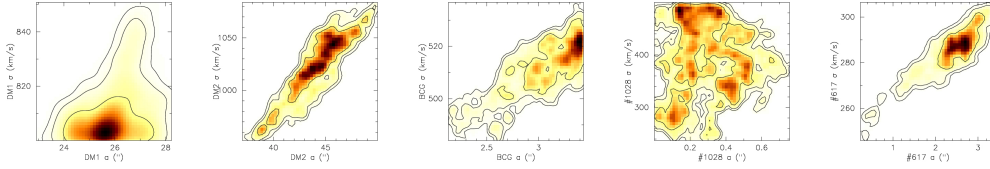
Figure 5.11 The degeneracy between the core radius, a, and σ_{dPIE} for DM1, DM2, BCG, #1028, #617 from left to right. These again arise from Equation B.10 requiring the aperture mass to remain constant. They show that to keep the mass constant, the σ_{dPIE} must increase when the core radius a is increased. This is consistent with the findings of Jullo et al. (2007) for the dPIE profile and the findings of Kochanek (1996) for more general profiles with core. The contours correspond to 1σ, 2σ and 3σ confidence levels.

explored whether this degeneracy can reduce both values. However, when forcing both a and σ_{dPIE} to be smaller, the posterior distribution of a always pushes to the upper limit of the input range. Therefore, the conclusion drawn is that this degeneracy is not the explanation for the high a and σ_{dPIE} found for DM2. This flat profile is further supported by the 'blind tests' performed in § 5.6.3.

In addition to the degeneracies associated with the profile itself, there may be degeneracies associated with the components included in the model, i.e., are all the components necessary and are they independent of each other? As mentioned in § 5.4.1, the model is strongly preferred to be bimodal. There is however degeneracy between the parameters of DM1 (and the BCG) and DM2 which is visualised in Figure 5.12. As for the BCG, the Evidence is found to be marginally higher when both the DM1 and BCG are included in the model, suggesting that the data are sufficient to model both separately. Therefore, although the model prefers the inclusion of all three components, the values for their parameters are not fully independent. Finally, the parameters for the scaled galaxies are studied with respect to DM1 and DM2 (see Figure 5.13). Although there is degeneracy the preferred value, in particular for the scale radius $s^{\star}$, is well constrained at low values ($\lesssim 4''$), consistent with the tidal stripping scenario.
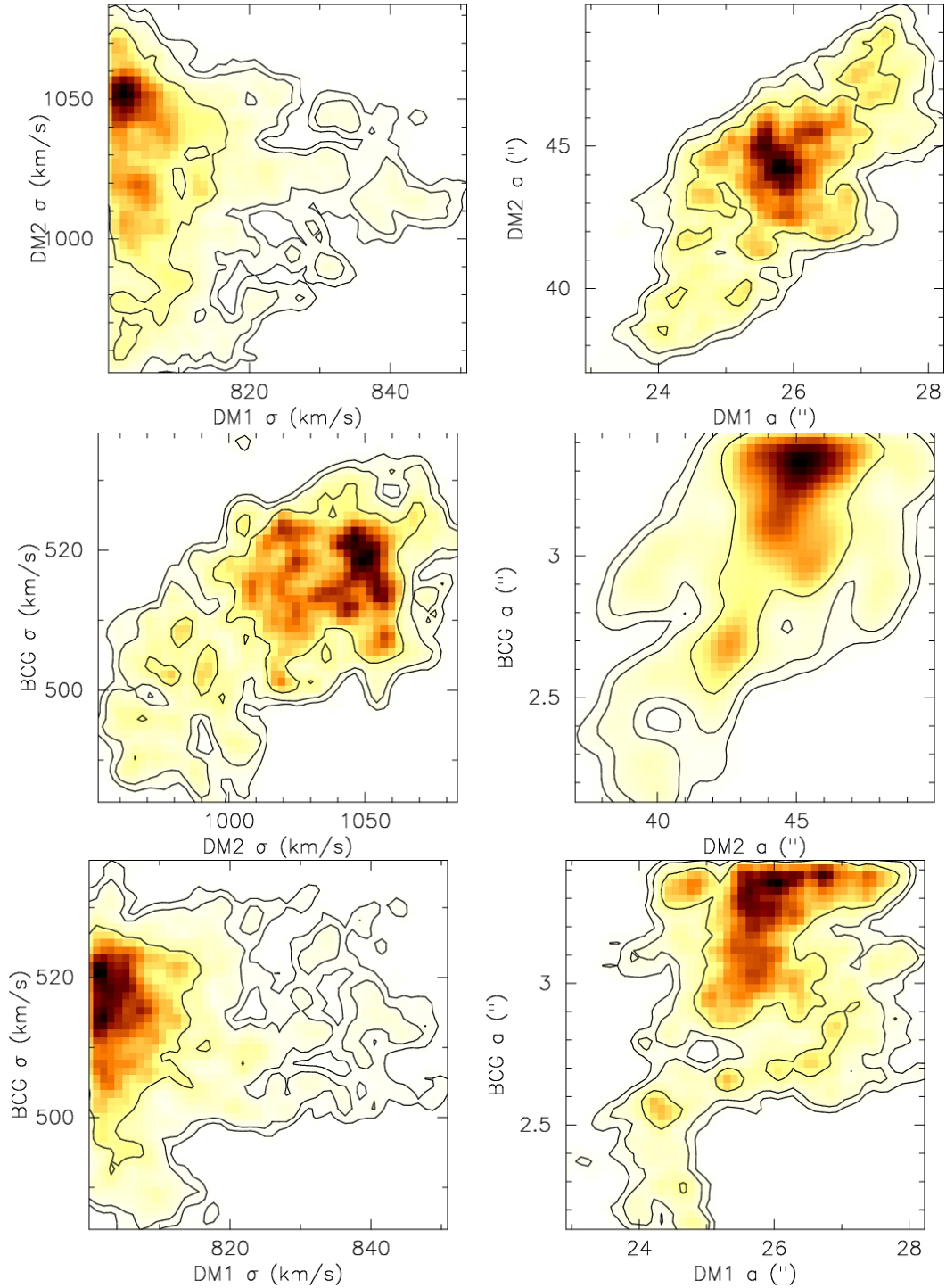
Figure 5.12 The 2D posterior distribution of the parameters of DM2 vs. DM1 and BCG. There is a clear degeneracy between the parameters of the two large scale components and the BCG. Therefore, although the model prefers the inclusion of all the components, the values of their parameters are not fully independent. The contours correspond to 1σ, 2σ and 3σ confidence levels.
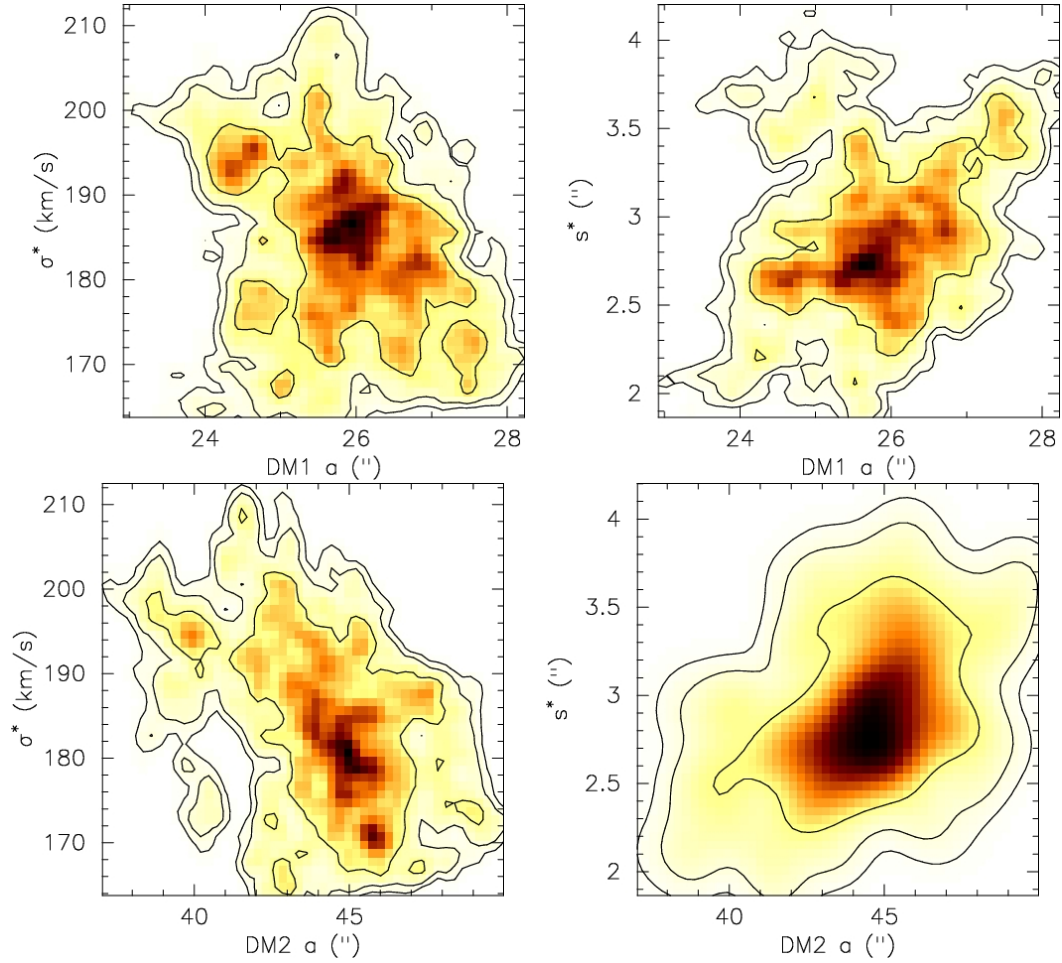
Figure 5.13 The 2D posterior distribution of the scaled galaxy parameters ($\sigma^\star$, $s^\star$) with respect to the core radii of the large scale dark matter clumps DM1 and DM2. Although there is a degeneracy between the parameters, the scale radius $s^\star$ is well constrained at low values. The contours correspond to 1σ, 2σ and 3σ confidence levels.
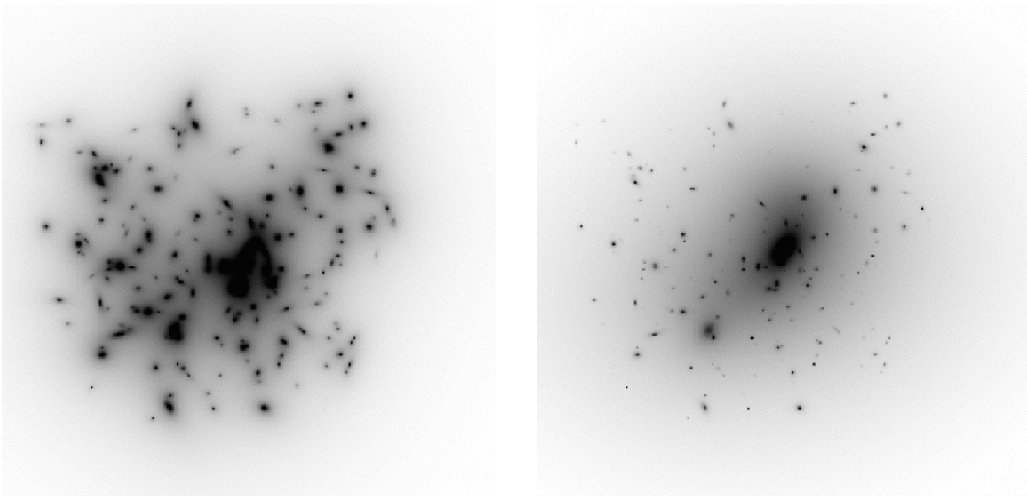
Figure 5.14 *Left panel:* The mass map from § 5.6.1 using only halos associated with the galaxies. *Right panel:* The mass map from § 5.4 consisting of large scale dark matter halos and galaxy halos. The mass map including the large scale dark matter halos, which is much smoother, provides a significantly better fit to the data than the clumpy galaxy-only model (rms$_s$ = 0''.12 vs. rms$_s$ = 1''.62). The maps are 300'' × 300'' and are centred on the BCG with North being up and East being left.

5.6 Reliability of the Mass Map

The mass map inferred from the strong lensing analysis has been presented in
§ 5.4 (Figure 5.4). In short, evidence is found for a bimodal mass distribution
described by two large scale smooth dark matter clumps, on top of which some
extra mass associated with the cluster galaxies is added. Moreover, a significant
mass concentration is associated with the location of the BCG galaxy. These two
conclusions are believed to be robust, and the aim of this section is to perform a
series of tests in order to check our main findings regarding how the dark matter
is distributed in Abell 2218.

5.6.1 Is the smoothly distributed dark matter component needed?

The aim is to test whether the smoothly distributed component is necessary to
reproduce a good fit, or whether mass associated with the galaxies alone can
provide an equally good fit. To this end, a model is constructed where the
mass is only in halos associated with the galaxies, without the inclusion of any
smoothly distributed dark matter component. The galaxies are included in a
scaled manner, allowing the $\sigma_{\mathrm{dPIE}}^{\star}$ and $s^{\star}$ to move to higher values to increase
their mass. As a result of the optimisation, a very poor fit is found ($\mathrm{rms}_s = 1\rlap{.}''62$
instead of $0\rlap{.}''12$ for the model from § 5.4). As the model from § 5.4 individually
fits three of the galaxies, one needs to check whether this difference arises from
these extra free parameters. The analysis is therefore redone using only DM1
and DM2, and scaling all the cluster galaxies. The resulting fit is worse than
the original ($\mathrm{rms}_s = 0\rlap{.}''22$) but still significantly better than the fit without any
smooth component.

   The resulting mass map is shown in Figure 5.14 alongside the model from
§ 5.4. The mass map without a smooth component is very 'clumpy', whereas
the latter is smooth. As expected, the enclosed mass derived from each model
is comparable for any radius where there are observational constraints (see Fig-
ure 5.15). Therefore, the poorness of the 'clumpy' fit is not due to the fact that it
is not massive enough to reproduce the lensing constraints. Moreover, it is worth
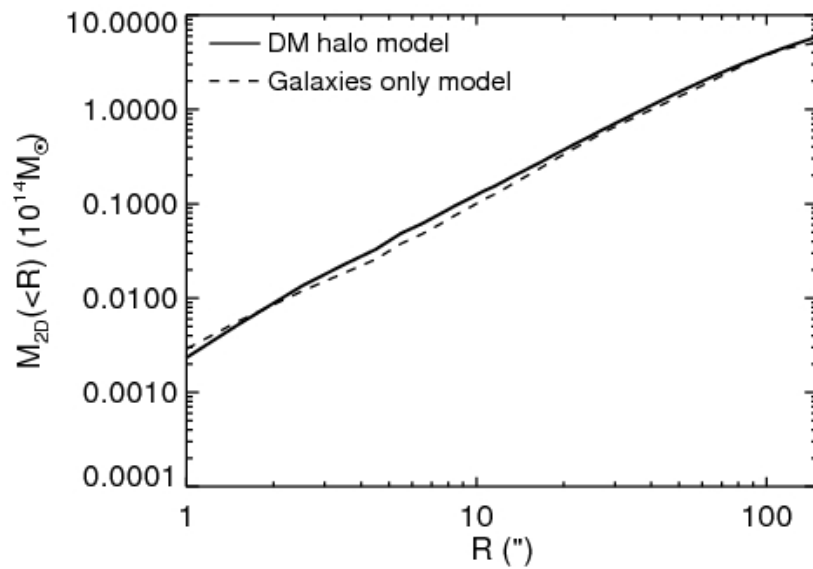
Figure 5.15 The total mass as function of radius (centred on the BCG) for the two models. Although the total mass within any given radii is similar, the pure-galaxy-mass map gives a significantly worse fit to the data ($\mathrm{rms}_s = 0.12$ vs. $\mathrm{rms}_s = 1.62$), confirming the need for a large scale dark matter halo to accurately fit the data (see § 5.6.1).

Table 5.4. Goodness of fit for different cut off magnitudes

Cut off magnitude in K	# of galaxy members	log E	rms$_s$ ($''$)	rms$_i$ ($''$)
19.6	197	-205	0.12	1.49
19.0	145	-192	0.12	1.05
18.0	110	-238	0.14	1.77
17.0	62	-284	0.17	1.87
16.0	35	-216	0.12	1.18

Note. — The χ^2 and Evidence (E) for different cut off magnitude in the galaxy catalogue. All the models are optimised in the same way, the only difference being the number of galaxy members which are optimised using the scaling relations in section 5.3.1.

noting that the 'clumpy' model is not very satisfactory in the sense that it describes the cluster galaxies as being very massive (around a few times $10^{12} M_\odot$ on average), which is not compatible with independent galaxy-galaxy lensing probes of cluster galaxy masses (see e.g., Mandelbaum et al., 2005). The difference in the goodness of fit is interpreted as evidence for the dark matter being distributed smoothly in the cluster, with only small perturbations from the cluster galaxies. This is further supported by the X-ray emission (see § 5.7).

5.6.2   Sensitivity to the galaxy scale perturbers

It has already been seen that individual galaxies are important to the overall lens model if they are close to a multiply imaged system (see also § 5.6.3), but in general the cluster galaxies only add small perturbations to the overall mass distribution of the cluster, with $\sim$ 5-6% of the total mass being associated with the galaxy sized halos (excluding the BCG, see Figure 5.5). To check whether those small scale perturbations are important, a subset of the galaxy catalogue is used to see if this affects the results. The original catalogue contains 197 cluster members down to $K = 19.6$ (including the individually fitted galaxies), but catalogues are also created using a cut off magnitude of $K = 19, 18, 17, 16$ with $145, 110, 62, 35$ members respectively. The overall quality of the fit is found to be only weakly affected (see Table 5.4), suggesting that for the purposes of lensing

studies, it is sufficient to include the brightest galaxy members in the modelling in addition to those which clearly locally perturb given multiply imaged systems. This point is important in order to save computing time, as increased number of clumps, even if modelled by scaling, significantly increases the required CPU (Central Processing Unit) time.
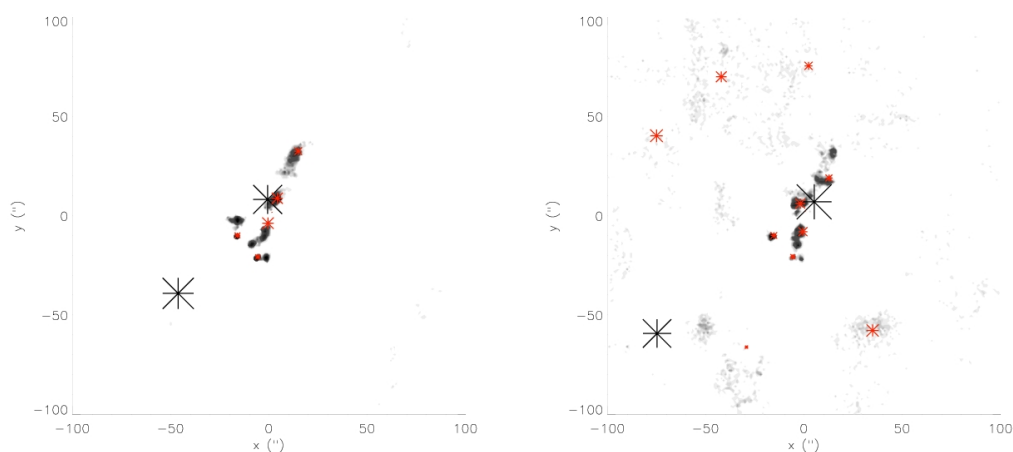
Figure 5.16 Density plots for the positions of the galaxy sized clumps for the models discussed in § 5.6.3. The locations of the clumps for the best model are marked with red stars. The size of the stars is proportional to their velocity dispersion. The two big black stars show the two large dark matter clumps, their size again proportional to the velocity dispersion. *Left panel:* Configuration (A): The model consists of five freely placed galaxy sized halos in addition to DM1 and DM2. *Right panel:* Configuration (B) The model consists of ten freely placed galaxy sized halos in addition to DM1 and DM2. Both configurations place galaxy scaled clumps where the BCG and the galaxies responsible for the local splitting of S1 are located. The maps are $200'' \times 200''$ and are centred on the BCG with North being up and East being left.

5.6.3   Blind tests - can galaxy scale substructure be localised?

Normally galaxy sized perturbers are added to the model by placing a dark matter clump at the location of a known cluster member. This method is by construction not able to detect dark substructure directly. To test how sensitive the model is to these substructures, luminous or dark, 'blind tests' are performed, where the cluster is modelled with (A) five and (B) ten freely placed galaxy sized dark matter clumps, in addition to the two large scale dark matter clumps DM1 and DM2.

In order to limit the number of free parameters, both $a = 1$ kpc and $s = 40$ kpc are fixed for the galaxy sized dark matter clumps, but all the parameters of the large scale clumps are optimised as before. The positions of the galaxy scale clumps are allowed to vary from $-100''$ to $100''$, corresponding roughly to the ACS field of view. The velocity dispersion, σ_{dPIE}, of each clump is allowed to vary from 0-500 km s^{-1}.

The results are shown in Figure 5.16, showing a density plot of the position of the clumps for the 1000 best realisations (in the lowest χ^2 sense), for both configurations (A) and (B). The locations of the clumps corresponding to the best realisation are marked by stars. Both configurations are found to give a good fit to the data (rms$_s$ = 0.17 and rms$_s$ = 0.19 for (A) and (B) respectively). Configurations (A) and (B) are consistent with each other: setup (A) finds five well defined clumps. Setup (B) finds the same well defined five clumps, whereas it tries to marginalise the five extra clumps that seem not to be needed in the optimisation.

For both configurations, the model places two large halos where the BCG is, clearly demonstrating the need for significant mass at the location of the BCG galaxy. Another common feature, is the lack of a galaxy sized clump in the vicinity of DM2, suggesting a very flat profile is preferred there. Both configurations place clumps in the positions of galaxies #1028 and #993, which are responsible for the local splitting of S1. This shows that lensing analysis can reliably detect galaxy sized dark substructure if it causes the local splitting of images, although

the lensing map is not very sensitive to galaxy sized substructure in general (see also § 5.6.2).

5.7 Bimodality of the Mass Distribution: Evidence of a Merger

The strong lensing analysis shows that Abell 2218 has a bimodal mass distribution: even if the dominant mass component is the BCG and DM1 halos, the second large scale dark matter clump DM2 is also significant, contributing around 20% of the total mass within $100''$. This second smooth mass component is associated with the bright cluster galaxy in the south-east called #617. To further interpret this bimodality, two different available probes of the cluster are studied: the X-ray map and the velocity of cluster members.

The X-ray map The X-ray flux map in the central parts of the cluster shows a complex morphology with no outstanding central peak. The offset between the X-ray peak at (R.A., Dec.)$=(248.967, 66.210)$ and the BCG is significant, $\sim 20''$, with the X-ray peak located in the direction of DM2, but there is no evident peak in the X-ray emission in the vicinity of DM2. The X-ray flux map within about 1 arcmin of the peak of the X-ray emission is clearly elongated in the SE-NW direction, but becomes more spherical with increasing distance from the cluster centre (see Figure 5.4). Comparing the contours for the X-rays and the mass map one sees that the elongation of the two are very similar, although the X-rays become more spherical at large radii. To get more quantitative values for comparison of the two maps, a 2-dimensional β model (Cavaliere & Fusco-Femiano, 1978) is fitted to both maps.

For the X-ray map, the best fit beta-model to the inner 2 arcmin by 2 arcmin (centred on the X-ray centroid) has an eccentricity ($\epsilon^\beta \equiv \sqrt{1 - (B/A)^2}$) of $\epsilon_X^\beta(\text{inner}) = 0.27 \pm 0.12$ and a position angle of $\theta_X(\text{inner}) = 39° \pm 16°$ (measured anti-clockwise from West). Fitting to the the 4 arcmin by 4 arcmin X-ray map (centred on the X-ray centroid) results in eccentricity of

5. WHERE IS THE MATTER IN THE MERGING CLUSTER ABELL 2218?

$\epsilon_X^{\beta}(\text{outer}) = 0.18 \pm 0.08$ and a position angle of $\theta_X(\text{outer}) = 17° \pm 14°$. A similar analysis for the mass map in a 5 arcmin by 5 arcmin (centred on the BCG) gives an eccentricity of the overall mass map as $\epsilon_{\text{mass}}^{\beta} \approx 0.25$ with $\theta_{\text{mass}} \approx 39°$, consistent with that found for the X-ray map, in particular in the inner regions.

Distribution in velocity space If a merger has taken place in Abell 2218, then this should be imprinted in the velocity distribution of the cluster members: it should be possible to identify two structures in velocity space; one associated with the BCG galaxy, and one associated with galaxy #617.

Girardi et al. (1997) studied the structure of Abell 2218 using the spectroscopic data from Le Borgne et al. (1992). They found evidence for two structures (labelled MS1 and MS2) separated by 2000 km s^{-1}. The larger of these two structures, MS2, contains both the BCG and the brightest galaxy in DM2. The two structures are superimposed along the line of sight and do not correspond exactly to the clumps found for the strong lens modelling. Such superimposed structures are hard to separate using lensing as it is not sensitive to the 3D distribution of the matter.

To look for substructure associated with the BCG and #617he separation ($\Delta v = c(z_i - z_j)/(1 + z_i)$) between them and the other cluster members has been calculated using spectroscopic data from Le Borgne et al. (1992). Out of the 50 galaxies in the catalogue 13 are found with $\Delta v < 500$ km s^{-1} and 25 with $\Delta v < 1000$ km s^{-1} for the brightest galaxy in DM2 while for DM1 the numbers are 11 and 21 respectively. The $\Delta v < 500$ km s^{-1} cut defines two structures without any common members, while the $\Delta v < 1000$ km s^{-1} cut starts mixing the two groups. While all the galaxies found with a $\Delta v < 500$ km s^{-1} for the BCG and #617 would belong to MS2 found by Girardi et al. (1997), the data suggests that MS2 may be further subdivided into two smaller structures, corresponding to the DM1 and DM2 found by the lens models.

The X-ray data and the distribution of the cluster members in velocity space, indicates that the bimodal mass distribution is caused by a merger. The main

cluster is the one associated with the BCG (DM1 and BCG in the lensing analysis) which the second cluster associated with #617 (DM2 in the lensing analysis) has merged with, thus displacing the centre of the X-ray peak from the BCG galaxy.

5.8 Conclusions

A mass map of the rich galaxy cluster Abell 2218 has been reconstructed using strong lensing constraints. The model is based on 7 multiply imaged systems and 1 arc with spectroscopic redshifts, and 6 systems without spectroscopic redshifts, of which 5 are new candidate systems proposed in this work. The model is sampled and optimised in the source plane by a Bayesian Monte Carlo Markov Chain implemented in the publicly available software Lenstool. The best model has $\mathrm{rms}_s = 0\rlap{.}''12$ in the source plane, corresponding to $\mathrm{rms}_i = 1\rlap{.}''49$ in the image plane.

In agreement with previous models of Abell 2218, the mass distribution is found to be bimodal. DM2 is found to be larger and have a flatter core than previous models have found. The flatness of the profile near DM2 is further supported by the 'blind tests', which do not place a galaxy sized component near its centre. The BCG and DM1 are the dominant component of the mass model in the inner regions ($< 100''$) of the cluster. The distribution of galaxies in velocity space has been analysed, finding evidence for two substructures, separated by $\sim 1000\,\mathrm{km\,s^{-1}}$, corresponding to DM1 and DM2. Although both the light and the X-ray contours are consistent with the mass map, the centre of the X-ray emission is offset from the central peak of the BCG. The X-ray data and the distribution in velocity space are found support the interpretation that the bimodal mass distribution arises from a cluster merger.

The degeneracy of the mass model has been explored, both those inherent to the dPIE profile and those arising from the mass model components themselves. For the dPIE, the results are in agreement with those of Jullo et al. (2007). The large scale dark matter clumps are found to be a necessary component of the model, i.e., using only the dark matter halos associated with the galaxies does not give a good fit to the data ($\mathrm{rms}_s = 1\rlap{.}''62$ vs. $\mathrm{rms}_s = 0\rlap{.}''12$), even if they are allowed to become much more massive.

5. WHERE IS THE MATTER IN THE MERGING CLUSTER ABELL 2218?

At around $100''$ the two large scale halos contribute $\sim 85\%$ of the enclosed projected mass, while the BCG contributes $\sim 9\%$ and the remaining cluster galaxies $\sim 6\%$. 'Blind tests' have been performed to check where the model requires a galaxy scale component to reproduce the lensing constraints, and they show that both the BCG and galaxies which locally perturb given multiply imaged systems are reliably reclaimed. However, the inclusion of the cluster galaxies (excluding the BCG) only weakly affects the model unless they locally perturb a multiply imaged system. Assuming that mass scales with light, this shows that strong lensing constraints can reliably detect substructure, dark or luminous, if the substructure is massive or locally perturbs a system.

The accurate mass map presented here is made available to the community and can be used to exploit Abell 2218 as a gravitational telescope, probing the high redshift universe. In this work the cosmology has been fixed, but with the increased number of constraints it may be possible to simultaneously fit it with the mass distribution. However, the bimodal structure of Abell 2218, and the remaining uncertainty in the mass model (around $\sim 1''$ in the image plane) may make it challenging to reach competitive accuracy in the derived cosmological parameters.

Chapter 6

The Chapter of Small Things

Great things are not done by impulse,
but by a series of small things brought together.
Vincent van Gogh (1853-1890)

This chapter presents two smaller projects conducted by the candidate, where lensing has been used as a tool to study the universe. The first part of this chapter briefly discusses the contribution of the candidate to the lensing analysis of the galaxy cluster Abell 1689. This work has previously been published in Limousin et al. (2007b) and is of similar nature to the lensing analysis presented in Chapter 5. The second part of this chapter discusses a project involving the possible lensing of a gamma ray burst (GRB), previously published in Pedersen et al. (2005). The burst is aligned with a bright elliptical galaxy in the cluster ZwCl 1234.0+02916 making it a likely[1] candidate for the origin of the burst. Therefore, it is possible that GRB 050509B is a background object and that it may be lensed by the foreground cluster. As no lensing data exist for this cluster, the lens modelling was performed using simple mass distribution profiles and an estimate of the mass was obtained from velocity dispersion measurements.

---

[1]This is not certain as the redshift of the burst was not determined.

6.1   Abell 1689

Abell 1689 is a galaxy cluster at $z = 0.18$ with a very rich catalogue of multiply imaged systems to constrain the mass distribution. The work of Limousin et al. (2007b) is the first to successfully combine the analysis of the weak lensing data and the numerous strong lensing constraints obtained with ACS imaging. The strong lensing analysis is analogous to that presented for Abell 2218 in § 5.3 and is discussed in detail in Limousin et al. (2007b).
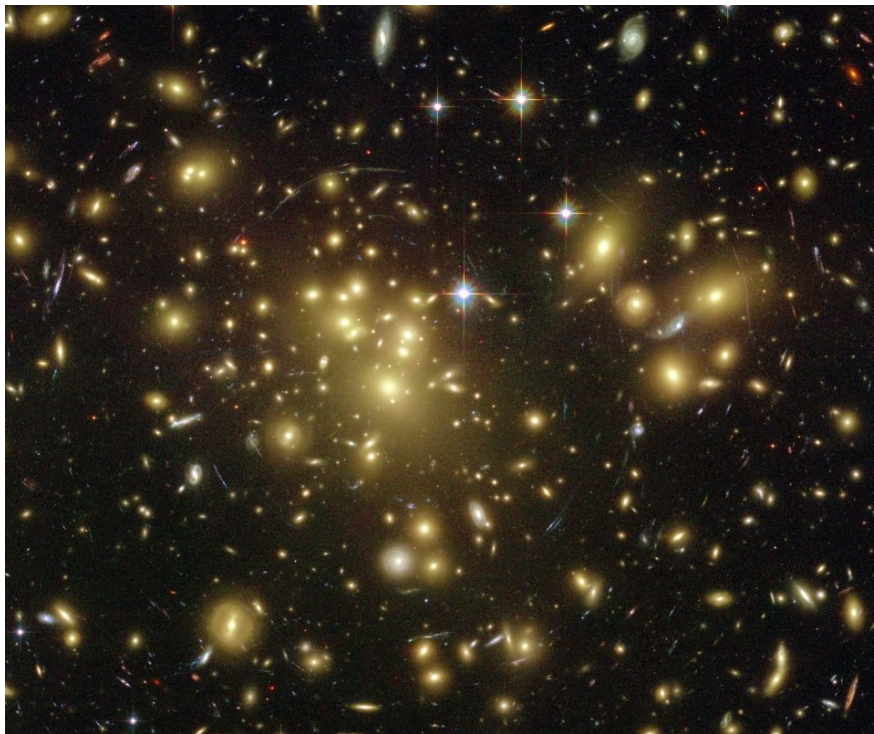
Figure 6.1 A colour image of Abell 1689. This galaxy cluster has the highest number of strongly lensed background sources known, many of which can be easily identified by eye in this figure. *Credit: Marceau Limousin.*

Although the underlying mass profiles for the individual halos used in the strong lensing analysis is the dPIE (see Appendix B), the overall mass profile is fitted using an NFW profile (see § 4.1.1). This is done to estimate of the concentration parameter, c_{200}, to compare with the weak lensing analysis. The fit

to the strong and weak lensing mass profiles are consistent with each other with $c_{200}^{\text{strong}} = 6.0 \pm 0.6$ (3σ error) and $c_{200}^{\text{weak}} = 7.6 \pm 1.6$ (1σ error). This is slightly higher than, although marginally consistent with, the average value predicted by N-body simulations of cluster formation and evolution in the ΛCDM simulations by Bullock et al. (2001) that predicts a concentration parameter $c_{200} \sim 5.5$. It is however not surprising that lensing clusters should have somewhat higher concentration than those of Bullock et al. (2001) as they are very massive compared to an 'average' cluster and a higher concentration (i.e. more matter in the centre of the cluster) will enhance the strong lensing signal. A more detailed discussion of the concentration parameter can be found in Limousin et al. (2007b).

Based on the results in Chapter 4, if the mass distribution of Abell 1689 is better described by an underlying Sérsic profile rather than an NFW profile, these concentration values would suggest a Sérsic index of around $n \sim 2.5$–3.5 (see Figure 4.9). As shown in Chapter 4, the difference in the lensing signal between an NFW profile and a Sérsic profile with those values of n is minimal. Therefore, Abell 1689 is not a good candidate to test whether real lensing clusters are better fitted by an NFW or a Sérsic profile.

6.2 The Possible Lensing of GRB 050509B

6.2.1 Introduction

Gamma ray bursts are extremely energetic short duration bursts of gamma ray emission at cosmological distances (for a review on GRBs see e.g., Woosley & Bloom, 2006; Zhang & Mészáros, 2004). Their origin is not fully understood, although current scenarios relate subgroups of GRBs to supernova explosions or merging neutron stars. GRBs are referred to as 'short' if the duration of the gamma ray emission is $\lesssim$ 2 s and 'long' if the duration is greater than 2 s (Kouveliotou et al., 1993). Most of the information deduced about GRBs comes from studying their afterglow in different wavelengths, including the optical and X-ray, which lasts significantly longer than the initial burst.

GRB 050509B was the second burst detected on the 9th of May 2005 (hence the name). It is the first short GRB with a detected X-ray afterglow, enabling

an accurate localisation (within $10''$, Gehrels et al., 2005), using the *Swift* X-Ray Telescope (XRT). Imaging of the XRT error box shows that it overlapped with an elliptical galaxy, G1, at a redshift of $z = 0.2248$ (Bloom et al., 2006) and is in the direction of a nearby galaxy cluster, identified in the Zwicky catalogue (ZwCl 1234.0+02916, Zwicky et al., 1963) and in the Northern Sky Optical Cluster Survey with a photometric redshift of $z = 0.2214$ (NSC J123610+285901, Gal et al., 2003). Based on the unlikeliness of a chance alignment between GRB 050509B and such a galaxy it is argued that this is the host galaxy of the burst (Bloom et al., 2006; Gehrels et al., 2005). However, several much fainter (and presumably more distant) galaxies are also detected within the XRT error circle (see Figure 6.2, Hjorth et al., 2005). Therefore, it is possible that
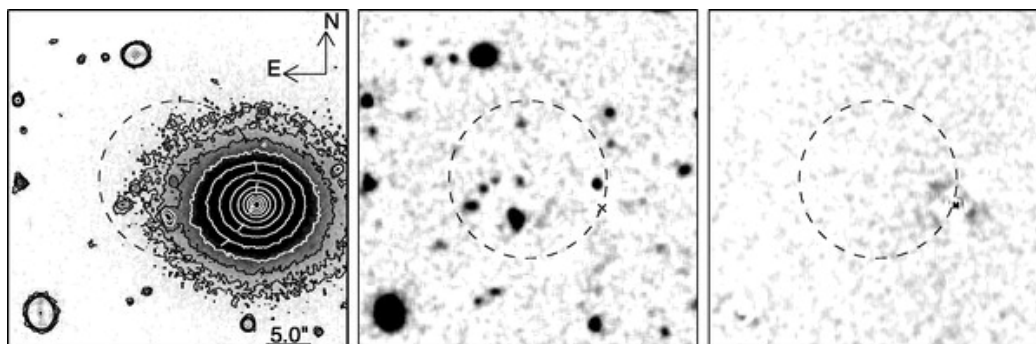
Figure 6.2 *Left:* A V-band image (taken with the ESO VLT around 4 days after the burst) of the field of GRB 050509B. It shows the possible host elliptical galaxy G1 and several faint galaxies in the XRTerror circle. *Middle:* Same, after subtraction of a fit to G1. The cross marks the location of the centre of G1. *Right:* Difference between a V image taken around 23 days after the burst and the image in the left panel. *Credit: Hjorth et al. (2005).*

GRB 050509B is a background object being lensed by the galaxy cluster and the elliptical galaxy (Engelbracht & Eisenstein, 2005). In this chapter, the possible lensing signal is estimated, assuming that GRB 050509B is a background object, for several possible redshifts of GRB 050509B. The mass estimate of the galaxy are based on velocity dispersion measurements and the mass estimate of

the cluster is based on its X-ray mass. More details on the X-ray properties of the environment of GRB 050509B are given in Pedersen et al. (2005).

6.2.2 Gravitational lensing magnification

The gravitational lensing calculations were carried out using the *gravlens* software package (Keeton, 2001). The galaxy is modelled as a singular isothermal ellipsoid with an axis ratio of 0.81 (Bloom et al., 2006) with the semimajor axis aligned along a position angle 90°, a velocity dispersion of 260 ± 40 km s^{-1} (Bloom et al., 2006), and the cluster is modelled as a singular isothermal sphere with $M_{500} = 2.2^{+3.3}_{-0.6} \times 10^{14}$ M$_\odot$ (for details on how the X-ray mass is measured see, Pedersen et al., 2005). The centre of the XRT error circle is taken to be at R.A.(J2000)= $12^\mathrm{h}36^\mathrm{m}13\overset{\mathrm{s}}{.}58$ and decl.(J2000)= $+28°59'01''\!\!.3$ (Gehrels et al., 2005) and is chosen as the centre of the coordinate system. The centre of the galaxy G1 is placed at R.A.(J2000)=$12^\mathrm{h}36^\mathrm{m}12\overset{\mathrm{s}}{.}86$ and decl.(J2000)= $+28°58'58''\!\!.0$ and the centre of the cluster is placed at the X-ray centroid of the diffuse cluster emission (Pedersen et al., 2005).

Below results for point sources are given at the expected lower and upper limit on the GRB 050509B redshift $z = 1.3$ and $z = 3$, respectively. Due to the blue continuum and lack of emission lines in the faint galaxies in the XRT error box, the lower limit on their redshift is $z \approx 1.3$ (Bloom et al., 2006). The upper limit on the redshift is motivated by models predicting an intrinsic duration of a GRB longer than 8 ms (Lee et al., 2005). Choosing a larger upper limit does not affect the conclusions.

Taking uncertainties in the velocity dispersion of G1 into account this gives an Einstein radius for G1 of $b = 1.67^{+0.55}_{-0.47}$ arcsec for $z = 3$ and $b = 1.50^{+0.49}_{-0.42}$ arcsec for $z = 1.3$. Similarly we get for the cluster (taking the uncertainty in the cluster mass into account) that $b = 9.7^{+8.2}_{-1.8}$ arcsec for $z = 3$ and $b = 9.0^{+7.6}_{-1.7}$ arcsec for $z = 1.3$. We then calculate the median magnification within the XRT error circle of radius 9.3″ (Gehrels et al., 2005), see Fig. 6.3. Most of the magnification is provided by the galaxy G1, and the main effect of the cluster is to increase the magnification in the East-West direction.
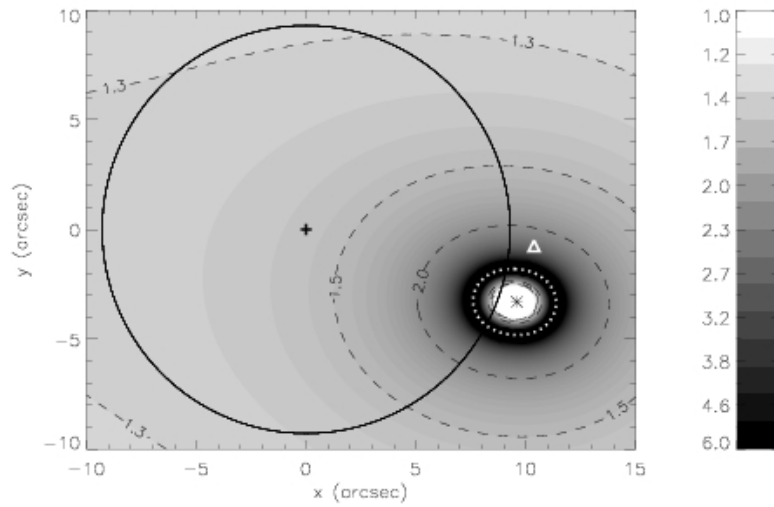
Figure 6.3 Gravitational lensing magnification in and around the XRT error circle (centred on the black cross) shown as logarithmic grey scale (intensity scale on the right) and contours (dashed lines). North is up and East to the left. The source was placed at a redshift $z = 3$, and the mass distribution of the galaxy G1 and the cluster ZwCl 1234.0+02916 were modelled as isothermal ellipsoids with masses determined from the velocity dispersion and the X-ray temperature, respectively. The black star is the centre of the galaxy G1. The white triangle marks the location of the source revealed by subtracting a model of galaxy G1 (Hjorth et al., 2005), and the white, dotted line is a critical curve.

The XRT error circle crosses the critical curves (paths in the image plane where a point source will be exposed to infinite magnification) for nearly all mass models of G1 and the cluster. The median of the magnification within the error circle is a factor of $1.3^{+0.4}_{-0.1}$ for $z = 3$ and $1.3^{+0.3}_{-0.1}$ for $z = 1.3$. We thus find that the potential magnification of GRB 050509B is typically a factor 1–2, fairly independent of the redshift of GRB 050509B. However, if GRB 050509B is positioned within $\sim 2''$ of G1 it could be more strongly magnified. We note that the source revealed by subtracting away G1 (Hjorth et al., 2005), situated $2.68''$ from the centre of G1, is not a strongly lensed background source.

6.2.3 Conclusions

The environment of GRB 050509B has been analysed assuming that it is a background source being lensed by the associated elliptical galaxy and cluster. It has been found that the typical magnification factor is around 1–2, suggesting that GRB 050509B is not strongly affected by the lensing even if it is a background object. Part of the XRT error circle lands in the region where the lensing signal would produce multiple images and/or high magnification. However, this is a small part of the total XRT error circle, and as no second burst was detected it is clear that GRB 050509B is at least not multiply imaged. Therefore, the analysis of the burst is not expected to be strongly affected by the lensing signal even if the burst does not originate in the elliptical galaxy but in a background object. However, it should be noted, that this work does not address whether GRB 050509B is indeed such a background object or not (see Pedersen et al., 2005, for such a discussion).

Chapter 7

Conclusions

Lensing has developed into a unique tool which allows exploration of structures which are hard to detect in other ways. In particular, lensing is an ideal method to study dark matter as it is sensitive to the total matter along the line of sight, irrespective of its nature or state. More generally, lensing is sensitive to the exact geometry of spacetime. Additionally, lensing opens a window on dust extinction in distant galaxies, which is a field requiring significantly more study. This thesis has focused on two main topics, namely dust and dark matter in extragalactic environments, and the main conclusions are summarised here.

The first of main topic, presented in Chapter 3, is dust extinction in distant galaxies. This chapter reports on the first systematic study of extinction curves of lensed galaxies, using data from the ESO Very Large Telescope for 10 gravitationally lensed quasars. The study finds that distant lensing galaxies can vary greatly in both the amount and type of dust, and that the type of dust can differ significantly from that of the Milky Way. This is a significant result, since due to the scarcity of information on higher redshift dust, Milky type of extinction is commonly applied in various extragalactic studies. However, if the dust properties are different, this can cause a non-negligible bias in any derived quantity. Due to the large scatter found for individual systems and the small sample size

it is not possible to make statistically robust claims for the dust evolution with redshift. It is of great interest to expand this study to a significantly larger sample size. To do so, higher resolution is required and ideally the method should be further developed to apply to finite sources (and not just quasars which act as point sources) to take advantage of the more numerous lensed galaxies. As planned future space missions will have the ability to find thousands of lenses, it is highly relevant to prepare for these missions by developing the method for finite sources to take advantage of the huge data sets. A successful completion of such a project would not only impact the field of lensing, but any cosmological and astrophysical probe where accurate calibration of data is required, such as current and future supernova dark energy surveys.

The second main topic of this thesis, is dark matter in galaxies and clusters. Chapter 4 reports on a theoretical study of the strong lensing properties of the Sérsic profile and compares it to those of the NFW profile. The NFW profile is the standard description of dark matter, but recently it has been suggested that the Sérsic profile, more commonly used to describe baryonic matter in galaxies, may be a more accurate description. The results show that it is often possible to find an NFW profile which accurately reproduces the strong lensing signal of a Sérsic profile. However, in other cases, the difference between these profiles could contribute to explaining the discrepancy in the mass and concentration estimates from strong lensing on the one hand, and from weak lensing and X-ray measurements on the other. As a first step towards testing the Sérsic profile on real lensing clusters, it has been incorporated into the publicly available lensing software Lenstool. However, as parametric cluster lens models are still far from being able to reproduce all the observed images (the offset is around $1''$, which is significantly higher than the current measurement error in the image positions), it may prove challenging to reach a robust conclusion on which profile better describes real systems.

Continuing with the theme of dark matter, Chapter 5 presents the mass reconstruction of the galaxy cluster Abell 2218 using strong lensing constraints. The mass model is optimised in the source plane and the best model is found to have rms$= 0\rlap{.}''12$ in the source plane which translates into $1\rlap{.}''49$ in the image

plane. The mass distribution is found to be bimodal in agreement with previous models of Abell 2219. However, the second large scale dark matter clump is found to be larger and with a flatter core than previous models have found. This flatness is further supported by 'blind tests' which do not place galaxy sized components near its centre. An analysis of the cluster galaxies in velocity space finds evidence for two substructures corresponding to the two large scale dark matter halos. The X-ray data and the distribution in velocity space are found to support the interpretation that the bimodal mass distribution arises from a cluster merger. The modelling also shows that the large scale dark matter halos are a necessary component of the model, i.e., using only the dark matter halos associated with the galaxies does not give a good fit to the data, even if they are allowed to become much more massive. Furthermore, the 'blind tests' show that both the BCG and galaxies which locally perturb given multiply imaged systems are reliably reclaimed. However, the inclusion of the cluster galaxies (excluding the BCG) only weakly affects the model unless they locally perturb a multiply imaged system. Assuming that mass scales with light, this shows that strong lensing constraints can reliably detect substructure, dark or luminous, if the substructure is massive or locally perturbs a system.

As observations of galaxy clusters increase in resolution and depth, ever more strongly lensed background sources are found to constrain the mass model. Therefore, the mass models of clusters from lensing are becoming increasingly accurate. However, a significant discrepancy is still found between the lens models and the observed images signifying that the mass distribution has not yet been fully understood. It is possibly to gain more insight into the mass distribution by studying the cluster in alternative ways. For example, an X-ray analysis will give information about the distribution of the gas in the cluster while a detailed analysis of the cluster members in velocity space gives information about the distribution of baryonic matter and the formation history of the cluster. It is also possible that part of the answer lies in substructure not yet accounted for or mass along the line of sight, but not in the lens plane itself. All these are issues worthy of further investigation leading to a fuller understanding of the mass distribution of galaxy clusters which is important if lensing clusters are to reach the goal of independently constraining cosmological parameters.

7. CONCLUSIONS

The thesis finishes with discussion of two smaller projects related to dark matter and lens modelling presented in Chapter 6. The first is the concentration of the dark matter profile for the galaxy cluster Abell 1689. Its concentration from the strong lensing constraints is found to agree with the concentration found using the weak lensing constraints. It is slightly higher than, although consistent with, the predicted values from numerical simulations. However, this may be a selection effect as high concentration enhances strong lensing and Abell 1689 is the most spectacular strong lensing cluster there is (it has the largest number of multiple images known). The final project is the lens modelling of an elliptical galaxy and a galaxy cluster related to the gamma ray burst GRB 050509B. The elliptical galaxy is within the XRT error circle. Such a chance alignment has led to suggestions that it is the host for GRB 050509B. However, as no redshift has been determined for GRB 050509B, it is also possible that it originates in one of the several fainter (and hence most likely more distant) galaxies also found within the XRT. In such a case the elliptical galaxy and the cluster would act as lenses, enhancing and even possibly creating multiple images of the burst. This lensing signal is calculated using estimates of the mass of the cluster from X-ray analysis and of the elliptical galaxy from stellar dynamics. The conclusion is that GRB 050509B is most likely only weakly enhanced, although a small part of the XRT falls within the region of high magnification and multiple imaging. However, as no second burst was observed, the possibility that the burst is multiply imaged can be excluded.

Appendix A

VLT Extinction Study - Observations

Why then do we not turn our eyes to the stars? Why?

Mikhail Bulgakov (1891-1940)

Here the observations from the VLT extinction study from Chapter 3 and published in Elíasdóttir et al. (2006) are presented. The data reduction was performed by Ingunn Burud, but is included here in this thesis for completeness.

A.1 Overview of Observations

The lens systems were chosen to fulfil the criteria that they have an image separation larger than $0\overset{''}{.}4$ to ensure that the images of the quasar could be resolved, that they have declination $\delta < 33°$ to be visible with the ESO Very Large Telescope (VLT) at Paranal observatory and that the lens and quasar redshifts be known in order to reduce the number of unknowns when fitting the extinction curve. At the time of the application, this left us with ten systems, five doubly imaged quasars (doubles) and five quadruply imaged quasars (quads). The

A. VLT EXTINCTION STUDY - OBSERVATIONS

Table A.1. Overview of observations

Lens	U	B	V	R	I	z	J_s	H	K_s	Delay
	(s)	(s)	(s)	(s)	(s)	(s)	(s)	(s)	(s)	(d)
Q2237+030	180	60	60	40	60	40[b]	$\cdots$	60	60	-13
PG1115+080	30	15	9	9	9	9[a]	180	300	180	-20
B1422+231	180	60	40	40	40	40[b]	$\cdots$	120	120	48
B1152+199	3000	180	80	40	60	60[b]	60	60	60	47
Q0142$-$100	60	60	40	40	60	60[b]	$\cdots$	$\cdots$	$\cdots$	$\cdots$
B1030+071	9300	3600	3000	1400	1600	2000[a]	840	1280	2470	-5
RXJ0911+0551	900	30	15	15	25	15[a]	180	216	360	5
HE0512$-$3329	30	15	9	9	9	9[a]	216	216	216	-18
MG0414+0534	$\cdots$	5400	4200	270	60	120[a]	240	240	240	-11
MG2016+112	2400	1200	720	300	400	600[b]	480	960	1500	-71

Note. — Total exposure time (in seconds) and delay between optical and NIR observations (in days), where a negative value denotes that the NIR were carried out before the optical.

[a]The observing band was $z_{special}$.

[b]The observing band was z (Gunn)

images are labelled according to the CfA-Arizona-Space-Telescope-LEns-Survey (CASTLES)[1] notation (see Fig. 3.1).

Multi waveband imaging observations of the 10 gravitational lens systems was obtained with the VLT. A list of the systems and their main properties known from the literature is given in Table 3.2, and a gallery of how they appear in the VLT observations is shown in Figure 3.1. Optical observations (in the U, B, V, R, I and z band) was carried out with the FORS1 instrument (which with the high resolution collimator has a pixel scale of $0\overset{''}{.}1$), and near infrared (NIR) observations (in the J_s, H and K_s band) were carried out with the ISAAC instrument (which has a pixel scale of $0\overset{''}{.}147$).

---

[1]http://www.cfa.harvard.edu/castles/

Table A.2.   Relative photometry

Lens	Image	U	B	V	R	I	z	J_s	H	K_s
Q2237+030	A	1.00	1.00	1.00	1.00	1.00	1.00	$\cdots$	1.00	1.00
	σ_A	0.02	0.02	0.01	0.01	0.02	0.02	$\cdots$	0.01	0.01
	B	0.36	0.24	0.30	0.39	0.30	0.32	$\cdots$	0.33	0.36
	σ_B	0.02	0.02	0.01	0.01	0.02	0.02	$\cdots$	0.01	0.01
	C	0.26	0.35	0.40	0.29	0.37	0.45	$\cdots$	0.47	0.41
	σ_C	0.02	0.02	0.01	0.01	0.02	0.02	$\cdots$	0.01	0.01
	D	0.24	0.21	0.29	0.27	0.27	0.35	$\cdots$	0.38	0.35
	σ_D	0.02	0.02	0.01	0.01	0.02	0.02	$\cdots$	0.01	0.01
PG1115+080	A1	1.00	1.000	1.000	1.000	1.000	1.00	1.000	1.000	1.000
	σ_{A1}	0.01	0.006	0.006	0.005	0.003	0.01	0.001	0.002	0.002
	A2	0.63	0.615	0.676	0.675	0.710	0.67	0.747	0.710	0.771
	σ_{A2}	0.02	0.009	0.007	0.008	0.004	0.02	0.002	0.003	0.002
	B	0.26	0.246	0.253	0.257	0.262	0.27	0.268	0.270	0.266
	σ_B	0.02	0.009	0.008	0.008	0.004	0.02	0.002	0.003	0.003
	C	0.18	0.17	0.17	0.17	0.170	0.17	0.177	0.178	0.176
	σ_C	0.02	0.01	0.01	0.01	0.006	0.01	0.003	0.005	0.005
B1422+231	A	0.105	0.15	0.16	0.15	0.18	0.16	$\cdots$	$\cdots$	0.31[a]
	σ_A	0.008	0.02	0.01	0.01	0.02	0.01	$\cdots$	$\cdots$	0.02[a]
	B	0.09	0.14	0.16	0.15	0.17	0.16	$\cdots$	$\cdots$	0.35[a]
	σ_B	0.01	0.02	0.02	0.02	0.02	0.01	$\cdots$	$\cdots$	0.02[a]
	C	0.08	0.10	0.10	0.09	0.11	0.10	$\cdots$	$\cdots$	0.18[a]
	σ_C	0.02	0.03	0.04	0.03	0.04	0.01	$\cdots$	$\cdots$	0.02[a]
	D	0.01	0.004	0.005	0.005	0.007	0.006	$\cdots$	$\cdots$	0.02[a]
	σ_D	0.01	0.018	0.016	0.014	0.019	0.013	$\cdots$	$\cdots$	0.02[a]
B1152+199	A	$\cdots$	1.000	1.000	1.000	1.000	1.000	1.000	1.000	1.000
	σ_A	$\cdots$	0.007	0.002	0.002	0.003	0.005	0.004	0.002	0.004
	B	$\cdots$	0.0024	0.010	0.018	0.044	0.074	0.172	0.293	0.289
	σ_B	$\cdots$	0.0006	0.001	0.001	0.002	0.003	0.002	0.004	0.003
Q0142−100	A	1.000	1.00	1.0000	1.0000	1.0000	1.0000	$\cdots$	$\cdots$	$\cdots$
	σ_A	0.008	0.01	0.0003	0.0002	0.0002	0.0004	$\cdots$	$\cdots$	$\cdots$

Table A.2 (cont'd)

Lens	Image	U	B	V	R	I	z	J_s	H	K_s
	B	0.13	0.12	0.134	0.138	0.152	0.159	$\cdots$	$\cdots$	$\cdots$
	σ_B	0.03	0.01	0.001	0.001	0.001	0.002	$\cdots$	$\cdots$	$\cdots$
B1030+071[†]	A	$\cdots$	1.00	1.00	1.00	1.00	1.00	1.00	1.00	1.00
	σ_A	$\cdots$	0.01	0.01	0.01	0.01	0.02	0.02	0.03	0.02
	B	$\cdots$	0.16	0.23	0.30	0.41	0.64	0.378	0.29	0.28
	σ_B	$\cdots$	0.01	0.01	0.01	0.01	0.02	0.008	0.01	0.01
RXJ0911+0551	A	1.000	1.00[b]	1.00	1.00	1.00	$\cdots$	1.000	1.000	1.000
	σ_A	0.008	0.02[b]	0.01	0.01	0.02	$\cdots$	0.008	0.008	0.006
	B	0.62	0.94[b]	0.73	0.72	0.74	$\cdots$	0.923	0.919	0.970
	σ_B	0.01	0.02[b]	0.02	0.02	0.02	$\cdots$	0.009	0.008	0.006
	C	0.33	0.51[b]	0.37	0.40	0.41	$\cdots$	0.49	0.51	0.50
	σ_C	0.02	0.03[b]	0.04	0.03	0.04	$\cdots$	0.02	0.01	0.01
	D	0.37	0.40[b]	0.38	0.37	0.37	$\cdots$	0.39	0.44	0.40
	σ_D	0.01	0.02[b]	0.02	0.01	0.02	$\cdots$	0.02	0.02	0.01
HE0512−3329	A	1.000	1.000	1.000	1.0000	1.000	$\cdots$	1.0000	1.0000	1.0000
	σ_A	0.008	0.002	0.002	0.0009	0.001	$\cdots$	0.0005	0.0004	0.0005
	B	1.141	1.021	0.887	0.738	0.651	$\cdots$	0.5813	0.5667	0.5593
	σ_B	0.007	0.002	0.002	0.001	0.002	$\cdots$	0.0008	0.0007	0.0009
MG0414+0534	A1	$\cdots$	$\cdots$	1.000	1.000	1.00	1.00[c]	1.000	1.000	1.000
	σ_{A1}	$\cdots$	$\cdots$	0.005	0.008	0.01	0.02[c]	0.004	0.003	0.001
	A2	$\cdots$	$\cdots$	0.41	0.34	0.39	0.89[c]	0.567	0.748	0.780
	σ_{A2}	$\cdots$	$\cdots$	0.01	0.02	0.03	0.02[c]	0.008	0.004	0.003
	B	$\cdots$	$\cdots$	0.818	0.592	0.50	0.78[c]	0.416	0.394	0.385
	σ_B	$\cdots$	$\cdots$	0.005	0.009	0.01	0.02[c]	0.006	0.004	0.006
	C	$\cdots$	$\cdots$	0.396	0.29	0.24	0.34[c]	0.18	0.179	0.175
	σ_C	$\cdots$	$\cdots$	0.008	0.01	0.02	0.03[c]	0.01	0.006	0.005
MG2016+112	A	$\cdots$	1.00	1.00	1.00	1.00	1.00[d]	1.0	1.00	$\cdots$
	σ_A	$\cdots$	0.01	0.01	0.01	0.01	0.02[d]	0.1	0.03	$\cdots$
	B	$\cdots$	0.60	0.68	0.81	0.87	1.04[d]	1.08	0.94	$\cdots$
	σ_B	$\cdots$	0.02	0.01	0.01	0.01	0.02[d]	0.09	0.03	$\cdots$

Table A.2 (cont'd)

Lens	Image	U	B	V	R	I	z	J_s	H	K_s

Note. — Data table with the results from the deconvolution. Missing data are either due to lack of observations (see overview in Table A.1) or failure of the deconvolution to converge.

†The photometry of the B component is believed to be contaminated by the lensing galaxy.

ᵃThe images are not well resolved. This system shows very weak extinction, and no detailed extinction curve analysis is performed, so the exclusion of this point should not affect the results.

ᵇSeeing too high to separate components ($0\rlap{.}''70$).

ᶜVery faint detection.

ᵈVery faint detection.

The data were collected in excellent seeing conditions (FWHM $\lesssim 0\rlap{.}''65$, see Figure A.1) with mean seeing of $0\rlap{.}''57$ for the full data set. Photometric conditions were not necessary since only relative photometry is considered. An effort was made to carry out the different waveband observations of each system as close in time as possible to each other, to minimise the effects of time dependent intrinsic quasar variation and achromatic microlensing. For each system, the optical wavebands were observed on the same night in immediate succession, while the NIR observations were observed as close in time as scheduling allowed (the mean delay was 18 days, see Table A.1). The effects of time delayed intrinsic variations between the individual images is thus reduced to a possible shift between the optical and NIR fluxes. Details of the observations are summarised in Table A.1.
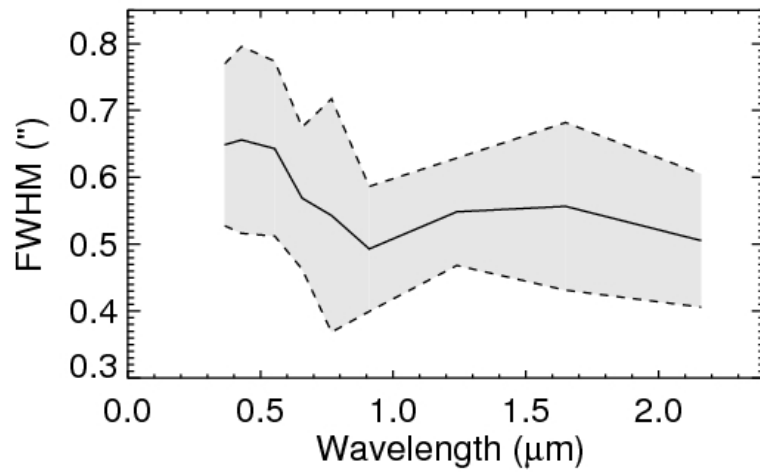
Figure A.1 Mean FWHM measured in the VLT observations of the 10 systems, as a function of wavelength (full curve). The shaded area between the dashed curves indicates the RMS scatter around the mean. Approximately 80% of the observations were carried out in $\lesssim 0.65''$ seeing.

A.2   Data Reduction

The individual optical data frames were bias subtracted and flat fielded using the standard ESO pipeline, and cleaned for cosmic rays using Laplacian edge detection (van Dokkum, 2001). In some of the frames the background was found to have large-scale gradients over the field. To properly account for this, all the frames were run through the SEXTRACTOR software (Bertin & Arnouts, 1996), with options set to save a full resolution interpolated background map, which was then subtracted from the science frames.

The NIR data were reduced using a combination of the ECLIPSE software (Devillard, 1997) and the IRAF "Experimental Deep Infrared Mosaicing Software" XDIMSUM. The ECLIPSE software was used to remove the effects of electrical ghosts from science and calibration frames, and to construct flat fields and bad-pixel maps from a series of twilight sky flats. Sky subtraction and combination of the individual science frames was carried out with XDIMSUM.

A.3   Deconvolution and Photometry

All photometry was carried out using the MCS deconvolution (Magain et al., 1998). This method uses a model PSF, measured directly from the data, to deconvolve the images, assuming that the gravitational lens systems can be decomposed into a number of point source (the quasar images) and a diffuse extended component (the lensing galaxy). Positions and amplitudes of the quasar images are left free in the fit, and relative photometry can be derived from the best fitting amplitude. No functional form was assumed for the diffuse component, which is a purely numerical component. In the cases when there was more than one image of a given system available (in a given waveband), a simultaneous deconvolution of the individual images was performed rather than deconvolving the combined image.

Photometric errors were estimated by the MCS algorithm, and include photon noise and errors associated with deconvolution (Burud et al., 1998b; Magain et al., 1998). A full list of the results from the MCS deconvolution is given in Table A.2.

A. VLT EXTINCTION STUDY - OBSERVATIONS

In addition to the MCS errors, a 0.05 mag error was applied on all the calculated magnitude differences to account for other sources of systematic noise.

Data points are excluded from the sample where the deconvolution did not converge or where only one component was detected (7 data points). In addition, 4 data points are excluded from further analysis. These points are marked in Table A.2 and an explanation of the exclusion of each point is given in a footnote. Also excluded from further analysis are all the data taken for B1030+071 as the B component is heavily contaminated by the lens galaxy (separated by $0\rlap{.}''11 \pm 0\rlap{.}''01$ (Xanthopoulos et al., 1998)).

Appendix B

The Dual Pseudo Isothermal

Elliptical Mass Distribution

I admit that twice two makes four is an excellent thing,

but if we are to give everything its due,

twice two makes five is sometimes a very charming thing too.

Fyodor Mikhailovich Dostoevsky (1821-1881)

The Pseudo Isothermal Elliptical Mass Distribution (PIEMD) was first introduced by Kassiola & Kovner (1993a) and it and its variants are frequently used in lensing analysis (see e.g., Keeton & Kochanek, 1998; Kneib et al., 1996; Limousin et al., 2007b; Natarajan et al., 2007; Richard et al., 2007; Smith et al., 2005). The main advantage of using the PIEMD for lensing analysis is that its potential, as well as its first and second partial derivatives, can be expressed analytically to derive deflections, distortions, amplifications and time delays for any ellipticity (see also Keeton & Kochanek (1998)). One of the most commonly used variants, and the one used in this work, is a two component PIEMD with both a core radius and a scale radius. This profile is sometimes referred to as the "truncated PIEMD" or simply the "PIEMD", although it differs in significant ways from the original PIEMD proposed by Kassiola & Kovner (1993a). An equivalent family

B. THE DUAL PSEUDO ISOTHERMAL ELLIPTICAL MASS DISTRIBUTION

of mass models was introduced independently by Merritt & Valluri (1996) who used it as a starting point in an investigation of the orbital properties of triaxial stellar systems. In this appendix a self-contained description is given of this profile, which is called the 'dual Pseudo Isothermal Elliptical mass distribution' (dPIE) and t its derived quantities most relevant to lensing are presented. This appendix is based on an unpublished paper by Jens Hjorth and Jean-Paul Kneib.

B.1 The 3D Density Profile

The 3D density distribution of the dPIE is

$$\rho(r) = \frac{\rho_0}{(1 + r^2/a^2)(1 + r^2/s^2)}; \quad s > a. \tag{B.1}$$

This distribution represents a spherical system with scale radius s, core radius a and central density ρ_0 [1]. In the centre $\rho \approx \rho_0/(1 + r^2/a^2)$ which describes a core with central density ρ_0. The core is not strictly isothermal (in which case $\rho \sim (1 + r^2/a^2)^{-3/2}$ (Binney & Tremaine, 1987)) but in the transition region, $a \lesssim r \lesssim s$, one has $\rho \sim r^{-2}$ as for the isothermal sphere. In the outer parts the density falls off as $\rho \sim r^{-4}$.

The density distribution can be rewritten as

$$\rho(r) = \frac{\rho_0}{(1 + (\eta\xi)^2)(1 + \xi^2)}; \quad \eta > 1 \tag{B.2}$$

with $\xi \equiv r/s$ and $\eta \equiv s/a$. Thus s acts as a scale parameter and η is a shape parameter.

---

[1] Note that s corresponds to $r_{\rm cut}$ and a to $r_{\rm core}$ in previous publications (e.g. Jullo et al. (2007); Limousin et al. (2007b)), but this new notation is adopted to avoid confusion, as s is not a 'cut-off' nor a truncation radius, but the a scale radius, with $\rho \sim r^{-4}$ for $r >> s$ (see also § B.3 for how the mass depends on s).

B.2   The 2D Density Profile

The projected density, which is the relevant quantity for lensing, is given by

$$\Sigma(R) = 2 \int_R^\infty \frac{\rho(r)r}{\sqrt{r^2 - R^2}} \mathrm{r}r = \Sigma_0 \frac{as}{s-a} \left(\frac{1}{\sqrt{a^2 + R^2}} - \frac{1}{\sqrt{s^2 + R^2}} \right) \qquad (B.3)$$

with

$$\Sigma_0 = \pi \rho_0 \frac{as}{s+a}. \qquad (B.4)$$

and R is the 2D radius. For a vanishing core radius it reduces to

$$\Sigma(R) = \Sigma_0 \frac{a}{R} \left(1 - \frac{1}{\sqrt{1 + s^2/R^2}} \right); \qquad a << R \qquad (B.5)$$

which is the surface mass profile proposed by Brainerd et al. (1996) for modelling galaxy-galaxy lensing. In this special case, a becomes a simple amplitude scaling parameter and, as shown below, s is the half-mass radius, r_h.

Defining the critical surface mass density

$$\Sigma_{\mathrm{crit}} \equiv \frac{c^2}{4\pi G} \frac{D_S}{D_L D_{LS}}. \qquad (B.6)$$

where D_L, D_S, and D_{LS} are the angular diameter distances to the lens, the source, and between the lens and source respectively, the convergence is

$$\kappa(R) \equiv \frac{\Sigma(R)}{\Sigma_{\mathrm{crit}}} \qquad (B.7)$$

and the corresponding shear is

$$\begin{aligned}
\gamma(R) \;=\; & \frac{\Sigma_0}{\Sigma_{\mathrm{crit}}} \frac{as}{s-a} \left[2 \left(\frac{1}{a + \sqrt{a^2 + R^2}} - \frac{1}{s + \sqrt{s^2 + R^2}} \right) \right] \\
& + \frac{\Sigma_0}{\Sigma_{\mathrm{crit}}} \frac{as}{s-a} \left[\frac{1}{\sqrt{a^2 + R^2}} - \frac{1}{\sqrt{s^2 + R^2}} \right].
\end{aligned} \qquad (B.8)$$

B.3   Mass Relations

The mass inside physical radius r is

$$M_{3D}(r) = 4\pi \int_0^r \rho(\tilde{r}) \tilde{r}^2 \mathrm{r}\tilde{r} = 4\pi \rho_0 \frac{a^2 s^2}{s^2 - a^2} \left(s \arctan\left(\frac{r}{s}\right) - a \arctan\left(\frac{r}{a}\right) \right) \quad (B.9)$$

and the mass inside projected radius R is

$$
\begin{aligned}
M_{2D}(R) &= 2\pi \int_0^R \Sigma(\tilde{R})\tilde{R}\mathrm{r}\tilde{R} \\
&= 2\pi\Sigma_0 \frac{as}{s-a}\left(\sqrt{a^2+R^2} - a - \sqrt{s^2+R^2} + s\right).
\end{aligned}
$$
(B.10)

The dPIE has a finite total mass, given by

$$
M_{\mathrm{TOT}} = 2\pi^2\rho_0 \frac{a^2 s^2}{a+s} = 2\pi\Sigma_0 as.
$$
(B.11)

The half-mass radius defined by $M_{3D}(r_h) = M_{\mathrm{TOT}}/2$ obeys the relation

$$
s\arctan\left(\frac{r_h}{s}\right) - a\arctan\left(\frac{r_h}{a}\right) = \frac{\pi}{4}(s-a).
$$
(B.12)

For $a \ll r_h,\ s$

$$
r_h \approx s + \frac{\pi}{2}a
$$
(B.13)

i.e., $r_h \geq s$ with equality for $a \to 0$. Similarly, the effective radius defined by $M_{2D}(R_e) = M_{\mathrm{TOT}}/2$ is

$$
R_e = \frac{3}{4}\sqrt{a^2 + \frac{10}{3}as + s^2}
$$
(B.14)

which for $\eta^{-1} \ll 1$ ($a \ll s$) reduces to

$$
R_e \approx \frac{3}{4}s + \frac{5}{4}a,
$$
(B.15)

i.e., $R_e \approx (3/4)r_h$ for $a \to 0$.

B.4 The Potential

The gravitational potential $\Psi = -\Phi$ is

$$
\begin{aligned}
\Psi(r) &= G\int_r^\infty \frac{M_{3D}(r)}{r^2}\mathrm{r}r \\
&= 4\pi G\rho_0 \frac{a^2 s^2}{s^2-a^2}\left(\frac{s}{r}\arctan\left(\frac{r}{s}\right) - \frac{a}{r}\arctan\left(\frac{r}{a}\right) + \frac{1}{2}\ln\left(\frac{s^2+r^2}{a^2+r^2}\right)\right)
\end{aligned}
$$
(B.16)

and the central potential is

$$
\Psi(0) = 4\pi G\rho_0 \frac{a^2 s^2}{s^2-a^2}\ln\frac{s}{a}
$$
(B.17)

which is finite for finite a.

The projected potential is given by

$$
\begin{aligned}
\Psi(R) &= 2G \int_R^{R_L} \frac{M_{2D}(\tilde{R})}{\tilde{R}} \mathrm{r}\tilde{R} \\
&= 4\pi G \Sigma_0 \frac{as}{s-a} \\
&\quad \left(\sqrt{s^2 + R^2} - \sqrt{a^2 + R^2} + a \ln(a + \sqrt{a^2 + R^2}) - s \ln(s + \sqrt{s^2 + R^2}) \right) \\
&\quad + \text{constant},
\end{aligned}
\tag{B.18}
$$

where R_L is a limiting radius leading to the constant term. The deflection then is

$$
\alpha(R) = -\frac{2}{c^2} \frac{D_{LS}}{D_S} \frac{\mathrm{r}\Psi}{\mathrm{r}R} = \frac{8\pi G}{c^2} \frac{D_{LS}}{D_S} \Sigma_0 \frac{as}{s-a} f(R/a, R/s)
\tag{B.19}
$$

where

$$
f(R/a, R/s) \equiv \left(\frac{R/a}{1 + \sqrt{1^2 + (R/a)^2}} - \frac{R/s}{1 + \sqrt{1^2 + (R/s)^2}} \right).
\tag{B.20}
$$

B.5   Ellipticity

An elliptical projected mass distribution with ellipticity $\epsilon \equiv (A - B)/(A + B)$, where A and B are the semi major and minor axes respectively, can be introduced by substituting $R \to \tilde{R}$, with

$$
\tilde{R}^2 = \frac{X^2}{(1 + \epsilon)^2} + \frac{Y^2}{(1 - \epsilon)^2},
\tag{B.21}
$$

where X and Y are the spatial coordinates along the major and minor projected axes, respectively. With this definition of the ellipticity, the quantity $e \equiv 1 - B/A$ is related to ϵ through $e = 2\epsilon/(1 + \epsilon)$. For further details see Kassiola & Kovner (1993a), and note that in their notation the model discussed in this thesis corresponds to

$$
J_{as,3/2}^* = \frac{as}{s-a} (a^{-1} I_{a,1/2}^* - s^{-1} I_{s,1/2}^*).
\tag{B.22}
$$

and the analytical potential is given by solving

$$
\frac{\delta^2 \Phi}{\delta X^2} = \Re \frac{\delta J_{as,3/2}^*}{\delta X}; \qquad \frac{\delta^2 \Phi}{\delta Y^2} = \Im \frac{\delta J_{as,3/2}^*}{\delta Y}; \qquad \frac{\delta^2 \Phi}{\delta X \delta Y} = \Im \frac{\delta J_{as,3/2}^*}{\delta X} = \Re \frac{\delta J_{as,3/2}^*}{\delta Y}.
$$

B. THE DUAL PSEUDO ISOTHERMAL ELLIPTICAL MASS DISTRIBUTION

B.6   The dPIE in Lenstool

The dPIE is incorporated into the Lenstool software using the full elliptical expressions. The profile is given by specifying 8 parameters, its redshift z, its central position (R.A.,Dec.), its ellipticity and orientation $(\hat{\epsilon}, \theta_{\hat{\epsilon}})$, the core radius a, the scale radius s and a fiducial velocity dispersion σ_{dPIE}. This fiducial velocity dispersion is related to the deflection, α, by

$$\alpha = \frac{a+s}{s} E_0 f(R/a, R/s) \tag{B.23}$$

where

$$E_0 = 6\pi \frac{D_{LS}}{D_S} \frac{\sigma_{dPIE}^2}{c^2}. \tag{B.24}$$

In terms of Σ_0, a and s (or ρ_0, a and s) σ_{dPIE} is given by

$$\sigma_{\mathrm{dPIE}}^2 = \frac{4}{3} G \Sigma_0 \frac{as^2}{s^2 - a^2} = \frac{4}{3} G \pi \rho_0 \frac{a^2 s^3}{(s-a)(s+a)^2}. \tag{B.25}$$

The ellipticity is defined by

$$\hat{\epsilon} = \frac{A^2 - B^2}{A^2 + B^2} \tag{B.26}$$

corresponding to

$$e = 1 - \frac{B}{A} = 1 - \frac{\sqrt{1-\hat{\epsilon}}}{\sqrt{1+\hat{\epsilon}}}. \tag{B.27}$$

Its direction, $\theta_{\hat{\epsilon}}$, is measured anti-clockwise from the West and is related to the position angle (P.A.) by P.A.$= \theta_{\hat{\epsilon}} - 90°$.

B.7   Velocity Dispersions

Although σ_{dPIE} is a fiducial velocity dispersion, one wishes to relate it to the measured velocity dispersion of galaxies, assuming that their profile is described by a dPIE. In this derivation the most simple case is studied, assuming no anisotropy and a spherically symmetric dPIE profile. Even under these assumptions, the

central velocity dispersion and the velocity dispersion profiles for the dPIE cannot be expressed analytically and must be computed numerically. The velocity dispersion (Binney & Tremaine, 1987) is

$$\sigma^2(r) = \frac{G}{\rho(r)} \int_r^\infty \frac{M_{3D}(r)\rho(r)}{r^2} \mathrm{r}r \tag{B.28}$$

and the projected (line-of-sight) velocity dispersion is

$$\sigma_P^2(R) = \frac{2G}{\Sigma(R)} \int_R^\infty \frac{M_{3D}(r)\rho(r)}{r^2} \sqrt{r^2 - R^2} \mathrm{r}r. \tag{B.29}$$

The average line-of-sight velocity dispersion inside a given radius R can also be computed as

$$\langle \sigma_P^2 \rangle (R) = \frac{2\pi \int_0^R \sigma_P^2(R)\Sigma(R)R \mathrm{r}R}{M_{2D}(R)}. \tag{B.30}$$

This is the quantity measured by velocity dispersion measurements, and for galaxies the relevant radius corresponds roughly to the slit width used for the spectrograph. For the galaxies in the model (see Table 5.2) and a spectrograph resolution of $\sim 1''$, this corresponds to an observable region of $0.01 \lesssim (R/R_e) \lesssim 2$. In Figure B.1 the average line-of-sight velocity dispersion over the fiducial velocity dispersion σ_{dPIE} is plotted for different values of η. For a/s values similar to those found in the modelling, $\sqrt{\langle \sigma_P^2 \rangle}/\sigma_{\mathrm{dPIE}} \approx 0.85 \pm 0.10$ in the observable region.

Finally, to facilitate comparison with velocity dispersion profiles from different profiles, a 'standard' velocity dispersion σ_e is defined. This velocity dispersion is motivated by the velocity dispersion of the isothermal profile (for which $\sigma_{\mathrm{iso}}^2 = 2GM_{\mathrm{2D}}(R)/R$ for all R), calculated at the effective radius R_e:

$$\sigma_e^2 \equiv 2G \langle \Sigma \rangle_e R_e \tag{B.31}$$

where $\langle \Sigma \rangle_e$ is the mean surface density at R_e. For the dPIE profile, one finds that:

$$\frac{\sigma_e^2}{\sigma_{\mathrm{dPIE}}^2} = \frac{2(s^2 - a^2)}{s\sqrt{a^2 + (10/3)as + s^2}} \tag{B.32}$$

which goes to 2 when the core radius a goes to zero. For a/s values similar to those found in the modelling $\sigma_e/\sigma_{\mathrm{dPIE}} \approx 1.3 \pm 0.2$.

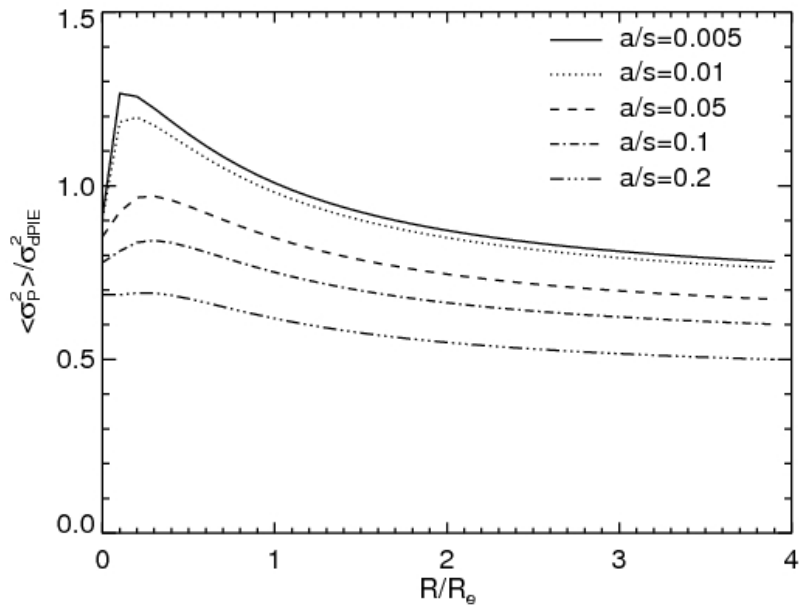# B. THE DUAL PSEUDO ISOTHERMAL ELLIPTICAL MASS DISTRIBUTION

Figure B.1 The squared measured velocity dispersion ($\langle \sigma_P^2 \rangle$) vs. the squared fiducial σ_{dPIE}^2. The ratio varies depending on both the observed radius R, and the ratio of a and s. For values similar to those found for the galaxies in the model (Table 5.2) one finds $\sqrt{\langle \sigma_P^2 \rangle} \approx (0.85 \pm 0.10) \sigma_{\mathrm{dPIE}}$.

Appendix C

Abell 2218 - Data

And our galaxy is only one of millions of billions

in this amazing and expanding universe.

Monty Python

This appendix lists the data used in the analysis of Abell 2218 in Chapter 5 and published in Elíasdóttir et al. (2007). The data were analysed by co-authors on that paper (Johan Richard: optical data, Kristian Pedersen/Danuta Paraficz: X-ray data), but are included here for completeness.

Data from several different sources is used for the lens modelling and analysis. The basis of the modelling is Advanced Camera for Surveys (ACS) data from the Hubble Space Telescope, which allows to identify and accurately locate multiply imaged systems. The cluster member catalogue is also selected using the ACS data and the magnitude of each cluster member is given in the Ingrid K-band of the William Herschel Telescope. In addition, a spectroscopic redshift has been obtained of a system using the Keck telescope and archival Chandra X-ray Observatory data have been used to produce an X-ray map of Abell 2218.

C.1   The Galaxy Catalogue

Cluster members were selected based on the ACS data using the characteristic cluster red-sequences (V-Z) and (I-Z) in two colour-magnitude diagrams and selecting objects lying within the red-sequences of both diagrams (see Figure C.1).
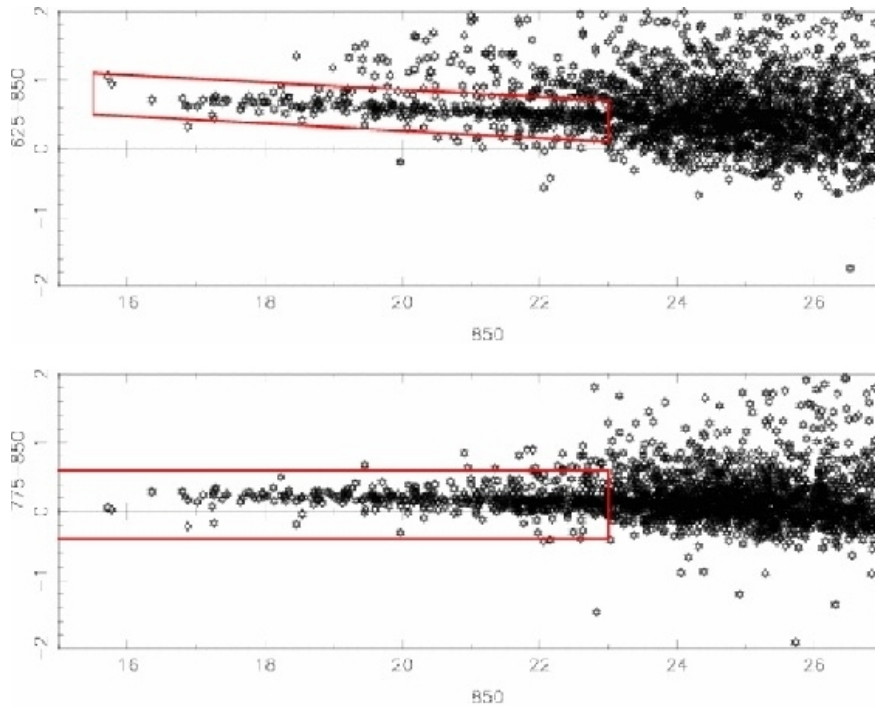

Figure C.1 Colour-magnitude diagrams, (V-Z) and (I-Z), used for selecting the cluster members (see § C.1). The red quadrilaterals define the red sequence and galaxies lying within are considered cluster members.

The ACS data were used to select the galaxy members due to their better photometric accuracy compared to the K-band data. Nevertheless, the catalogue is given in the K band since it is more representative of the galaxy population in elliptical galaxies. This selection gave 203 cluster galaxies down to $K = 19.6$. However, six galaxies were rejected from the catalogue, of which four have measured redshifts showing them to be background galaxies, leaving 197 cluster members.

C.2   X-ray Data

The X-ray data were taken with the Advanced CCD Imaging Spectrometer (ACIS) on NASA's Chandra X-ray Observatory. The ACIS is an array of 10 CCD's, capable of simultaneously imaging and measuring the energy of the incoming X-rays. Three images were combined taken at different epochs to construct the final X-ray map of Abell 2218. Two of the images were taken in October 1999 and one in August 2001, with 5960 s, 11560 s and 49240 s exposure times respectively. The data reduction was performed using standard pipelines from the Chandra Interactive Analysis of Observations (CIAO) software. The X-ray data is used for comparison with the lensing data in § 5.7.

C.3   Spectroscopic Redshift for an Arc

The Low Resolution Imager and Spectrograph (LRIS, Oke et al. (1995)) at Keck was used to measure the spectroscopic redshift of an arc, S8, to the south-east of the second dark matter clump (see Figure 5.1). Two exposures of 1800 seconds were obtained on June 29th 2007 with a $175'' \times 1''$ long slit placed along the brighter components of this arc (Figure C.2).   A 600 l mm^{-1} grism blazed at 4000 Å and a 400 l mm^{-1} grating blazed at 8500 Å were used in the blue and red channels of the instrument, both lightpaths being separated by a dichroic at 5600 Å. The corresponding dispersions are 0.6/1.85 Å and resolutions are 4.0/6.5 Å in the blue/red channel, respectively.

The resulting spectrum (see Figure C.3) is dominated by the light coming from the very bright neighbour cluster member at $z = 0.177$, yet shows Lyman-α in emission and UV absorption features of SiII, CI, CII and CIV from the arc, giving a redshift $z = 2.74$. These features are not compatible with any line at the redshift of the lens galaxy, giving a redshift class of 2 for this spectrum, with 75% probability of being correct, following the classification of Le Fevre et al. (1995). The model is not consistent with this object being multiply imaged, and when including it as a constraint as multiply imaged (using spots in the arclike structure as independent images), the model predicts additional counter images
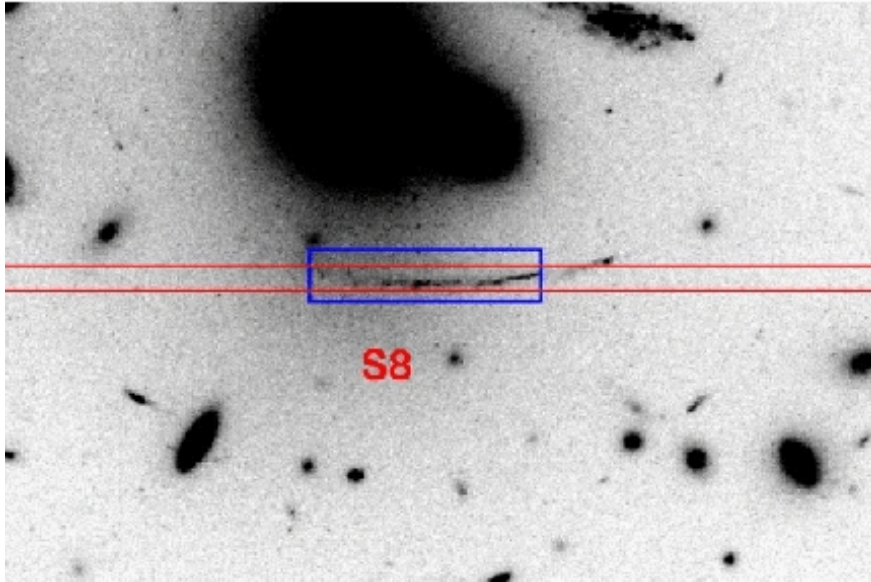
Figure C.2 The alignment of the slit for the spectra of S8. The box shows the area used to extract the spectrum (see Figure C.3).

which are not seen. The conclusion is therefore that although this arc is lensed, it is not multiply imaged, and it is included as a singly imaged system in the model constraints.
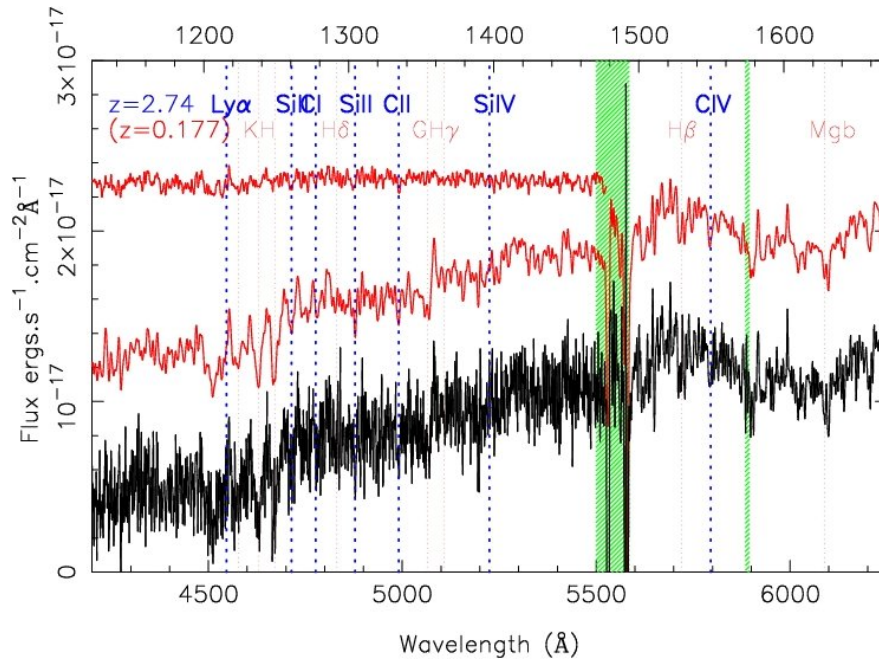
Figure C.3 The spectrum of system S8. The plot shows lines for the arc at $z = 2.74$ (blue) and the nearby galaxy (#617) at $z = 0.177$ (red). The spectrum shows Lyα absorption and emission and a number of absorption lines in the UV which are marked in the figure. At this redshift, $z = 2.74$, the model predicts S8 to be singly imaged.

Appendix D

List of Publications - Co-Author Statements

Great discoveries and improvements

invariably involve the cooperation of many minds.

Alexander Graham Bell (1847-1922)

This appendix lists papers of which the candidate is a first or co-author which are related to the thesis. Each section mentions where that paper features in the thesis and states the contribution of the candidate in each paper. The statements are signed by the candidate and one of the co-authors.

D.1   Paper I

Extinction Curves of Lensing Galaxies out to $z = 1$

by

Á. Elíasdóttir, J. Hjorth, S. Toft, I. Burud & D. Paraficz

The Astrophysical Journal Supplement Series, **166**, 443-469 (2006)

Chapter 3 is based mostly on this paper and Appendix A contains the data reduction from the paper. Á. E. did all the data analysis, wrote most of the software, including the Monte Carlo routine, simulations, plots and wrote all the text, excluding the data reduction chapter which is presented in Appendix A. The data reduction done by S. T. and the deconvolution by I. B. The observations were planned by S. T. and J. H. D. P. assisted with part of the data analysis.

Árdís Elíasdóttir   Jens Hjorth

D.2 Paper II

A Comparison of the Strong Lensing Properties of the Sérsic and the Navarro, Frenk and White Profiles

by

Á. Elíasdóttir & O. Möller

Journal of Cosmology and Astroparticle Physics, **07**, 006 (2007)

Chapter 4 is based mostly on this paper. Á. E. performed all the calculations (some were independently checked by O. M.), excluding the ones using multiple Einstein rings as constraints which were performed by O. M. The glens software was written by O. M but other code was written by Á. E. All the figures were done by Á. E. The text was written jointly by Á. E. and O. M.

Árdís Elíasdóttir   Ole Möller

D.3   Paper III

Where is the Matter in the Merging Cluster Abell 2218?

by

Á. Elíasdóttir, M. Limousin, J. Richard, J. Hjorth, J.-P. Kneib, P. Natarajan,
K. Pedersen, E. Jullo & D. Paraficz

The Astrophysical Journal, submitted (2007) (arXiv:0710.5636 - astro-ph)

Chapter 5, Appendix B and Appendix C are based mostly on this paper. Á. E. did the majority of the work, including all the lensing analysis (excluding the weak lensing analysis discussed in § 5.4.6) and the analysis of the cluster members in velocity space. The X-ray data were analysed by K. P. The data (included in Appendix C) were acquired and reduced by various co-authors (J. R.: optical data, K. P./D. P.: X-ray data). Appendix B is based on an unpublished paper by J. H. and J.-P. K. All figures were made by Á. E. excluding Figure 5.9 and the figures in Appendix C. The text was mostly written by Á. E. Other authors contributed to the paper in various ways.

Árdís Elíasdóttir   Marceau Limousin

D.4 Paper IV

The Host Galaxy Cluster of the Short Gamma-Ray Burst GRB 050509B

by

K. Pedersen, Á. Elíasdóttir, J. Hjorth, R. Starling, J. M. Castro Cerón, J. P. U. Fynbo, J. Gorosabel, P. Jakobsson, J. Sollerman & D. Watson

The Astrophysical Journal, **634**, L17-L20 (2005)

Chapter 6 is based on a section in this paper. The paper deals with the environment of the gamma ray burst GRB 050509B and the majority of the work was done by K. P. The section on the lensing analysis of the host galaxy cluster, which is included in Chapter 6, was done and written by Á. E. Other authors contributed to the work in various ways.

Árdís Elíasdóttir

Kristian Pedersen

D.5 Paper V

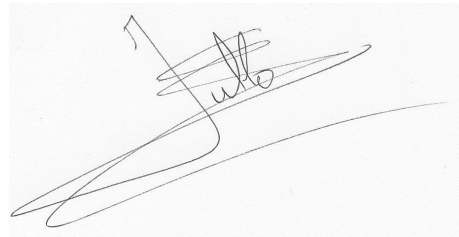### A Bayesian Approach to Strong Lensing Modelling of Galaxy Clusters

by

E. Jullo, J.-P. Kneib, M. Limousin, Á. Elíasdóttir, P. J. Marshall & T. Verdugo

New Journal of Physics, **"Gravitational Lensing" Focus Issue**, accepted (2007)

Chapter 4, § 4.5, is based in part on this paper. The paper discusses the implementation of a Bayesian MCMC sampler into the publicly available lensing software Lenstool and compares three different kinds of matter profiles incorporated into the software using simulated data. E. J. did the vast majority of the work. Á. E. was deeply involved in the testing of the software. The code needed for the Sérsic profile to be included in Lenstool was written by Á. E. and she contributed to the text, especially the part dealing with the description of the Sérsic profile. Other authors contributed to the paper in various ways.

Árdís Elíasdóttir   Eric Jullo

D.6   Paper VI

Combining Strong and Weak Gravitational Lensing in Abell 1689

by

M. Limousin, J. Richard, E. Jullo, J.-P. Kneib, B. Fort, G. Soucail,
Á. Elíasdóttir, P. Natarajan, R. S. Ellis, I. Smail, O. Czoske, G. P. Smith,
P. Hudelot, S. Bardeau, H. Ebeling, E. Egami & K. .K. Knudsen

The Astrophysical Journal, **668**, 643-666 (2007)

This work is briefly discussed in Chapter 6. It discusses the combined strong and weak lensing analysis of the galaxy cluster Abell 1689. M. L. did the vast majority of the work. Á. E. did the NFW fitting of the strong lensing profiles, assisted with the debugging of the lensing code and contributed to the text. Other authors contributed to the paper in various ways.

Árdís Elíasdóttir   Marceau Limousin

D. LIST OF PUBLICATIONS - CO-AUTHOR STATEMENTS

References

Abdelsalam, H. M., Saha, P., & Williams, L. L. R. 1998, AJ, 116, 1541 118, 137, 139

Abell, G. O. 1958, ApJS, 3, 211 118

Abell, G. O., Corwin, Jr., H. G., & Olowin, R. P. 1989, ApJS, 70, 1 118

Alcalde, D., Mediavilla, E., Moreau, O., Muñoz, J. A., Libbrecht, C., Goicoechea, L. J., Surdej, J., et al. 2002, ApJ, 572, 729 54

Angonin-Willaime, M.-C., Vanderriest, C., Courbin, F., Burud, I., Magain, P., & Rigaut, F. 1999, A&A, 347, 434 66

Bacon, D. J., Refregier, A. R., & Ellis, R. S. 2000, MNRAS, 318, 625 8, 18, 21

Bade, N., Siebert, J., Lopez, S., Voges, W., & Reimers, D. 1997, A&A, 317, L13 60

Baltz, E. A., Marshall, P., & Oguri, M. 2007, ArXiv e-prints:0705.0682 111

Bardeau, S., Soucail, G., Kneib, J.-P., Czoske, O., Ebeling, H., Hudelot, P., Smail, I., & Smith, G. P. 2007, A&A, 470, 449 139, 140

Barnothy, J. & Barnothy, M. F. 1968, Science, 162, 348 6

Barnothy, J. M. & Barnothy, M. F. 1972, ApJ, 174, 477 6

Bartelmann, M. 1996, A&A, 313, 697 92

REFERENCES

Beaulieu, J.-P., Bennett, D. P., Fouqué, P., Williams, A., Dominik, M., Jorgensen, U. G., Kubas, D., et al. 2006, Nature, 439, 437 8, 18, 20

Bechtold, J. & Yee, H. K. C. 1995, AJ, 110, 1984 55

Bertin, E. & Arnouts, S. 1996, A&AS, 117, 393 173

Bianchi, L., Clayton, G. C., Bohlin, R. C., Hutchings, J. B., & Massey, P. 1996, ApJ, 471, 203 27

Binney, J. & Tremaine, S. 1987, Galactic dynamics (Princeton, NJ, Princeton University Press, 1987, 747 p.) 176, 181

Bliokh, P. V. & Minakov, A. A. 1975, Ap&SS, 34, L7 6

Bloom, J. S., Prochaska, J. X., Pooley, D., Blake, C. H., Foley, R. J., Jha, S., Ramirez-Ruiz, E., et al. 2006, ApJ, 638, 354 158, 159

Bolzonella, M., Miralles, J.-M., & Pelló, R. 2000, A&A, 363, 476 137

Bourassa, R. R. & Kantowski, R. 1975, ApJ, 195, 13 6

Bradač, M., Clowe, D., Gonzalez, A. H., Marshall, P., Forman, W., Jones, C., Markevitch, M., Randall, S., Schrabback, T., & Zaritsky, D. 2006, ApJ, 652, 937 118

Brainerd, T. G., Blandford, R. D., & Smail, I. 1996, ApJ, 466, 623 128, 177

Broadhurst, T., Benítez, N., Coe, D., Sharon, K., Zekser, K., White, R., Ford, H., et al. 2005, ApJ, 621, 53 90, 92, 96

Bullock, J. S., Kolatt, T. S., Sigad, Y., Somerville, R. S., Kravtsov, A. V., Klypin, A. A., Primack, J. R., & Dekel, A. 2001, MNRAS, 321, 559 157

Burud, I., Courbin, F., Lidman, C., Jaunsen, A. O., Hjorth, J., Ostensen, R., Andersen, et al. 1998a, ApJ, 501, L5+ 49, 60, 62

Burud, I., Stabell, R., Magain, P., Courbin, F., Østensen, R., Refsdal, S., Remy, M., & Teuber, J. 1998b, A&A, 339, 701 173

Caon, N., Capaccioli, M., & D'Onofrio, M. 1993, MNRAS, 265, 1013 90

Cardelli, J. A., Clayton, G. C., & Mathis, J. S. 1989, ApJ, 345, 245 26, 32

Cardone, V. F. 2004, A&A, 415, 839 93, 94

Cavaliere, A. & Fusco-Femiano, R. 1978, A&A, 70, 677 151

Chae, K.-H., Biggs, A. D., Blandford, R. D., Browne, I. W., de Bruyn, A. G., Fassnacht, C. D., Helbig, P., et al. 2002, Physical Review Letters, 89, 151301 111

Christian, C. A., Crabtree, D., & Waddell, P. 1987, ApJ, 312, 45 54

Chwolson, O. 1924, Astron. Nachr., 221, 329 6

Ciotti, L. 1991, A&A, 249, 99 90

Ciotti, L. & Bertin, G. 1999, A&A, 352, 447 93

Clowe, D., Bradač, M., Gonzalez, A. H., Markevitch, M., Randall, S. W., Jones, C., & Zaritsky, D. 2006, ApJ, 648, L109 18, 19

Comerford, J. M. & Natarajan, P. 2007, MNRAS, 379, 190 98, 106, 108, 111, 112

Corrigan, R. T., Irwin, M. J., Arnaud, J., Fahlman, G. G., Fletcher, J. M., Hewett, P. C., Hewitt, J. N., et al. 1991, AJ, 102, 34 50

de Propris, R., Stanford, S. A., Eisenhardt, P. R., Dickinson, M., & Elston, R. 1999, AJ, 118, 719 128

Devillard, N. 1997, The Messenger, 87, 19 173

Dye, S., Smail, I., Swinbank, A. M., Ebeling, H., & Edge, A. C. 2007, MNRAS, 379, 308 111

Ebbels, T., Ellis, R., Kneib, J.-P., Leborgne, J.-F., Pello, R., Smail, I., & Sanahuja, B. 1998, MNRAS, 295, 75 124

Ebbels, T. M. D., Le Borgne, J.-F., Pello, R., Ellis, R. S., Kneib, J.-P., Smail, I., & Sanahuja, B. 1996, MNRAS, 281, L75 123

REFERENCES

Egami, E., Kneib, J.-P., Rieke, G. H., Ellis, R. S., Richard, J., Rigby, J., Papovich, C., et al. 2005, ApJ, 618, L5 23, 119, 124

Einstein, A. 1911, Ann. Phys. (Leipzig), 35, 898 5

—. 1916, Ann. Phys. (Leipzig), 49, 769 6

—. 1922, Vier Vorlesungen über Relativitätstheorie (Braunschweig, Germany: Vieweg) 6

—. 1936, Science, 84, 506 6

Elíasdóttir, Á., Hjorth, J., Toft, S., Burud, I., & Paraficz, D. 2006, ApJS, 166, 443 23, 25, 96, 167

Elíasdóttir, Á., Limousin, M., Richard, J., Hjorth, J., Kneib, J.-P., Natarajan, P., Pedersen, K., Jullo, E., & Paraficz, D. 2007, ArXiv e-prints:0710.5636 17, 117, 183

Elíasdóttir, Á. & Möller, O. 2007, Journal of Cosmology and Astro-Particle Physics, 7, 6 89

Ellis, R., Santos, M. R., Kneib, J.-P., & Kuijken, K. 2001, ApJ, 560, L119 118, 119, 124

Ellison, S. L., Hall, P. B., & Lira, P. 2005, AJ, 130, 1345 27

Engelbracht, C. W. & Eisenstein, D. J. 2005, GRB Coordinates Network, 3420, 1 158

Falco, E. E., Impey, C. D., Kochanek, C. S., Lehár, J., McLeod, B. A., Rix, H.-W., Keeton, C. R., Muñoz, J. A., & Peng, C. Y. 1999, ApJ, 523, 617 23, 25, 28, 55, 56, 59, 60, 66, 71, 72

Falco, E. E., Lehar, J., Perley, R. A., Wambsganss, J., & Gorenstein, M. V. 1996, AJ, 112, 897 50, 54

Falco, E. E., Lehar, J., & Shapiro, I. I. 1997, AJ, 113, 540 17, 49, 66

Fassnacht, C. D. & Cohen, J. G. 1998, AJ, 115, 377 60

Ferreras, I., Saha, P., & Williams, L. L. R. 2005, ApJ, 623, L5 90

Fischer, P., Bernstein, G., Rhee, G., & Tyson, J. A. 1997, AJ, 113, 521 7

Fitzpatrick, E. L. 1999, PASP, 111, 63 26

Gal, R. R., de Carvalho, R. R., Lopes, P. A. A., Djorgovski, S. G., Brunner, R. J.,
    Mahabal, A., & Odewahn, S. C. 2003, AJ, 125, 2064 158

Garrett, M. A., Muxlow, T. W. B., Patnaik, A. R., & Walsh, D. 1994, MNRAS,
    269, 902 71

Gavazzi, R. & Soucail, G. 2007, A&A, 462, 459 118

Gehrels, N., Sarazin, C. L., O'Brien, P. T., Zhang, B., Barbier, L., Barthelmy,
    S. D., Blustin, A., et al. 2005, Nature, 437, 851 158, 159

Gil-Merino, R., Wambsganss, J., Goicoechea, L. J., & Lewis, G. F. 2005, A&A,
    432, 83 54

Girardi, M., Fadda, D., Escalera, E., Giuricin, G., Mardirossian, F., & Mezzetti,
    M. 1997, ApJ, 490, 56 152

Goicoechea, L. J., Gil-Merino, R., & Ullán, A. 2005, MNRAS, 360, L60 25, 28

Golse, G. & Kneib, J.-P. 2002, A&A, 390, 821 92, 114, 115

Golse, G., Kneib, J.-P., & Soucail, G. 2002, A&A, 387, 788 21, 22

Goudfrooij, P. 2000, in Astronomical Society of the Pacific Conference Series, Vol.
    209, IAU Colloq. 174: Small Galaxy Groups, ed. M. J. Valtonen & C. Flynn,
    74–+ 25, 28

Goudfrooij, P., de Jong, T., Hansen, L., & Norgaard-Nielsen, H. U. 1994, MN-
    RAS, 271, 833 28, 67

Graham, A. W. & Guzmán, R. 2003, AJ, 125, 2936 90

REFERENCES

Greenfield, P. D., Roberts, D. H., & Burke, B. F. 1985, ApJ, 293, 370 6

Gregg, M. D., Wisotzki, L., Becker, R. H., Maza, J., Schechter, P. L., White, R. L., Brotherton, M. S., & Winn, J. N. 2000, AJ, 119, 2535 49, 62

Halkola, A., Seitz, S., & Pannella, M. 2006, MNRAS, 372, 1425 106, 126

—. 2007, ApJ, 656, 739 128

Hayashi, E., Navarro, J. F., Power, C., Jenkins, A., Frenk, C. S., White, S. D. M., Springel, V., Stadel, J., & Quinn, T. R. 2004, MNRAS, 355, 794 90

Hege, E. K., Hubbard, E. N., Strittmatter, P. A., & Worden, S. P. 1981, ApJ, 248, L1 54

Hennawi, J. F., Dalal, N., Bode, P., & Ostriker, J. P. 2007, ApJ, 654, 714 108

Hewitt, J. N., Turner, E. L., Lawrence, C. R., Schneider, D. P., & Brody, J. P. 1992, AJ, 104, 968 66, 67

Hjorth, J., Burud, I., Jaunsen, A. O., Schechter, P. L., Kneib, J.-P., Andersen, M. I., Korhonen, H., et al. 2002, ApJ, 572, L11 62

Hjorth, J., Sollerman, J., Gorosabel, J., Granot, J., Klose, S., Kouveliotou, C., Melinder, J., et al. 2005, ApJ, 630, L117 158, 160, 161

Hogg, D. W. 2000, arXiv:astro-ph/9905116v4 5

Huchra, J., Gorenstein, M., Kent, S., Shapiro, I., Smith, G., Horine, E., & Perley, R. 1985, AJ, 90, 691 50

Irwin, M. J., Webster, R. L., Hewett, P. C., Corrigan, R. T., & Jedrzejewski, R. I. 1989, AJ, 98, 1989 50, 54

Jakobsson, P., Hjorth, J., Fynbo, J. P. U., Weidinger, M., Gorosabel, J., Ledoux, C., Watson, D., et al. 2004, A&A, 427, 785 28

Jaunsen, A. O. & Hjorth, J. 1997, A&A, 317, L39 28

Jørgensen, I., Franx, M., Hjorth, J., & van Dokkum, P. G. 1999, MNRAS, 308, 833 134, 135, 136

Jullo, E., Kneib, J.-P., Limousin, M., Elíasdóttir, Á., Marshall, P., & Verdugo, T. 2007, New Journal of Physics, accepted (arXiv:0706.0048) 89, 114, 115, 119, 126, 127, 139, 141, 142, 153, 176

Kann, D. A., Klose, S., & Zeh, A. 2006, ApJ, 641, 993 25, 28

Kassiola, A. & Kovner, I. 1993a, ApJ, 417, 450 175, 179

—. 1993b, ApJ, 417, 474 127

Katz, C. A. & Hewitt, J. N. 1993, ApJ, 409, L9 67

Keeton, C. R. 2001, arXiv:astro-ph/0102340v1 159

Keeton, C. R., Falco, E. E., Impey, C. D., Kochanek, C. S., Lehár, J., McLeod, B. A., Rix, H.-W., Muñoz, J. A., & Peng, C. Y. 2000, ApJ, 542, 74 6

Keeton, C. R. & Kochanek, C. S. 1998, ApJ, 495, 157 86, 175

Klimov, Y. 1963, Sov. Phys. Dokl., 8, 119 6

Kling, T. P., Dell'Antonio, I., Wittman, D., & Tyson, J. A. 2005, ApJ, 625, 643 106

Kneib, J.-P. 1993, PhD thesis, Ph. D. thesis, Université Paul Sabatier, Toulouse, (1993) 114, 126

Kneib, J.-P., Cohen, J. G., & Hjorth, J. 2000, ApJ, 544, L35 62

Kneib, J.-P., Ellis, R. S., Santos, M. R., & Richard, J. 2004a, ApJ, 607, 697 23, 119, 124

Kneib, J.-P., Ellis, R. S., Smail, I., Couch, W. J., & Sharples, R. M. 1996, ApJ, 471, 643 118, 123, 124, 126, 137, 175

Kneib, J.-P., Hudelot, P., Ellis, R. S., Treu, T., Smith, G. P., Marshall, P., Czoske, O., Smail, I., & Natarajan, P. 2003, ApJ, 598, 804 90, 96, 106

REFERENCES

Kneib, J. P., Mellier, Y., Pello, R., Miralda-Escude, J., Le Borgne, J.-F., Boehringer, H., & Picat, J.-P. 1995, A&A, 303, 27 118

Kneib, J.-P., van der Werf, P. P., Kraiberg Knudsen, K., Smail, I., Blain, A., Frayer, D., Barnard, V., & Ivison, R. 2004b, MNRAS, 349, 1211 124, 137

Kochanek, C. S. 1996, ApJ, 466, 638 141, 142

—. 2004, ApJ, 605, 58 54

Kochanek, C. S., Falco, E. E., Impey, C. D., Lehár, J., McLeod, B. A., Rix, H.-W., Keeton, C. R., Muñoz, J. A., & Peng, C. Y. 2000, ApJ, 543, 131 84

Koopmans, L. V. E., Treu, T., Bolton, A. S., Burles, S., & Moustakas, L. A. 2006, ApJ, 649, 599 18, 90, 111

Koopmans, L. V. E., Treu, T., Fassnacht, C. D., Blandford, R. D., & Surpi, G. 2003, ApJ, 599, 70 118

Kouveliotou, C., Meegan, C. A., Fishman, G. J., Bhat, N. P., Briggs, M. S., Koshut, T. M., Paciesas, W. S., & Pendleton, G. N. 1993, ApJ, 413, L101 157

Krisciunas, K., Hastings, N. C., Loomis, K., McMillan, R., Rest, A., Riess, A. G., & Stubbs, C. 2000, ApJ, 539, 658 27, 82

Kristian, J., Groth, E. J., Shaya, E. J., Schneider, D. P., Holtzman, J. A., Baum, W. A., Campbell, B., et al. 1993, AJ, 106, 1330 49

Krolik, J. H. 1999, Active galactic nuclei : from the central black hole to the galactic environment (Active galactic nuclei : from the central black hole to the galactic environment /Julian H. Krolik. Princeton, N. J. : Princeton University Press, c1999.) 36

Kundic, T., Cohen, J. G., Blandford, R. D., & Lubin, L. M. 1997a, AJ, 114, 507 54

Kundic, T., Hogg, D. W., Blandford, R. D., Cohen, J. G., Lubin, L. M., & Larkin, J. E. 1997b, AJ, 114, 2276 55

Kundic, T., Turner, E. L., Colley, W. N., Gott, J. R. I., Rhoads, J. E., Wang, Y., Bergeron, L. E., et al. 1997c, ApJ, 482, 75 6, 21

Lawrence, C. R., Elston, R., Januzzi, B. T., & Turner, E. L. 1995, AJ, 110, 2570 66

Lawrence, C. R., Neugebauer, G., & Matthews, K. 1993, AJ, 105, 17 71

Lawrence, C. R., Neugebauer, G., Weir, N., Matthews, K., & Patnaik, A. R. 1992, MNRAS, 259, 5P 55

Lawrence, C. R., Schneider, D. P., Schmidet, M., Bennett, C. L., Hewitt, J. N., Burke, B. F., Turner, E. L., & Gunn, J. E. 1984, Science, 223, 46 71

Le Borgne, J. F., Pello, R., & Sanahuja, B. 1992, A&AS, 95, 87 123, 152

Le Fevre, O., Crampton, D., Lilly, S. J., Hammer, F., & Tresse, L. 1995, ApJ, 455, 60 185

Lebach, D., Corey, B., Shapiro, I., Ratner, M., Webber, J., Rogers, A., Davis, J., & Herring, T. 1995, Phys. Rev. Lett., 75, 1439 6

Lee, W. H., Ramirez-Ruiz, E., & Granot, J. 2005, ApJ, 630, L165 159

Lehár, J., Falco, E. E., Kochanek, C. S., McLeod, B. A., Muñoz, J. A., Impey, C. D., Rix, H.-W., Keeton, C. R., & Peng, C. Y. 2000, ApJ, 536, 584 49, 96

Lewis, G. F. & Gil-Merino, R. 2006, ApJ, 645, 835 96

Li, L.-X. & Ostriker, J. P. 2002, ApJ, 566, 652 111

Liebes, S. 1964, Phys. Rev., 133, B835 6

Limousin, M., Kneib, J. P., Bardeau, S., Natarajan, P., Czoske, O., Smail, I., Ebeling, H., & Smith, G. P. 2007a, A&A, 461, 881 141

Limousin, M., Richard, J., Kneib, J. ., Jullo, E., Fort, B., Soucail, G., Elíasdóttir, Á., et al. 2007b, ApJ, 668, 643 17, 18, 98, 99, 106, 112, 118, 126, 128, 139, 155, 156, 157, 175, 176

REFERENCES

Limousin, M., Sommer-Larsen, J., Natarajan, P., & Milvang-Jensen, B. 2007c, ArXiv e-prints:0706.3149 141

Lynds, R. & Petrosian, V. 1986, in Bulletin of the American Astronomical Society, Vol. 18, Bulletin of the American Astronomical Society, 1014–+ 7

MacAlpine, G. M. & Feldman, F. R. 1982, ApJ, 261, 412 59

Madau, P., Pozzetti, L., & Dickinson, M. 1998, ApJ, 498, 106 26

Magain, P., Courbin, F., & Sohy, S. 1998, ApJ, 494, 472 173

Malhotra, S. 1997, ApJ, 488, L101+ 27

Mandelbaum, R., Tasitsiomi, A., Seljak, U., Kravtsov, A. V., & Wechsler, R. H. 2005, MNRAS, 362, 1451 148

Markevitch, M., Gonzalez, A. H., Clowe, D., Vikhlinin, A., Forman, W., Jones, C., Murray, S., & Tucker, W. 2004, ApJ, 606, 819 19

Marshall, P., Blandford, R., & Sako, M. 2005, New Astronomy Review, 49, 387 87

Massa, D., Savage, B. D., & Fitzpatrick, E. L. 1983, ApJ, 266, 662 26

Maughan, B. J., Jones, C., Jones, L. R., & Van Speybroeck, L. 2007, ApJ, 659, 1125 112

McGough, C., Clayton, G. C., Gordon, K. D., & Wolff, M. J. 2005, ApJ, 624, 118 34

Meneghetti, M., Argazzi, R., Pace, F., Moscardini, L., Dolag, K., Bartelmann, M., Li, G., & Oguri, M. 2007, A&A, 461, 25 133

Meneghetti, M., Jain, B., Bartelmann, M., & Dolag, K. 2005, MNRAS, 362, 1301 118

Merritt, D., Graham, A. W., Moore, B., Diemand, J., & Terzić, B. 2006, AJ, 132, 2685 96

Merritt, D., Navarro, J. F., Ludlow, A., & Jenkins, A. 2005, ApJ, 624, L85 90, 93, 108, 113

Merritt, D. & Valluri, M. 1996, ApJ, 471, 82 176

Meylan, G., Jetzer, P., North, P., Schneider, P., Kochanek, C. S., & Wambsganss, J., eds. 2006, Gravitational Lensing: Strong, Weak and Micro, ed. G. Meylan, P. Jetzer, P. North, P. Schneider, C. S. Kochanek, & J. Wambsganss 5

Motta, V., Mediavilla, E., Muñoz, J. A., Falco, E., Kochanek, C. S., Arribas, S., García-Lorenzo, B., Oscoz, A., & Serra-Ricart, M. 2002, ApJ, 574, 719 28, 82

Muñoz, J. A., Falco, E. E., Kochanek, C. S., McLeod, B. A., & Mediavilla, E. 2004, ApJ, 605, 614 28

Murphy, M. T. & Liske, J. 2004, MNRAS, 354, L31 25, 27

Myers, S. T., Rusin, D., Fassnacht, C. D., Blandford, R. D., Pearson, T. J., Readhead, A. C. S., Jackson, et al. 1999, AJ, 117, 2565 49, 56

Nadeau, D., Yee, H. K. C., Forrest, W. J., Garnett, J. D., Ninkov, Z., & Pipher, J. L. 1991, ApJ, 376, 430 23, 28, 30

Nair, S. & Garrett, M. A. 1997, MNRAS, 284, 58 71

Nandy, K., Morgan, D. H., Willis, A. J., Wilson, R., & Gondhalekar, P. M. 1981, MNRAS, 196, 955 26

Narayan, R. & Bartelmann, M. 1996, arXiv:astro-ph/9606001v2 5

Natarajan, P., De Lucia, G., & Springel, V. 2007, MNRAS, 376, 180 118, 137, 139, 175

Natarajan, P. & Kneib, J.-P. 1997, MNRAS, 287, 833 133

Natarajan, P., Kneib, J.-P., & Smail, I. 2002a, ApJ, 580, L11 141

Natarajan, P., Kneib, J.-P., Smail, I., & Ellis, R. S. 1998, ApJ, 499, 600 141

Natarajan, P., Loeb, A., Kneib, J.-P., & Smail, I. 2002b, ApJ, 580, L17 118, 141

REFERENCES

Navarro, J. F., Frenk, C. S., & White, S. D. M. 1995, MNRAS, 275, 720 90, 91

—. 1996, ApJ, 462, 563 91

Navarro, J. F., Hayashi, E., Power, C., Jenkins, A. R., Frenk, C. S., White, S. D. M., Springel, V., Stadel, J., & Quinn, T. R. 2004, MNRAS, 349, 1039 90

Oguri, M. 2007, ApJ, 660, 1 21

Oguri, M. & Keeton, C. R. 2004, ApJ, 610, 663 90

Oke, J. B., Cohen, J. G., Carr, M., Cromer, J., Dingizian, A., Harris, F. H., Labrecque, S.,et al. 1995, PASP, 107, 375 185

Östman, L., Goobar, A., & Mörtsell, E. 2006, A&A, 450, 971 27, 82

Patnaik, A. R., Browne, I. W. A., Walsh, D., Chaffee, F. H., & Foltz, C. B. 1992, MNRAS, 259, 1P 55, 56

Patnaik, A. R. & Narasimha, D. 2001, MNRAS, 326, 1403 55

Pedersen, K., Elíasdóttir, Á., Hjorth, J., Starling, R., Castro Cerón, J. M., Fynbo, J. P. U., Gorosabel, J., et al. 2005, ApJ, 634, L17 155, 159, 161

Pei, Y. C. 1992, ApJ, 395, 130 79

Pei, Y. C., Fall, S. M., & Bechtold, J. 1991, ApJ, 378, 6 27

Perlmutter, S., Aldering, G., Goldhaber, G., Knop, R. A., Nugent, P., Castro, P. G., Deustua, S., et al. 1999, ApJ, 517, 565 26

Perlmutter, S., Gabi, S., Goldhaber, G., Goobar, A., Groom, D. E., Hook, I. M., Kim, A. G., et al. 1997, ApJ, 483, 565 27

Prevot, M. L., Lequeux, J., Prevot, L., Maurice, E., & Rocca-Volmerange, B. 1984, A&A, 132, 389 27

Refsdal, S. 1964a, Mon. Not. R. Astron. Soc., 128, 295 6

—. 1964b, Mon. Not. R. Astron. Soc., 128, 307 6

—. 1966a, Mon. Not. R. Astron. Soc., 132, 101 6

—. 1966b, Mon. Not. R. Astron. Soc., 132, 101 6

Remy, M., Surdej, J., Smette, A., & Claeskens, J.-F. 1993, A&A, 278, L19 55

Richard, J., Kneib, J.-P., Jullo, E., Covone, G., Limousin, M., Ellis, R., Stark, D., et al. 2007, ApJ, 662, 781 175

Riess, A. G., Filippenko, A. V., Challis, P., Clocchiatti, A., Diercks, A., Garnavich, P. M., Gilliland, R. L., et al. 1998, AJ, 116, 1009 26

Riess, A. G., Press, W. H., & Kirshner, R. P. 1996a, ApJ, 473, 88 25, 27

—. 1996b, ApJ, 473, 588 27, 82

Rix, H.-W., Schneider, D. P., & Bahcall, J. N. 1992, AJ, 104, 959 49

Rusin, D., Kochanek, C. S., Falco, E. E., Keeton, C. R., McLeod, B. A., Impey, C. D., Lehár, J., et al. 2003, ApJ, 587, 143 49, 75

Rusin, D., Norbury, M., Biggs, A. D., Marlow, D. R., Jackson, N. J., Browne, I. W. A., Wilkinson, P. N., & Myers, S. T. 2002, MNRAS, 330, 205 17, 49, 54, 56, 57, 59, 90

Sand, D. J., Treu, T., Smith, G. P., & Ellis, R. S. 2004, ApJ, 604, 88 90

Schechter, P. L., Bailyn, C. D., Barr, R., Barvainis, R., Becker, C. M., Bernstein, G. M., Blakeslee, J. P., et al. 1997, ApJ, 475, L85+ 21, 55, 118

Schechter, P. L. & Wambsganss, J. 2002, ApJ, 580, 685 96

Schneider, D. P., Gunn, J. E., Turner, E. L., Lawrence, C. R., Hewitt, J. N., Schmidt, M., & Burke, B. F. 1986, AJ, 91, 991 71

Schneider, D. P., Lawrence, C. R., Schmidt, M., Gunn, J. E., Turner, E. L., Burke, B. F., & Dhawan, V. 1985, ApJ, 294, 66 71

Schneider, D. P., Turner, E. L., Gunn, J. E., Hewitt, J. N., Schmidt, M., & Lawrence, C. R. 1988, AJ, 95, 1619 50

REFERENCES

Schneider, P., Ehlers, J., & Falco, E. E. 1992, Gravitational Lenses (Gravitational Lenses, XIV, 560 pp. 112 figs.. Springer-Verlag Berlin Heidelberg New York. Also Astronomy and Astrophysics Library) 5, 14, 93

Sersic, J. L. 1968, Atlas de galaxias australes (Cordoba, Argentina: Observatorio Astronomico, 1968) 90

Smail, I. & Dickinson, M. 1995, ApJ, 455, L99+ 118

Smail, I., Ellis, R. S., Dressler, A., Couch, W. J., Oemler, A. J., Sharples, R. M., & Butcher, H. 1997, ApJ, 479, 70 118

Smail, I., Hogg, D. W., Blandford, R., Cohen, J. G., Edge, A. C., & Djorgovski, S. G. 1995, MNRAS, 277, 1 118

Smith, G. P., Kneib, J.-P., Smail, I., Mazzotta, P., Ebeling, H., & Czoske, O. 2005, MNRAS, 359, 417 119, 120, 126, 137, 139, 175

Soldner, J. 1805, Berliner Astronomisches Jahrbuch, 1804, 161 5

Soucail, G., Fort, B., Mellier, Y., & Picat, J. P. 1987, A&A, 172, L14 7

Soucail, G., Kneib, J.-P., & Golse, G. 2004, A&A, 417, L33 21, 118, 119

Sullivan, M., Ellis, R. S., Aldering, G., Amanullah, R., Astier, P., Blanc, G., Burns, M. S., et al. 2003, MNRAS, 340, 1057 82, 84

Surdej, J., Swings, J.-P., Magain, P., Courvoisier, T. J.-L., & Borgeest, U. 1987, Nature, 329, 695 59

Swinbank, A. M., Smith, J., Bower, R. G., Bunker, A., Smail, I., Ellis, R. S., Smith, G. P., et al. 2003, ApJ, 598, 162 124

Toft, S., Hjorth, J., & Burud, I. 2000, A&A, 357, 115 28, 56

Tonry, J. L. 1998, AJ, 115, 1 55

Tonry, J. L. & Kochanek, C. S. 1999, AJ, 117, 2034 66

Udalski, A. 2003, ApJ, 590, 284 26

van Dokkum, P. G. 2001, PASP, 113, 1420 173

Vanden Berk, D. E., Richards, G. T., Bauer, A., Strauss, M. A., Schneider, D. P., Heckman, T. M., York, D. G., et al. 2001, AJ, 122, 549 36

Verdugo, T., de Diego, J. A., & Limousin, M. 2007, ApJ, 664, 702 112

Walsh, D., Carswell, R. F., & Weymann, R. J. 1979, Nature, 279, 381 6

Wambsganss, J. 1998, Living Reviews in Relativity, 1, 12 5

Wambsganss, J., Bode, P., & Ostriker, J. P. 2004, ApJ, 606, L93 8, 21

Wang, L. 2005, ApJ, 635, L33 82

Wang, X., Wang, L., Pain, R., Zhou, X., & Li, Z. 2006, ApJ, 645, 488 27, 82

Wayth, R. B., Warren, S. J., Lewis, G. F., & Hewett, P. C. 2005, MNRAS, 360, 1333 92

Weymann, R. J., Latham, D., Roger, J., Angel, P., Green, R. F., Liebert, J. W., Turnshek, D. A., Turnshek, D. E., & Tyson, J. A. 1980, Nature, 285, 641 54

Williams, L. L. R. & Saha, P. 2004, AJ, 128, 2631 92

Wisotzki, L., Becker, T., Christensen, L., Jahnke, K., Helms, A., Kelz, A., Roth, M. M., & Sánchez, S. F. 2004, Astronomische Nachrichten, 325, 135 28, 59

Wood-Vasey, W. M., Miknaitis, G., Stubbs, C. W., Jha, S., Riess, A. G., Garnavich, P. M., Kirshner, R. P., et al. 2007, ApJ, 666, 694 1, 86

Woosley, S. E. & Bloom, J. S. 2006, ARA&A, 44, 507 157

Wright, C. O. & Brainerd, T. G. 2000, ApJ, 534, 34 92

Wucknitz, O., Wisotzki, L., Lopez, S., & Gregg, M. D. 2003, A&A, 405, 445 28, 37, 65, 82

Xanthopoulos, E., Browne, I. W. A., King, L. J., Koopmans, L. V. E., Jackson, N. J., Marlow, D. R., Patnaik, A. R., Porcas, R. W., & Wilkinson, P. N. 1998, MNRAS, 300, 649 59, 60, 174

REFERENCES

Yee, H. K. C. 1988, AJ, 95, 1331 50

Yee, H. K. C. & Ellingson, E. 1994, AJ, 107, 28 49, 55

York, D. G., Khare, P., Vanden Berk, D., Kulkarni, V. P., Crotts, A. P. S., Lauroesch, J. T., Richards, G. T., et al. 2006, MNRAS, 367, 945 26, 27

Zhang, B. & Mészáros, P. 2004, International Journal of Modern Physics A, 19, 2385 157

Ziegler, B. L., Bower, R. G., Smail, I., Davies, R. L., & Lee, D. 2001, MNRAS, 325, 1571 133, 134, 135, 136

Zwicky, F. 1937a, Phys. Rev. Lett., 51, 290 6

—. 1937b, Phys. Rev. Lett., 51, 679 6

Zwicky, F., Herzog, E., & Wild, P. 1963, Catalogue of galaxies and of clusters of galaxies, Vol. 2 (Pasadena: California Institute of Technology (CIT)) 158